ATOMISTIC SIMULATIONS OF DEFECT NUCLEATION AND FREE VOLUME IN NANOCRYSTALLINE MATERIALS

A Thesis
Presented to
The Academic Faculty

by

Garritt J. Tucker

In Partial Fulfillment
of the Requirements for the Degree
Doctor of Philosophy in the
School of Materials Science and Engineering

Georgia Institute of Technology
August 2011

ATOMISTIC SIMULATIONS OF DEFECT NUCLEATION AND FREE VOLUME IN NANOCRYSTALLINE MATERIALS

Approved by:

David L. McDowell, Advisor
School of Materials Science and Engineering
Georgia Institute of Technology

Ken Gall
School of Materials Science and Engineering
Georgia Institute of Technology

Thomas H.B. Sanders
School of Materials Science and Engineering
Georgia Institute of Technology

Min Zhou
School of Materials Science and Engineering
Georgia Institute of Technology

Naresh Thadhani
School of Materials Science and Engineering
Georgia Institute of Technology

Jonathan A. Zimmerman
Mechanics of Materials Department
Sandia National Laboratories

Date Approved: May 5, 2011

ACKNOWLEDGEMENTS

A number of people in my life have contributed greatly to my educational path and to this thesis. First and foremost, I want to thank my advisor, Dr. David L. McDowell, for his role as an academic advisor and mentor. His support and guidance over the past six years have shaped my graduate school career and research interests. I want to thank him for his advice during numerous discussions regarding education, research, employment, and extracurricular interests. Second, I would like to thank the members of my thesis reading committee: Dr. Thomas Sanders, Dr. Naresh Thadhani, Dr. Min Zhou, Dr. Ken Gall, and Dr. Jonathan Zimmerman.

Additional support for this thesis includes US National Science Foundation grant CMMI-0758265 on Multiresolution, Coarse-Grained Modeling of 3D Dislocation Nucleation and Migration, the Carter N. Paden, Jr. Distinguished Chair in Metals Processing, the National Science Foundation through Teragrid resources provided by the Teragrid Science Gateways Program, and support from the Enabling Predictive Simulation Research Institute (EPSRI) at Sandia National Laboratories in Livermore, CA as a student intern with Dr. Jonathan Zimmerman. I would like to further acknowledge and thank Dr. Zimmerman for the opportunity to work with him, and for his guidance both during and since my internship at Sandia National Laboratories.

There are a number of others I would also like to thank, including current and former graduate students at Georgia Tech. My work benefited greatly from many discussions with Doug Spearot, Mark Tschopp, Jason Mayeur, Ryan Austin, Austin Leach, and Shreevant Tiwari. Each of you have helped me at times throughout my graduate school career and I have enjoyed our discussions, both academic and non-academic.

I would also like to thank my family and friends for their continuous support over the years. My parents, Terry and Arnette, have sacrificed so much in their own lives to provide opportunities for my education. It is impossible to fully describe the influence that their

example regarding both perseverance and hard-work has had in my life. Finally, I want to acknowledge the unconditional love and encouragement of my wife, Ashley. I cannot express the impact of your resolve and determination throughout graduate school and the last ten years have had on me. Your passion for science and education have always stimulated my own, and I look forward to whatever God brings our way.

TABLE OF CONTENTS

LIST OF TABLES

LIST OF FIGURES

LIST OF SYMBOLS OR ABBREVIATIONS

bcc	Body-Centered-Cubic.
CNA	Common Neighbor Analysis.
CSL	Coincident Site Lattice.
EAM	Embedded Atom Method.
ECAE	Equal-Channel Angular Extrusion.
ECAP	Equal-Channel Angular Pressing.
ED	Electrodeposition.
fcc	Face-Centered-Cubic.
GB	Grain Boundary.
GBE	Grain Boundary Engineering.
HAGBs	High-Angle Grain Boundaries.
hcp	Hexagonal-Close-Packed.
HPT	High-Pressure Torsion.
HRTEM	High-Resolution Transmission Electron Microscopy.
LPFs	Lineal Path Functions.
MD	Molecular Dynamics.
MS	Molecular Statics.
NC	Nanocrystalline.
NE	Non-Equilibrium.
NEGB	Non-Equilibrium Grain Boundary.
NEMS	Nano-Electro-Mechanical Systems.
NS	Nanostructured.
PC	Polycrystalline.
SPD	Severe Plastic Deformation.
STGBs	Symmetric Tilt Grain Boundaries.
SUM	Structural Unit Model.
TJs	Triple Junctions.
TPCFs	Two-Point Correlation Functions.
UFG	Ultra-fine Grained.

SUMMARY

In this dissertation, atomistic simulations are employed to investigate defect nucleation and free volume of grain boundaries and nanocrystalline materials. Nanocrystalline materials are of particular interest due to their improved mechanical properties and alternative strain accommodation processes at the nanoscale. These processes, or deformation mechanisms, within nanocrystalline materials are strongly dictated by the larger volume fraction of grain boundaries and interfaces due to smaller average grain sizes. The behavior of grain boundaries within nanocrystalline materials is still largely unknown. One reason is that experimental investigation at this scale is often difficult, time consuming, expensive, or impossible with current resources. Atomistic simulations have shown the potential to probe fundamental behavior at these length scales and provide vital insight into material mechanisms. Therefore, work conducted in this thesis will utilize atomistic simulations to explore structure-property relationships of face-centered-cubic (fcc) grain boundaries, and investigate the deformation of nanocrystalline copper as a function of average grain size.

Molecular statics employing an embedded atom method potential are utilized in this thesis to construct fcc bicrystalline grain boundary structures. The boundaries are then deformed at 10K under uniaxial tension and simple shear at a constant strain rate to elucidate the influence of interfacial structure on inelastic deformation. An algorithm is also presented to compute interfacial free volume in the bicrystalline structures and quantitatively track its evolution with imposed strain. Representative non-equilibrium grain boundaries are instantiated using excess free volume as a measure of the degree of non-equilibrium state, and then deformed to explore the influence of structure on deformation response. It is shown that excess free volume alters interfacial atomic processes critical for dislocation nucleation and grain boundary sliding, resulting in lower grain boundary strength.

Volume-averaged kinematic metrics are formulated from continuum mechanics theory

and applied to the results of atomistic simulations to provide new insight into atomic deformation and rotation fields. Inelastic deformation mechanisms common to nanocrystalline metals, such as heterogeneous dislocation nucleation, grain boundary sliding, and grain boundary migration are analyzed with the proposed metrics using bicrystalline grain boundaries. The results indicate that unique deformation fields are associated with each mechanism and a sense of the deformation history of the atomic fields are provided through the utilization of neighbor lists from the reference configuration. Other metrics use current configuration quantities to display the fronts of propagating dislocation networks.

The kinematic metrics are also leveraged to explore the tensile deformation of nanocrystalline copper at 10K. The distribution of different strain accommodation mechanisms is estimated and we are able to partition the role of competing mechanisms in the overall strain of the nanocrystalline structure as a function of grain size. Grain boundaries are observed to be influential in smaller grained structures, while dislocation glide is more influential as grain size increases. Under compression, however, the resolved compressive normal stress on interfaces hinders grain boundary plasticity, leading to a tension-compression asymmetry in the strength of nanocrystalline copper. The mechanisms responsible for the asymmetry are probed with atomistic simulations and the volume-averaged metrics. Finally, the utility of the metrics in capturing non-local nanoscale deformation behavior and their potential to inform higher-scaled models is discussed.

CHAPTER I

INTRODUCTION

1.1 Motivation

As the theoretical physicist, Sir Frederick Charles Franck, said, 'Crystals are like people: it is the defects in them that make them interesting.' Fundamental research in Materials Science and Engineering focuses on linking structure and behavior, and elucidating the influence of defects on material behavior. Although the atomic-scale contributes to the origins of bulk properties, material functionality is ultimately realized on the macroscale. Therefore, the advancement and novel contributions of research in Materials Science and Engineering will eventually be determined by our ability to understand and tailor material properties for engineering applications and technological innovations.

Defects and other nanoscale features are paramount in this quest, and often leveraged for bulk functionality. This idea parallels the profound thoughts by Richard Feynman in 1959 [70], when he questioned, 'What would happen if we could arrange the atoms one by one the way we want them?' His insight might be in part responsible for the past 50 years of materials innovation, related to scientific thrusts in the atomic-scale and the emergence of *Nanotechnology*.

Nanostructured (NS) materials are defined as materials composed of structural elements with nanoscale dimensions (less than 100 nm). Due to the limited size of morphological features comprising nanostructured materials, unique properties are often encountered. With regard to metallic structures, nanocrystalline (NC) metals are composed of crystalline grains with an average diameter of less than 100 nm. Therefore, it is critical to understand the fundamental attributes of nanoscale features in NC materials, such as grain boundaries (GBs), other intercrystalline regions, and their junctions.

In the past 20 years, intercrystalline regions (e.g., GBs and triple junctions (TJs)) have received increasing attention from the materials science and mechanics communities due

to their importance in NC materials behavior. Advanced properties commonly observed in these materials have stimulated substantial research efforts in nanoscale behavior [82]. Improvements in mechanical, chemical, thermal, and other functional properties relative to those observed in traditional coarse-grained polycrystalline (PC) materials have further fueled considerable interest across the scientific and engineering communities. For example, deformation accommodation processes and their cooperation leading to the enhanced mechanical properties commonly observed are still not quantitatively well understood. Furthermore, reducing the average grain size to the nanoscale generates a larger concentration of GBs and TJs and a higher percentage of atoms located within these regions; therefore, it is crucial to understand the influence of GBs on material properties and behavior.

With regard to the mechanical behavior of PC metals, the well known Hall-Petch relation [87, 166] correlates yield strength to average grain size, i.e.,

$$\sigma_y = \sigma_o + \frac{k}{\sqrt{d}} \tag{1}$$

where σ_y is the yield stress, σ_o is a material constant detailing the resistance of the lattice to migrating dislocations, k is a strengthening parameter, and d is the average grain diameter, or grain size. Yield strength increases with decreasing average grain size according to this relation. The Hall-Petch relationship essentially reflects the physical phenomenon of grain boundary (GB) strengthening, where GBs act as a barrier for dislocation motion. In materials where dislocation glide is the primary carrier of deformation, a greater number density of GBs generally leads to higher yield stresses. A series of tensile stress-strain plots are shown in Figure 1 for aluminum at a constant strain rate with varying grain sizes [106] to elucidate the influence of average grain size on the bulk mechanical behavior. As average grain size in the aluminum sample processed by ball milling is reduced to 40 nm from 45000 nm, the associated yield strength increases.

Since the original formulation of the Hall-Petch relation and the development of materials with average grain sizes less than 100 nm, experimental [39, 140, 182] and theoretical [140, 186] investigations have demonstrated a breakdown of this relationship at average grain sizes on the order of 10-20 nm (i.e., the so called 'Inverse Hall-Petch' relationship)

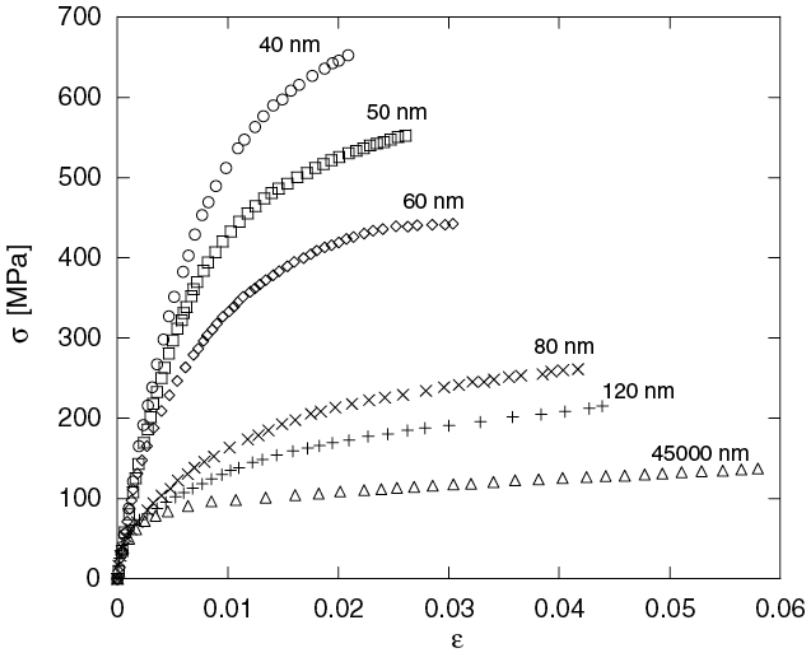

Figure 1: Tensile stress-strain plots for aluminum at a constant strain rate. The average grain size ranges from 45000 nm down to 40 nm [106].

in face-centered-cubic (fcc)metals. Furthermore, the results of [39, 140, 182, 186] agree that deformation mechanisms active at this scale need to be better understood, and investigations into specific GB deformation phenomena are necessary. Advancements in GB engineering [173, 289] are also possible by investigating the role of GB structure on the mechanical behavior (i.e., dislocation nucleation and interaction) and in the underlying nanoscale processes of NC metals. Fundamental insight into damage evolution and failure can only be developed across a range of length scales, starting with the nanoscale structure of NC materials.

The development of NS materials and nanodevices (i.e., nano-electro-mechanical systems, NEMS) is currently of great technological interest. However, small-scale experiments on these materials/structures are time consuming and technically challenging due to the length and time scales involved. Thus, experimental investigations into the dynamic deformation behavior at this length scale is a grand challenge. Therefore, one avenue is to employ atomistic simulations to examine defect nucleation phenomena under multiple deformation modes for various GB structures in NC materials. Spearot *et al.* [207, 209] have

shown through bicrystal simulations that GB structure plays a critical role in defect nucleation in copper symmetric tilt GBs. An additional significant contribution would be to systematically characterize dislocation nucleation and shuffling of atoms in GB segments of NC materials as a function of GB degrees of freedom (misorientation and boundary plane). Furthermore, free volume evolution and its relationship to GB structure and dislocation nucleation are also of great importance. Such knowledge can advance our understanding and promote the development of NC materials with improved strength, ductility, fracture and/or fatigue resistance.

Molecular dynamics (MD) simulations represent a small portion of computational methods aimed at uncovering the basic physical principles and phenomena which govern material behavior. Traditionally, MD was employed to study the behavior of hard spheres, gases, and liquids or simple particle systems with classical dynamics relationships in the 1950s and 1960s [5, 4, 6, 172]. The application of MD to the study of materials behavior has since advanced the field of Materials Science and Engineering. However, inherent to atomistic simulations (such as MD) are limited length and time scales, which will be further discussed in later sections.

In 2004, Buehler and coworkers [28] used atomistic simulations consisting of a one billion atom system to explore dynamic dislocation processes of nucleation and arrangement, equal to a sample with dimensions of $1/3\mu m^3$, as shown in Figure 2. They used MD simulations to investigate dislocation plasticity and provided information about possible mechanisms critical for material hardening during dynamic deformation near crack tips for large dislocation populations. While these results display the potential of MD simulations to elucidate vital material behavior, the translation of these results into continuum models is still not well understood nor currently feasible for most research groups.

However, research such as this highlight the importance of exploring defects and nanoscale deformation behavior, where atomistic simulations offer one potential avenue for exploration. Furthermore, it will be imperative in the future to provide the necessary framework to translate data and information extracted from MD simulations to larger scaled models, such as crystal plasticity, micropolar/micromorphic theories, and strain-gradient methods.

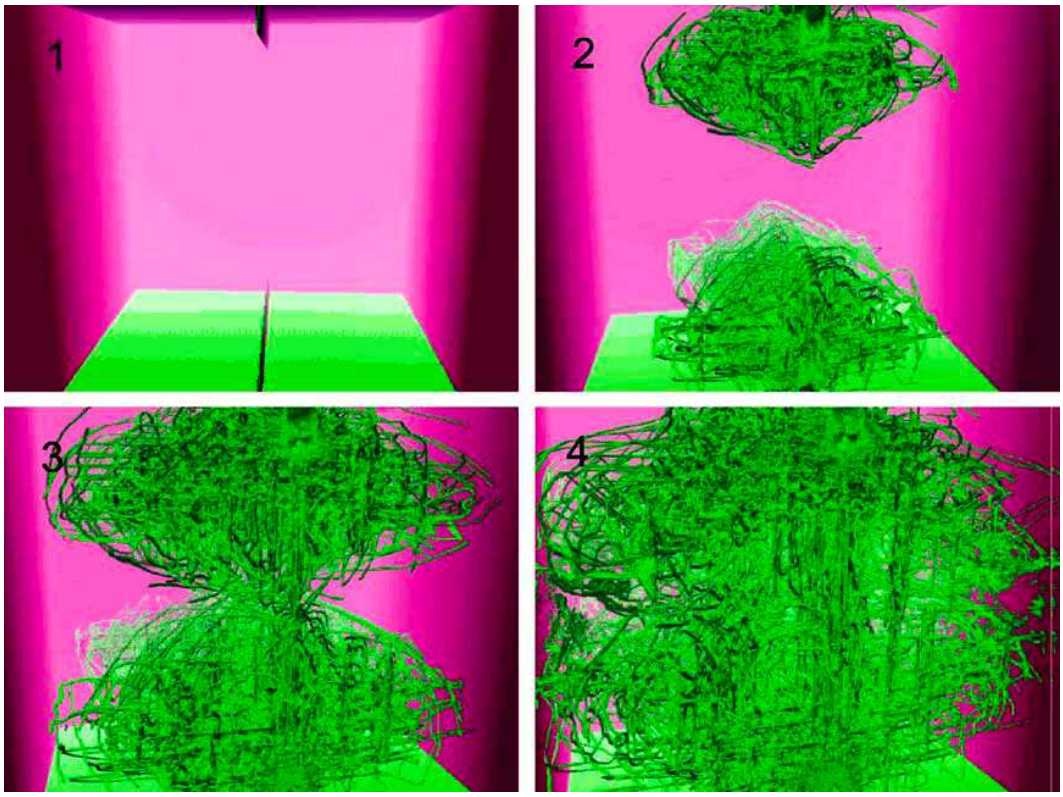

Figure 2: A billion atom simulation performed by Buehler *et al.* [28] exploring dislocation nucleation, interaction, and arrangement near opposing crack tips in a ductile material, only atoms with higher potential energy are shown for ease in defect visualization.

As Buehler *et al.* emphasize [28], 'A very important point is that it is not until clever analysis schemes are applied that useful information can be extracted from the simulations.' Coarse-grained MD approaches and extraction of vital nanoscale information from atomistic simulations will be important milestones for the computational Materials Science and Engineering field. Our ability to capture key behavior and the multiscale relationships that dictate material functionality will advance the capabilities of computational resources as a tool for Materials Science and Engineering research.

1.2 Problem Definition

In this thesis, atomistic simulations will be employed to investigate the deformation mechanisms governing material behavior observed in NC materials, including atomic shuffling,

free volume evolution, dislocation nucleation/mediation and other features of GB mechanisms during inelastic deformation. The specific aim of this research is to elucidate the influence of nanoscale structural features and deformation phenomena affecting the behavior of interfaces and NC metals. The post-processing analysis offered in this dissertation is performed using traditional quantities such as atomic energy, centrosymmetry, and crystal structure in addition to newly developed volume-averaged kinematic metrics that are able to capture the nonlocality of various deformation fields.

GB structure is known to have significant influence on dislocation nucleation [203, 204, 207, 225, 226, 230]. However, the impact of inherent free volume (whether near-equilibrium or non-equilibrium) and its evolution on dislocation behavior is still not well understood. Van Swygenhoven *et al.* [264] have shown that free volume influences dislocation emission from GBs in NC materials, and Randle discusses its affect on GB thermodynamics [173]. Additionally, atomic shuffling and free volume migration from nearby TJs are also linked to GB sliding and rearrangement [188, 260, 264, 265], mechanisms commonly found in NC metals.

Furthermore, these phenomena have been observed to occur just prior to dislocation nucleation from GB networks in NC materials [264]. During plastic deformation, the nanoscale structure of metallic polycrystals evolves substantially. This includes point defect and dislocation generation [115, 185, 50, 295]. For example, uniaxial compression tests on copper samples by Ungar and coworkers [241, 240, 318] have shown increasing dislocation density levels and vacancy concentrations with plastic deformation. Correlations between evolving dislocation density and vacancy concentration at the nanoscale can be further understood by performing MD simulations, providing insight into evolution of structure during deformation of high angle boundaries in NC and PC materials.

For this reason, in the past 20-25 years, GBs have been the subject of numerous research efforts, and the driving factor of GB engineering (GBE) [173, 174, 177, 178, 290, 289, 294, 291, 292, 293]. The structure-property relationships of GBs and their influence on macroscopic material behavior is still an area of active research. The complexity of GB structure is but one obstacle in defining GB properties. To address this issue, atomistic

simulations have been used to study both GB structure and deformation using bicrystalline geometries [29, 49, 180, 181, 183, 184, 203, 204, 207, 208, 221, 223, 222, 229, 226, 230, 235, 234]. In addition, NC materials and the active strain accommodation mechanisms are being explored using atomistic methods. However, an efficient technique to translate this nanoscale information up into larger-scaled computational models is still being developed. Accordingly, this research will address the following questions concerning GB structure and deformation.

1. How are GB structure and interfacial free volume related in near-equilibrium planar symmetric tilt GBs (STGBs)? Are certain minimum energy atomic structural units responsible for higher free volume interfaces in fcc metals? How does the distribution of free volume change as misorientation angle and GB structure change? Is there an efficient method to compute the spatial distribution and concentration of free volume in nanoscale structures?

2. How does the deformation behavior of copper bicrystalline boundaries change as the stress state changes? Is there an asymmetry in the dislocation nucleation processes under tension and compression? What are the important factors in dislocation emission from GBs during uniaxial loading? Is there a correlation between certain structural units and GB strength during dislocation nucleation?

3. How does interfacial free volume evolve during dislocation nucleation/emission from planar GBs? Does free volume migration occur within bicrystalline boundaries during dislocation emission? Are certain structural units more susceptible to deformation and free volume evolution during dislocation nucleation? Can free volume migration relate to important GB deformation mechanisms during straining?

4. Can non-equilibrium (NE) boundary structures be instantiated in an approximate way using excess free volume addition? How does the structure and energy differ for NE boundaries as compared to their equilibrium counterparts? Is excess interfacial free volume a useful measure of the NE state of a boundary? How does the deformation of

boundaries change as a function of their NE state? Are either dislocation nucleation under tension or GB sliding under shear enhanced for non-equilibrium GBs (NEGBs)?

As each of these questions are addressed, fundamental information about GB structure and deformation will be provided.

The role of GBs and other nanoscale features in the deformation kinematics and kinetics of NC metals is still not well understood, particularly the competition and interplay of GB-mediated and bulk-mediated mechanisms. Therefore, this research aims to address the following questions.

1. Can microscale metrics for deformation be formulated from continuum mechanics theory for utilization in interpreting atomistic simulations? Can the nonlocality of nanoscale deformation be probed using different averaging domains for the kinematic metrics? What information can be extracted from atomistic simulations using microscale metrics? Can the metrics differentiate between various mechanisms in nanoscale structures?

2. Can the deformation processes of NC metals be explored using kinematic metrics? What are advantages of kinematic metrics as compared to traditional atomistic quantities used in analysis? Is it possible to resolve and partition the inelastic deformation in NC structures?

3. What are the mechanisms underlying tension-compression asymmetry in the deformation of NC metals? How does the distribution of dislocation activity and GB mechanisms differ as a function of grain size and loading state?

The deformation kinematics of NC metals is complex, and answers to these questions can be explored using metrics from continuum mechanics theory within an atomistic framework. Furthermore, the metrics proposed in this work have the potential to inform higher-order computational models of vital nanoscale interface and lattice deformation behavior.

1.3 Thesis Objectives

There are five primary objectives in this dissertation dealing with atomistic investigations into face-centered-cubic (fcc) GB behavior and NC deformation; specifically, this dissertation is aimed at:

- Investigating the relationship between structure and free volume in planar near-equilibrium bicrystalline GBs for fcc metals (e.g., copper and aluminum).
- Exploring the inelastic deformation behavior of metallic bicrystalline boundaries under tension, compression, and shear. Also, computing the evolution of free volume during dislocation nucleation for planar STGBs.
- Develop a methodology to construct representative NE interfacial structures based on excess free volume without the necessity of simulating numerous defect/boundary interactions. The uniaxial tensile and simple shear deformation of NEGBs is also explored to further relate excess free volume concentration to interface behavior.
- Formulating kinematic quantities from continuum mechanics within an atomistic framework for analyzing nanoscale deformation processes.
- Utilizing fully 3D NC fcc structures to gain further understanding in the role of various structural features on deformation and free volume migration.
- We will also use the kinematic metrics to filter different deformation mechanisms accommodating strain in NC materials, creating a multiscale viewpoint of such processes.

Based on previous research completed in our research group [205, 203, 204, 207, 221] on calculating and constructing a range of equilibrium STGB structures for copper and aluminum using an embedded atom method potential, we develop a method for computing the associated interfacial free volume. The details will be outlined later in this dissertation, but we are able to determine that different free volume distributions correlate directly with different near-equilibrium GB structures. As the misorientation angle changes for STGBs,

the structural unit composition and atomic structure changes. Therefore, there is an inherent relationship between GB structure and free volume for interfaces and NE atomic configurations. It is imperative to relate interface structural units with the spatial distribution of free volume, and understand how connected free volume configurations emerge as a function of misorientation angle.

Second, using MD simulations on the near-equilibrium GB structures, the inelastic deformation behavior under uniaxial tension, uniaxial compression, and simple shear is explored. Building on previously found relationships for boundary strength and misorientation [184, 207], suggestions on the role of free volume in boundary deformation and its evolution during straining are made [229, 235]. Also, the influence of both Schmid and non-Schmid stresses on dislocation nucleation under tension and compression are outlined for a specific class of high free volume GBs in copper [230]. As GB structure changes due to imposed deformation, free volume evolves and certain structural units have a greater propensity for atomic rearrangement. GBs accommodate the nucleation of dislocations through atomic rearrangement and free volume migration away from nucleation sites.

Third, motivated by recent investigations into the structure of interfaces by materials that have undergone severe plastic deformation [42, 154, 155, 156, 249, 248, 243, 244, 247, 245, 252, 305], we develop a technique for instantiating representative NEGB structures within a bicrystalline framework using excess free volume as an approximate measure of NE state. The structure of boundaries that have experienced multiple interactions with lattice defects are altered and contain excess levels of free volume. These boundaries are called 'non-equilibrium' and provide nanostructured materials with altered bulk properties. NEGBs differ from their near-equilibrium counterparts with regard to structure, energy, free volume, and deformation. MD simulations investigate the uniaxial tension and shear deformation at low temperature and are used to explore the dependence of boundary mechanics on structure. Various deformation mechanisms are observed and atomic rearrangement in the boundaries is enhanced due to an altered atomic structure and excess free volume concentration. Peak boundary strength under both tension and shear is directly influenced by the level of excess free volume and NE state.

Fourth, continuum mechanics based measures of deformation are formulated within an atomistic framework based on the description of interatomic strain and the deformation gradient [330, 236]. As the deformation gradient is formulated based on atomic neighbor lists in the reference configuration [330], a range of additional kinematic quantities can then be formulated [236]. Measures of lattice rotation, microrotation, strain, velocity gradient, curvature, and vorticity are developed, where each metric provides additional information of nanoscale behavior during deformation. Some metrics are based on the reference configuration (e.g., deformation gradient, microrotation, and strain), while others (e.g., velocity gradient, and vorticity) are based on current configuration quantities (i.e., neighbor lists). GBs and NC materials offer an extraordinary platform to exercise the ability of these metrics in uncovering information. As a first step in understanding the kinematics of deformation, dislocation nucleation, GB sliding, and GB migration in bicrystals is explored utilizing the metrics.

Finally, although there has been significant research in NC materials (especially using atomistic simulations), additional research on the role of structural features is necessary. Therefore, we employ three-dimensional NC structures to investigate relationships between nanoscale structure and bulk mechanical behavior. This research highlights the fundamental role that GBs have on inelastic deformation mechanisms. Furthermore, it will be imperative for larger-scaled models to incorporate mechanisms understood by application of kinematics applied at the nanoscale to accurately capture multiscale deformation phenomena.

1.4 Significance of Research

Understanding the role of both GB structure and interfacial free volume in inelastic deformation, such as dislocation nucleation, GB sliding, atomic shuffling, and migration is critical for innovative areas such as GBE. For GBE purposes, GBs possessing unique properties can be preferentially populated within engineered materials for advanced functionality, such as $\Sigma 3$ and $\Sigma 9$ GBs [175, 176]. In this regard, fundamental knowledge about how GB structure and free volume influence interfacial deformation mechanisms, such as dislocation nucleation and GB sliding, provided in this thesis can significantly help in the development of

materials with enhanced mechanical properties.

This thesis explores correlations between GB structure and the associated strain accommodation mechanisms and quantitatively tracks free volume evolution during the nucleation/emission of GB dislocations. Efforts to improve bulk material properties can significantly benefit from insight gained in this work, possibly through modified GB deformation rules and nanoscale structure-property relationships for strain accommodation in NC fcc metals. For example, recent work by both Capolungo *et al.* [33] and Warner *et al.* [288] have shown the potential for MD simulations to inform higher-order computational models. Important aspects of plastic deformation (such as competing deformation mechanisms and interfacial dislocation nucleation) can either be incorporated or modeled using insight gained through MD simulations. However, a broader understanding of GB deformation processes is still necessary in the context of NC material behavior, and the influence of different plastic deformation mechanisms in NC materials behavior is still not well understood.

As discussed in upcoming chapters, recent work has shown that many strain accommodation processes are active in NC materials and depend on the average grain size, GB structure/network, grain size distribution, and loading conditions [19, 18, 36, 39, 44, 45, 66, 69, 79, 75, 80, 84, 102, 117, 121, 123, 126, 127, 125, 135, 138, 145, 160, 187, 192, 269, 274, 277]. Since the importance of GB plasticity (i.e., dislocation nucleation/emission, sliding, and atomic reordering) increases as grain size is reduced, as in NC metals, this dissertation provides vital knowledge about GB structure-property relationships critical to NC material behavior. However, translating information obtained from MD into large-scaled computational methods is no trivial task [28]. Therefore, research conducted in this thesis also presents a new framework (through volume-averaged metrics) for estimated nonlocal kinematic behavior from MD simulations as a means to inform higher-order models. By leveraging these metrics, atomic deformation fields and strain accommodation mechanisms are investigated and we are able to resolve the role of various mechanisms in NC metal deformation. Recent models [299, 300, 306] have also shown the advantages of improved GB descriptions and capturing nanoscale behavior (such as dislocation nucleation and migration) with regard to modeling bulk material behavior. Therefore, we also discuss the potential for linking the

atomistic scale with higher-order models using both MD simulations and the microscale kinematic metrics.

1.5 Thesis Structure

This dissertation is organized as follows. Chapter 2 provides the background information regarding GBs, NC materials, and the simulation methodology. First, the theory of atomistic simulations is detailed, outlining both Molecular Statics and Molecular Dynamics. Then, the embedded atom method is discussed along with the bicrystalline and NC simulation methodology. Because different loading states are utilized in this work, each is described in detail with appropriate illustrations. Following simulation methodology, specific concepts critical to understanding GBs and their structure are given. Free volume is an important aspect of GB studies in this thesis, so its description and methodology for computation are detailed. Finally, NC materials are introduced, beginning with their processing/fabrication, then their microstructural features, and lastly, their mechanical properties will be discussed.

The research results in this thesis are subdivided into four categories: GB structure and deformation (Chapter 3), excess free volume and interfaces (Chapter 4), microscale kinematic metric development (Chapter 5), and NC metal deformation (Chapter 6). Each results chapter is organized with introduction, methodology, results/discussion, and summary sections so that it is self-contained. The *results* chapters presented in this dissertation are based on published/submitted journal manuscripts or articles in preparation.

GB structure, free volume, and interfacial deformation are investigated in Chapter 3. This chapter is a compilation and restatement of the contributions of the present author to three separate journal publications [229, 230, 235] in separate sections within the chapter. The first section of this chapter is dedicated to the investigation of GB structure and free volume within symmetric tilt GBs for planar fcc boundaries containing the E structural unit. All work dealing with the calculation, analysis, and visualization of free volume was a valuable contribution of the present author and critical for additional work conducted in later chapters. Next, an investigation into the tension-compression asymmetry of E structural unit boundaries is presented, and differences in the dislocation nucleation mechanism

are explained with regard to the resolved stress state. The present author was partially responsible for analyzing the asymmetry and investigating differences in dislocation emission with regard to the distribution of E structural units in the GB. Finally, the evolution of GB structure and free volume during dislocation nucleation is discussed for various GB structures and misorientation angles. This research investigates whether certain GB structural units have a greater propensity for atomic rearrangement and free volume migration during dislocation nucleation.

The influence of excess free volume on GB structure and properties is explored in Chapter 4, and represents the work published by the author [234]. Non-equilibrium GBs and their associated excess free volume are the subject of this chapter. In addition, investigations are undertaken regarding differences in structure, energy, free volume, and deformation behavior under uniaxial tension and shear.

Chapter 5 outlines the development of microscale kinematic metrics from continuum mechanics theory for use in rendering results of atomistic simulations [236, 237]. Various volume-averaged metrics are formulated to analyze nanoscale simulations and provide valuable and novel insight into nonlocal atomic deformation fields. The utility of the metrics are shown using bicrystalline boundaries under tension and shear, analyzing the deformation fields during dislocation nucleation, GB sliding, and GB migration.

The deformation of fcc NC structures are outlined in Chapter 6 using atomistic simulations [233]. The objective here is to ascertain the mechanical dependence on structure and grain size for NC ensembles deformed under uniaxial tension at low temperature. To further analyze the results, the kinematic metrics derived in Chapter 5 are leveraged to uncover vital deformation behavior not accessible to commonly employed atomic measures. Furthermore, the metrics are used to resolve the contribution of various mechanisms to the overall strain accommodation, and show potential for extracting key nanoscale kinematical information from atomistic simulations.

Finally, Chapter 7 summarizes the significant findings of this thesis and the overall contribution of this dissertation as a whole. Important conclusions and a short summary of each chapter is provided along with potential extensions for each chapter. Last, we discuss

additional work and future research directions that build upon this thesis.

CHAPTER II

BACKGROUND AND METHODOLOGY

2.1 Overview of Atomistic Simulation

The atomistic viewpoint of material behavior has long been sought after to understand the fundamental nature of key processes responsible for material deformation and failure. Atomistic simulations represent the collection of computational methods used to achieve such goals. In particular, both molecular statics (MS) and molecular dynamics (MD) are included as atomistic simulations in this work. Grain boundaries (GBs), dislocations, and other defects all represent ideal attributes amenable to understanding using atomistic simulations. Simplicity and efficient computational implementation has often been noted to be two of the main strengths of atomistic simulations and has lead to its ever increasing role in modern materials science research [27].

From the beginning of MD simulations, which explored the thermodynamical behavior of liquids and gases, to more recent explorations of multi-billion atom simulations [28, 101, 157], both the utility and simplicity of the atomistic viewpoint is evident. In the atomistic framework, point masses in space represent atoms and their interaction is captured via the interatomic potential which describes potential energy as a function of atomic spacing or distance (r). Thus, the force ($\mathbf{F}$) on an atom α is related to the interatomic potential ($\mathbf{U}$) through the gradient operator acting on $\mathbf{U}$ or the relationship,

$$\mathbf{F}^{\alpha} = -\frac{\partial \mathbf{U}(\mathbf{r}^{N})}{\partial \mathbf{r}^{\alpha}} \tag{2}$$

where $\mathbf{r}^{\alpha}$ represents the position vector of atom α in terms of the global coordinate axis, and $\mathbf{U}(\mathbf{r}^{N})$ therefore represents the potential energy as a function of the position vectors to all N neighboring atoms influencing atom α (i.e., nonlocal interactions). The force on an individual atom α is thus the negative derivative of $\mathbf{U}$ with respect to the position vector of atom α, $\mathbf{r}^{\alpha}$, relative to surrounding atoms. This formulation is straightforward in nature, and the resulting behavior of a particular material system of point masses (or atoms) is

then defined when the appropriate interatomic potential is chosen to govern interactions of the point masses. Therefore, proper choice of an interatomic potential is fundamental in atomistic simulations, and thus will be discussed in detail in later sections.

2.1.1 Molecular Statics and Dynamics

Atomistic simulations employed in this work encompass two types of simulations: MS and MD. MS simulations represent numerical techniques leveraged to minimize the potential energy of the system of interest. MD simulations consider not only atomic positions, but velocity (due to thermal contribution) and force (due to the interatomic potential). To solve for the resulting evolution of position and velocity of the atoms in the system, an iterative process which numerically integrates Newton's second law is performed for all mobile particles. Then the system trajectory is solved, and various phenomena and behavior can be extracted through post-processing tools and calculation of both local and nonlocal metrics (as will be discussed).

In MS, the global minimum of the potential energy function describing the system is iteratively calculated. This potential energy function is minimized producing the atomic positions expected at 0K and therefore specifies the most probable athermal system state, and is important as a precursor to subsequent finite temperature dynamics analysis for structures that are initially near equilibrium. Such structures, in the context of nanocrystalline (NC) metals, might be processed by electrodeposition. As an example, Spearot *et al.* [207] used an energy minimization scheme to compute bicrystal structures to conduct uniaxial tension simulations. There are a variety of MS methods. Monte Carlo methods sample a collection of random system arrangements [144, 143] and others use conjugate gradient schemes [275, 196]. In the proposed research, conjugate gradient methods will be employed, based on solving for the minimum energy configuration by utilizing previous atomic positions and a properly chosen interatomic potential. Since no method guarantees the absolute minimum energy configuration, numerous starting configurations are used to obtain the minimum energy structure for bicrystalline configurations, utilizing in-plane rigid body translations and normal volume expansion at the interface.

After a minimum energy configuration is found, MD is employed to solve for resulting atomic motion controlled by equations of classical dynamics, specifically Newton's second law of motion. The atomic movements are calculated by numerical integration of this relationship, and are constrained by coupling the equations of motion of all atoms in the system. The resulting atomic positions after a single time step are calculated using the finite difference method based on acceleration. However, the initial conditions are the two prior atomic positions; therefore, use of the velocity Verlet algorithm is generally preferred. The Velocity Verlet algorithm only requires the initial position and velocity of each atom. The MD simulations used in this work are also capable of performing constant strain-rate conditions in the framework of the isothermal-isobaric (NPT), canonical (NVT), and micro-canonical (NVE) equations of motion updating atomic positions and velocities throughout the simulation.

The goal of many atomistic studies is to elucidate the role of nanoscale features on behavior or material properties. To attain this information, it is beneficial to study atomic scale behavior that is representative of what might occur in bulk. However, the number of atoms to achieve this objective would overwhelm most available computational resources. Therefore, periodic boundary conditions are often implemented in atomistic simulations to approximate bulk behavior of atomic systems. In this thesis, both periodic and 'constrained' surface boundary conditions are utilized for different purposes of equilibration and deformation.

Periodic boundary conditions are leveraged to approximate bulk material behavior for a single simulation cell. The idea behind periodic boundary conditions is that the one simulation cell of interest is infinitely duplicated in chosen orthogonal spatial dimensions; therefore, no free surfaces exist in these dimensions. 'Constrained' surfaces (as will be detailed later) provide the appropriate framework for simulating shear deformation of bicrystalline structures accompanied by non-orthogonal shape changes to the simulation cell. We employ in such cases 'constrained' surfaces, where all atoms located within an a certain distance of the surface are held fixed in their perfect equilibrium positions and constrained to move as a rigid group. Atoms located in neighboring positions to the rigid atoms will then only be

affected by the imposed surface displacement boundary conditions on the rigid group. Figure 3 shows an illustration of both (a) 3D periodic boundary conditions and (b) constrained surface displacement for shear simulations.

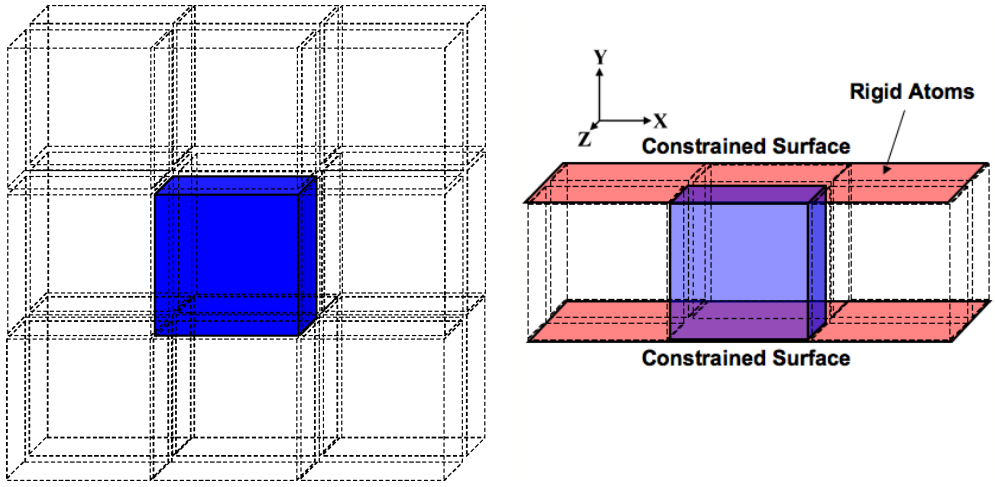

(a) (b)

Figure 3: A schematic showing (a) 3D periodic boundary conditions and (b) 2D periodic boundary conditions with constrained surfaces to impose desired shear displacements.

In Figure 3(a), periodic boundary conditions are employed in all directions. The computational cell is highlighted blue and is effectively duplicated in all dimensions. Therefore, atoms on the upper and lower surfaces of the computational cell are interacting as neighbors, as well as atoms located on the lateral faces of the cell. In 3(b), periodicity is maintained in the X and Z directions, but with constrained surfaces in the Y direction. This means that the computational cell is duplicated due to periodicity only in the X and Z directions, but not in Y.

For highly non-equilibrium (NE) structures processed using severe plastic deformation (SPD) methods, alternative schemes must be developed to reflect the much higher defect densities and associated change of structure observed within intercrystalline regions. For this purpose, we have developed a biased Monte Carlo approach based on constructing non-equilibrium grain boundaries (NEGBs) starting from equilibrium boundaries. This approach is premised on the concept of excess free volume, which we will discuss in great detail later, where we leverage the level of excess interfacial free volume in non-equilibrium boundaries as compared to their equilibrium counterparts as the degree of non-equilibrium

state of a boundary. Many researchers have noted higher energy boundaries in materials deformed via SPD techniques [42, 148, 153, 154] along with excess defect content; however, as Chuvil'deev suggests [42], the degree of non-equilibrium state of a boundary can be estimated by its excess free volume content.

Two atomistic codes (WARP and LAMMPS [167]) were used in this dissertation, and both were written by Dr. Steve Plimpton at Sandia National Laboratories in Albuquerque, NM. Modifications to the original WARP code were implemented by Dr. Doug Spearot to (i) perform energy minimization (via a conjugate gradient algorithm written by Dr. Jonathan Zimmerman at Sandia National Laboratories in Livermore, CA) calculations, (ii) perform simulations in the isobaric-isothermal canonical (NPT) ensemble, and (iii) perform constant strain-rate MD simulations. However, the current version of LAMMPS, has newly developed features that mirror those of our modified WARP; therefore, most MD simulations performed in this work utilize LAMMPS, while the minimum energy bicrystalline structures were constructed from WARP.

2.1.2 The Embedded-Atom Method

To effectively account for atomic interactions, this research will employ potentials based on the Embedded Atom Method (EAM) for the appropriate fcc metals. The EAM was developed by Daw and Baskes [46, 47] to approximate interatomic interactions in fcc metallic materials. Since the EAM is designed to characterize metallic bonding interactions, the potential energy functions must consider the background electron density present in this environment. Therefore, energy ($\mathbf{E}$) is a function of both the energy required to embed an atom into this local electron density resulting from all neighboring atoms in the system and a pair potential term for each atom and its neighbors. To capture this effect in addition to the pair interaction, two terms are included in the energy function, i.e.,

$$\mathbf{E}(r_\alpha) = \frac{1}{2} \sum_{\alpha,\beta(\beta\neq\alpha)} \phi_{\alpha\beta}(r_{\alpha\beta}) + \sum_{\alpha} \mathbf{\Phi}(\rho_\alpha) \tag{3}$$

The first term defines pair interactions dependent on the interatomic distance between atoms α and β, and the second term ($\mathbf{\Phi}(\rho_\alpha)$) is the embedding energy contribution which

relies on the averaged local electron density, ρ_α, calculated from

$$\rho_\alpha = \sum_{\alpha \neq \beta} \mathbf{\Omega}(r_{\alpha\beta}) \tag{4}$$

The function $\mathbf{\Omega}(r_{\alpha\beta})$ represents the contribution of individual atoms to the electron density field at a particular point. However, a key assumption in EAM potentials is that the electron density, or bonding nature of each element is spherical (non-directional). Therefore, it is not applicable to materials for which angular-dependent bonding is important. This assumption in the formulation EAM potentials is therefore not valid for body-centered-cubic (bcc) and hexagonal-close-packed (hcp) materials. Even some fcc material systems exhibit more directional bonding character [48].

The interatomic bonding in aluminum is slightly directional; however, the calculated stacking fault energies from the EAM potentials used in this work do a better job than other EAM potentials, as will be discussed later. For material systems exhibiting directionality in their interatomic bonding or where angular dependencies are necessary in the development of the potential, Baskes *et al.* [12, 11, 13, 14] formulated the modified embedded atom method (MEAM). However, several problems with the original MEAM formulation surfaced in MD simulations; therefore, the second nearest neighbor MEAM (2MEAM) was developed [119]. Applying the 2MEAM to fcc metals resulted in a much better fit to experimental values of surface energies and structure from MD [120]. Although improvement was attained with the 2MEAM for fcc metals, the stacking fault energies in aluminum from the original EAM potential from Mishin *et al.* [149] were still superior when compared to experimental data.

In this research, we use EAM potentials fit to both aluminum [149] and copper [150]. Important physical properties such as the equilibrium lattice parameter, the cohesive energy, the vacancy formation energy, elastic constants, vacancy formation energy, phonon frequencies, energies of hcp, bcc, and diamond cubic structures, and intrinsic stacking fault energy were used to fit these potentials. However, various weights were also imposed to each variable when developing the potential. This fitting procedure led to good estimations of both the stable and unstable stacking fault energies in aluminum and copper [21, 333], which are crucial in determining the proper defect structures and deformation processes

investigated in this dissertation (i.e., partial and full dislocation nucleation). Additionally, according to density functional theory calculations [88], the EAM potentials of Mishin *et al.* [149, 150] provide better estimates of the stacking fault energies (i.e., stable and unstable) than other common EAM potentials [59, 71, 128, 281] used in MD simulations found in the literature.

The importance of both the stable (γ_{sf}) and unstable (γ_{usf}) stacking fault energies in terms of dislocation nucleation, GB structure, and splitting distance between partial dislocations has recently been discussed by Van Swygenhoven and coworkers [76, 262]. They contend that the partial dislocation splitting distance (i.e., stacking fault width) in fcc metals such as copper and aluminum is more dependent on the ratio of the γ_{usf} to γ_{sf} than just the stacking fault energy alone. Following the work of Rice [179], who detailed the influence of both γ_{sf} and γ_{usf} with regard to dislocation nucleation from crack tips, Van Swygenhoven and coworkers [262] argue that a deformation map for NC metals (offered by Yamakov *et al.* [311]) considering only the stacking fault energy is too simplistic.

Rice [179] found that the γ_{sf} is the proper zero energy reference when considering the stress required to emit the trailing partial dislocation from a crack tip (or GB), not the perfect fcc lattice configuration energy. This new reference point for the energy barrier alters the calculated stress required for the nucleation of the trailing partial dislocation. Now, the ratio of the γ_{usf} to γ_{sf} defines the energetic barrier for nucleation of the trailing partial dislocation, not just the stacking fault energy and its width. This idea was confirmed by Van Swygenhoven *et al.* [262] when they used three EAM potentials for nickel, aluminum, and copper to study the deformation mechanism landscape as a function of stacking fault energy using MD simulations. Their results show that for copper, the lowest γ_{sf} of the three potentials, and nickel, with the highest γ_{sf}, only partial dislocations are observed with trailing intrinsic stacking faults connecting to the GB. However, for aluminum, the middle γ_{sf} of the three, full dislocations are observed for similar grain sizes. These results show that the stacking fault energy alone is not sufficient in understanding dislocation nucleation or the crossover from partial to full dislocation emission. Therefore, the use of the generalized planar fault curve is supported.

The generalized planar fault (GPF) curve, which relies on both γ_{sf} and γ_{usf}, is key in understanding dislocation motion and emission from GBs in NC materials, as discussed. The ratio of these two energies can lend insight into the transition from partial to full dislocation emission often observed in fcc metals. As this ratio approaches unity, as in Al, the emission of a trailing partial from a GB is more likely because the energetic barrier is low, using γ_{sf} as the zero energy point for the trailing partial dislocation. On the other hand, a ratio far from unity leads to a more significant energy barrier for emission of the trailing partial dislocation, as observed for copper and Ni. Therefore, good agreement between calculated stacking fault energy values and both experimental and *ab initio* studies given by Mishin *et al.*, show that these potentials are sufficient in studying defect structures and deformation processes.

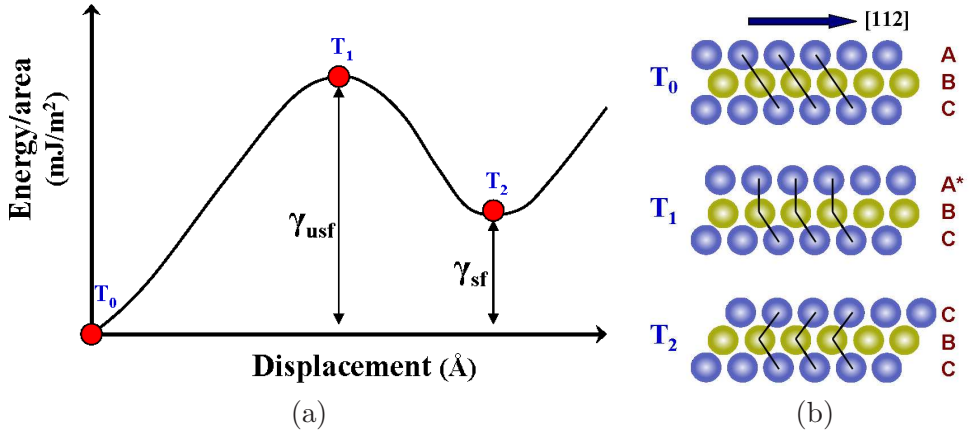

Figure 4: A schematic showing (a) a representative GPF curve and (b) the corresponding lattice shear configurations for a stacking fault in a fcc lattice.

In Figure 4, a representative GPF curve is shown along with the corresponding lattice shear configurations. The schematic in (a) shows a plot of normalized planar energy as a function of shear displacement along [112] (representing partial slip in fcc metals), and (b) provides the accompanying lattice plane configurations to generate the curve shown in (a). The applied shear displacement occurs between two {111} planes along [112], and the original fcc stacking sequence, ABCABCABC, is broken once the two planes are shifted relative to one another (as shown in 4(b)). The peak in the energy curve is γ_{usf} (corresponding to the transition state displayed in the middle image in (b)), while the local minimum after

peak energy is γ_{sf}. Once the upper plane of atoms in (b) shifts along [112], the stacking sequence changes to that of an intrinsic stacking fault, ABCACBCABC. This configuration occurs in NC materials when a single partial dislocation has been emitted from a GB, without the accompanying trailing partial dislocation.

The intrinsic stacking fault energy is relevant for investigating the splitting distance of partial dislocations in NC materials [92, 76, 262], as the unstable stacking fault energy has been argued to be vital for dislocation nucleation [179]. It is noteworthy that the unstable stacking fault energy is not used as a fitting parameter for the Mishin EAM potentials used in this thesis [149, 150], but both the unstable and stable stacking fault energies for copper and aluminum using the Mishin EAM potentials have good agreement with experimental and *ab initio* calculations [34, 88, 141, 152, 328]. So, their use in this thesis (along with the results of Zimmerman *et al.* [328] showing the GPF curve for the Mishin EAM potentials as compared to other common potentials) for investigating dislocation nucleation/emission from GBs in NC fcc metals is validated.

2.2 Simulation Methodology

2.2.1 Bicrystal Methodology and Boundary Conditions

The size of the simulation cell and accompanying boundary conditions varies within this dissertation depending on the structure and specific aim of each individual effort, but the cell dimensions are set to minimize image effects, preserve computational efficiency, and not hinder or change material behavior for the particular systems studied. It is convenient to separate each type of bicrystal configuration and discuss each accordingly. Several different methodologies are employed in bicrystalline simulations: (1) minimum energy configurations/bicrystalline structure construction, (2) uniaxial tension/compression simulations and (3) simple shear simulations. To properly construct each bicrystalline cell geometry and impose deformation, a different set of conditions are required for each case.

For the equilibrium bicrystalline structures studied under uniaxial tension and compression, we use a simulation cell with the approximate dimensions of $16nm \times 32nm \times 16nm$, where each lattice dimension is approximately $16nm$. This leads to systems containing

$7.0 - 9.5 \times 10^5$ atoms depending on crystal orientations and GB misorientation. When NEGB structures are investigated, a bicrystalline geometry which is slightly smaller in the tilt axis dimension is used, leading to systems containing approximately $1.1-2.0\times10^5$ atoms and lattice dimensions of approximately $16nm \times 32nm \times 6nm$. Initial bicrystalline GBs are constructed using a combination of MS and MD simulations at the desired temperature. A planar boundary is generated by rotating the lattice orientations from a common 0° direction in opposite directions by the same rotation angle magnitude (symmetric tilt boundary), followed by atom deletion along the interface. The two lattices are then shifted parallel to the boundary plane in both in-plane coordinate directions (rigid body translation), followed by energy minimization. Hundreds of iterations are performed with varying rigid body translations to converge on a minimum energy GB structure, as shown in Figure 5. Once the minimum energy structure is obtained [204, 207, 206, 223, 222, 229, 230, 235, 234], equilibration at the desired temperature for at least 10,000 timesteps (10 ps) allows residual pressures along the lateral sides of the simulation cell to relax to zero.

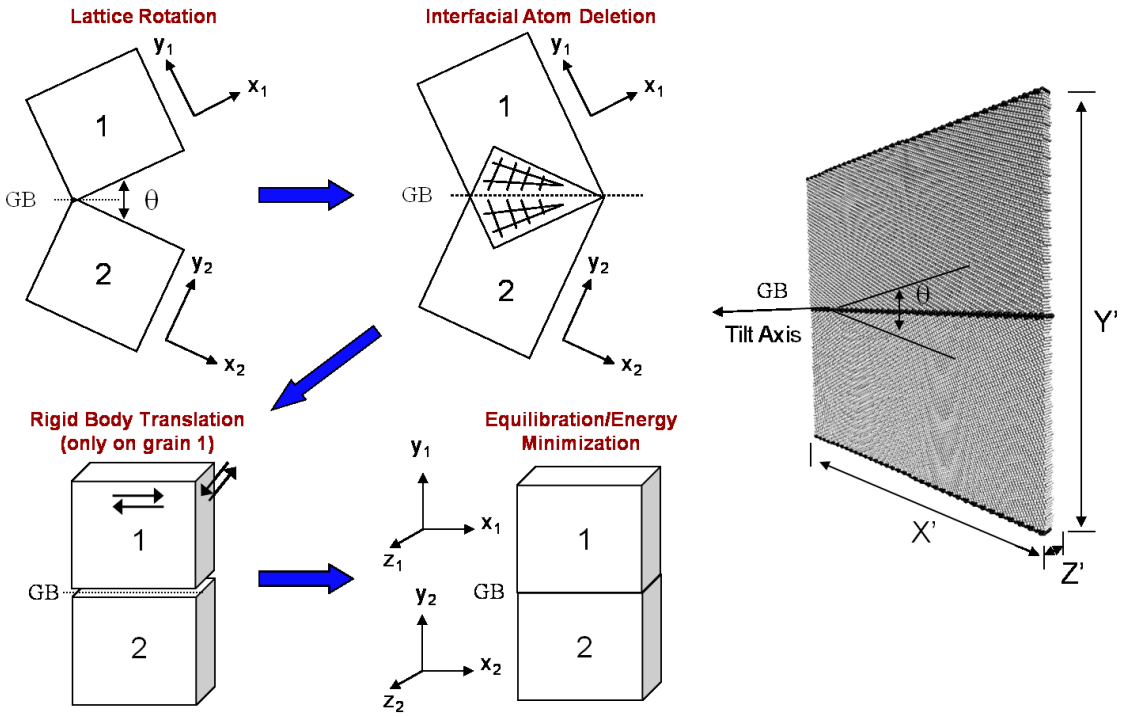

Figure 5: A schematic showing an example of the series of steps taken to converge on an initial bicrystalline structure.

Following the generation of initial GB structures, two types of boundary conditions were utilized in this thesis for deformation of bicrystals: 3D periodic (uniaxial tension/compression) [230, 235, 234, 237, 233], and 2D periodic with constrained surfaces (with shear displacements applied to the constrained surfaces) [236, 234, 237]. Three-dimensional (3D) periodic boundary conditions were used for two purposes: (1) to construct initial minimum energy structures (bicrystalline and NC), and (2) to simulate bulk material behavior without the requirement of excessive simulation domain size (uniaxial tension/compression). For 3D dimensional periodic boundary conditions used in bicrystalline studies, a second GB was naturally introduced into the simulation cell. It is located at both the upper and lower bounds of the cell, and identical to the other GB contained within the simulation cell. All structures were equilibrated at the desired temperature for at least 10 ps prior to any deformation to allow domain stresses to approach zero. For structures employing 3D periodic boundary conditions, atomic trajectories are governed by NPT equations of motion [142], which have been commonly used for both bicrystal [206, 207, 204, 225, 230] and NC simulations [260, 263, 262, 265, 264, 309, 308]. For structures employing 2D periodic boundary conditions with constrained surfaces, NVT or NVE equations of motion govern dynamics during both equilibration and deformation [236, 234, 237].

2.2.1.1 Uniaxial Tension and Compression

For uniaxial tension and compression simulations, 3D periodic boundary conditions are maintained and dynamics consistent with the NPT equations of motion [142]. The lateral simulation cell bounds are maintained at zero normal stress according to the NPT equations of motion, while the stress normal to the surface of imposed straining is not controlled by any set of equations of motion. Rather, the stress in the loading direction is computed (as will be described later) for a prescribed strain rate in the loading direction. Both uniaxial tension and compression are imposed by deforming the simulation cell in the loading direction at a constant strain rate applied perpendicular to the GB plane, with zero lateral normal stress. A schematic of the methodology employed for uniaxial tension or compression of bicrystalline simulation cells is shown in Figure 6.

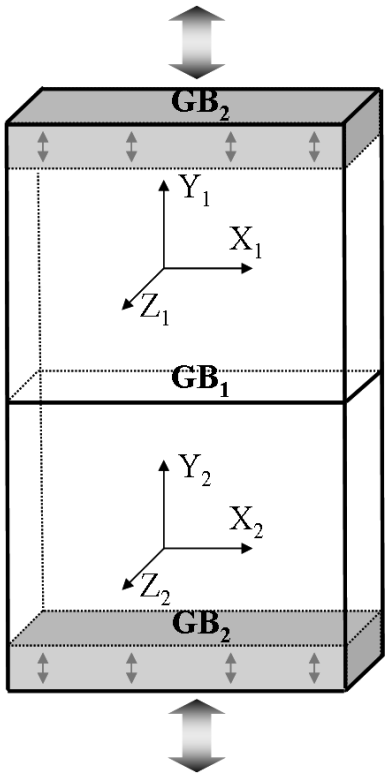

Figure 6: A schematic showing the setup for uniaxial tension and compression simulations on bicrystalline geometries.

2.2.1.2 Shear

To impose shear deformation, a mixed set of boundary conditions is required. First, two atomic slabs are defined encompassing all atoms located within 15Å of either the top or bottom surface. All atoms located within these slabs are held fixed in their perfect fcc lattice positions and designated to move as two separate 'Rigid' atomic groups. All resulting forces on these rigid groups during the simulation are zeroed, while the velocity is defined separately by the prescribed boundary conditions. Second, all atoms sandwiched between these two rigid slabs are designated as 'Mobile' and their dynamics governed by the selected set of equations of motion. Third, the lower rigid slab of atoms is held fixed from movement in any direction and the upper slab is given a constant velocity in the shear direction (X). Fourth, to alleviate the possible generation of a shock wave within the 'Mobile' atomic group due to the constant velocity given to the upper slab, a linearly ramped velocity field is applied to all 'Mobile' atoms. This velocity field varies from zero to the prescribed shear

velocity of the upper slab as a function of position between the two slabs. Such prescribed atomic velocities supplement atomic fluctuations due to temperature. A schematic showing the shear deformation boundary conditions is shown in Figure 7.

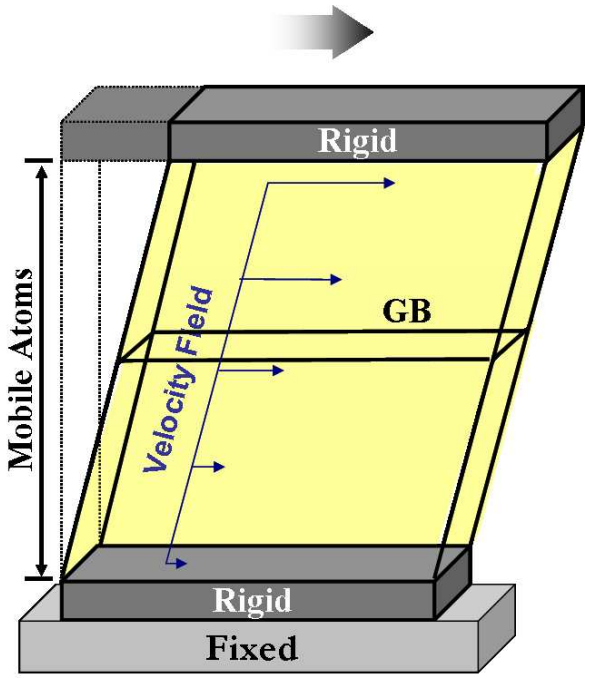

Figure 7: A schematic showing the setup for shear simulations of bicrystalline geometries with linearly ramped prescribed velocity field applied to all 'Mobile' atoms.

2.2.2 Nanocrystalline Methodology and Boundary Conditions

Three-dimensional NC structures are generated by filling a simulation cell with convex polyhedra using Voronoi Tessellation [280]. Lattice orientations for each grain are randomly determined and each polyhedra is filled with non-overlapping lattices. Each NC structure initially contains 25 grains with random orientations of varying average grain size. The number of total atoms contained within each simulation cell range between 2.0×10^5 for the small structures (5 nm average grain size) and 7.1×10^6 for the larger structures (15 nm average grain size). The resulting GB structures tend to be of random high-angle character containing both tilt and twist components (discussed later) relative to the GB plane.

Periodic boundary conditions are employed and each structure's energy is minimized by a conjugate gradient scheme followed by thermal equilibration under NPT at 10K for 50

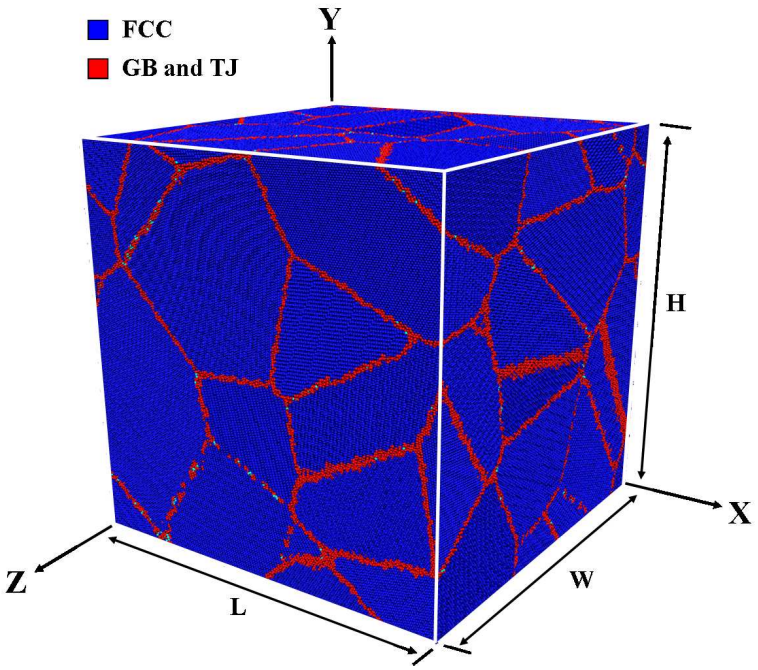

Figure 8: Example of an initial NC copper structure containing around 7 million atoms, composed of 25 grains with an average grain size of 15 nm. Atoms are colored according to the common neighbor analysis (CNA) method, where fcc atoms are blue and GB/TJ atoms are red.

ps. This allows for GBs to relax to near equilibrium structures and the cell stresses tend toward zero. Once the equilibrated structure is obtained, deformation simulations are then performed. Figure 8 displays a NC structure containing approximately 7 million atoms with an average grain size of around 15 nm.

For uniaxial tension simulations performed on the NC structures, periodic boundary conditions are maintained in all dimensions. A constant strain rate deformation is imposed in the Y direction while the domain stresses in X and Z are governed according to NPT equations of motion at the desired temperature. Just as in the case for bicrystalline simulations, stress is not controlled by the equations of motion in the Y direction, only in the X and Z directions. Deformation simulations are carried out at constant temperature, and lateral stresses are set to zero. All imposed deformation simulations continue to strains exceeding that required for the onset of inelastic deformation processes, and multiple strain accommodation mechanisms are observed in each structure. Resulting atomic data of each simulation are output and then analyzed by numerous post-processing in-house FORTRAN

codes. The objective of the post-processing efforts are to investigate the influence of various structural elements (e.g., GBs and TJs) at the nanoscale to the mechanical behavior observed during deformation (e.g., dislocation nucleation, GB sliding, and migration) and to free volume evolution during inelastic deformation. Furthermore, microscale metrics are used to investigate the kinematic deformation behavior of the NC structures.

2.3 Grain Boundary Structure and Free Volume

Preliminary investigations into GBs and their structure were performed by Pond and coworkers [168], Smith *et al.* [202], and Ashby *et al.* [9]. Later, Sutton and Vitek [212, 213, 214] provided a detailed description of tilt boundaries in metals, outlining various atomic units composing periodic boundary structures (structural unit model). This model describes the atomic composition of GBs as a linear combination of structural units. Since then, a wide array of research has focused on linking GB structure and behavior. For example, Bayer *et al.* [15] examined compatible deformation mechanisms in NiAl bicrystals, Farkas and coworkers [65, 68] investigated GB fracture, and Cao *et al.* [30] simulated the effect of GBs on dislocation nucleation in copper nanowires. Moreover, the influence of GBs and their structure on deformation in NC metals has been discussed by many authors [271, 266, 35, 84, 104, 19, 319, 303]. These results point to the importance of understanding GB deformation and the associated strain accommodating mechanisms. However, it is often difficult to understand specific GB structure-property relationships in NC structures, including the effects of various loading conditions and different GB states. Therefore, Van Swygenhoven *et al.* [263] emphasize the benefit of bicrystalline structures within simulations to gain additional understanding.

To study relationships between structure and behavior, researchers have employed various techniques to investigate GBs and interfaces [288, 43, 91, 90, 197, 327]. For example, Spearot *et al.* [207] investigated $\langle 100 \rangle$ and $\langle 110 \rangle$ symmetric tilt GBs (STGBs) in copper using MD simulations, and developed a correlation for interfacial strength as a function of misorientation range. This model considers GB structure degrees of freedom, non-Schmid

stresses, and an average interfacial nanoporosity measure to predict interfacial strength under uniaxial tension. The strength correlation proposed by Spearot *et al.* [207] is adequate for ⟨100⟩ boundaries and correctly captures the interfacial strength values for most ⟨110⟩ GBs in Cu. However, for boundaries containing higher levels of free volume, it fails to anticipate an abrupt drop in the observed interfacial strength, where greater free volume in these boundaries is due to the E structural unit.

Sansoz *et al.* [184] used the quasicontinuum method to study the mechanical behavior of ⟨110⟩ copper and aluminum GBs under simple shear. Their results also point out that boundaries with the E structural unit contain large amounts of free volume and exhibit different nanoscale behavior during deformation. GB sliding was found to be an important deformation mechanism, and excess free volume at the interface promoted atomic shuffling events prior to GB sliding [183]. These results agree with those of Van Swygenhoven *et al.* [260], who showed GB sliding is a major deformation accommodation mechanism in small grains of NC Ni. In the boundaries investigated, excess free volume at the interface was found to contribute significantly to the nanoscale deformation behavior of the boundary, and atomic shuffling was also discovered in interfacial regions containing high free volume. The authors state that free volume in the intercrystalline regions enhance atomic shuffling between neighboring grains, leading to the observed sliding of the boundary, in agreement with Derlet *et al.* [55].

Free volume is a fundamental attribute of GBs and influences many physical properties [173, 200, 253]. For example, diffusion in GBs was investigated by Aaron and Bolling [1] in 1972, who found that lower atomic density (or greater free volume) within certain interfacial regions enhances diffusion. Additional work by Kuriplach and coworkers [118, 254] utilized positron annihilation to investigate free volume in metal GBs, and noted distinct differences between various GB structures. It is clear that free volume plays a crucial role in GB properties above consideration of structure, and that the mechanical deformation in NS materials is therefore influenced. However, questions still remain regarding the role of structure and free volume on GB deformation. How does free volume change with changes in GB structure? Do particular free volume distributions enhance stress-induced

atomic shuffling or dislocation nucleation? How does the evolution of free volume correlate with certain deformation mechanisms? Can the distribution of GB free volume be understood in the context of activating dislocation nucleation and other strain accommodating mechanisms? Understanding the connection between GB structure, free volume, and GB deformation could provide valuable insight into the origins of inelastic mechanisms present in NC materials, and provide important thermodynamic information regarding deformed (or non-equilibrium) interfaces. These issues motivate our approach to understand the roles of GB structure and free volume on GB and NC deformation.

To address these issues and more thoroughly understand GBs, a comprehensive treatment of structure and free volume is necessary. Therefore, important terms regarding GB structure and free volume are defined and discussed in this section. First, coincident site lattice notation is summarized. Second, an overview of the structural unit model is provided. Finally, we will define free volume and its importance to GB behavior.

2.3.1 Coincident Site Lattices

The notion of coincident sites between two adjacent lattices is a useful avenue to understand the degree of atomic fit at their interface, the GB [173]. The coincident site lattice (CSL) concept has now become a useful tool in GB studies and engineering. The degree of atomic fit at a GB is easily captured by a GB's CSL designation. If the two lattices were allowed to overlap, a certain number of sites along lattice rows would be coincident, the reciprocal density of the number of these coincident sites gives the Σ designation for the GB. For example, in Figure 9, one in seven sites are coincident in the overlapping lattices shown; therefore, the CSL designation of the interface of these two lattices is $\Sigma 7$.

Applying the CSL notation in GB studies is a convenient way to link GB structure to properties. GBs inherently have greater atomic volume as compared to each adjoining lattice. This excess atomic volume relative to that of the perfect lattice is free volume (which will be revisited later in this section). Free volume and lower atomic density are key physical characteristics of GBs which alter their properties. As the atomic structure of GBs change, so does the free volume and properties of that boundary. There is an inherent link between

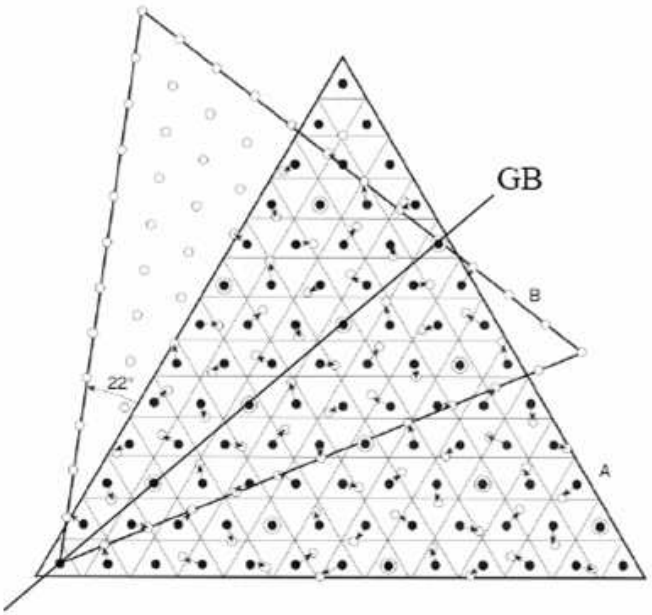

Figure 9: Example of CSL notation, showing a Σ7 boundary for which 1 in 7 sites are coincident between the two overlapping lattices. The solid GB line represents the GB for a symmetric tilt boundary.

structure and free volume (as further detailed in Chapter 3). Certain GBs are called 'special boundaries', and they have lower numeric Σ values and lower free volume than non-special boundaries or general boundaries [173]. In addition to lower average free volume, special boundaries are also composed of periodic polyhedral atomic structures as shown in Figure 10, where the atomic structure of both a Σ11 (113) and a Σ9 (221) aluminum boundaries are shown comparing the high resolution transmission electron microscopy (HRTEM) image [147] with the predicted interface structure from our energy minimization calculations.

2.3.2 Structural Unit Model

A useful classification scheme for identifying specific repeating atomic defect structures which comprise equilibrium or minimum energy GB structures, is the Structural Unit Model (SUM) [212]. However, this classification does not pertain to characterizing the macroscopic degrees of freedom of GBs, like CSL notation. A structural unit is a minimum energy atomic configuration where a single structural unit entirely defines the GB structure of certain CSL boundaries. For example, in Figure 10(a), C type structural units comprise the entire

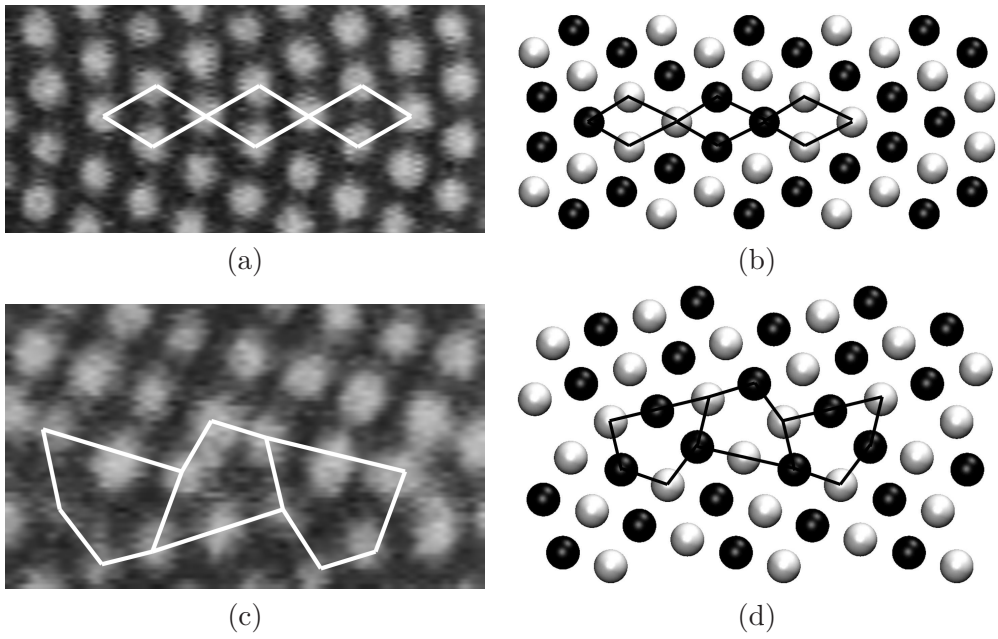

Figure 10: A comparison of aluminum symmetric tilt GBs investigated using HRTEM (a,c) [147] and those same structures using atomistic simulations (b,d) (as first outlined by Spearot in [205]). The structural units in each boundary are shown for comparison and in the computer generated structures, two atomic planes are shown (black and white atoms). Clearly there is good agreement for symmetric tilt GB structures using the Mishin EAM interatomic potential and computational methodology employed in this work.

Σ11 (113) GB for aluminum [147], and in 10(c), E structural units make up the Σ9 (221) boundary in aluminum [147]. These boundaries where only one type of structural unit are present are called 'favored' boundaries. Non-favored boundaries are comprised of two types of structural units.

To clarify, a particular group of high-angle $\langle 110 \rangle$ STGBs are shown in Figure 11. Consider the Σ11 (113) GB shown in (a) which contains only C structural units and has a misorientation angle of 50.5°, and the (c) Σ3 (111) boundary (coherent twin boundary) which is totally comprised of D structural units and has a misorientation angle of 109.5°. These boundaries are favored boundaries because they are entirely composed of only one type of structural unit. All GBs with misorientation angles between 50.5° and 109.5° have a combination of both C and D structural units; however, the arrangement and concentration of each type of unit varies as a function of misorientation angle. For example, in Figure 11(b), the Σ3 (112) GB is shown which has a misorientation of 70.5°, and this GB

structure is composed of both C and D structural units in identical ratio. Although the D structural units are dissociated from the boundary in this example, this will not be true for all boundaries with misorientation angles between favored boundaries.

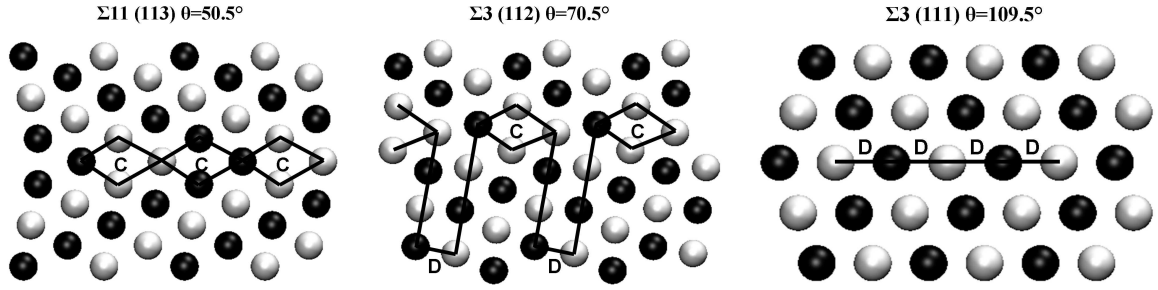

Figure 11: Three STGBs with different structural unit compositions illustrating the relationship between favored and non-favored boundaries and their associated units. The structures in both (a) and (c) are favored boundaries composed entirely of C and D structural units, respectively, while a non-favored boundary (b) with a misorientation angle between that of (a) and (c) is composed of a combination of both C and D units.

2.3.3 Free Volume

A GB is defined as the interface of two crystal lattices of different orientations within the same phase. The average atomic volume at this boundary is greater than in the bulk lattice or grain interior. Therefore, GBs are said to possess *free volume*. Free volume is therefore a fundamental physical property of GBs [173], and has been noted to be the principle physical feature designating GB structure [170]. One of the first efforts in understanding free volume and its influence on GB properties was undertaken by Aaron and Bolling [1]. They developed an approach for quantifying interfacial free volume for tilt GBs. Their conclusions state that free volume directly affects GB diffusion along with other properties (references therein). This structural feature of boundaries is the foundation for differences observed from GBs as compared to grain interiors or lattices. Free volume is therefore a useful measure of atomic coordination or density, as the structure of GBs change with varying misorientation angles and boundary plane inclination angles. Therefore, the interfacial free volume of near equilibrium GBs is not equal to that of non-equilibrium GBs. The inherent correlation between GB structure and free volume (as discussed in Chapter 3) leads to differences in

both the concentration and spatial distribution of free volume as GB structure changes.

It is then reasonable to assume that certain GBs will have lower free volume than others, depending on their structure, as first indicated by Aaron and Bolling [1]. For example, if atomic mismatch at an interface is lower than the corresponding free volume will be lower as well. These boundaries are called 'special' boundaries, and their properties can differ substantially from properties exhibited by 'general' boundaries [173]. Numerous important GB properties relate to free volume, such as energy, diffusivity, segregation, mobility, corrosion, and the source/sink nature of GBs to defects [173].

Previous studies have utilized MD simulations to explore the effect free volume on GB behavior. Van Swygenhoven *et al.* [260] used MD simulations to show that GB sliding is a major deformation accommodation mechanism in small grains of NC Ni. In their simulations, excess free volume was found to significantly contribute to the nanoscale deformation behavior of boundaries, and atomic shuffling was common in interfacial regions of high free volume content. It was concluded that excess free volume aids in atomic shuffling events that are critical for GB deformation, specifically GB sliding. These results agree with the findings of Derlet *et al.* [55] who investigated dislocation nucleation events in NC nickel samples of 12 nm average grain size. Free volume was shown to be a significant factor in the localized atomic rearrangement necessary to activate dislocation nucleation. It was also found that free volume migration away from nucleation regions within the GBs accompanied dislocation emission in NC fcc metals.

2.3.3.1 Free Volume Measurement

After atomic structures are obtained, a post-processing code is used to quantitatively measure and characterize the free volume within particular regions of interest. Free volume calculations can be performed over an entire simulation cell, or specific regions can be targeted for more detailed free volume measurements or averaging. One-point (volume fraction) and two-point statistics (e.g., two-point correlations functions and lineal path functions) are determined from these calculations and provide important spatial information about both free volume and the atomic structure.

This procedure is outlined in [229]. The present author's contributions to this work include the writing of the algorithm to compute free volume and a significant contribution to the development of the outlined procedure in conjunction with Dr. Mark Tschopp. In addition, the design and calculation of the two-point statistics was additional work by the present author. To compute free volume, a full three-dimensional grid of points (representing an indicator matrix, N_{ijk}) was laid over the volume of interest where each point represents a small volume box (v_b), and the range of i, j, and k depend on the simulation dimensions and grid size. For more detailed free volume measurements in a finite GB layer, free volume was calculated within 1nm on either side of the initial GB, but was still normalized by one half the simulation cell volume. The volume of each box was no larger than $(0.05a_o)^3$, where a_o is the lattice parameter. Each box was then labeled as 'free volume' ($N_{ijk} = 1$) or 'atom' ($N_{ijk} = 0$) depending on its distance, d_{ijk} to the nearest atom, i.e.,

$$N_{ijk} = \begin{cases} 1, & d_{ijk} > ca_o \\ 0, & d_{ijk} \leq ca_o \end{cases} \tag{5}$$

where the indicator function N_{ijk} defines whether each grid point is free volume or not, $_{ijk}$ are integers in the X, Y, and Z directions defining the grid point number ($n_x n_y n_z$, respectively), and c is the criteria constant ($c = 0.5$). Numerous volume boxes (or grid points) lie between neighboring atoms, and the grid point mesh is independently generated from the atom positions. The free volume criteria is based on the fact that a perfect face-centered cubic (fcc) unit cell has no free volume. Therefore, if atoms lie in their equilibrium lattice positions, no grid points or boxes within that volume would be characterized as free volume and $\sum_{ijk} N_{ijk} = 0$. When a GB is present within the volume of interest, some boxes are designated as free volume and $\sum_{ijk} N_{ijk} \neq 0$. The total free volume concentration in the computational cell (f_1) was then calculated by summing all free volume boxes and normalizing by the total volume of interest (V), i.e.,

$$f_1 = \frac{v_b}{V} \sum_{ijk} N_{ijk} \tag{6}$$

This approach for calculating free volume allows for the spatial arrangement, or distribution of free volume to be determined for each boundary by considering the moments of N_{ijk}. As

shown in [229], the distribution of free volume varies for different GBs and this will influence GB deformation. Many times the dimensions of the region of interest vary, so it is vital to obtain a value that is not biased by differing sizes. Second, for larger regions or more detailed free volume measurements within certain regions, the free volume concentration is simply f_1.

2.3.3.2 Two-Point Correlation Functions and Lineal Path Functions

Additional free volume information can be obtained from two-point statistical data from stereology-based measurements. Two-point correlation functions [83, 218] and lineal path functions [130] are traditionally used in stereology and microstructure characterizations to gain information about the spatial arrangement of various microstructural elements (e.g. phases, particles, voids). Two-point correlation functions (TPCFs) are specifically well-suited to provide information about spatial arrangement or elemental spacing. TPCFs calculate the mean probability, $< P_{ij}(r) >$, that two points separated by a distance r are contained within phases i and j, respectively, as shown in Figure 12. For free volume measurements, $P_{11}(r_k)$ is the quantity of interest measuring the mean probability these two points are free volume, where k is included to denote a certain directionality of r. Therefore, TPCF data can be measured along specific directions within the simulation grid based on **N**. The three directions for measurements in bicrystalline structures are the GB period (X) direction, the GB plane normal (Y) direction, and the tilt axis (Z) direction. These calculations can provide vital information about free volume and atomic motion within the GB plane (which will be discussed later). Normalizing $P_{11}(r_k)$ by the volume fraction provides an unbiased value for the TPCF due to the number of grid points.

$$P_{11}^{*}(r_k) = \frac{P_{11}(r_k)}{f_1} \tag{7}$$

Lineal path functions (LPFs) calculate the probability, $L_i i(r_k)$, that a line of length r along direction k is entirely contained within 'phase' i. LPF data provides insight into the connectivity of i. So, in free volume calculations, L gives information about the connectivity and clustering behavior of free volume packets within the GB along direction k. Similarly

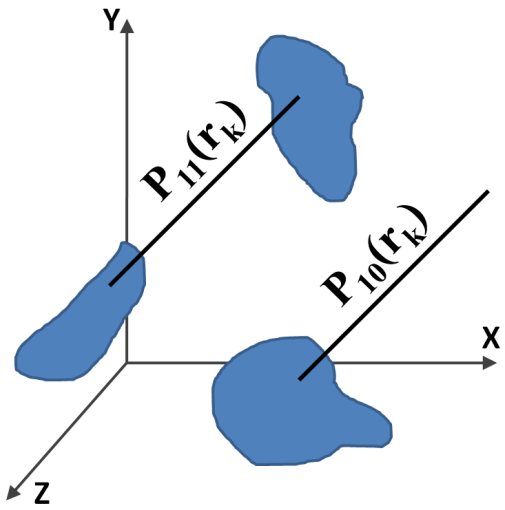

Figure 12: An illustration showing the microstructural calculation of two different TPCF scenarios. Once where both ends of the line are contained within one 'phase' of the material, and the other where the ends lie in different 'phases'.

to TPCFs, LPFs are calculated along the three primary directions, and collectively give crucial information about the spatial arrangement of free volume because the spacing of free volume is provided from TPCFs, and their connectivity from LPFs [229]. As was true with TPCFs, to account for differences in the number of grid points for different structures, we normalize $L_i i(r_k)$ by f_i.

$$L_{11}^{*}(r_k) = \frac{L_{11}(r_k)}{f_1} \tag{8}$$

To calculate both TPCFs and LPFs from atomistic data, values of N_{ijk} are used. Since the distance scale is based on the grid point spacing, only discrete integer values of r can be used in the calculations. Figure 13 shows a simple illustration of TPCF and LPF free volume scenarios for each grid point distance. In the left column, the discrete integer r values are listed based on grid point spacings. The middle and right columns show a complete set of scenarios for each distance/function combination for TPCF and LPF respectively. Since TPCF measurements only rely on the two endpoints, more possible scenarios exist for this function for r values greater than one. Grid points lying between the two endpoints can be either free volume or not, as long as the two endpoints are free volume. However, for LPFs, the entire 'line', or length between the two endpoints, must lie within free volume. Therefore, for each r value, only one scenario exists that contribute to

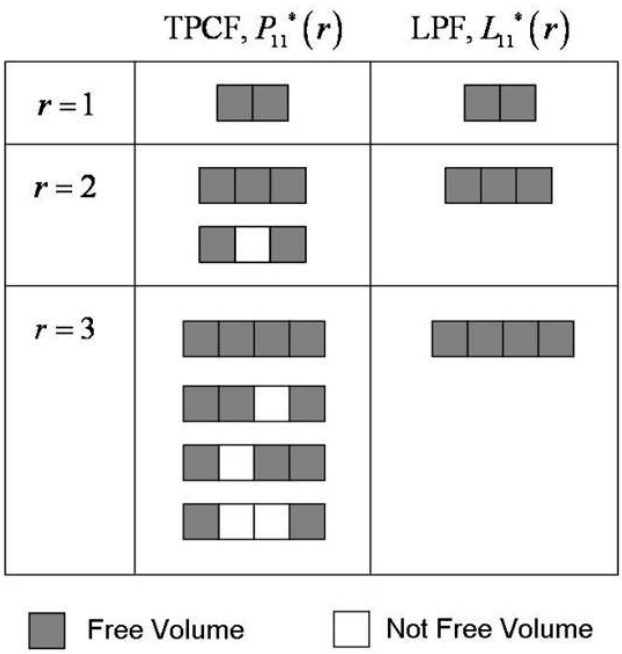

Figure 13: The conditions for computing TPCFs and LPFs for free volume in our computation framework. Gray boxes are 'free volume' and white boxes represent part of the 'atom'. Different scenarios for each r value are possible for TPCFs, while only one scenario exists for LPFs.

$L_{11}(r_k)$. In a later section, TPCFs and LPFs will be used to obtain spatial statistics and free volume distribution information for a specific class of GBs, accompanied by images of the corresponding free volume distributions.

2.4 Atomic Properties and Visualization

Various visualization techniques can be applied in atomistic simulation results in post-processing to leverage different atomic properties or metrics. These methods rely on displaying atomic structures by particular computed atomic quantities. For example, it is customary to calculate certain values for each atom and then visualize the atomic structure according to that quantity, and often to filter the image further by employing cut-off criteria. Common quantities include energy, centrosymmetry [105], slip vector [329], and common neighbor analysis (CNA) [63, 231], where each measure provides different but important atomic information.

Vital insight pertaining to particular defects, such as dislocations, stacking faults, and

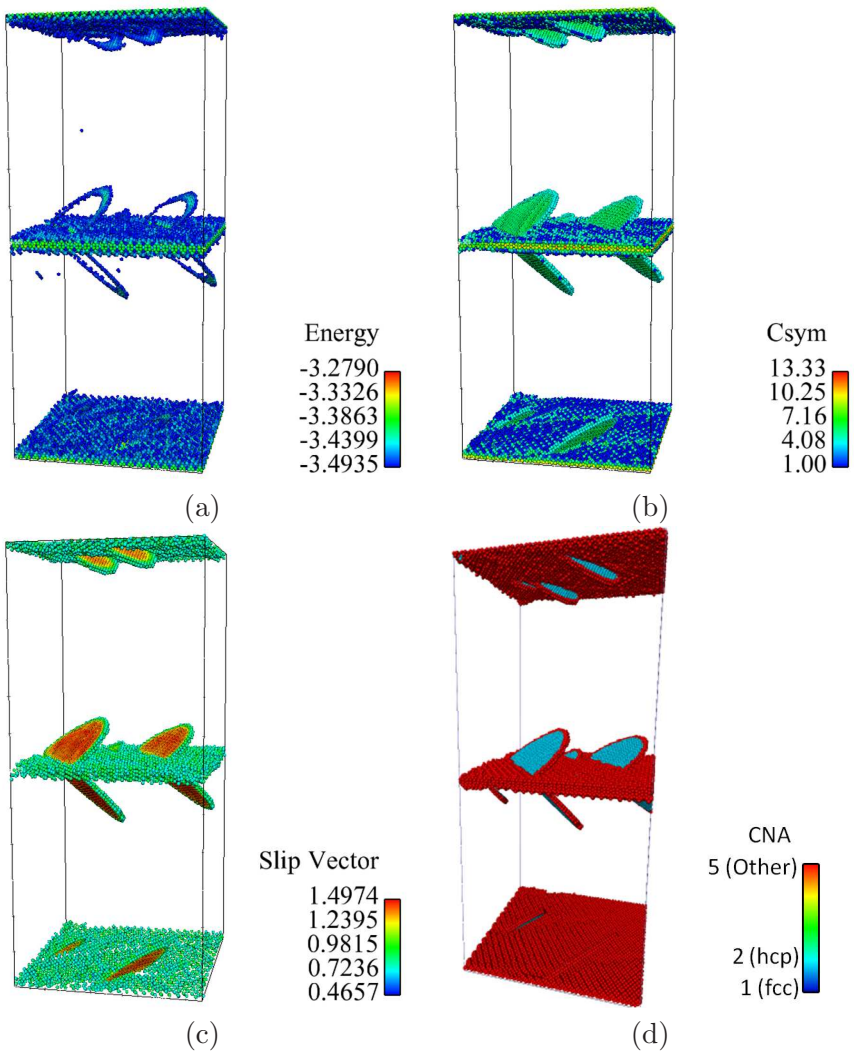

Figure 14: Images of heterogeneous dislocation nucleation from a bicrystalline GB subjected to deformation normal to the GB plane, where atoms are colored according to (a) energy, (b) centrosymmetry, (c) slip vector, and (d) the CNA method. For the CNA method, a CNA value of 1 corresponds to fcc atoms, a value of 2 is hcp atoms, and a value of 5 identifies other atoms (e.g., GBs, TJs, and additional defect structures).

GBs can be attained though the application of each of these measures. For example, Figure 14 shows a partial dislocation emitted from a GB colored and filtered according to (a) energy, (b) centrosymmetry, (c) slip vector, and (d) CNA. Atomic energy, calculated from potential energy as defined by the interatomic potential, is a useful measure or metric to visualize deformed configurations from MD simulations. For example, atomic energy for atoms residing in GBs or on surfaces will be greater than that for atoms lying in a grain or lattice in a close-packed position. Therefore, as shown in Figure 14(a), energy can

help resolve defect atoms (i.e., partial dislocations and GBs) or structures in large atomic systems.

The centrosymmetry parameter by Kelchner *et al.* [105] is another useful measure in identifying defect atomic structures in fcc metals. For fcc atoms that have undergone a homogeneous elastic distortion, the centrosymmetry value is zero. A centrosymmetric atom will have neighbors residing in opposing directions but at equal distances from the atom of interest. However, the utility of this parameter is apparent when visualizing structures for which nonelastic deformation has occurred, such as dislocations, as shown in Figure 14(b). Atoms near these defects will have centrosymmetry values other than zero. Centrosymmetry is defined as

$$P = \sum_{i=1,6} |R_i + R_{i+6}|^2 \tag{9}$$

where a perfect fcc lattice is assumed as reference (12 nearest neighbors, 6 pairs), and R_i and R_{i+6} are the corresponding vectors to each neighbor in each pair. The $\mathbf{R}$ vectors are determined in the current or deformed configuration from reference configuration neighbor lists.

Slip vector (as shown in Figure 14(c) aids in both identifying atoms in defect structures, but also is estimating the Burgers vector of dislocation structures [329]. For example in 14(c), a stacking fault trailing the leading partial dislocation is shown, where atoms lying in the stacking fault have a slip vector magnitude of approximately 1.48Å. This value is the theoretical Burgers vector for partial slip in an fcc lattice with a lattice parameter of 3.615Å (corresponding to Cu). Slip vector relies on both the current and reference atomic configurations, through the use of neighbor lists. This is why slip vector is valuable in estimating the deformation path of certain atomic regions due to the deformation of an atom's neighborhood. Slip vector (s^α) [329] is calculated as

$$s^\alpha = -\frac{1}{n_s} \sum_{\beta \neq \alpha}^{n} \left(x^{\alpha\beta} - X^{\alpha\beta} \right) \tag{10}$$

where n is the number of nearest neighbors, n_s is the number of slipped neighbors, and $x^{\alpha\beta}$ and $X^{\alpha\beta}$ represent the interatomic vectors in the current and reference configurations, respectively, for an atom α and its neighbor β.

The CNA method [63, 231] is an additional useful measure for visualizing atomic structures and is a current configuration measure, not a function of reference configurations. Therefore, no history dependent information is contained in this measure. It's value lies in its simplicity for identifying particular atomic groups based on their local lattice structure. For example, it's benefit is in identifying the various crystal structures of fcc (CNA=1), hcp (CNA=2), bcc (CNA=3), and other non 12 coordinated atoms (CNA = 5), such as GB atoms. Therefore, hcp atoms will have a different CNA value than GB atoms. This distinction is evident in Figure 14(d) where stacking fault atoms are colored aqua (hcp, CNA =2), while GBs and the leading partial dislocation are colored red (CNA=5).

2.4.1 Calculation of Atomic Stress

Throughout this thesis it is often necessary to calculate the atomic system stress. Volume-averaged stress calculations can be useful for a variety of purposes, but we intend to use stress calculations for two reasons. First, the ensemble averaged stress can be useful for assessing the mechanical (stress-strain) behavior of both bicrystalline and NC configurations. Second, the build up, and eventual stress softening within intercrystalline regions during NC structure deformation is an important phenomenon related to the activation of particular mechanisms, such as dislocation nucleation and GB sliding. There are a number of methods that have been proposed to calculate stress within atomistic simulations (the reader is encouraged to review Zimmerman *et al.* [332]), but the calculated stress values provided in this thesis are ensemble-averaged and follow the virial definition without the kinetic portion, as outlined in [326], i.e.,

$$\sigma_{ij} = \frac{1}{N\Omega} \sum_{\alpha}^{N} \sum_{\beta \neq \alpha}^{N^{\alpha}} f_i^{\alpha\beta} r_j^{\alpha\beta} \tag{11}$$

In this equation, atomic volume is defined by Ω, N is the total atom count in the system, N^{α} represents the number of neighboring atoms for atom α, $f_i^{\alpha\beta}$ is the interatomic force vector between atom α and neighbor β along the i direction, and $r_j^{\alpha\beta}$ is the interatomic distance of atoms α and β in the j direction. This approach for computing stress also allows us to calculate a volume-averaged stress over particular regions (e.g., the interface region)

in each simulation cell, similar to the calculations shown by Horstemeyer and coworkers [97, 96, 98]. We note that disposing the kinetic contribution to the virial stress at finite temperature renders very little difference between σ_{ij} from equation (11) and the full virial stress for temperatures below 300K.

2.4.2 Calculation of Strain

The calculation of strain in our simulations depends on the chosen imposed deformation mode and the reference configuration. For example, during uniaxial tension or compression, strain is calculated according to engineering strain, i.e.,

$$\epsilon = \frac{\Delta h}{h_o} \tag{12}$$

where uniaxial strain (ϵ) is a function of the change in dimension length (Δh) along the loading axis (Y-direction in Figure 6), and the original length in this dimension (h_o). For shear simulations, shear strain (valid for finite strain) is calculated as

$$\gamma = arctan\frac{l}{d_o} \tag{13}$$

In this equation, l is the imposed displacement in the shear direction (X-direction in Figure 7) and d_o is the distance between the lower and upper rigid atomic regions (in the Y-direction in Figure 7), normal to the constrained surfaces.

2.5 Nanocrystalline Materials

Since the pioneering work by Gleiter [80, 81] on NC and nanostructured (NS) materials, significant research has been focused on exploring the fundamental and underlying mechanisms of NC materials. This is partly due to early measurements showing improved mechanical properties [82, 113, 160, 161, 244] (as shown in Figures 15 and 16) as grain size is reduced, and partly due to basic scientific interest in understanding complex material physics. NS materials possess a main structural dimension smaller than 100 nm, and more specifically, NC metals are polycrystalline (PC) metals with an average grain size less than 100 nm. Figure 15(a) shows the stress-strain behavior of (A) coarse-grained copper compared to

(B-E) NC copper samples with modified grain structures. This graph shows the influence of microstructure on bulk mechanical properties. With an altered grain structure, the yield strength increases dramatically (as displayed in plots B, C, and D), and eventually the elongation to failure increases as well (plot E), as compared to the coarse-grained sample (plot A). These results by Wang *et al.* [283] show that NC metals with altered microstructures display altered mechanical properties with higher yield strength; however, the sample in plot E has a bimodal grain distribution thereby increasing both strength and ductility.

In Figure 15(a), the stress-strain behavior of copper is shown as a function of both imposed deformation and thermal equilibration by Wang *et al.* [283]. Specifically, curve A is a coarse-grained sample, B is a sample that has been rolled to 95% cold work at room temperature, and C has been rolled to 93% cold work at liquid nitrogen temperature. Changes to the microstructure due to imposed deformation to 95% cold work (curve B) as compared to the coarse-grained sample (curve A) results in a large increase in the yield strength and decrease in the elongation to failure. However, if the imposed deformation occurs at liquid nitrogen temperatures (curve C), further improvement is observed in the yield strength accompanied by an increase in elongation to failure. Curve D represents the behavior of the sample from curve C after equilibration at 180° for 3 minutes. Clearly, partial recrystallization (as noted by the authors) due to equilibration leads to a slightly lower yield strength and significantly improved elongation to failure. Finally, concurrent improvement in yield strength and elongation to failure is observed when a bimodal grain size distribution is present, as in curve E. Although the high strength and improved elongation to failure measurements seen by Wang *et al.* [283] in Figure 15(a) is due to a bimodal grain size distribution, changes to the strain accommodation mechanisms can also be influential on material behavior.

For example, in Figure 15(b) the stress-strain responses of both PC and NC cobalt are shown for different strain rates, where both high strength and good ductility in the electrodeposited NC samples were observed. For the strain rates shown in Figure 15(b), $\dot{\epsilon_1}$ is less than $\dot{\epsilon_2}$ which is less than $\dot{\epsilon_3}$. In addition to the comparison of the mechanical behavior of NC cobalt and PC cobalt, Figure 15(b) also shows their dependence on different strain

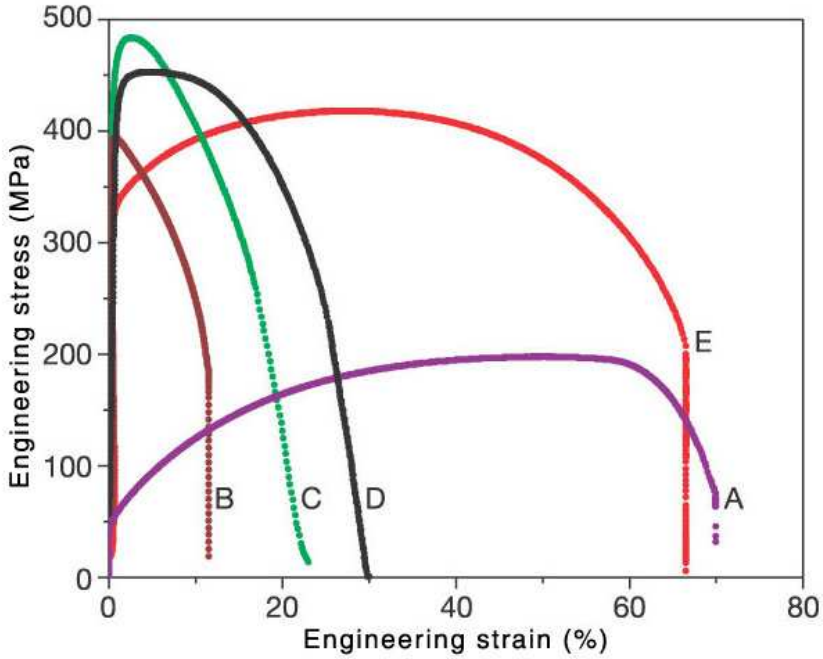

(a)

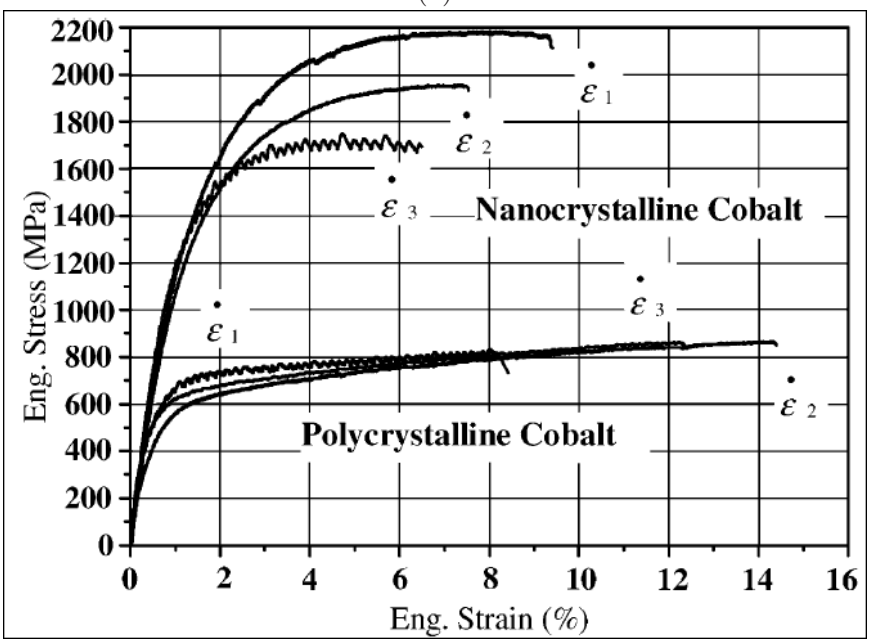

(b)

Figure 15: (a) The engineering stress-strain plots for copper with different grain sizes and distributions (A: course-grained and E: bimodal grain size distribution) [283]. Note the high strength and good elongation to failure observed for plot E as compared to plot A. (b) A comparison of the stress-strain behavior of both NC and PC cobalt at different strain rates ($\dot{\epsilon_1} < \dot{\epsilon_2} < \dot{\epsilon_3}$); NC cobalt exhibits a much higher yield strength than PC cobalt, and a higher yield strength is also observed with a slower strain rate in NC cobalt [103].

rates. For the NC structures, cobalt exhibits both higher yield strength and ductility with lower strain rates. This behavior is contradictory to known results for materials that deform predominantly by dislocation activity. Karimpoor *et al.* [103] suggest that the major strain accommodation mechanism in NC cobalt is deformation twinning. These results stress the importance of both grain size and deformation mechanisms on determining bulk material properties, such as yield strength and ductility.

Another example showing the influence of grain size on bulk mechanical behavior was offered by Koch and coworkers [111, 317]. Figure 16 shows a tensile stress-strain plot for both coarse-grained and NC copper prepared by the inert gas condensation method with an average grain size of 23 nm. The NC copper sample consisted of equiaxed grains, similar to the bulk specimen, with negligible porosity and minimal impurity content after preparation. Tensile data shows that the yield strength of the NC copper sample is at least an order of magnitude higher than the coarse-grained sample, accompanied by good ductility. Additionally, strain hardening was also observed suggesting that dislocation nucleation and migration is present in the nanograins. The presence of both high yield strength, improved ductility, and strain hardening is thought to be due the improved processing method leading to artifact-free NC samples.

The last decade has seen expanded interest in materials nanostructuring and innovative fabrication techniques aimed at producing bulk NC and ultra-fine grained (UFG) samples. The use of NC materials in advanced engineering applications therefore relies on the ability to fabricate bulk samples and tailor the resulting functional properties. Understanding the nanoscale mechanisms and realizing the macroscopic implications are imperative for the engineering community. Therefore, we begin our discussion outlining two common methods for NS material synthesis/fabrication and their associated mechanical enhancements.

2.5.1 Preparation of Nanocrystalline Materials

Over the past couple of decades, a number of approaches have surfaced for the preparation of ultra-fine grained (UFG) and NC materials, among these are (1) electrodeposition and (2) severe plastic deformation methods. These two methods are outlined here for their direct

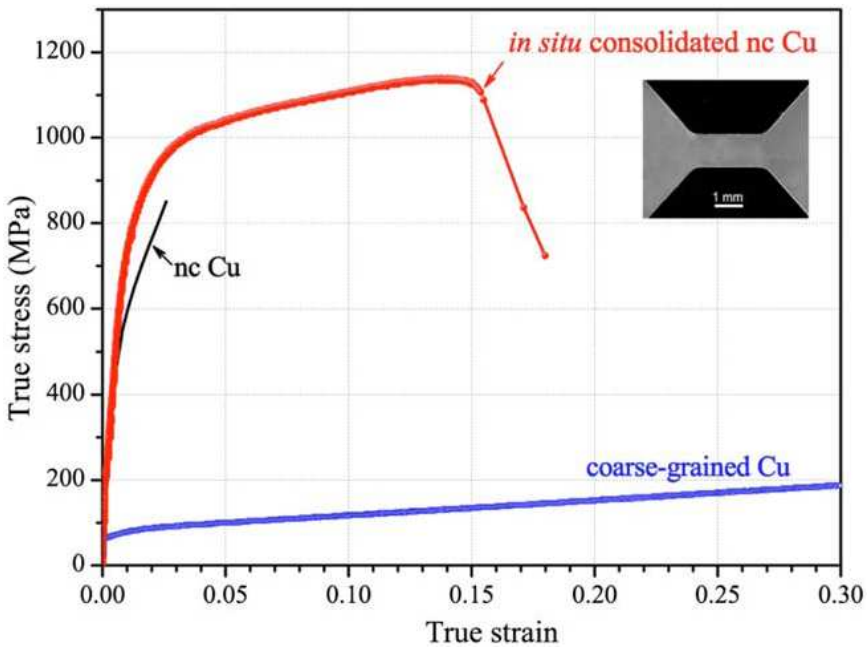

Figure 16: A comparison of the tensile stress-strain behavior of coarse-grained copper and NC copper. Two different NC copper plots are shown, an *in situ* consolidated sample and a sample prepared by inert-gas condensation. The grain size of the NC copper sample is 23 nm, where the average grain size of the coarse-grained sample is larger than 80 μm [111, 317].

implication on the type of GB structures investigated in this work. Electrodeposition (ED) is known to produce near equilibrium boundary structures due to the factors that dictate whether grain growth of grain nucleation is favored. Over-potential, deposition rate, and the bath *ph* are major factors influencing this trade-off during the production of UFG and NC metals. Methods of severe plastic deformation (SPD) are widely used for bulk sample preparation with nanosized grains, where GB structures are heavily altered due to plastic deformation imposed during straining. Numerous defect/GB interactions lead to structures with higher energy, greater dislocation content, and excess free volume.

ED has the advantage of being a one-step process and thereby reducing the potential for processing artifacts, such as porosity, that might lead to material degradation often experienced by consolidation techniques. For example, the use of ball milling for fine NC powder processing, can introduce significant contamination into the sample, thereby influencing the properties. The microstructure/properties of NC metals processed via ball milling have been noted to be directly influenced by impurities introduced during processing. On the other

hand, impurities are often introduced during ED to hinder grain growth, since these additives affect interfacial strength and energy. Near equilibrium grain and interface structures are common for NC materials processed using ED; therefore, many computational efforts dealing with equilibrium interfaces cite the importance of electrodeposited materials.

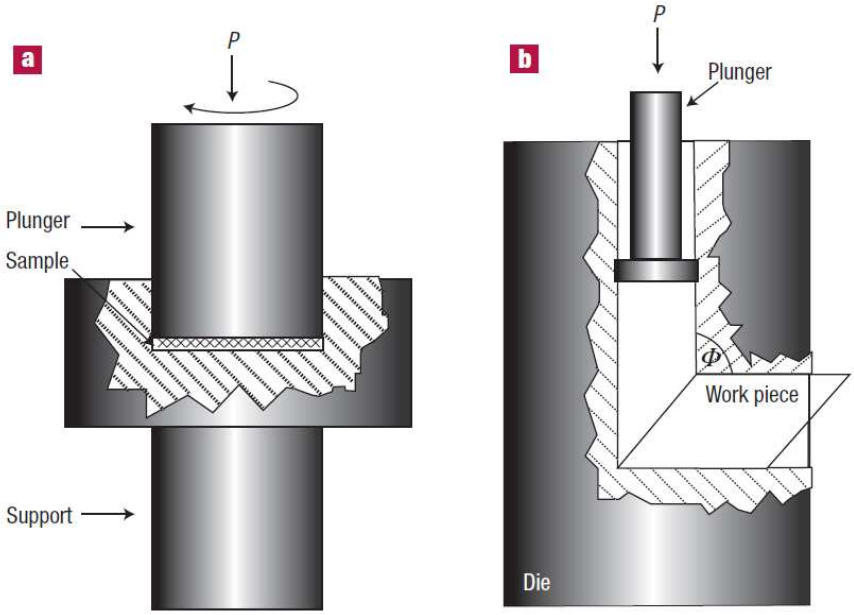

Figure 17: Two common SPD techniques for processing bulk NS materials: (a) high pressure torsion (HPT) and (b) equal channel angular pressing (ECAP) [244].

SPD techniques include methods such as equal channel angular pressing (ECAP), extrusion (ECAE), and high pressure torsion (HPT) (as shown in Figure 17 [244]). The purpose behind SPD methods is to produce bulk sized UFG and possibly NC materials, where the source for nanostructuring is the extensive production of dislocations during imposed shear strains. For at least 50 years, it has been known that the microstructure of metals is heavily altered due to increasing plastic deformation and excessive dislocation content. The dislocations produced during plastic deformation tend to arrange in low energy configurations such as cells and sub-grains. As more dislocations rearrange into these lower energy structures, lower dislocation densities are observed in the lattices while the misorientation angles between the cells increase. An extensive review on bulk NC processing methods such as SPD is given by Valiev *et al.* [248].

2.5.2 Microstructure and Grain Boundaries of Nanocrystalline Materials

A common feature to all NC materials is the high percentage or volume fraction of GBs. Also, since the intersection of GBs form a triple junction (TJ), the number density of TJs is higher in NC materials as well as compared to coarse-grained PC materials. Therefore, the structural length of GBs in NC materials must also be less than those in coarse-grained materials and, due to the influence of TJs on GBs, the structure and properties of GBs differ as well. The description of GBs based on misorientation angle (θ) between the adjoining lattices can either be low-angle ($\theta < 15°$) or high-angle ($\theta \geq 15°$), and GBs can also be described as near equilibrium or non-equilibrium (NE) based on structure. Additional properties can also be used to describe GBs, such as energy, defect content, and free volume, where processing history strongly influences each property. For example, extrinsic defects reside in NEGBs from SPD, where the defect content of near-equilibrium boundaries is usually defined by intrinsic GB dislocations/disclinations.

The elastic and inelastic deformation behavior of NC and UFG metals is heavily influenced by processing history. This is due to the microstructural features generated during specific routes used for metal processing. For example, as grain size is reduced below a few hundred nanometers, mechanical properties such as yield strength, ductility, fatigue/fracture resistance, and superplasticity have been observed to be altered from what is expected from conventional PC metals. But to fully understand the resulting mechanical properties, a better understanding of the microstructural changes imparted by specific processing routes is required, and additional insight into the nanoscale structures that affect deformation is vital.

In NC and UFG materials, the mechanisms of deformation and the bulk properties not only depend on average grain size, but also on GB network character, the grain size distribution, and on GB structure. When discussing GB structure, not only is the comparison and distribution of low and high-angle boundaries important, but also the state of the boundary (i.e., equilibrium vs. NE) and excess free volume as well. Each of these factors help determine the overall GB structure and properties, and will be discussed in the context of GB behavior and structure. Furthermore, substantial experimental evidence supports the idea

that GBs in NC and UFG metals are usually about 1 nm thick (as displayed in Figure 18 by high resolution electron microscopy (HREM)) and absent of any type of amorphous structure [95, 94, 297]. These authors argue that crystallinity is maintained up to the interface in these metallic materials.

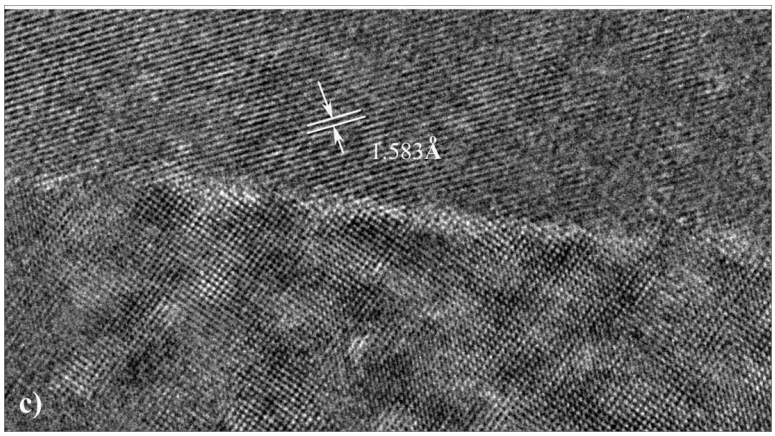

(a)

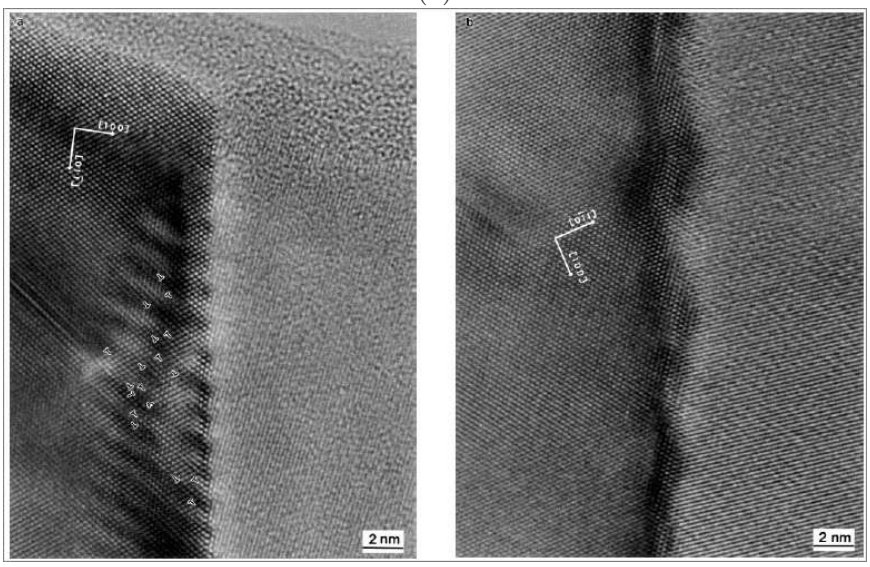

(b)

Figure 18: High resolution images of NEGBs in (a) nickel [297] and (b) Al-Mg alloy [94].

GBs within materials that have undergone SPD are significantly altered from those observed in ED, for example. Excess defect concentrations, and extensive GB/defect interactions lead to GB structures containing disordered regions, steps, ledges, extrinsic defects, and more complex dislocation content. The resulting behavior of these boundaries is therefore influenced [62, 99, 108, 155, 154, 246, 249, 250, 273, 304], and processes such as

dislocation emission, absorption, transmission, boundary migration, and sliding will likely be altered. As suggested, there is evidence offered by HREM (Figure 18) that the thickness of these GBs is about 1nm (atomically sharp) [95, 94, 249, 297], and there is also evidence of interfacial regions which are partially disordered that accompany the other extrinsic defects. These GBs have been termed 'non-equilibrium' due to their relative high energy, excess free volume, dislocation/disclination content, disordered atomic structure, and energetically metastable state as compared to their equilibrium counterparts. Excess GB free volume has been noted to be a good measure of the degree of 'non-equilibrium' state ([42]), and is defined as the additional amount of free volume as compared to that present in the equilibrium GB structure. Excess free volume correlates with higher interfacial energy and atomic misfit, and is therefore a key physical attribute directly affecting many important GB properties ([40, 42, 173, 253, 305]), such as sliding, migration, and dislocation mediation processes.

Although NEGBs seem to play an important role in the properties of UFG and NC metals that have undergone SPD, boundaries resulting from ED tend to be nearer to equilibrium and lower energy. It is also quite possible for boundaries produced during ED to contain impurities and organic elements due to the bath composition. This is one major drawback for NC metals from ED, and must be considered when interpreting microstructural results. Equilibrium GB structures in fcc metals have been recently probed by HRTEM, and a few example STGBs are shown in Figure 10 along with GB structures from atomistic simulations. However, as shown in this Figure, there is excellent agreement between minimum energy GBs from atomistic simulations and those observed from HRTEM (as shown in Figure 10). The literature is filled with work investigating the minimum energy (near equilibrium) GB structure in metals, and a good portion of those studies utilize atomistic simulations [29, 49, 183, 184, 203, 204, 207, 208, 206, 223, 225, 220, 229, 230, 236, 235, 237].

2.5.3 Mechanical Behavior

A brief overview of the experimental results concerning the mechanical behavior of NC metals will be given first, followed by results of computer simulations. The majority of

literature focused on the mechanical properties of NC and UFG metals/alloys deals with hardness [117, 146, 201, 296], yield strength [3, 16, 24, 37, 44, 62, 112, 140, 182, 285, 296, 317], elongation to failure [64, 103, 113, 112, 134, 137, 136, 283, 317, 320], and elastic modulus [72, 193, 302]. Our brief outline here discusses each property, structural features that influence each property, and the accompanying results found in the literature. There have been a number of efforts to summarize/review the mechanical behavior of NC materials [84, 111, 117, 145, 296], but only a brief discussion of each property will be provided here.

The hardness of NC metals has been recently reviewed by both Weertman *et al.* [296] and Milligan [146], as well as others. In the literature, results show that the hardness of NC metals is dramatically higher than the corresponding coarser-grained metals. In fact, Youssef *et al.* [316] found that NC copper with an average grain size of 23 nm exhibited a hardness of about 22 times greater than its large-grained counterpart. The dependence of hardness on grain size parallels that of yield strength in metals, where the Hall-Petch relationship describes an increase as grain size is reduced. However, recent data [190, 219] show that at the smallest of grain sizes (e.g., $< 10 - 20$ nm) in fcc metals, there is a reverse in this relationship, the so called 'Inverse Hall-Petch' relationship (first noted by Chokshi *et al.* [39]). An illustration of this trend is provided in Figure 19 provided by (a) Pande *et al.* [164] and (b) Kumar *et al.* [117].

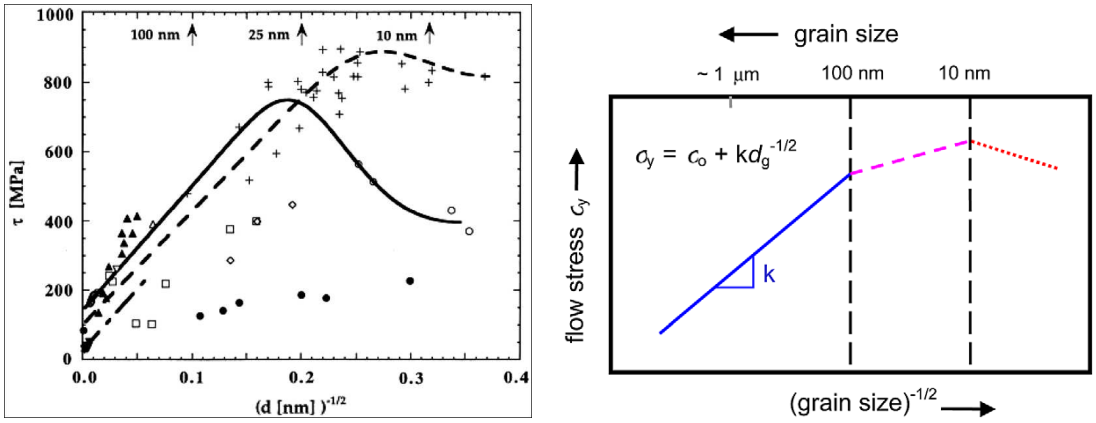

(a) (b)

Figure 19: (a) Yield stress as a function of grain size for pure copper [140, 164], and (b) a schematic illustration of the Hall-Petch breakdown for metals and alloys [117].

To understand this behavior, a consideration of the underlying mechanisms is needed. In coarser-grained PC metals, dislocations glide along slip planes within the lattice and eventually interact with GBs and activate dislocation sources in neighboring grains, leading to work hardening. But, in materials with smaller grain sizes (e.g., 20-50 nm), traditional dislocation sources (e.g., Frank-Read) and multiplication mechanisms are not dominant. Alternative deformation mechanisms (e.g., heterogeneous dislocation nucleation and GB sliding) become the dominant carriers of deformation. In the last decade, significant research has shown that at even smaller grain sizes (e.g., 5-10 nm), dislocation activity might be only a small fraction of the active deformation mechanisms, giving way to GBs playing the dominant role. This transition has recently been explored with atomistic simulations [187, 269, 260] as well.

To investigate hardness and yield strength, uniaxial tension/compression experiments are undertaken at a variety of strain rates and temperatures. Most of the early work studying uniaxial deformation behavior of NC fcc metals was performed using indentation [44, 182, 285, 296]. However, recently, more advanced testing and characterization methods, such as micropillar compression tests [57, 239, 238, 278, 279] have been leveraged to probe material strength and plasticity for small volumes. It has been found that as the grain size is reduced below 100 nm, fcc metals exhibit significantly higher yield strength and reduced ductility.

Modulus is also influenced by average grain size in PC metals. Clearly, as grain size is reduced, GBs compose a larger percentage of material volume; therefore, it was thought that the lower atomic density associated with GBs will affect bulk modulus values. Early measurements of different modulus value in NC metals [210] have recently been shown to be a consequence of inaccurate experimental measurement techniques [296]. In recent years, more comparable modulus values were recorded in NC metals as compared to conventional coarse-grained metals [302, 193].

In addition to yield strength, ductility is the most explored mechanical property of NC materials. Ductility is the ability of a material to deform under applied stress or imposed strain without failure. Its importance in structural applications and technological materials

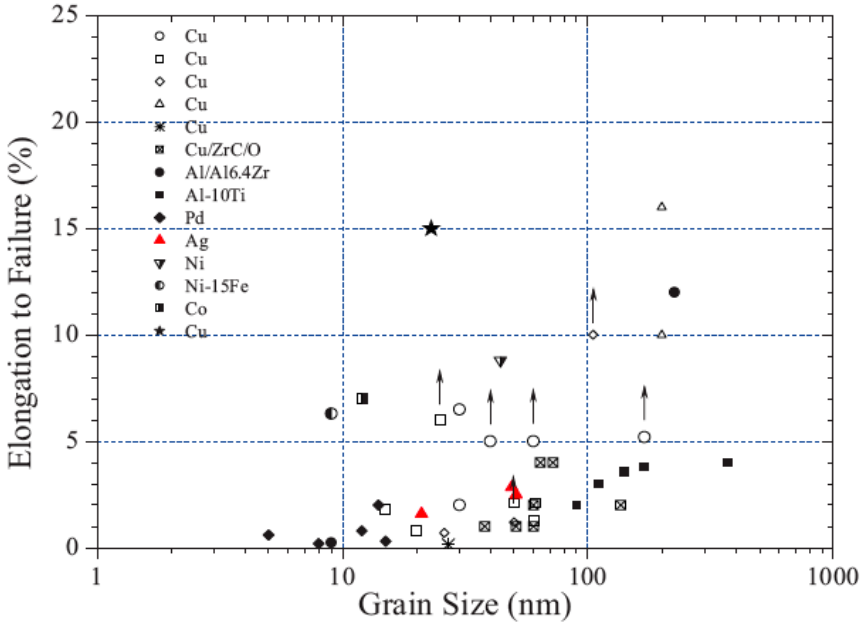

Figure 20: Elongation to failure as a function of grain size for a large number of metals and alloys [111].

cannot be overstated. It is therefore one of the more critical properties to understand for functional materials. The most common measure for ductility is elongation to failure. In NC metals, early measurements showed that ductility decreased with a reduction in average grain size [113, 111] (as shown in Figure 20), which is contrary to traditional thought [20].

As yield strength increases in NC metals, ductility usually decreases. Therefore, in recent years numerous research efforts have aimed at optimizing both strength and ductility [62, 131, 136, 195, 194, 244, 246, 283, 317, 320, 322, 321]. Common attributes that decrease ductility in NC metals are processing artifacts, such as impurities and porosity, mechanical instability, and the lack of strain hardening mechanisms (i.e., dislocation slip). Using *in situ* TEM observations during straining, Youssef *et al.* [317] recorded dislocation processes and pile-ups at GBs in NC copper with a narrow grain size distribution. This work showed the importance of dislocation activity in strain-hardening in NC metals to preserve ductility, and it is possible to achieve both high strength and ductility in artifact free NC copper. Similar results regarding the role of crystallographic slip and GBs as a source for dislocations in nanograins have been recorded in NC materials with broad grain size distributions [195, 307]. Furthermore, recent work has also shown the influence of high-angle GBs (HAGBs)

on ductility [62, 136, 320, 323]. GBs influence NC deformation mechanisms, either as a dislocation source/sink or through GB-mediated accommodation mechanisms such as sliding, migration, and shuffling. To gain insight into interface-mediated phenomena in NC metals, a multitude of computational studies have been undertaken. With regard to the objectives of this thesis, we will only summarize and provide a brief overview of atomistic simulations.

2.5.3.1 Computational Studies

Although various computational techniques are used to study deformation and fracture in NC materials, only atomistic simulations are covered in this section. The last decade has witnessed a surge of research across the scientific and engineering communities utilizing atomistic simulations to probe material behavior at the nanoscale. The most widely used technique is MD simulations. As previously discussed, MD simulations have inherent limitations: short time and length scales. Due to the small required timestep (e.g., 1 femtosecond) to properly capture atomic processes, there is a limit in the time (number of integrated timesteps) a MD simulation can handle, usually around 10 ns (or 10 million timesteps). Usual strain rates in most MD simulations range from 10^7 to $10^9 s^{-1}$. Clearly, strain rates in this regime are too high to compare with most experimental results. Additionally, an important factor determining atomic system behavior is the chosen interatomic potential(s). Some interatomic potentials are better than others for capturing certain behavior and mechanisms at work at the nanoscale, and the results of MD are heavily influenced by the chosen potential.

Some of the more well-known MD simulations probing GBs and the mechanical behavior of NC metals have been performed by Schiotz *et al.* [186, 188, 187, 189], Van Swygenhoven and coworkers [52, 53, 54, 55, 51, 75, 74, 79, 78, 77, 89, 256, 255, 257, 266, 268, 267, 270, 269, 258, 260, 272, 264, 273, 271, 261, 265, 262, 263, 274], and Yamakov *et al.* [301, 313, 308, 314, 312, 309, 310, 311]. The results of these investigations agree that inelastic deformation processes of NC metals are quite different than those of coarse-grained PC metals. In addition to the differences in strength and ductility observed (as described earlier), there

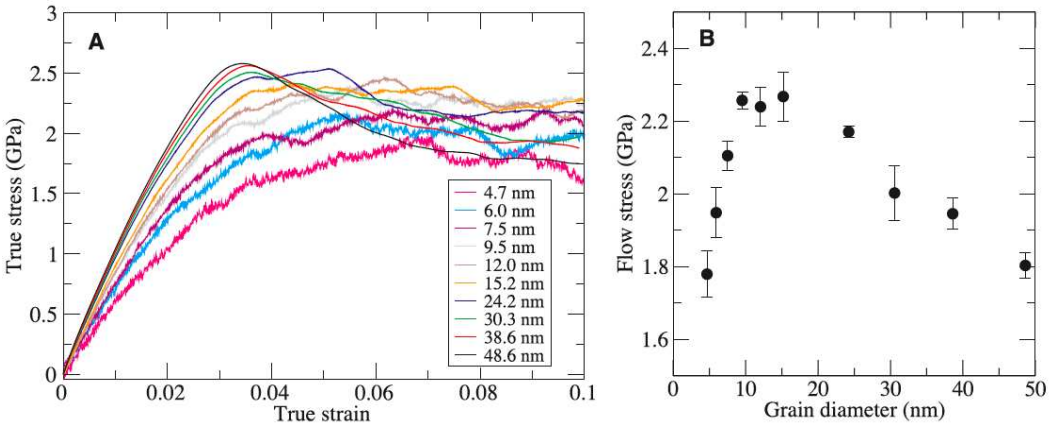

Figure 21: (a) The tensile stress-strain behavior of NC copper with varying average grain sizes deformed under uniaxial tension. (b) The flow stress as a function of grain diameter [187], where flow stress is calculated as the average stress between 7% and 10% strain.

is a transition from dislocation-mediated deformation, where crystallographic slip is the dominant carrier of plasticity, to a regime where GB-mediation is dominant as a function of average grain size. The general consensus is that this transition regime is between 10 and 30 nm average grain diameter. In addition, this transition coincides with a maximum in the strength of NC materials [187, 265] (as shown in Figure 21), where lower strengths are observed in MD simulations for NC structures with smaller grain sizes [186].

Dislocation nucleation and emission from GBs is an important strain accommodation mechanism in NC metals. Instead of tradition Frank-Read sources, GBs become the source for both partial and full dislocations in NC materials (as shown in Figure 22). Due to the small grain size, the emitted dislocations tend to glide across the grain and become absorbed in other GBs, sometimes leaving behind a stacking fault for the case of partial dislocation emission. This plastic deformation mechanism was verified experimentally by Liao *et al.* [125] in NC aluminum. Figure 23 shows a HRTEM image of both partial dislocation emission from GBs and the presence of deformation twinning through successive partial dislocation emission on neighboring glide planes. The agreement between atomistic simulations and experiment concerning the role of dislocation slip and GBs as a source for dislocations in NC metals is encouraging.

Since GBs act as dislocation sources, their structure is influential in plastic deformation

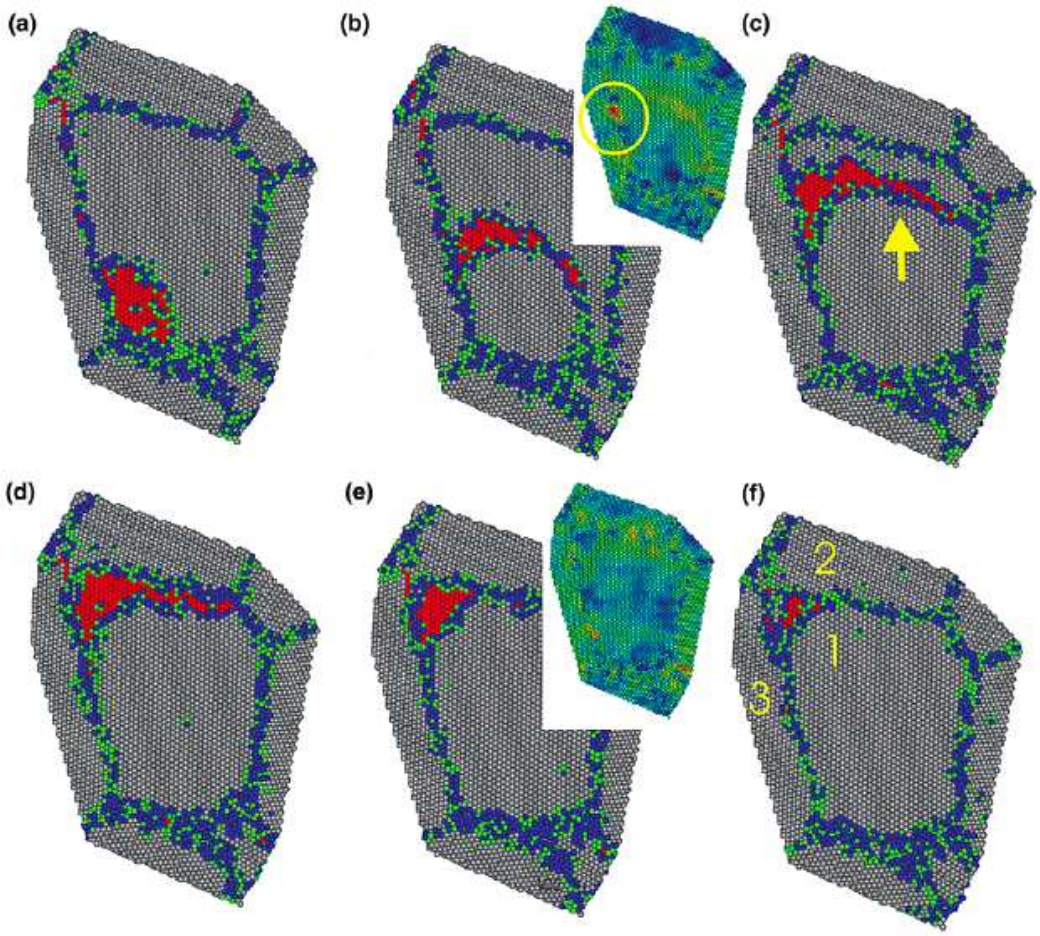

Figure 22: A MD simulation showing the nucleation/emission of a full dislocation from a GB/TJ region and traversing the entire grain being absorbed into another GB/TJ region [75]. In this case, the full dislocation has split into two partial dislocations separated by a stacking fault. The two insets show the resolved shear stress in the GB that hinders the dislocation migration.

in NC materials. Recent MD simulations by Van Swygenhoven *et al.* [273] explored the consequence of altering the structure of GBs (equilibrium vs. NE) in a NC nickel structure with an average grain size of 12 nm. Three different NC samples were studied: (1) the as-prepared sample from the initialization procedure (Voronoi method), (2) the as-prepared sample after being annealed for 100 ps at high temperature, and (3) a GB-disorder sample in which interfacial atoms in the as-prepared sample were randomly moved some fraction of an atomic spacing within the interface. The GB-disorder sample contains excess atomic disorder and free volume in the intercrystalline regions as compared to both the as-prepared sample and the equilibrated sample. The interfacial regions in the equilibrated sample are

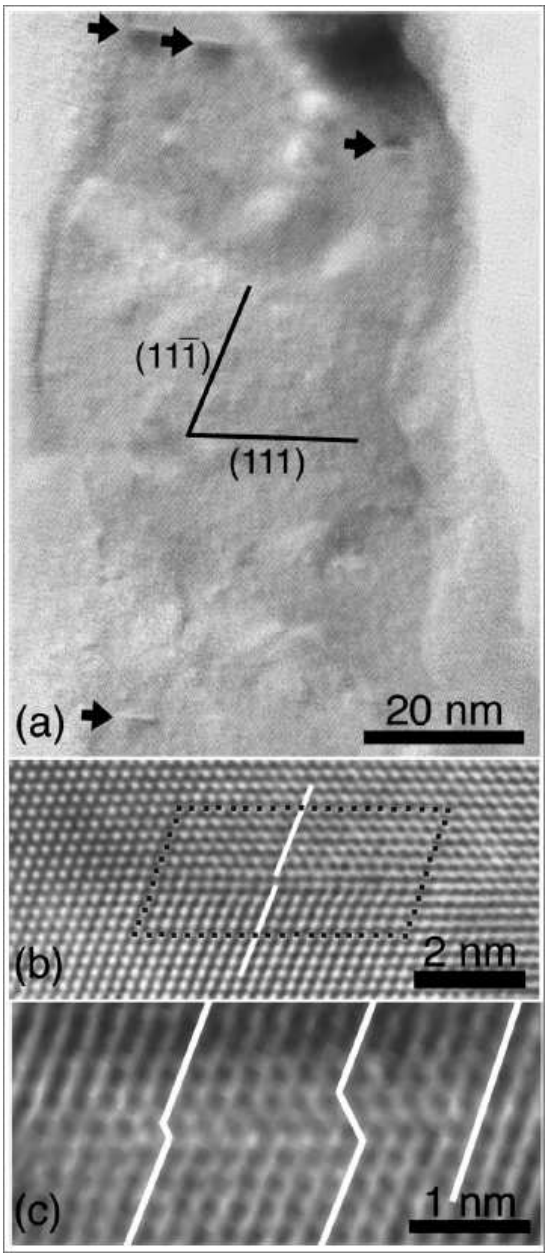

Figure 23: (a) A nanograin containing stacking faults and dislocations emitted from GBs in NC aluminum. (b) A Burgers circuit around a stacking fault lying between two partial dislocations found in the NC sample. (c) The presence of a deformation twin from partial slip on two adjacent slip planes [125].

more compact and are lower energy structures as compared to those in the as-prepared sample. Figure 24 shows both the (a) mechanical behavior and (b) energy profiles of the three different NC structures. Clearly, as Figure 24(a) displays, strength decreases with more equilibrium (and lower energy) GB structures, and increases with the introduction

of NEGBs through additional atomic disorder and excess free volume. The energy distributions shown in 24(b) also demonstrates that GB relaxation does indeed occur with high temperature equilibration compared to the as-prepared sample, and the presence of higher energy NEGB structures are present in the GB-disorder structure as compared to both of the other NC structures. The influence of GB structure on the mechanical behavior of each NC sample is evident in this work, and indicates the role of GB-mediated deformation mechanisms in NC deformation.

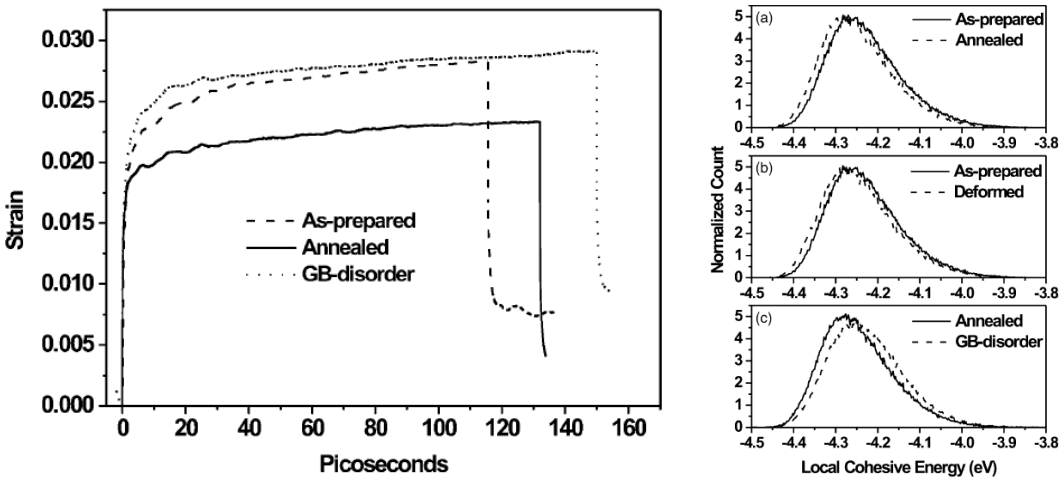

Figure 24: (a) The stress-strain behavior of three NC structures with different GB structures. (b) The energy profiles of non-fcc atoms in the three NC structures [273].

In NC structures where GBs and other intercrystalline regions control plastic deformation, dislocations are still observed. However, their emission from GBs aids in the accommodation of GBs through sliding/shuffling mechanisms [189, 186, 188, 260, 268, 269, 301]. Atomic shuffling in GBs is also an important mechanism during GB sliding in NC metals [260, 269], and in the shear deformation of bicrystalline boundaries [184, 183, 236, 234]. It has also been recognized that during the deformation of NC metals, both GB and TJ migration occur as well as the migration of free volume within GBs to and from TJs.

An important plastic deformation mechanism in NC metals is GB sliding. This mechanism is in competition with both dislocation slip and diffusional deformation modes in NC structures. GB sliding is defined as the translation of one grain relative to another where deformation accommodation only occurs within the interface, and usually only occurs in

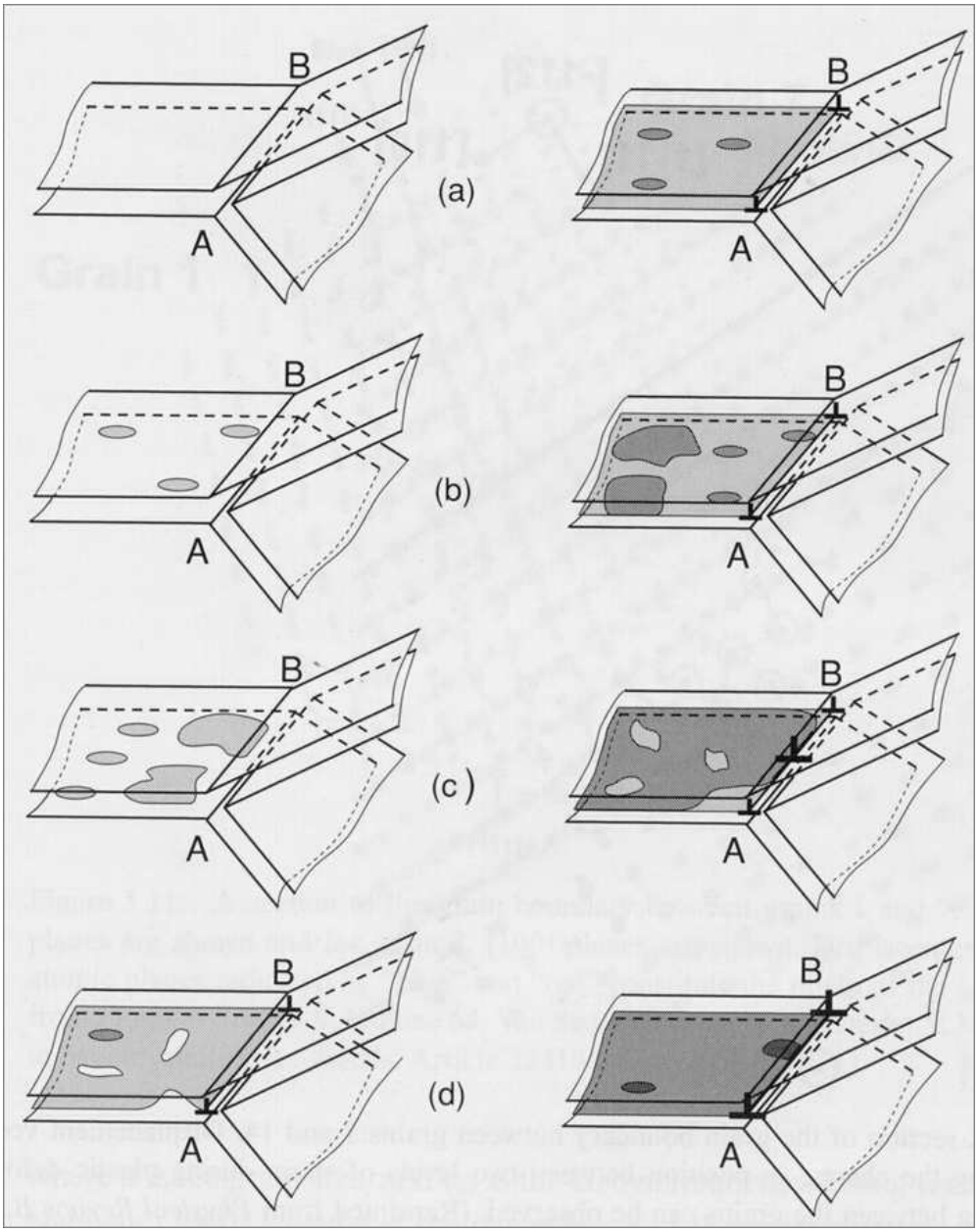

Figure 25: A schematic showing GB sliding through local shear events (grey loops). Through GB sliding, the formation of a dislocation at the TJ (AB), is shown (d-h) [114].

HAGBs or NEGBs. The most common type of GB sliding that is observed in NC structures is when local shear events within the GB (as shown in Figure 25 [114]) are activated due to both the resolved shear stress and thermal contributions to atomic mobility [163, 211, 260].

These local shearing events during GB sliding, occur as either single atomic jumps or the simultaneous transformation of a group of atoms [163]. It was previously stated that

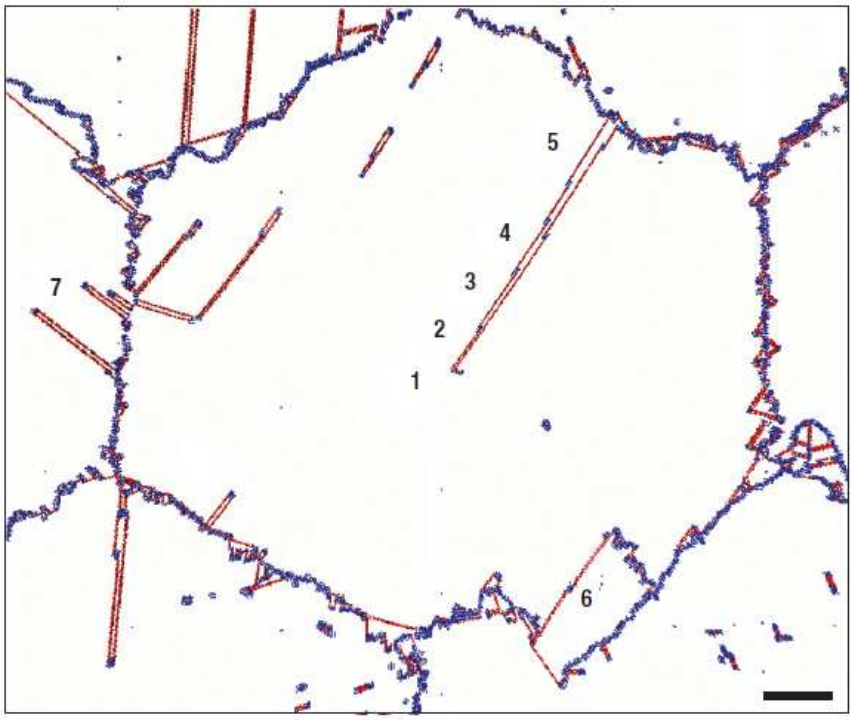

Figure 26: The plastic deformation of a NC hexagonal columnar structure in aluminum. Stacking faults, dislocations, and twinning is observed within the structure. Atoms are colored according to their crystal structure, red is hcp and blue is non-12 coordinated atoms (fcc atoms have been removed from this image). A numeric sequence outlines various planes within a twinned region corresponding to the provided stacking sequence beneath the image, where red letters represent hcp atomic planes [314].

interfacial free volume influences atomic mobility and is therefore a key component during atomic shuffling and GB sliding. Free volume is also important for the local shearing events as well. The barrier to activate local shear events is lower with higher concentrations of free volume [108, 234]. Therefore, higher free volume interfacial regions deform by local shearing events prior to other regions and at lower resolved stresses. With excess free volume present, these types of local shear events during GB sliding are expected to be even more common in NEGBs. In either structure, as grain size is reduced, GB sliding becomes a more dominant strain accommodation mechanism and is heavily influenced by interfacial free volume.

Additional work using atomistic simulations to investigate the mechanical behavior of NC metals by Yamakov *et al.* [311, 310, 314, 313], have explored the complex interplay of dislocation-mediated and GB deformation processes. Using ⟨110⟩ textured columnar NC structures in aluminum, Yamakov and coworkers observed a variety of plastic deformation mechanisms. For example, as displayed in Figure 26(a), numerous dislocations are seen gliding inside the grain. The partial dislocations are nucleated at GBs and propagate away creating a stacking fault. However, as the local stress within the boundaries rises, the emission of the trailing partial dislocation is often observed as well. Furthermore, deformation twinning is also observed in these MD simulations. Highlighted by the numeric sequence, partial dislocations on adjacent slip planes form a thin twinned region. The importance of this result, is that deformation twinning in NC aluminum was predicted using MD prior to the TEM evidence provided by Chen *et al.* [36].

There is a growing body of work in the literature concerning atomistic simulations of NC materials. Although only a small portion of the major themes of MD work on NC metals is presented here, most work is built upon these major achievements. The underlying theme to all the results summarized here is that the use of atomistic simulations to explore deformation behavior of NC materials is still ongoing and the ability of MD in this regard is promising. The research presented in this thesis using atomistic simulations compliments the results outlined above, and uncover many interesting characteristics and deformation phenomena of NC metals.

CHAPTER III

GRAIN BOUNDARIES AND FREE VOLUME

3.1 Introduction

Interfaces (i.e., GBs) confer properties to PC metals that differ from single crystalline metals. The atomic density of GBs is lower than that of the adjacent lattice, and its energy is greater as well. The additional volume GBs posses, as compared to a lattice with the same number of atoms, has been termed free volume. A better understanding of the relationship between GB structure and free volume can provide insight into the behavior and bulk properties of NC materials. Free volume influences GB behavior and is responsible for 'special' properties commonly attributed to GBs [173].

MD simulations investigating deformation in NC materials have shown that the initial free volume and its evolution within GBs is influential on GB sliding, grain rotation, and dislocation nucleation at nanoscale grain sizes [188, 260]. Prior to dislocation nucleation in NC materials, atomistic simulations have shown free volume migration occurs within the boundary and nearby TJs [55, 264]. In addition, excess free volume within certain GB regions promote the formation of the Burgers vector required for dislocation nucleation under applied load. The influence of GB structure on deformation behavior has also been explored using MD simulations of bicrystalline structures. Spearot and coworkers [204, 203] and Tschopp and McDowell [225] showed that GBs act as a dislocation source within nanosized grains, and the structural composition (i.e., structural units) affect the dislocation nucleation process. It is therefore imperative for additional studies to consider the composition and sequence of particular atomic structural units when exploring GB structure/property relationships.

In recent work, Sansoz and Molinari [183, 184] and Spearot [207] uncovered unique behavior offered by the GBs containing the E structural unit. This particular unit was found to be critical for the onset of atomic shuffling and GB sliding by Sansoz and Molinari

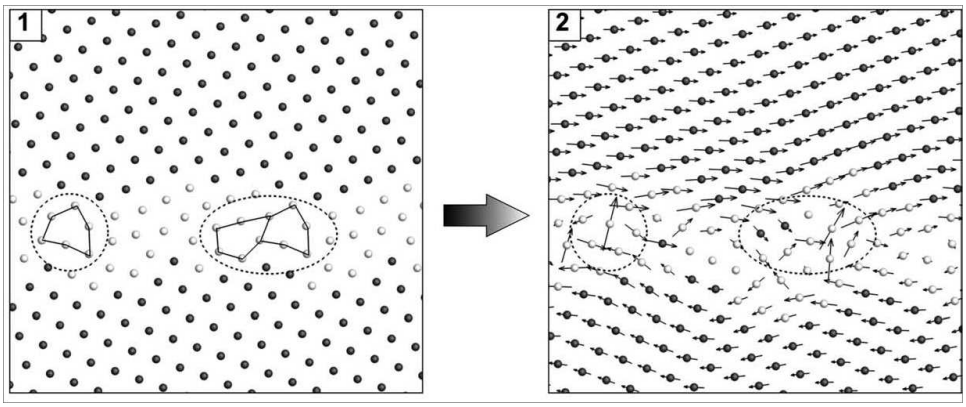

Figure 27: Image from Sansoz and Molinari [184], showing (1) the initial GB structure for the Σ9 (221) GB where E structural units are outlined. (2) A depiction showing atomic displacement vectors during shear deformation of the atoms within the GB. The two circled regions show atomic shuffling as a necessary component to GB sliding within high free volume E structural units.

[183, 184] during atomistic simulations under shear. In Figure 27, the influence of the E structural units on atomic shuffling behavior during shear deformation is displayed. Atoms within and around the E structural unit undergo significant rearrangement and shuffling to accommodate the imposed shear strain of the Σ9 (221) GB. Also, in Figure 28(a), the dependence of the maximum shear stress on the number of free atomic planes from the interface is shown, where three different regions of deformation behavior are found.

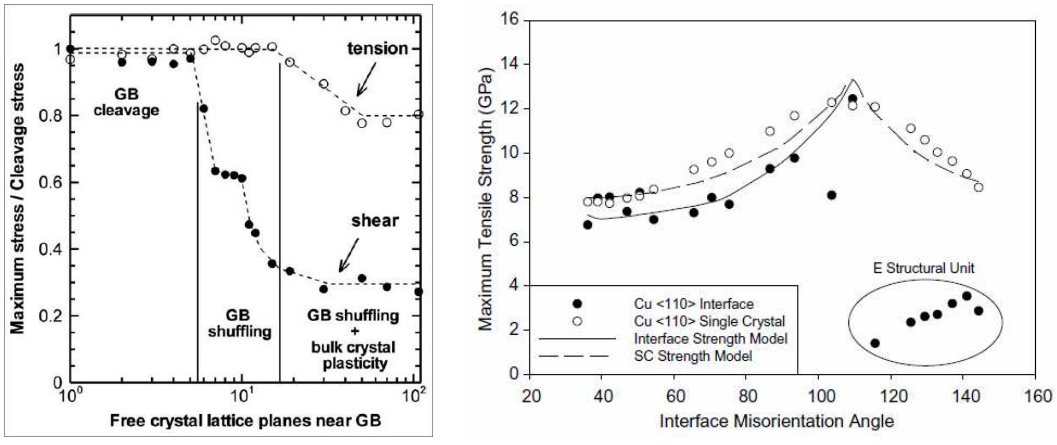

(a) (b)

Figure 28: (a) The maximum stress of the Σ9 (221) GB versus free atom planes near the GB from [184], showing the size effects and deformation behavior under tension and shear. (b) The interface strength model proposed by Spearot *et al.* [207], shown for copper ⟨110⟩ STGBs. Notice the drop in recorded interface strength for E structural unit boundaries.

Spearot and coworkers [207] formulated an interface strength model of STGBs as a function of misorientation angle and discovered distinct behavior for E structural unit boundaries. This model incorporates both lattice and GB (via free volume) variables, and sufficiently predicts the nucleation stress under uniaxial tension for most STGBs. However, for E structural unit boundaries the model fails to predict an abrupt drop in nucleation stress observed in MD simulations, as shown in Figure 28(b). E structural unit boundaries are those $\langle 110 \rangle$ STGBs with a misorientation angle between 109.5 and 180 degrees. Spearot *et al.* [207] hypothesized that a higher-order formulation that accounts for the distribution of free volume in the interface (e.g. two-point statistics) may be required to explain this effect. Therefore, the aim here is as follows:

- To explore the inherent relationship between GB structure and free volume for E structural unit boundaries, and to compute one and two-point statistics of interfacial free volume.
- Investigate the deformation asymmetry under uniaxial tension and compression for a group of E structural unit boundaries and highlight the possible effect of free volume and the resolved stress components on the activated slip planes.
- Quantitatively track the evolution of interfacial free volume for various STGBs (both with and without the E structural unit) during dislocation nucleation under uniaxial tension, and explore how individual structural units affect interfacial deformation.

3.2 Computational Methodology

For all simulations in this chapter, a three-dimensional periodic simulation cell was adopted containing two lattices separated by planar STGBs, as shown in Figure 29. To obtain the initial minimum energy bicrystalline structure, molecular statics employing energy minimization and numerous starting configuration (with different in-plane rigid body translations) was used along with an embedded atom method potential for copper developed by

Mishin *et al.* [150]. After energy minimization, equilibration at 10K under NPT was performed for at least 10 ps to allow simulation cell stresses to relax to zero. GB energies and simulation stress were both computed according to the aforementioned methods and compared to other reported values for accuracy. An example of a starting GB structure is shown in Figure 30(a), and a plot showing interface energy as a function of misorientation for ⟨110⟩ STGBs is displayed in 30(b).

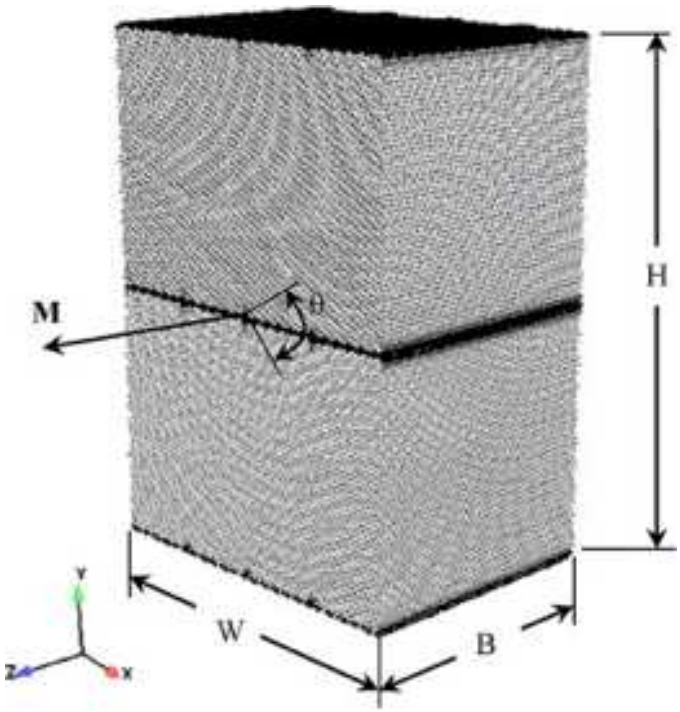

Figure 29: An example of a starting bicrystalline GB configuration with the tilt axis (M) shown, along with the misorientation angle (θ) and the cell dimensional length quantities as W, H, and B.

3.3 Structure and Free Volume of E Structural Unit Grain Boundaries

The initial minimum energy GB structures for various misorientation angles (θ) between the coherent twin boundary ($\theta = 109.5°$) and a single crystalline lattice ($\theta = 180°$) are shown in Figure 31 for ⟨110⟩ STGBs, viewing along the ⟨110⟩ tilt axis. Once each equilibrium GB structure is obtained, the interfacial free volume can be computed using the post-processing technique outlined in Chapter 2. As GB structure changes as a function of θ, the associated free volume changes as well. However, our method for computing free volume

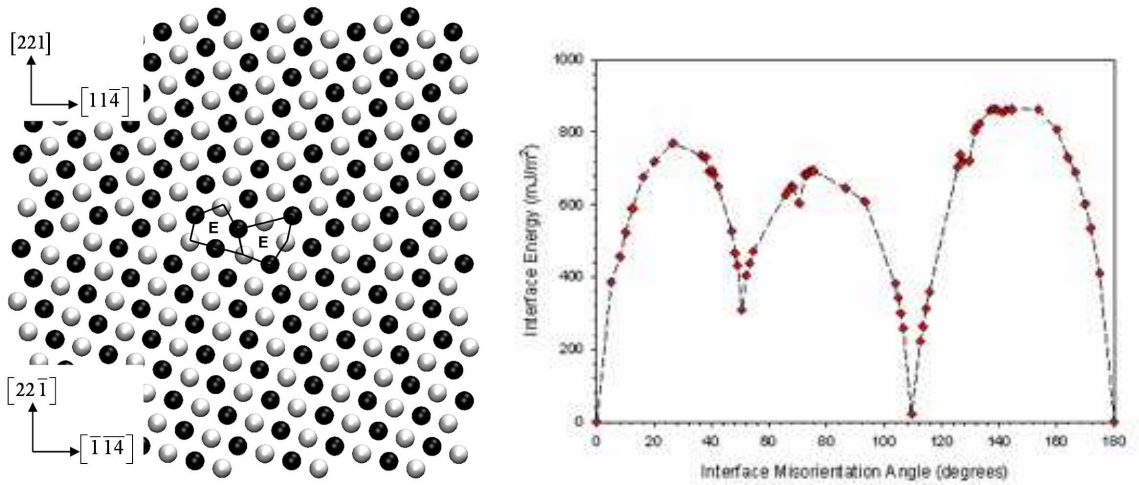

(a) (b)

Figure 30: (a) A view of the starting GB structure of the E structural unit Σ9 (221) boundary where the units for one period have been outlined and the lattice orientation vectors for both lattices are provided. (b) A plot of interfacial energy versus misorientation for ⟨110⟩ STGBs. Notice that there are three distinct energy cusps in this plot separated by three low energy GBs.

(as outlined in Chapter 2) has the advantage that both the volume fraction and spatial distribution of free volume within the interface can be computed simultaneously. There are other possible techniques to estimate GB free volume from volumetric expansion due to the presence of GBs; however, these approaches cannot distinguish free volume distribution within the boundary. Therefore, our method for computing free volume is better suited for the purposes of understanding free volume spatial distribution in addition to volume concentration. As stated, the concentration of GB free volume changes as θ changes, but the spatial distribution within the interface region also changes. For example, Figure 32 shows the distribution of free volume for 5 ⟨110⟩ STGBs, all containing the E structural unit. All images in Figure 32 are viewed normal to the GB plane.

After calculating the initial minimum energy GB structures, atoms associated with the GB were identified and characterized as structural units. The centrosymmetry parameter of Kelchner *et al.* [105] was used to identify the structural units. The centrosymmetry parameter permits the identification of those atoms whose local environment is elastically deformed (i.e., bulk crystal lattice) from atoms whose local environment is distorted due to lattice defects or, in this case, structural units. A threshold value of 0.25 was used as

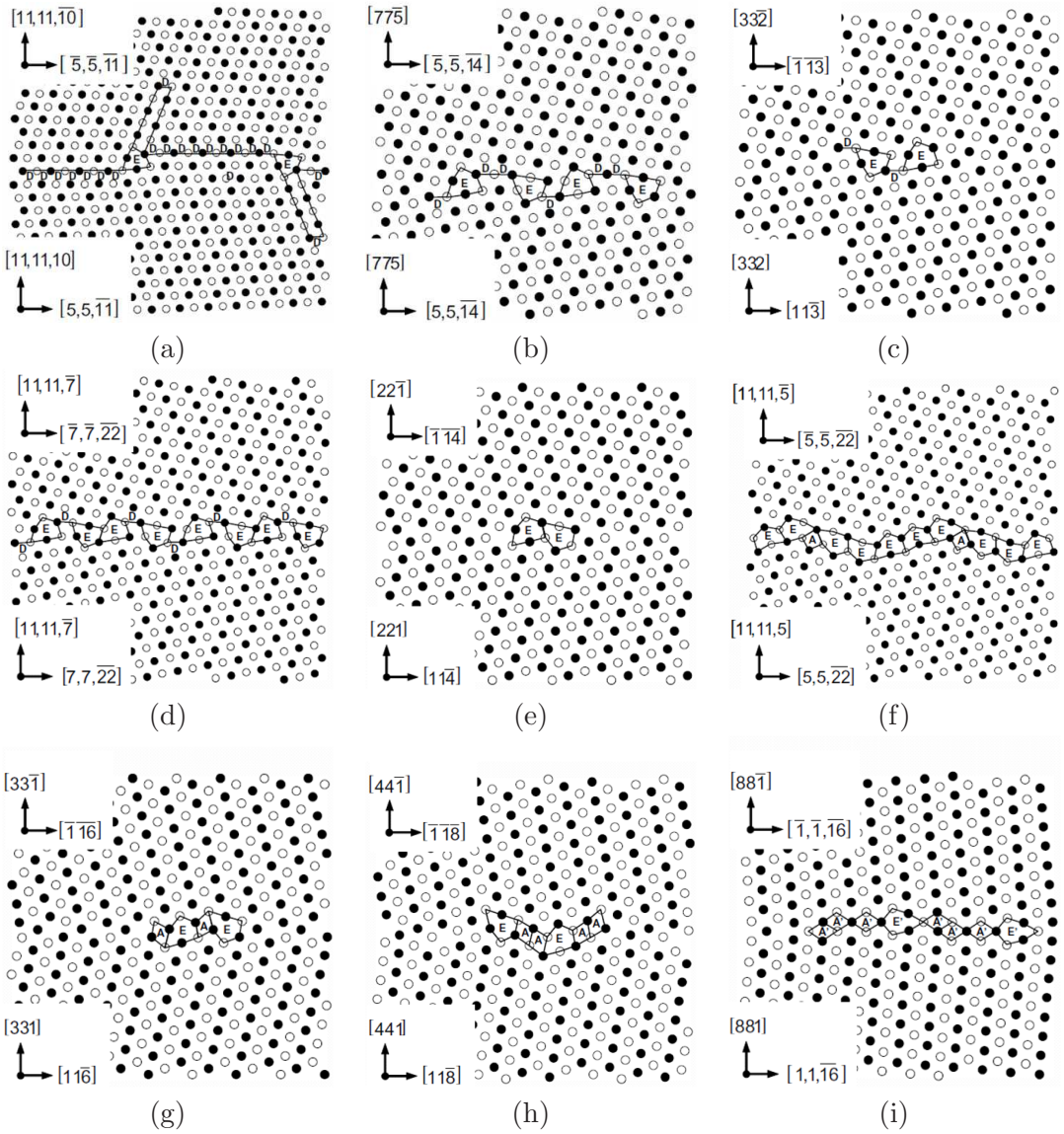

Figure 31: Nine ⟨110⟩ GB structures with the E structural unit in copper: (a) Σ171 (11,11,10), (b) Σ123 (775), (c) Σ11 (332), (d) Σ291 (11,11,7), (e) Σ9 (221), (f) Σ267 (11,11,5), (g) Σ19 (331), (h) Σ33 (441), and (i) Σ129 (881). The structures are viewed along the ⟨110⟩ tilt axis; atoms on consecutive (220) planes are shown as black and white. The GB normal and period vectors for the lower and upper crystals are also shown [229].

a guideline to designate atoms belonging to GB structural units from those belonging to the bulk lattice. The Σ9 (221) $\theta = 141.1°$ boundary is the favored boundary within this misorientation range [180]. This distinction means the Σ9 boundary is composed entirely of E structural units, and the E structural unit is common to all other GBs within this misorientation range ($109.5° < \theta < 180°$) for ⟨110⟩ STGBs. As θ decreases from the Σ9 value

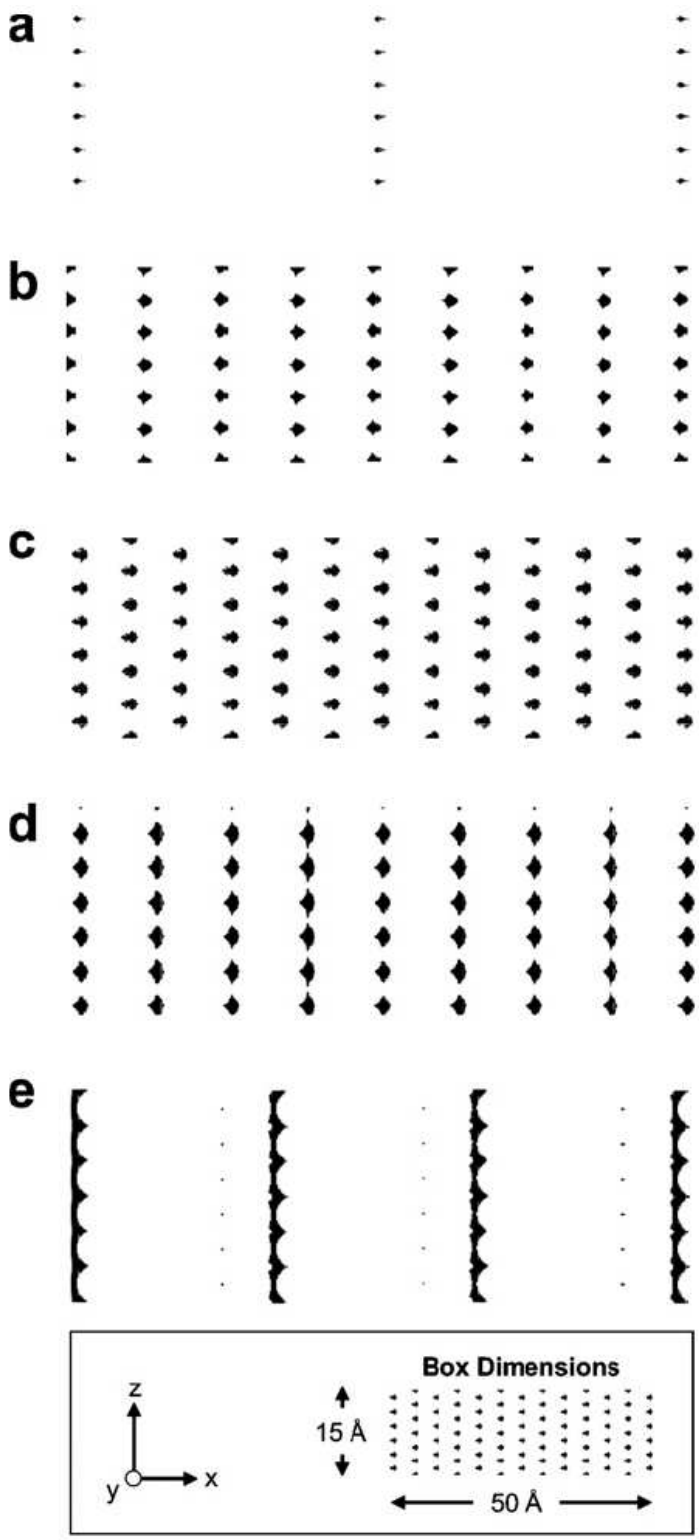

Figure 32: Two-dimensional projected view of the free volume in the GB plane for 5 GBs with misorientation angles in the range $109.5° < \theta < 180°$: (a) Σ171 (11,11,10), (b) Σ11 (332), (c) Σ9 (221), (d) Σ19 (331), and (e) Σ129 (881) [229].

of 141.1° toward the Σ3 (111) coherent twin boundary ($\theta = 109.5°$), the E structural unit composition decreases as the D structural unit composition increases. The D structural unit is associated with the coherent twin boundary; therefore, atoms composing the D structural unit are in a hcp configuration. All boundary structures between the Σ3 and Σ9 have a different composition of both D and E structural units. This same tendency is observed for boundary structures between the Σ9 and the single crystalline lattice ($\theta = 180°$), where the A structural unit defines perfect lattice coherency. Each boundary studied in this research, is listed in Table 1, according to misorientation angle (θ), coincident site lattice (CSL) designation and GB plane normal, and the structural unit description.

Table 1: Summary of initial GB information including CSL notation, GB normal, misorientation angle, and structural unit (SU) period [229].

Misorientation angle	CSL and GB plane normal	structural unit description
114.5°	Σ171 (11,11,10)	$\|9(D)E''.9(D)E''\|$
126.4°	Σ123 (775)	$\|DDEDE.DDEDE\|$
129.5°	Σ11 (332)	$\|DE.DE\|$
131.5°	Σ291 (11,11,7)	$\|3(DE)E.3(DE)E\|$
141.1°	Σ9 (221)	$\|E.E\|$
144.4°	Σ267 (11,11,5)	$\|5(E)A.5(E)A\|$
153.5°	Σ19 (331)	$\|EA.EA\|$
160.0°	Σ33 (441)	$\|EAA.EAA\|$
169.6°	Σ129 (881)	$\|EA'A'A'.EA'A'A'\|$

The free volume packets within the GB seen in Figure 32(c) are associated with the E structural unit. Therefore, as the concentration or number of E structural units along the GB period direction increases, more free volume packets are present. Free volume concentration per unit area can be calculated according to

$$f_1^* = \frac{1}{2A_{GB}} \left(\frac{V_{cell}}{n_x n_y n_z} \right) \sum_{ijk} N_{ijk} \tag{14}$$

where $2A_{GB}$ is the total GB area (contributions from both GBs in Figure 29) and V_{cell} is the simulation cell volume. This calculation removes the bias in computations due to differing computational cell volumes. Normalized free volume concentrations for a number of $\langle 110 \rangle$ STGBs as a function of θ are plotted in Figure 33.

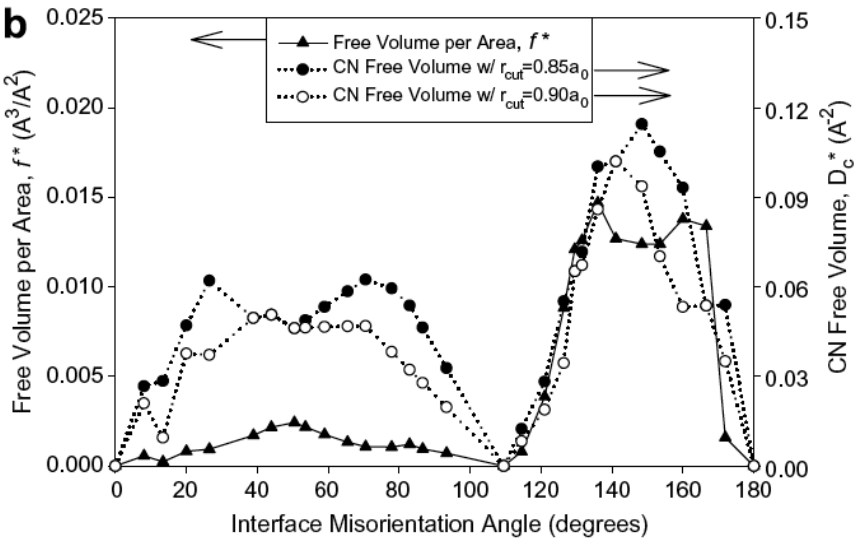

Figure 33: A plot of the normalized GB free volume concentrations as a function of misorientation angle for ⟨110⟩ STGBs [229].

3.3.1 Free Volume Two-Point Statistics

Spatial distribution statistics was obtained from both two-point correlation functions (TPCFs) and lineal path functions (LPFs). First, both these functions were calculated for the favored Σ9 (221) boundary, and the results are shown in Figure 34. Table 1 shows that this boundary is composed entirely of E structural units where its structural unit description is $|E.E|$. Figure 34 shows the (a) TPCF $P_{11}^*(r)$ and (b) LPF $L_{11}^*(r)$ as a function of the distance for the Σ9 (221) $\theta = 141.1^\circ$ STGB. For small distances, $P_{11}^*(r)$ shows the relative spacing between free volume grid points within a free volume cluster. However, at large distances the increase in $P_{11}^*(r)$ represents the spacing between free volume clusters. Notice that for the Z-direction (i.e., tilt axis direction), the spacing between clusters approaches $a_o/2$ ⟨110⟩ (2.556 Å) (i.e., every two {220} planes), as expected. In the X-direction (GB period), the spacing between clusters approaches $a_o/2$ ⟨114⟩ (7.669 Å), i.e. half of the GB period for the Σ9 (221) $\theta = 141.1^\circ$ GB. The spacing in the Y-direction (GB normal) is not shown; this is merely the spacing between the two periodic GBs in the simulation cell.

Figure 34(b) shows the $L_{11}^*(r)$ as a function of distance for the X, Y, and Z directions. Unlike the TPCF ($P_{11}^*(r)$), which refers to the free volume spacing, the LPF ($L_{11}^*(r)$) represents the connectivity of the free volume packets within the GB region. Notice that

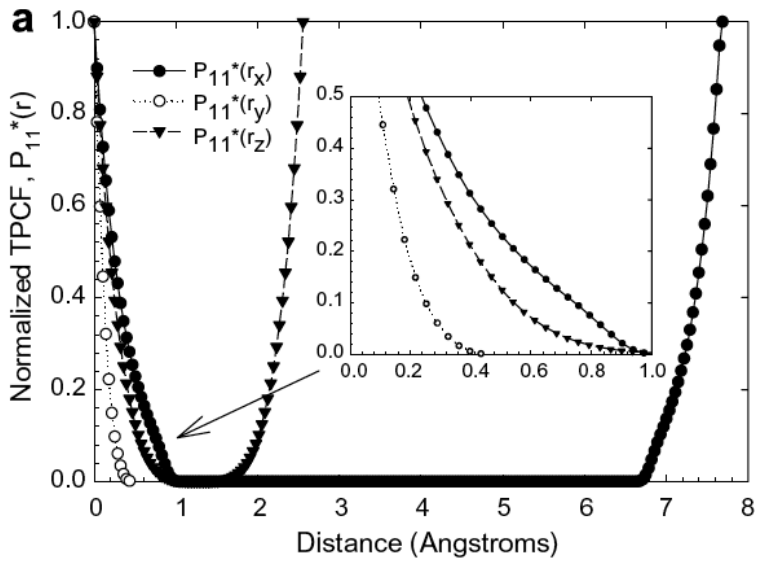

(a)

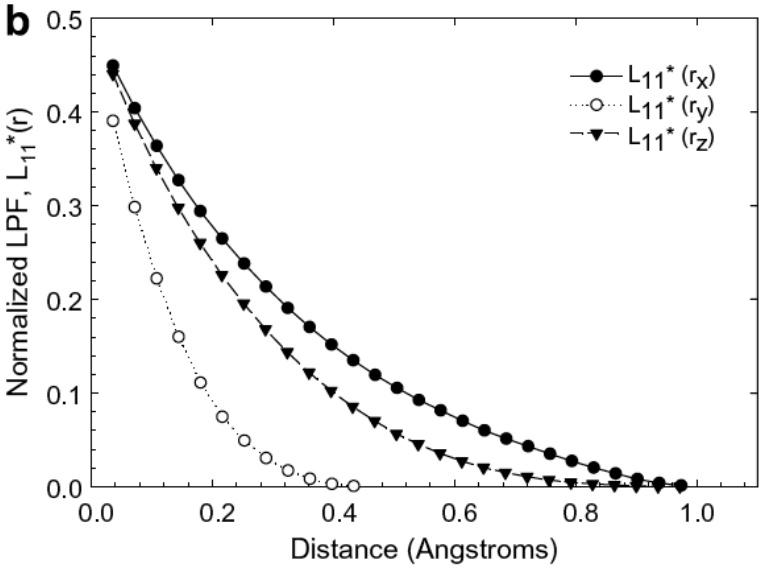

(b)

Figure 34: Normalized (a) TPCF ($P^*_{11}(r_i)$) data and (b) LPF ($L^*_{11}(r_i)$) data for free volume in the Σ9 (221) boundary along the GB period (x), GB normal (y), and tilt axis (z) directions within the GB plane as a function of distance (Å). Notice that the corresponding distances in both (a) and (b) agree with the image of Σ9 GB free volume shown in Figure 32(c) [229].

$L^*_{11}(r)$ is greater in both the X and Z directions (i.e. the GB plane directions) than the Y-direction (GB normal). Also, the maximum distance where $L^*_{11}(r) \neq 0$ is the maximum length of the free volume clusters in each direction; the free volume clusters have a maximum length of 1 Angstrom in the X and Z directions and a maximum length of 0.4 Angstroms

in the Y direction. While the LPFs show that the free volume has approximately the same length dimensions in the GB plane, the TPCFs show that the spacing between the free volume clusters is very different between the two in-plane directions; there is a much smaller spacing between clusters in the Z (tilt axis) direction.

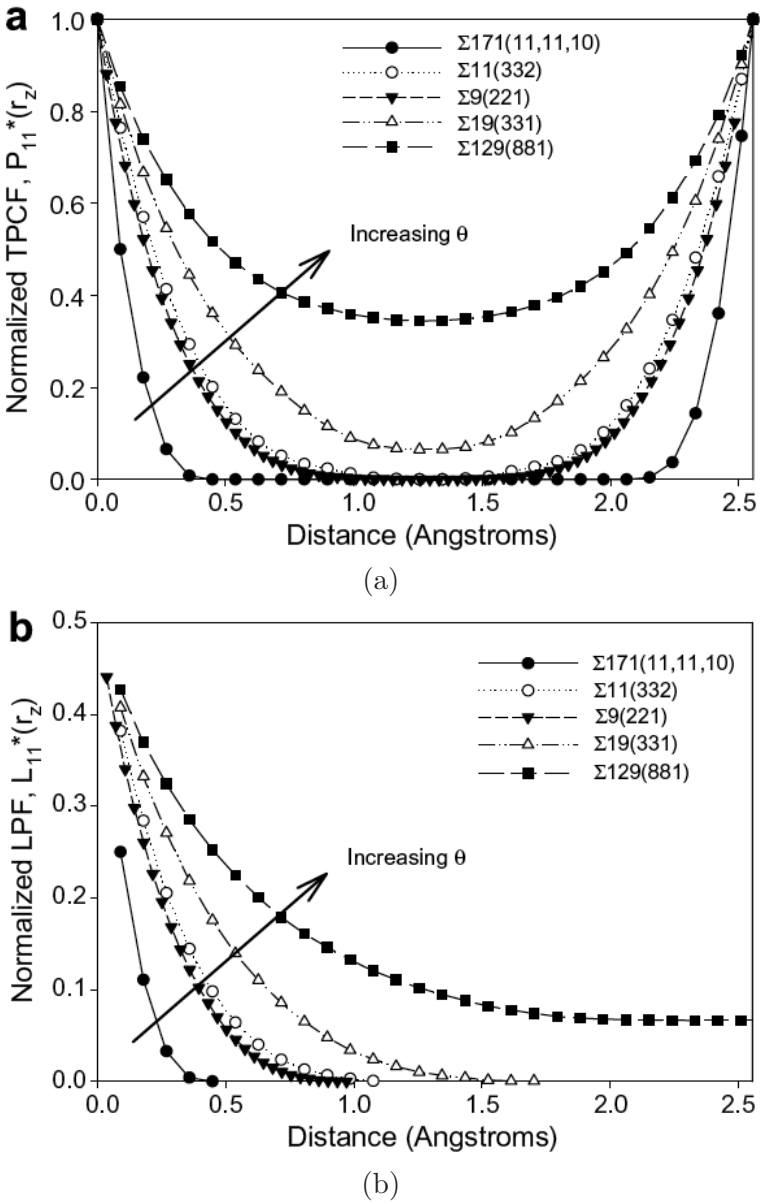

Figure 35: Normalized (a) TPCF ($P_{11}^*(r_z)$) and (b) LPF ($L_{11}^*(r_z)$) as a function of distance in the tilt axis direction for several GBs within the misorientation range $109.5° < \theta < 180°$. Notice that the spacing and connectivity of the free volume increases with increasing misorientation angle [229].

Figure 35 shows how several GB structures with $109.5° < \theta < 180°$ influence the (a)

TPCF and (b) LPF in the Z-direction (r_z). In (a), the free volume TPCF increases with increasing θ within the range of 109.5° to 180°, where the spacing of the free volume packets in the tilt axis direction (Z) is $a_o/2$ $\langle 110 \rangle$. In (b), the free volume LPF also increases with increasing θ. However, note that $L_{11}^{*}(r_z)$ for the Σ129 (881) $\theta = 169.9°$ boundary does not approach zero within the periodic length of the Z-direction as the other boundaries; this corresponds to a continuous line of free volume that spans the entire simulation cell. Therefore, free volume evolves to become long parallel needle-like structures in the Σ129 boundary. The lower limit of 0.0665 means that 6.65% of the free volume points are continuous in the Z-direction for this GB. While an infinite array of free volume points and the violation of the LPF limit, $lim_{r_z \to \infty} L_{11}^{*}(r_z) = 0$, is an artifact of using periodic boundaries. This behavior illustrates the propensity for GBs within this misorientation range to have interconnected free volume packets along the tilt axis.

The results of both the TPCFs and LPFs offer insight into the atomic structure of the E structural unit and the associated free volume packet over the misorientation range of $109.5° < \theta < 141.1°$ for $\langle 110 \rangle$ STGBs. Recall the GB structures shown in Figure 31 that lie within this range. The Σ9 (221) boundary consists of only E structural units, while the Σ11 (332) GB has equal E and D structural units. First, notice that a 1:1 D to E structural unit ratio results in very little change to the TPCF and LPF. These quantitative results are consistent with the qualitative GB structures results; the E structural units appear similar for both boundaries (i.e., no distortion or rotation). Additional TPCF and LPF results show that the E structural unit is similar with respect to free volume for θ values as low as 121.0°, which corresponds to the Σ33 (554) boundary. However, for the Σ171 vicinal coherent twin boundary, Figures 32 (a) and (b) show that the interfacial free volume packet transforms into a more compact cluster. This can also be noticed in the atomic structure of the Σ171 boundary in Figure 31. The transition of the E to E" structural unit within this misorientation range occurs when the ratio of D to E structural units exceeds some critical quantity between 3 (i.e., Σ33) and 7 (Σ11) according to our estimations. Interestingly, this critical point coincides with the Brandon criterion [23] for Σ3 STGBs (i.e., 8.7° from 109.5°).

The TPCFs and LPFs also offer insight into the atomic structure of the E structural unit for $141.1° < \theta < 180°$. An equal ratio of E and A structural units compose the $\Sigma 19$ (331) boundary, but the E structural unit undergoes a transformation as evidenced by the results in Figure 31. The E structural unit has elongated slightly compared to the E unit in the $\Sigma 9$ boundary. These data suggest that with the introduction of the A structural unit, interfacial free volume is influenced by the E structural unit elongation. As noted earlier, the TPCF and LPF results for the $\Sigma 129$ (881) boundary show that the changes to the E structural unit lead to a more connected free volume configuration within the GB region. Since free volume is not associated with either the A or D structural units, the TPCF and LPF results provide information on the E structural units only. Therefore, as the misorientation angle deviates from the $\Sigma 9$ boundary, the spacing of the E structural units along the GB period increases, as evidenced by the free volume calculations. Moreover, it is interesting that this transition to an E structural unit that is rotated to align with the GB period and contains connected free volume occurs near the window defined by the Brandon criterion [23] (i.e., 15° from the 180° perfect lattice).

3.3.2 The Influence of Free Volume on Grain Boundary Behavior

To connect free volume with GB structure, Figure 36 shows a close-up of the $\Sigma 9$ (221) boundary showing only those atoms with centrosymmetry > 0.25 around the interface. Directly below the atomic configuration of the boundary is the associated free volume distribution for the atomic structure. The individual free volume packets are shown that are due to E structural units. In the upper image, a detailed look at the structural unit configuration is displayed by the inset, looking down the tilt axis. On the lower image, two close-ups are shown, one looking normal to the GB plane and the other from the tilt axis perspective. These two insets show a detailed distribution of GB free volume for the $\Sigma 9$ boundary. The left inset is visualized along the tilt axis and each free volume packet is due to the middle volume of the E structural unit. The right inset displays the uniform distribution of the free volume packets within the GB plane, signifying the ordered atomic structure of this boundary.

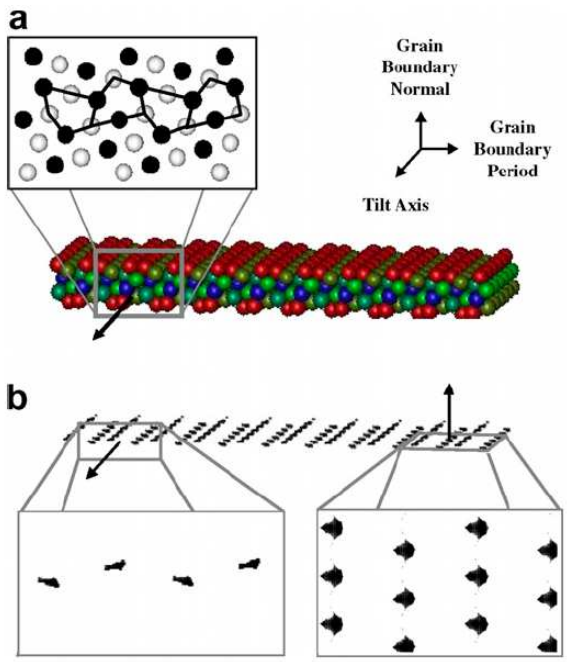

Figure 36: Three-dimensional view of (a) the distorted atoms around the interface and (b) the free volume in the interface for the Σ9 (221) GB. The magnified 2-D projected views show the structural units (a, above right), and the free volume as viewed from the tilt axis direction (b, below left) and the GB normal (b, below right) [229].

Figure 32 shows projected views for interfacial free volume of the 5 ⟨110⟩ STGBs used for the TPCF and LPF results in Figure 35, viewed along the GB normal direction. Two important features are present in these images. First, as θ increases from the Σ171 (a), to the Σ9 (c) the spatial separation of free volume packets along both the GB period and tilt axis directions decrease. Second, as θ increases from the Σ9 (c) to the Σ129 (e), free volume evolves to become connected along the tilt axis direction, and more spaced along the GB period. These qualitative results agree with the quantitative results for both TPCFs and LPFs provided in Figure 35. The tendency of free volume packets to both separate and become connected uncovers important information as to the atomic structure of the boundary.

As discussed in [203, 204, 207, 225], both the GB structure and free volume distribution are important factors in dislocation nucleation and emission from GBs under uniaxial loading perpendicular to the boundary plane. To further elucidate the role of free volume on dislocation nucleation, Figure 37 plots the normalized volume fraction f_1^* of free volume

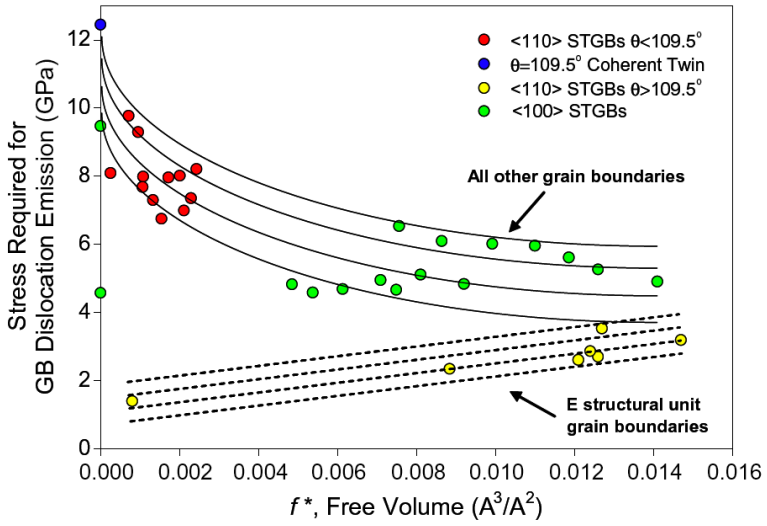

Figure 37: Free volume measure f_1^* versus the stress required for dislocation nucleation in both $\langle 100 \rangle$ and $\langle 110 \rangle$ STGBs. The trend appears entirely different between GBs with and without the E structural unit [229].

against the stress required to nucleate the first dislocation from the GB. All boundaries considered by Spearot *et al.* [207], are included in this plot, including $\langle 110 \rangle$ and $\langle 100 \rangle$ STGBs. The zero free volume boundaries account for the coherent twin boundary ($\Sigma 3$ (111) $\langle 110 \rangle$ $\theta = 109.5°$) and the single crystal systems (0° boundaries). Notice in Figure 37 that there are two distinct groups: STGBs with the E structural unit (i.e., $\langle 110 \rangle$ STGBs with $\theta > 109.5°$) and all other STGBs (both $\langle 100 \rangle$ and $\langle 110 \rangle$ STGBs with $\theta < 109.5°$). Lines are drawn in Figure 37 to highlight the general behavior of each group with regard to free volume and nucleation stress. For GBs without the E structural unit, the trend is that as free volume increases, nucleation stress decreases. However, for E structural unit boundaries, the nucleation stress is observed to increase slightly as free volume increases. This indicates a different interfacial mechanism responsible for dislocation nucleation from the structural units. A detailed discussion of these differences is provided in Tschopp *et al.*[229], but both free volume and the E structural unit appear to be influential on GB mechanics during uniaxial tension at 10K.

3.4 Tension-Compression Asymmetry

To further understand the role of both structure and free volume on GB mechanical behavior, the tension/compression asymmetry for E structural unit boundaries at 10K is investigated [230]. Then, the evolution of both structure and free are computed during dislocation nucleation for both E and non-E structural unit boundaries. utilizing bicrystalline boundaries. As previously mentioned, atomistic simulations are able to probe the differences in GB mechanical behavior and the associated mechanisms for both tension and compression. Limited work currently exists concerning the effect of uniaxial loading in materials with small volumes; however, recent work by Tschopp and McDowell [224] showed an asymmetry in the nucleation stress for homogeneous dislocation nucleation in single crystals. The significance of this research is that they showed the normal resolved stress on slip planes is crucial for understanding nucleation processes in crystalline materials. For example, it is often more difficult to nucleation a partial dislocation on a maximum Schmid factor slip plane under compression as compared to tension, due to the compressive stress normal to the slip plane. But it is still not well understood how interfaces affect the nucleation stress asymmetry of mechanisms required for dislocation nucleation. Therefore, in this chapter [230], 9 $\langle 110 \rangle$ STGBs containing the E structural unit (outlined in Table 1) are deformed under both uniaxial tension and compression, as shown in Figure 6. In addition, a quasistatic approach under tension is employed to explore the effect of strain rate on nucleation stress and deformation accommodation mechanisms observed.

The uniaxial stress-strain curves for the nine $\langle 110 \rangle$ STGBs with the E structural unit is shown in Figure 38, along with the quasistatic results for 5 boundaries. Each curve is slightly offset by 0.01 strain and the individual points show the quasistatic results. The implemented quasistatic (QS) approach alternated increments of strain and equilibration at the simulation temperature. Each strain increment was a small fraction of the lattice parameter and the following equilibration step was for 2 ps. During the equilibration step, the simulation boundary being strained was held fixed and the lateral dimensions were allowed to relax to zero stress under NPT. In Figure 38, the solid lines are the constant strain rate MD simulation results. Interestingly, the results of both the constant strain rate

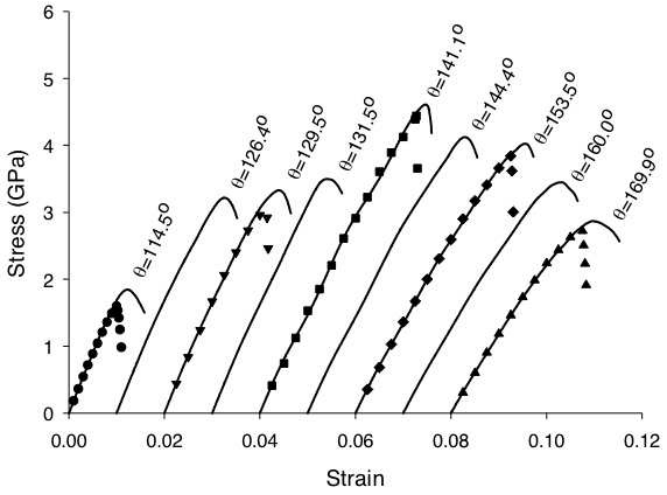

Figure 38: Stress-strain curves for the STGBs with the E structural unit under uniaxial tension. The solid line denotes the data obtained with a 10^9 strain rate and the symbols denote the data obtained with the incremental quasistatic (QS) approach [230].

and quasistatic simulations are very similar with regard to elastic response, peak stress, and the corresponding strain at peak stress. However, dislocation nucleation occurs at slightly lower stresses under quasistatic conditions, and each simulation continues until just after the first occurrence of dislocation nucleation (just after peak stress). The uniaxial compression results show similar results regarding the similarity of QS and constant strain rate simulations. An important result of this research is that the results of both the dynamic and constant strain rate deformation simulations were identical, and dislocation nucleation from the GBs was also observed in both types of simulations.

3.4.1 Dislocation Nucleation Stress

Figure 39 shows the stress required for heterogeneous dislocation nucleation in each boundary under uniaxial tension as a function of misorientation angle. Clearly, the maximum nucleation stress for this class of STGBs corresponds to the $\Sigma 9$ (221) $\theta = 141.1°$ boundary, composed entirely of E structural units. The lowest nucleation stresses are for both boundaries nearest to the $\Sigma 3$ (111) $\theta = 109.5°$ coherent twin boundary and the $\Sigma 1$ (110) $\theta = 180°$ perfect lattice. Interestingly, both the $\Sigma 3$ coherent twin boundary and $\Sigma 1$ single crystal

require greater stresses under uniaxial tension (12.4 GPa and 4.6 GPa, respectively) than these E structural unit boundaries. Clearly, this trend indicates that the presence of the E structural unit, or $a_o/3\langle 111\rangle$ disconnection, and its associated higher free volume results in a decrease in the nucleation stress. The spacing of the E structural unit might also play a definitive role in dislocation nucleation. The smallest spacing between E structural units are smallest in the $\Sigma 9$ boundary and increases as θ moves away from 141.1°.

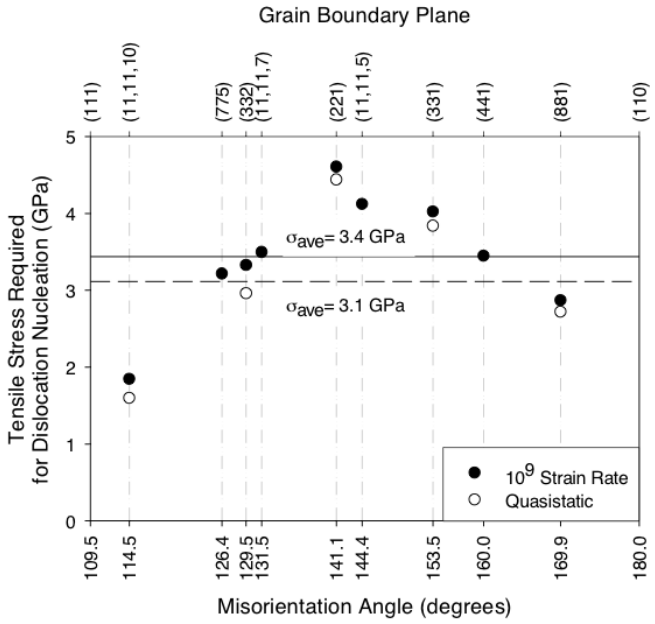

Figure 39: Stress required for dislocation nucleation for the nine STGBs with the E structural unit in uniaxial tension. The black and dotted horizontal lines represent the average nucleation stress for all STGBs using the 10^9 strain rate and the QS approach, respectively [230].

The uniaxial compression nucleation stresses as a function of misorientation angle are shown in Figure 40. The same correlation between misorientation angle (and E structural unit spacing) and nucleation stress is not observed under compression, and in general, the compressive nucleation stresses are greater in compression than in tension. One reason for this disparity, could be that under compression, the resolved stress normal to the activated slip plane is compressive under compression, and tensile under tension. In single crystal simulations, both Spearot *et al.* [207] and Tschopp *et al.* [228] found that resolved normal stresses strongly influence the stress required for homogeneous dislocation nucleation. In these bicrystalline structures, it appears that compressive resolved normal stresses on the

activated slip plane hinder the nucleation process, as was found in homogeneous dislocation nucleation by Tschopp and McDowell [224].

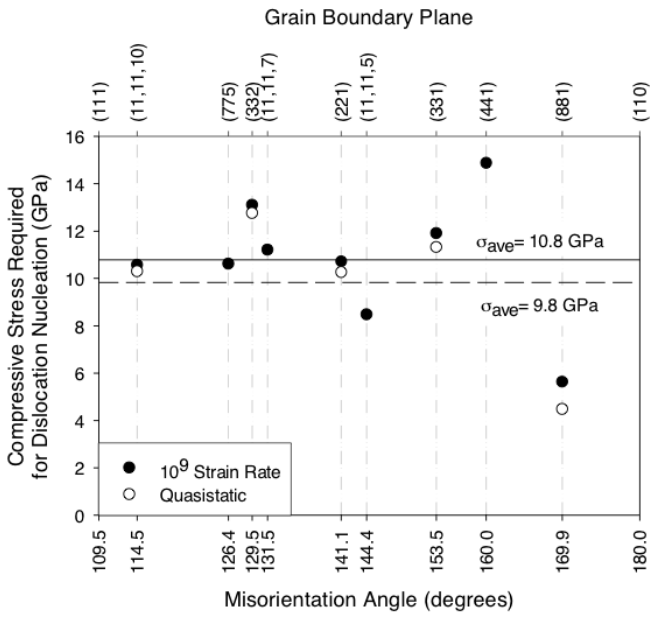

Figure 40: Stress required for dislocation nucleation for the nine STGBs with the E structural unit in uniaxial compression [230].

3.4.2 Dislocation Nucleation Tension-Compression Asymmetry

To compare the nucleation behavior under both uniaxial tension and compression, five ⟨110⟩ STGBs are displayed in Figure 41. The left column represents snapshots of each bicrystalline boundary after maximum tensile stress, the right column displays the structures under uniaxial compression, and the middle column provides the associated {111} and {100} slip planes in both the upper and lower lattices. These slip planes have normal components orthogonal to the tilt axis. Solid lines in the middle images indicate the maximum Schmid factor {111} planes and dotted lines outline both {111} planes with a lower resolved shear stress and the {100} planes. Each image is orthonormal and viewed along the ⟨110⟩ tilt axis, where only non-centrosymmetric atoms are shown with a cutoff value of 0.25. This particular visualization process enables easy viewing of the GB, nucleation dislocation structures, and stacking faults in each lattice. Each boundary's CSL designation is provided just above each snapshot, and the activated slip plane ({111} or {100}) are given either to the lower

left or right of each configuration.

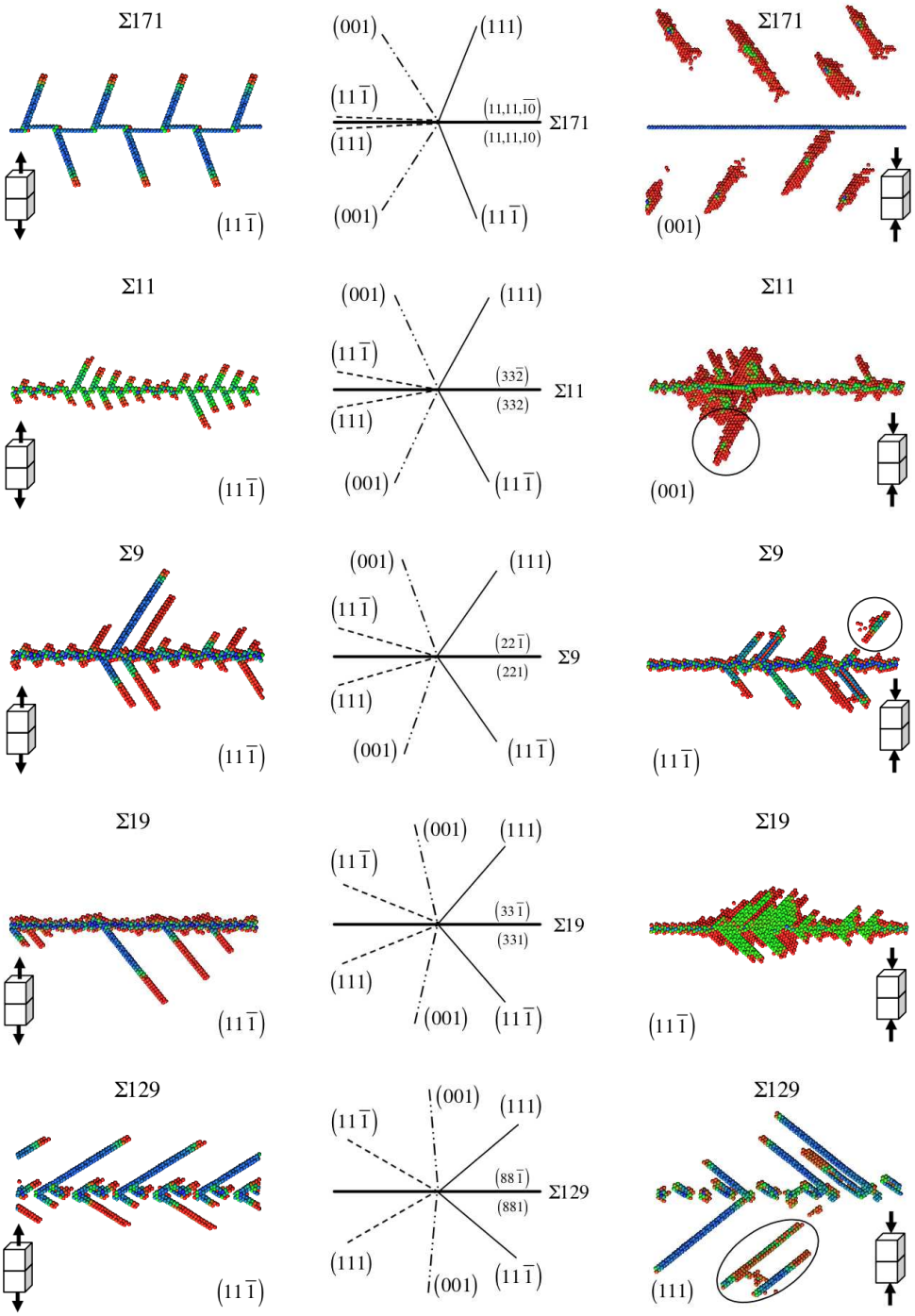

Figure 41: Dislocation nucleation at five STGBs with the E structural unit under uniaxial tension and compression applied perpendicular to the boundary. The first and third column are images of tension and compression, respectively. The second column depicts the orientation of (111) and (001) planes in each crystal to aid in comparison of the dislocation mechanism [230].

Under uniaxial tension, a partial dislocation is nucleated from each boundary leaves behind a stacking fault connecting it to the boundary. Because the simulations are stopped just after the maximum stress, no trailing partial dislocation is observed to be emitted. Each leading partial dislocation is emitted on the {111} slip plane with the greatest resolved shear stress in the slip direction. The spacing of GB dislocations is seen to influence the nucleation behavior of partial dislocations. In the Σ171 boundary, the GB dislocations (structural units) are separated by a large distance, while in the Σ11 boundary the GB dislocations are quite close. Therefore, once nucleation occurs, the leading partial dislocations in the Σ171 boundary are unaffected by other slip events, but for the Σ11 boundary, neighboring dislocations influence each other. GB dislocation sources are hindered in the Σ11 boundary due to nucleation partial dislocations on nearby slip systems.

Under uniaxial compression, both partial and full dislocations are observed. Simultaneous emission of full dislocations in the Σ171 are clear in Figure 41, and less obvious in both the Σ9 and Σ129 GBs. The only boundary that does not emit a full dislocation during the simulation time is the Σ19. Also, as noted in the lower left corner, the nucleated dislocations do not necessary slip on maximum resolved shear stress {111} planes in either lattice. In both the Σ171 and Σ11 boundaries, the full dislocations are emitted on the {100} slip plane, rather than the {111} plane. However, in the other three boundaries under uniaxial compression, the maximum Schmid factor {111} plane is the activated slip plane. Therefore, the resolved normal stress on both the {111} and {100} planes is crucial for understanding dislocation nucleation from bicrystalline boundaries in nanograins.

After all, the nucleation stress under compression are approximately three times greater than those for uniaxial tension. To better understand this distinction, Figure 42 shows the (a) Schmid and (b) Normal factors for the {111} and {100} plane under both tension and compression for the boundaries considered in this chapter. At lower misorientation angles, both the Schmid and Normal factor are greater for the {100} system than the {111} for uniaxial compression, possibly explaining the nucleation asymmetry in these boundaries. However, it is more probable that the resolved normal stress component is more influential on dislocation slip and the possibility for nucleation of the trailing partial dislocation. It

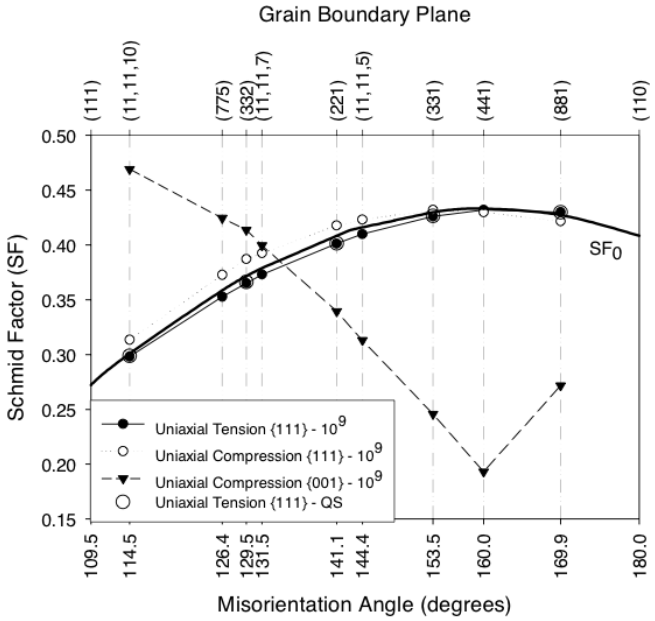

(a)

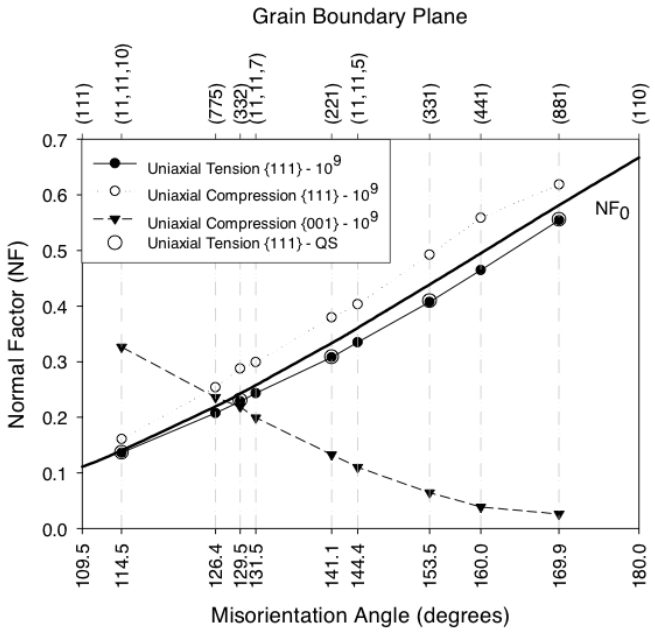

(b)

Figure 42: (a) The change in (a) Schmid factor, SF, and (b) normal factor, NF, at dislocation nucleation with GB misorientation angle. The legend shows that different symbols are used to distinguish between (a) tension and compression, (b) dynamic strain rate (10^9 s^{-1}) and QS, and (c) the {111} slip plane and the {001} slip plane. The change in SF and NF prior to deformation are labeled as SF_0 and NF_0 [230].

is compressive in compression and tensile in tension. An extensive review of two different nucleation behaviors are provided in Tschopp *et al.* [230], along with additional analysis

concerning the tension-compression asymmetry for this group of E structural unit ⟨110⟩ STGBs.

3.5 The Evolution of Grain Boundary Structure and Free Volume during Dislocation Nucleation

Dislocation nucleation from GBs is an important deformation mechanism in NC materials. Previous work by Van Swygenhoven *et al.* [269, 259, 264, 271, 262, 263, 274], Schiotz *et al.* [186, 188, 187, 189], Spearot *et al.* [203, 204, 207], and Tschopp *et al.* [225, 226, 230] have explored GBs and dislocation nucleation in nanograins. The atomic structure, energy, and free volume have all been found to be influential in determining GB behavior and dislocation nucleation. Free volume migration has also been noted in NC metals as an accompanying process to dislocation nucleation and interfacial reordering. Atomic shuffling and GB sliding are also important mechanisms in NC metals, and free volume has been noted to influence these mechanisms as well. It is clear that free volume plays a crucial role in GB properties, and that the mechanical deformation in nanostructured materials is therefore influenced. However, questions still remain regarding the role of free volume on GB deformation. Do particular free volume distributions enhance stress-induced atomic shuffling or dislocation nucleation? How does the evolution of free volume correlate with certain deformation mechanisms? Can the distribution of GB free volume be understood in the context of activating dislocation nucleation and other strain accommodating mechanisms? Understanding the connection between free volume and GB deformation could provide valuable insight into the origins of inelastic mechanisms present in NC materials, and provide important thermodynamical information about deformed (or non-equilibrium) interfaces. Accordingly, the objective of the current research is to compute the evolution of GB free volume during uniaxial tension (as shown in Figure 6) for different GB structures. Specific correlations between free volume and atomic processes during nanoscale deformation are explored, and the overall impact of free volume on GB deformation is investigated.

To investigate interfacial free volume and structural evolution, a select group of copper STGBs were constructed and deformed at 10K. The boundaries are listed in Table

2 according to their proper coincidence site lattice (CSL) notation, misorientation angle, structural unit composition, GB excess energy [184, 229], initial free volume, computational cell dimensions, and total number of atoms within the cell. They include both ⟨100⟩ and ⟨110⟩ STGBs, both favored and non-favored [212, 180], and boundaries containing various amounts of free volume. GBs boundaries composed entirely of a single type of structural unit are called favored boundaries, while those composed of two different structural units are non-favored [212, 180]. These boundaries were chosen for several reasons: (1) previous work has shown that differences in structure and free volume lead to significant differences in mechanical behavior [229, 230], (2) each boundary deforms via heterogeneous dislocation nucleation under uniaxial tension, and (3) free volume plays a critical role in GB properties and the associated atomic-scale processes - so understanding its evolution during deformation can contribute vital information regarding structure-property relationships.

Table 2: Summary of initial GB information including CSL notation, GB normal, misorientation angle, tilt axis, structural unit (SU) period, energy, initial free volume (FV), simulation cell dimensions (X |Y |Z), and the number of atoms.

GB	Misorientation Angle	Tilt Axis	SU Period	Energy (mJ/m^2)	Initial FV	Dim. X|Y|Z (nm)	Atoms
Σ9 (114)	38.9°	⟨110⟩	|CB |	665.22	1.83E-05	16.3|33.8|16.3	760,320
Σ11 (332)	129.5°	⟨110⟩	|ED.ED |	702.53	7.00E-05	16.8|33.9|16.4	786,688
Σ9 (221)	141.1°	⟨110⟩	|E.E |	833.15	7.60E-05	16.9|32.5|16.4	757,504
Σ19 (331)	153.5°	⟨110⟩	|EA.EA |	807.35	1.01E-04	17.8|34.7|16.4	856,064
Σ129 (881)	169.9°	⟨110⟩	|EA'A'A'.EA'A'A' |	587.07	6.27E-05	17.4|32.9|16.4	791,808
Σ13 (510)	22.6°	⟨001⟩	|CDD |	876.76	4.91E-05	16.6|33.2|16.3	758,160
Σ5 (310)	36.9°	⟨001⟩	|C |	904.09	7.43E-05	16.0|32.1|16.3	705,600
Σ5 (210)	53.1°	⟨001⟩	|B'.B' |	950.58	9.14E-05	16.2|32.4|16.3	720,000

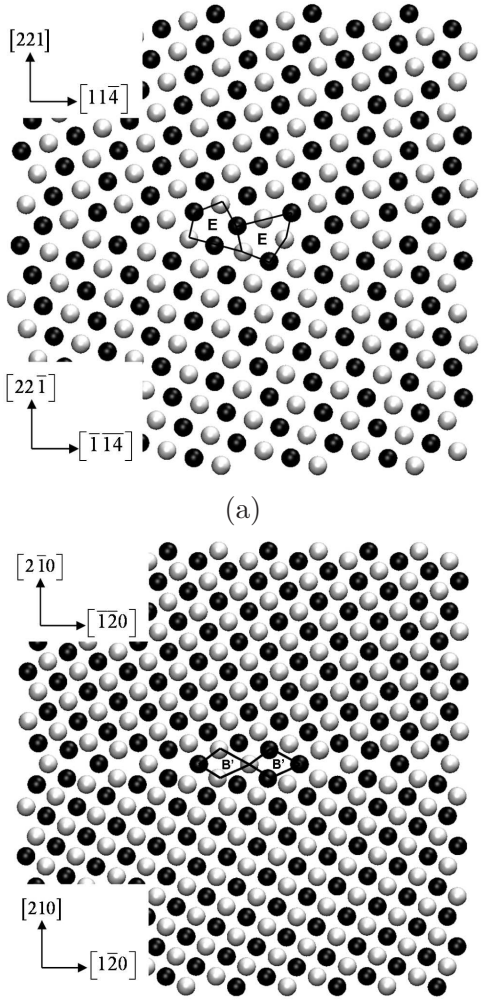

Figure 43: The (a) Σ9 (221) and (b) Σ5 (210) GB structures. In each case, one complete period of structural units is outlined along with the lattice orientation vectors. Black and white atoms corresponds to atoms on adjacent (220) atomic planes along the tilt axis.

The initial equilibrium GB structure and associated free volume distribution of each E structural unit boundary investigated in this research has been previously outlined and studied in [229]. Two sample STGBs investigated in the current research are shown in Figure 43, viewed along their tilt axis, along with their GB free volume distributions (shown in Figure 44), viewed along the boundary normal direction. According to their CSL notation and GB normal direction, they are termed Σ9 (221) and Σ5 (210).

In Figs. 43(a) and 43(b), the structural unit composition along one GB period is outlined, and the orientation vectors for both the GB period and normal directions are given

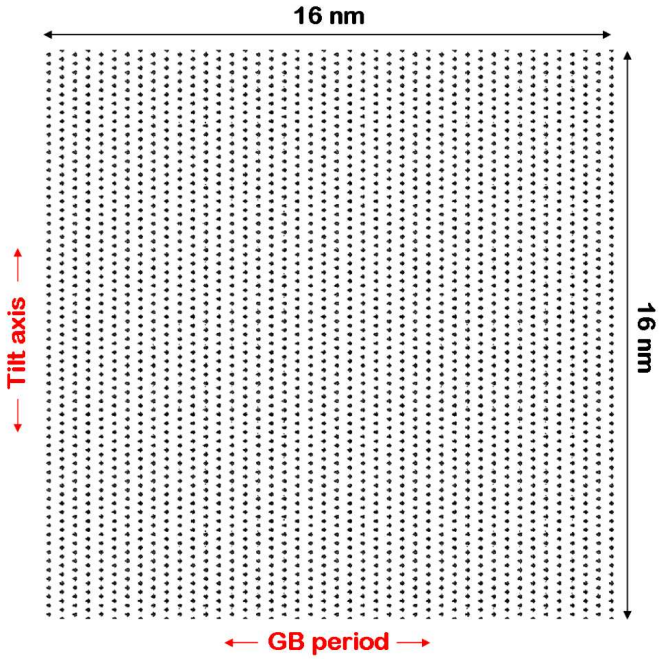

(a)

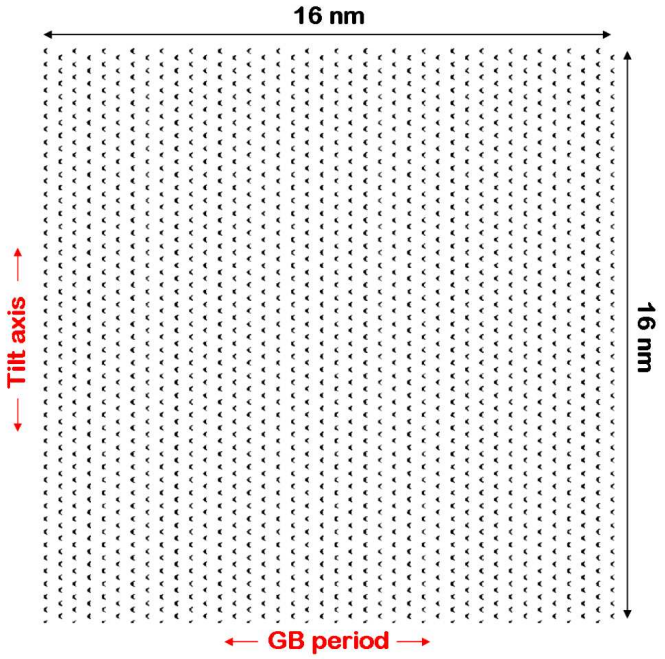

(b)

Figure 44: Free volume distributions associated with the (a) Σ9 (221) and (b) Σ5 (210) GB structures, viewing along the GB normal direction.

for each lattice. The black and white atoms define two adjacent atomic planes along the tilt axis direction, and it should be pointed out that each structural unit outlined in both 43(a)

and 43(b) are comprised of atoms lying on neighboring atomic planes. For these boundaries, the free volume arrangement (shown in Figure 44(a) and (b)) is ordered along both the tilt and GB period directions. This relates well to the ordered atomic structure of each GB. This relationship is important because as each boundary is deformed, the atomic structure and corresponding free volume arrangement will evolve accordingly.

The uniaxial tension stress-strain curves at 10K are shown in Figure 45. In 45(a), the tensile behavior of four E structural unit boundaries is shown, and 45(b) displays the response of four boundaries that do not contain the E structural unit. The presence of the E structural unit alters the observed tensile deformation behavior of the boundary (in agreement with Spearot *et al.* [207]). The maximum stress is lower for E structural unit boundaries than those boundaries shown in 45(b). In addition, the corresponding strain at which maximum tensile stress is reached is lower. For each boundary considered, the maximum $\{111\}\langle 112\rangle$ Schmid factor and $\{111\}\langle 112\rangle$ resolved shear stress at dislocation nucleation are calculated. Although the calculated $\{111\}\langle 112\rangle$ Schmid factors are similar for each boundary, the resolved shear stress at partial dislocation nucleation are lower for E structural unit boundaries. This implies that the $\{111\}\langle 112\rangle$ resolved shear stress at dislocation nucleation is influenced by GB structure. However, there is no direct correlation between the total initial free volume and $\{111\}\langle 112\rangle$ resolved shear stress at partial dislocation nucleation.

Recent work by both Tschopp *et al.* [227] and Spearot *et al.* [207] have investigated the influence of lattice orientation, GB structure, and non-Schmid stresses on shear strength. In single crystal calculations [230], shear strength varies with loading orientation and is similar to the theoretical shear strength of copper calculated by Ogata *et al.* [158]. However, the theoretical shear strength calculated by Ogata and coworkers is also dependent on normal stress to the slip plane. In this respect, our shear stress will not be constant but rather will change slightly with different orientations and GB structures. While the strength of non-E structural unit boundaries investigated in this research are similar to the theoretical value, the strength of E structural unit boundaries is less. This points out the importance of both the resolved stress state and GB structure on dislocation nucleation from interfaces.

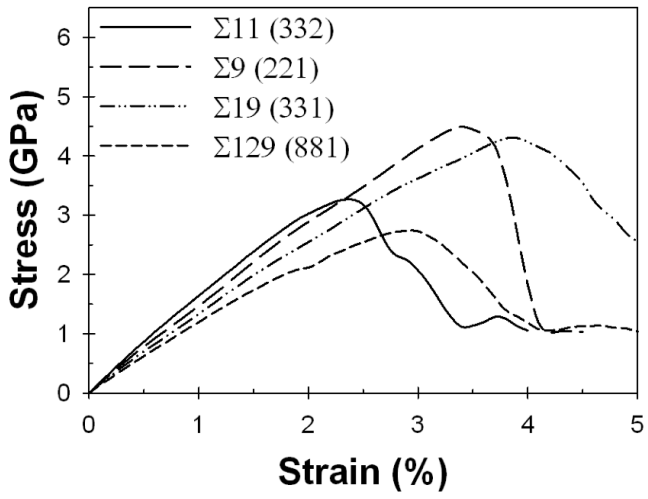

(a)

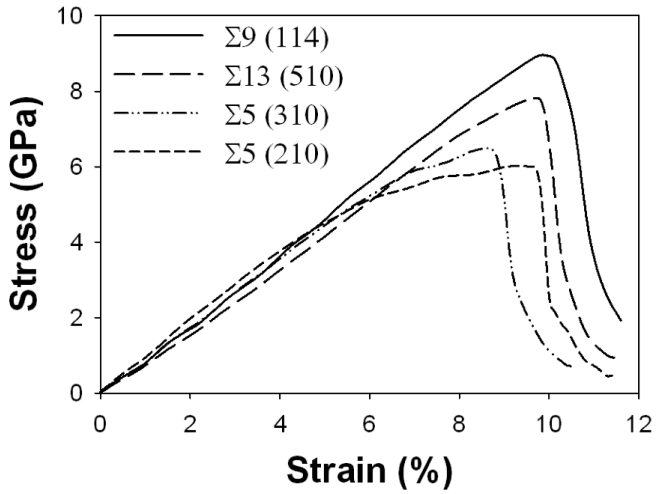

(b)

Figure 45: The stress-strain behavior of copper STGBs both (a) with and (b) without the E structural unit at 10K.

Figure 46 shows the evolution of GB free volume as a function of strain during uniaxial tension. Strain values reported in Figure 46 are normalized by the strain at dislocation nucleation, and the free volume concentration is normalized by the initial free volume concentration (at 0% tensile strain). One common attribute to all GBs investigated is the drop in GB free volume just after dislocation nucleation. Despite the initial free volume distribution, interfacial reordering occurs due to dislocation nucleation in each boundary.

Moreover, Figure 46 shows that free volume evolves differently for different boundaries,

and a simple relationship correlating only initial total free volume (f_1) and its evolution during uniaxial tension is not sufficient. Some boundaries (e.g., Σ9(221), Σ9(114), and Σ5(210)) experience a net increase in free volume prior to dislocation nucleation, in other boundaries free volume decreases (e.g., Σ11(332) and Σ129(881)), and still in others an abrupt change in free volume concentration occurs at some point during elastic deformation of the simulation cell (e.g., Σ13(510) and Σ5(310)). Structural transitions observed in the elastic regime in the Σ13(510) and Σ5(310) boundaries under uniaxial tension have also been observed by Spearot *et al.* [206]. The structural units composing these boundaries undergo distortions in the elastic regime leading to both an increase and decrease in free volume, respectively.

Structural units undergoing a slight expansion, compaction, and/or distortion prior to dislocation nucleation is a common mechanism by which the GBs experience an increase or decrease in free volume during deformation. Decreasing total free volume seen in the Σ11(332) and Σ129(881) boundaries is due to the dissociation of a partial dislocation from the E structural unit during elastic loading and a net compaction of the E structural unit. For the Σ9(221), Σ9(114), and Σ5(210) boundaries, an increase in total free volume prior to dislocation nucleation is observed due to structural unit expansion. These results show that GB structure, free volume, and stress state are all important factors when determining interfacial deformation behavior and the accompanying atomic rearrangements.

3.5.1 Σ9 (221) Boundary

To further investigate free volume evolution, the response of the Σ9 (221) GB will be detailed. In this Σ9 boundary, partial dislocation nucleation occurs from the boundary into each lattice on the maximum Schmid factor {111} plane near peak tensile stress; a common trait to all boundaries investigated herein. The E structural units composing the GB undergo a net expansion prior to dislocation nucleation, producing a slight increase in the GB free volume calculation (seen in Figure 46(a)). The imposed stress state causes structural unit expansion, and the deformation of the GB continues until the stress required for

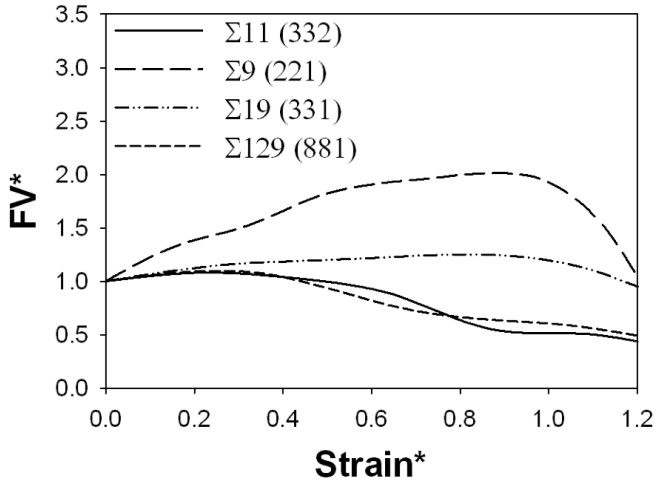

(a)

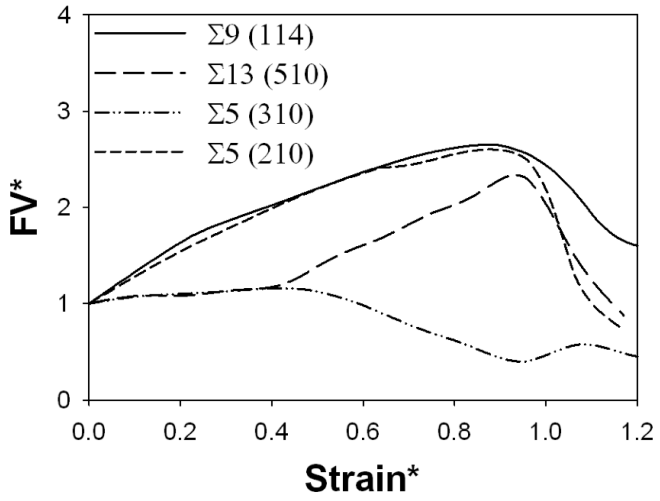

(b)

Figure 46: Total normalized free volume (FV*) evolution during uniaxial tension at 10K for boundaries (a) with and (b) without the E structural unit. The 'Strain*' is strain normalized by the dislocation nucleation strain, and 'FV*' is normalized by the initial free volume concentration.

dislocation nucleation is reached. As shown in Figure 47, substantial changes in the (a) distribution of GB free volume and (b) free volume evolution behavior accompanies dislocation nucleation. Following dislocation nucleation, interfacial atoms in specific regions undergo coordinated migration in the GB period direction toward areas in the GB where dislocations nucleate (nucleation regions), while free volume migrates in the opposite direction toward regions where dislocation nucleation has not occurred (non-nucleation regions). This process

is the interfacial activation event for partial dislocation nucleation, and produces a change in both structure and free volume. Free volume migration accompanying atomic reordering has been discussed as an activation mechanism for plasticity phenomena in nanostructured materials [117, 264], where GB atomic processes are critical for understanding material strength [136].

Immediately following partial dislocation nucleation, a significant drop in the free volume concentration is observed in nucleation regions. This is attributed to atomic rearrangements (or structural changes) occurring within the GB, which agrees with previous results [55, 117] in NC metals. Figure 47(a) shows the free volume distribution in the boundary after partial dislocation nucleation (corresponding to strain just after peak tensile stress). There are obvious regions of low free volume concentration that correspond to nucleation regions, and non-nucleation regions which experience a net increase in free volume. Nucleation regions comprised of several E structural units, undergo simultaneous atomic reordering during dislocation nucleation leading to the observed spacing (of nucleation regions) along the GB period direction. This behavior is influenced by both the spacing of preferred nucleation sites (E structural units), and the interaction of neighboring nucleated partial dislocations on the maximum Schmid factor {111} planes. Figure 47(b) shows a quantitative measurement of the GB free volume evolution in these specific regions parallel to the tilt axis before and after dislocation nucleation. The free volume evolution data is plotted as a function of a normalized measure of strain, Strain*. The strain values (calculated as engineering strain) are normalized by the strain when dislocation nucleation occurs, just prior to maximum tensile stress. The data indicates that the GB accommodates dislocation nucleation during uniaxial tension by reducing interfacial free volume at nucleation sites.

A more detailed analysis of this behavior can be obtained when the GB structure and free volume are simultaneously viewed after nucleation, as shown in Figure 48. Figure 48 shows the GB atomic structure and associated free volume distribution at (a) 0% strain and (b) after partial dislocation nucleation, viewed along the tilt axis. Atoms are colored according to the centrosymmetry parameter [105]. For clarity in visualizing defect structures, those atoms with near perfect centrosymmetry on either side of the GB are not shown,

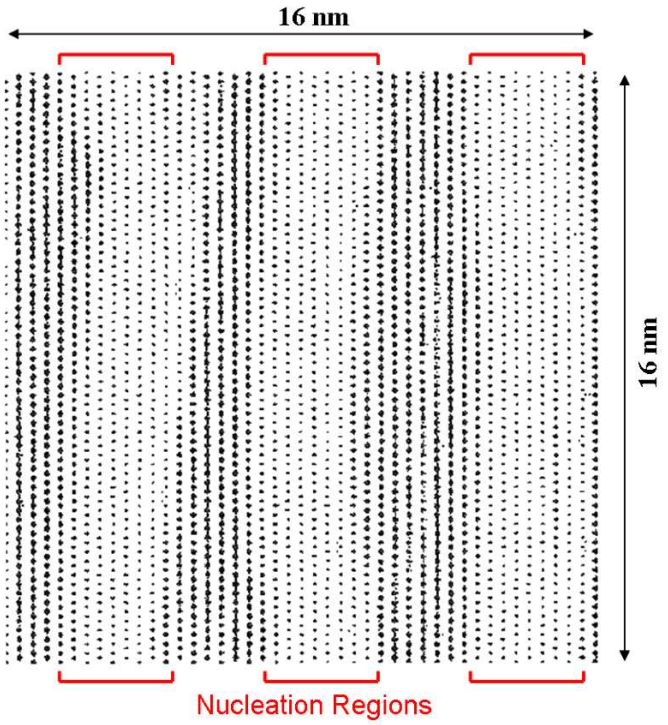

(a)

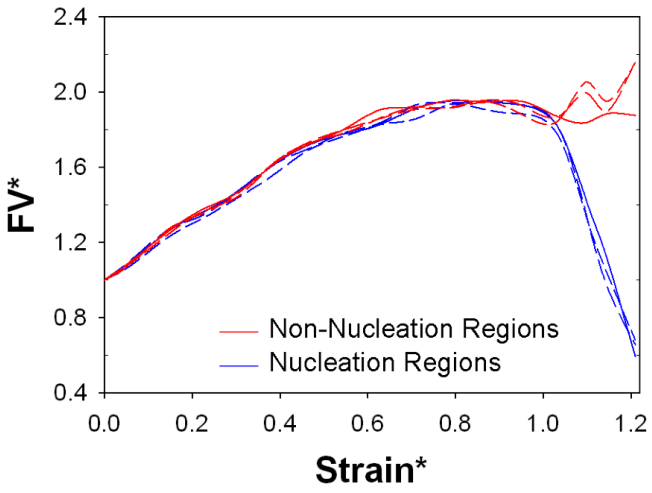

(b)

Figure 47: (a) Free volume distribution in the Σ9 (221) GB plane just after dislocation nucleation, viewed along the GB normal direction. Regions of high and low free volume clearly show where dislocation nucleation has occurred. (b) Free volume evolution in different regions within the boundary plane parallel to the tilt axis.

and interfacial free volume packets are colored black for comparison. Figure 48 shows that

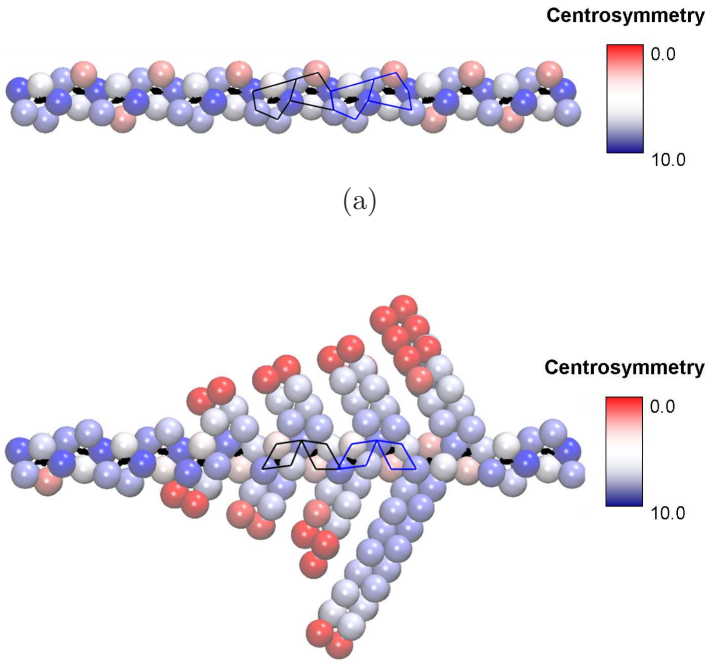

Figure 48: (a) GB and free volume structures just after energy minimization, and (b) after partial dislocation nucleation from the boundary, colored according to centrosymmetry.

the initially ordered structure (shown in 48(a)) evolves as consequence of partial dislocation nucleation under uniaxial tension, as in 48(b). In 48(b), a group of nucleated partial dislocations are shown, originating from the collapsed E structural units, connected to the boundary by a stacking fault. Note (in 48(b)) the smaller free volume packets located within the collapsed E structural units in the boundary structure as a result of dislocation nucleation.

Figure 48 expands on an earlier point that regions in the boundary undergoing dislocation nucleation experience a drop in free volume accompanying structural change as shown in 47(b), and an increase in free volume in non-nucleation regions. Figure 48(b) clearly shows that the E structural unit collapses (transforming into a C-type structural unit) during GB deformation and the associated free volume changes accordingly, as noted by Spearot [208]. The free volume packets decrease in size accompanying structural unit transformation during nucleation, which as stated earlier is a necessary condition for slip originating from this boundary. This structural unit transformation likely accommodates

the change of Burgers vector in the boundary associated with the Shockley partial dislocation that comprises structural units after dislocation nucleation.

The collective migration of atoms in the boundary region is further analyzed using a relative atomic displacement calculation for GB atoms. This calculation is based on the displacement of each atom from its initial position to the current position relative to the change in simulation domain size, similar to that performed by Schiotz *et al.* [188]. Once the relative displacement of each atom is calculated, it is possible to observe the coordinated atomic migration within the boundary region. Figure 49 shows (a) both the boundary structure and free volume distribution (displaced vertically downward for comparison) immediately following dislocation nucleation, and (b) the corresponding atomic migration within the boundary.

The most pronounced coordinated atomic migration within the boundary is directed toward nucleation regions from non-nucleation regions and is constrained primarily to atoms currently within nucleation regions. Figure 49(b) displays a transparent view of the GB structure seen in (a) where atoms participating in the coordinated migration are highlighted. Only atoms that shift in the GB period direction on the order of an atomic spacing or greater are highlighted in 49(b). Atoms participating in this rearrangement are located near activated slip planes within the nucleation regions, leading to a net increase in free volume in adjacent non-nucleation regions. This agrees with the general findings of Derlet *et al.* [55]. Figure 49(b) also shows that the coordinated shifts occur simultaneously for atoms lying along rows in the tilt axis direction within the boundary plane, indicating synchronized motion accompanies dislocation nucleation in this GB structure. Simultaneous atomic migration toward nucleation regions seen in the $\Sigma 9$ boundary is also common to all E structural unit boundaries studied in this work, and accompanies free volume migrating toward non-nucleation regions (similar to general GB behavior seen in NC copper by Derlet *et al.* [55]).

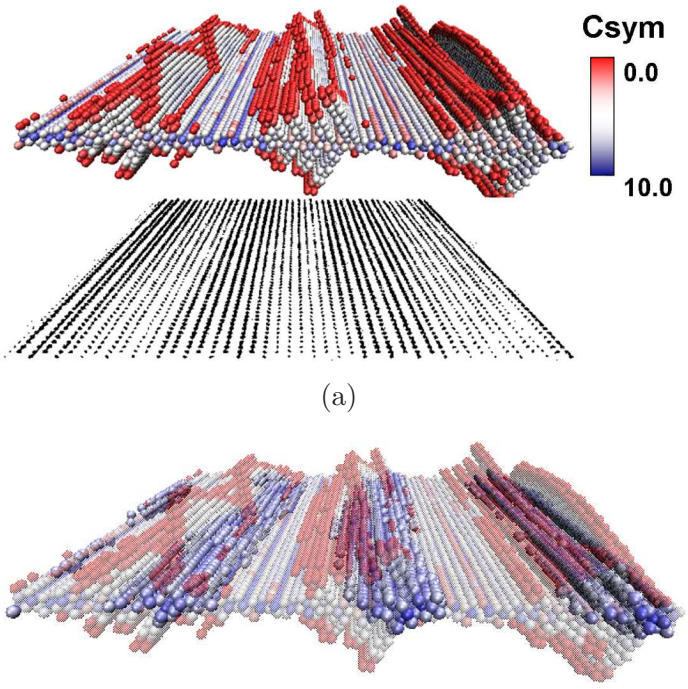

(a)

(b)

Figure 49: (a) GB structure and free volume distribution, and (b) atomic migration in the boundary plane during partial dislocation nucleation.

3.5.2 Σ13 (510) Boundary

The Σ13 (510) boundary is now detailed showing the evolution of non-E structural unit boundaries. Just prior to and during the initial stages of partial dislocation nucleation from the Σ13 (510) boundary, atomic shifts occur along the intersection of the activated slip plane and the GB. Figure 50(a) shows the nucleated partial dislocation connected to the GB (gray atoms) by a stacking fault and a displaced view (below) of the corresponding free volume. It is clear that the arrangement of free volume evolves as a partial dislocation is nucleated from the GB (located by the arrows). The free volume packets located within this nucleation region of the GB decrease substantially in size as atoms rearrange as a consequence of the local stress state reaching the conditions required for nucleation. In other GB regions, atomic structural transformations are causing the total GB free volume to increase. Structural units are slightly distorted and dissociate, causing the initial free volume packet to multiply. This leads to the overall increase in free volume calculated in

Figure 46(b) as a function of tensile strain.

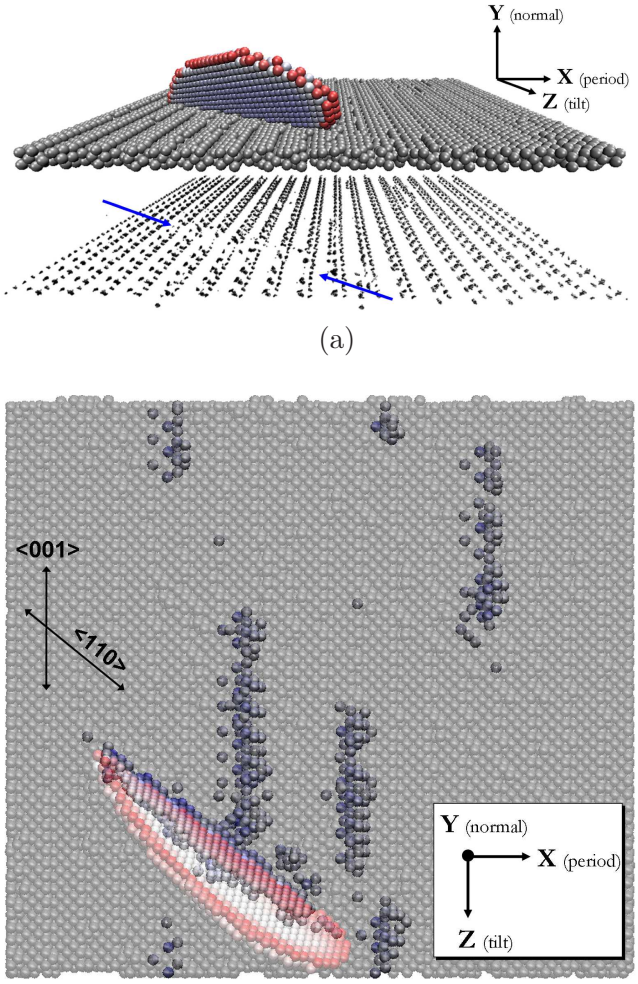

Figure 50: (a) Partial dislocation nucleation and free volume in the Σ13 (510) boundary at a strain just after peak stress, along with (b) a view normal to the GB plane at the same strain showing nucleation and atomic migration. In (b), the boundary structure in (a) is shown where atoms with larger displacements (relative to the initial structure) are highlighted showing regions where reordering is occurring.

Figure 50(b) is a transparent view of the structure shown in (a) but viewed along the GB normal (Y-direction). GB atoms are colored gray, while the nucleated partial and stacking fault are colored according to centrosymmetry. Once again, atoms undergoing larger displacements from their initial positions are also highlighted in this image, identical to the method used in Figure 49(b). Atomic rearrangements are activated along the tilt axis in numerous locations within the GB (including those at the intersection of the slip

plane and GB) induced by the local stress state. However, the only coordinated shifts in the slip direction occur where the activated slip plane intersects the GB (in regions where free volume has evolved substantially). This means that atomic groups undergoing coordinated large-scale rearrangements (accompanied by free volume migration) are a precursor to GB deformation mechanisms, such as dislocation nucleation.

From the uniaxial tension simulation data, it is clear that interfacial free volume affects atomic rearrangement; however, it is also clear in these GBs that the concentration and/or distribution of free volume alone cannot predict GB mechanical strength or dislocation nucleation stress. Data presented in this research expands on previous statements that the presence of high free volume atomic structural units enables cooperative atomic processes necessary for the activation of dislocation nucleation under tension, and that free volume migrates away from nucleation regions within the GB. In certain GBs (such as those in E structural boundaries), cooperative atomic migration correlates with the stress-induced collapse of GB structural units leading to dislocation nucleation aligned along the tilt axis. In other boundaries (e.g., $\Sigma 13$ (510)), only local collapses are observed during nucleation where the nucleation is isolated in the GB plane, and no large-scale cooperative atomic rearrangement is necessary for GB deformation.

CHAPTER IV

INTERFACES AND THE EFFECT OF EXCESS FREE VOLUME

4.1 Introduction

UFG and NC materials (i.e., polycrystalline materials with average grain sizes between 100nm and 1μm, and below 100nm, respectively) have been extensively researched and investigated over the past 10 years due to potential improvement of many functional material properties. For example, substantial differences in strength, ductility, hardening, fracture resistance, and fatigue life compared with traditional polycrystalline materials have been measured in these materials ([80, 106, 145, 276, 320]). Additional efforts have aimed at utilizing computational approaches to better understand the role of GBs and the overall mechanical behavior of NC metals [10, 32, 31, 69, 288]. Many investigations have further highlighted the importance of material quality through proper synthesis ([2, 107]). Despite these desirable characteristics, early measurements of low ductility inhibited the use of UFG and NC materials in important structural applications ([80, 112, 134]). Therefore, numerous research endeavors have aimed at increasing the strength and ductility of these materials through improved processing techniques and material preparation ([136, 246, 244, 252, 283, 284, 320]).

As both strength and ductility have risen in UFG and NC materials, they have been leveraged for applications requiring enhanced mechanical properties. This is largely due to atypical accommodation mechanisms and fundamental processes existing within the material substructure. Innovative processing routes such as SPD techniques ([250, 243, 252]) in addition to other recently developed methods ([136, 283, 320]) have encouraged the use of UFG and NC materials. Advantageous properties achieved by using these methods is rooted in novel structures formed at the sub-micron and nanoscale ([251, 249, 244]). However, the eventual application of such materials stems from the ability to produce bulk-sized samples without compromising properties ([252]).

Reducing grain size has long been known to affect material strength and ductility ([39, 140, 182, 186, 265]). Correlating grain size to strength was first outlined by Hall [87] and Petch [166]. As grain refinement continues to the submicron and nanometer scale, traditional strengthening and deformation mechanisms change as described by Schiotz *et al.* [188] and by Van Swygenhoven *et al.* [274]). However, beyond these factors, the state of GBs (e.g., equilibrium, non-equilibrium, special, general, etc.) within these materials has recently been noted to influence functional properties. SPD methods such as ECAP, ECAE, and HPT successfully produce UFG and NC samples with extensive defect content containing higher energy GBs ([42, 148, 153, 154]) as compared to processes such as electrodeposition. GBs within materials that have undergone SPD are significantly altered from those observed in electrodeposition, for example. Excess defect concentrations, and extensive GB/defect interactions lead to GB structures containing disordered regions, steps, ledges, extrinsic defects, and more complex dislocation content. The resulting behavior of these boundaries is therefore influenced ([62, 99, 108, 155, 154, 246, 249, 250, 273, 304]), and processes such as dislocation emission, absorption, transmission, boundary migration, and sliding will likely be altered. There is also evidence offered by high resolution electron microscopy that the thickness of these GBs can be less than 1nm (atomically sharp) [95, 94, 249, 297]. These GBs have been termed 'non-equilibrium' due to their relative high energy, excess free volume, dislocation/disclination content, disordered atomic structure, and energetically metastable state as compared to their equilibrium counterparts. Excess GB free volume has been noted to be a good measure of the degree of 'non-equilibrium' state ([42]), and is defined as the additional amount of free volume as compared to that present in the equilibrium GB structure. Excess free volume correlates with higher interfacial energy and atomic misfit, and is therefore a key physical attribute directly affecting many important GB properties ([40, 42, 173, 253, 305]), such as sliding, migration, and dislocation mediation processes.

As Valiev [245] states, 'grain boundaries engineering dealing with tailoring low-angle and high-angle boundaries, formation of special random or non-equilibrium GBs should be an area of ongoing research in order to produce bulk nanostructured materials with advanced properties'. The idea that excess interfacial free volume reflects the degree of the

non-equilibrium state of GBs motivates our approach. In this chapter, we will outline the method and results pertaining to the structure of NEGBs and their mechanical deformation using atomistic simulations. The objectives of this work are as follows: (1) ascertain the utility of this technique in constructing NEGBs by analyzing both the equilibrium and non-equilibrium interfacial characteristics, (2) explore the relationship between nanoscale interfacial free volume and atomic structure/order during deformation, and (3) investigate the influence of the initial excess free volume or non-equilibrium GB state on mechanical behavior.

4.2 Methodology

A bicrystalline simulation cell containing two lattices separated by a planar STGB was implemented in this work. The GB plane normal was in the Y-direction, the tilt axis in the Z-direction, and the GB period in the X-direction, as shown in Figures 6 and 7. Simulation cell dimensions were appropriately chosen to preserve periodicity and minimize image effects during inelastic deformation. Lattice orientations were chosen to share a common $\langle 110 \rangle$ tilt axis in the Z-direction where each lattice was rotated symmetrically in opposite directions around the tilt axis from a reference 0° direction ([110]). Initial GB structures were obtained by molecular statics using a conjugate gradient energy minimization method employing an embedded atom method potential for aluminum [149] and copper [150]. Numerous starting configurations were leveraged to ensure satisfactory convergence to the minimum energy structure, as compared with previous work ([180, 184, 229]). Following energy minimization, a short (10 ps) thermal equilibration was performed at 10K under NPT to allow residual domain stresses to relax. The final simulation cell size was approximately $12 \times 24 \times 6$ nm, which resulted in $1.1 - 1.9 \times 10^5$ atoms contained in the total cell volume. All MD simulations were performed using LAMMPS (lammps.sandia.gov, [167]).

To construct NEGBs by introducing excess free volume into initial equilibrium grain boundaries (EGBs), we used an approach based on a biased Monte Carlo method. Within this method, a thin interface region was defined in the EGB domain encompassing all non-centrosymmetric atoms (i.e., centrosymmetry values > 0.25 $\mathring{A}^2$), where centrosymmetry is

defined by Kelchner *et al.* [105]. A small number (e.g., three to five on average) of randomly chosen atoms (based on a uniform distribution) located within this interface region were removed simultaneously, followed by energy minimization with a relative energy convergence criteria of 10^{-12}. The number of atoms removed at each iteration has a slight effect on the generation of the NEGBs, especially when the number of deleted atoms is large. However, we investigated the influence of deleting only one atom per iteration in small GB structures as compared to three to five on average, and found no substantial difference in the results; therefore, for computational efficiency, three to five atoms were considered sufficient for our method. We note that additional NE states and structures can be instantiated by varying the interface region geometry, number of atoms removed per iteration, and extent of thermal equilibration period.

This procedure introduces vacancies within the interface region and stimulates atomic reordering within the GB. After energy minimization, equilibration at 10K is performed for 1 ps for further stress relaxation and atomic rearrangement. Each subsequent iteration (i.e., atom removal, energy minimization, and equilibration) created additional atomic disorder by iteratively adding excess interfacial free volume (through vacancy delocalization, [215, 216]) and stimulating atomic shuffling/reordering within numerous GB regions. This generally leads to higher GB energy and a higher non-equilibrium (NE) GB state. However, this trend does not continue indefinitely with additional iterations. For the defined interface region and atom removal criteria used in this work, a local maximum in GB energy was achieved within a hundred iterations. However, it is important to note the dependence of NEGB energy (and local maximum GB energy) on both the defined interface region, the number of atoms deleted per iteration, and the initial GB structure. Each factor will influence the resulting NEGB structure and energy. Further equilibration at higher temperatures (e.g., at 300K for 1 ns) induces further reordering which resulted in a lower energy GB containing less free volume.

To investigate the influence of excess GB free volume and higher energy on mechanical behavior, uniaxial tension and simple shear simulations were performed at 10K. Uniaxial tension was applied perpendicular to the GB plane employing three-dimensional periodic

boundary conditions (as shown in Figure 6). In nonloading directions (parallel with GB plane), atomic trajectories are governed by NPT equations of motion to relax the bounds to zero stress. In the loading direction, atomic trajectories are not controlled by NPT, but only according to the prescribed constant strain rate deformation of the simulation cell. Therefore, stress in the loading direction is not controlled, but computed according to the virial definition (as described later). For shear simulations, periodic boundary conditions were imposed in the X and Z directions parallel to the GB plane with constrained surfaces in Y (as shown in Figure 7). Additionally, atoms located within three times the potential cutoff distance from either the top or bottom vertical faces were held fixed in their equilibrium lattice positions ('rigid'); all other atoms were free from such constraints and designated as 'mobile' atoms. Shear deformation was achieved by iteratively looping through small displacements imposed on the top rigid group of atoms while holding the bottom rigid group of atoms completely fixed in all three dimensions followed by energy minimization and a 1 ps thermal equilibration at 10K, corresponding to a 10^9 s^{-1} shear strain rate ($\dot{\gamma}_{xy}$).

4.3 Results and Discussion

Two low-order Σ CSL bicrystalline structures with a common $\langle 110 \rangle$ tilt axis in copper and aluminum were investigated. The GBs considered are (according to their CSL notation, (GB normal), and misorientation angle) $\Sigma 11$ (113) $\theta = 50.5°$ and $\Sigma 9$ (221) $\theta = 141.1°$. These boundaries were investigated because they differ in GB structure, GB energy, atomic orientation, and initial free volume concentration and distribution. Previous work by both Hahn and Gleiter [86] and Suzuki and Mishin [215, 216] has investigated the role of GBs as sinks for vacancies. Both efforts have concluded that interface structure strongly influences the efficiency of GBs to act as a sink for vacancies and the rearrangement of surrounding atoms due to vacancies in the GB. Variations in initial and excess free volume distributions can therefore be directly compared using this approach for various planar bicrystalline boundaries.

This chapter is laid out as follows. EGB structures are presented and compared with regard to initial GB energy and free volume. Then the resulting NEGB structures are

explained. At this point, it is critical to correlate GB structure and free volume, so a brief discussion applicable to this point is also included. Finally, the mechanical deformation results are divided into 'Tension' and 'Shear', with respective discussion and comparisons. Then general comments and remarks are provided.

4.3.1 Equilibrium Grain Boundaries

Figure 51 displays initial GB structures, including the equilibrium atomic structural unit composition and lattice orientation vectors for both $\langle 110 \rangle$ STGBs viewing along their common tilt axis. Black and white atoms shown in the images correspond to adjacent atomic $[2\bar{2}0]$ planes along the $\langle 110 \rangle$ tilt axis direction. GB structural units were identified using the centrosymmetry parameter and the labeling convention used for structural units in this class of GBs is consistent with Rittner and Seidman [180]. In each Figure, at least one complete period of structural units is included and labeled. Each GB contains a repeating period of atomic structures (i.e., structural units) that fully define the GB structure; these GBs are ordered boundaries and are near equilibrium. The thickness of each EGB is less than 1nm, agreeing with results discussed by Rittner and Seidman [180].

Free volume is computed according to the method outlined in Section 2.2.3 and [229]. Free volume measurements are only performed within a GB region with thickness in the Y direction of 2nm (due to computational limitations). This GB thickness value was determined to be sufficient to include all non-centrosymmetric atoms even after the initial stages of dislocation nucleation, or inelastic deformation near maximum tensile or shear stress. Once the free volume concentration is computed within the GB region, it is then normalized by the entire bicrystalline cell. This assumes that free volume is only located within the GB region, which we have determined to be accurate for the level of deformation considered here. Since free volume concentrations (normalized by the cell volume) strongly depend on the assignment of the GB region and simulation cell dimensions, care must be taken when interpreting/comparing the reported free volume concentrations in this work to other related data.

To gain more insight into the spatial arrangement of free volume and its directional

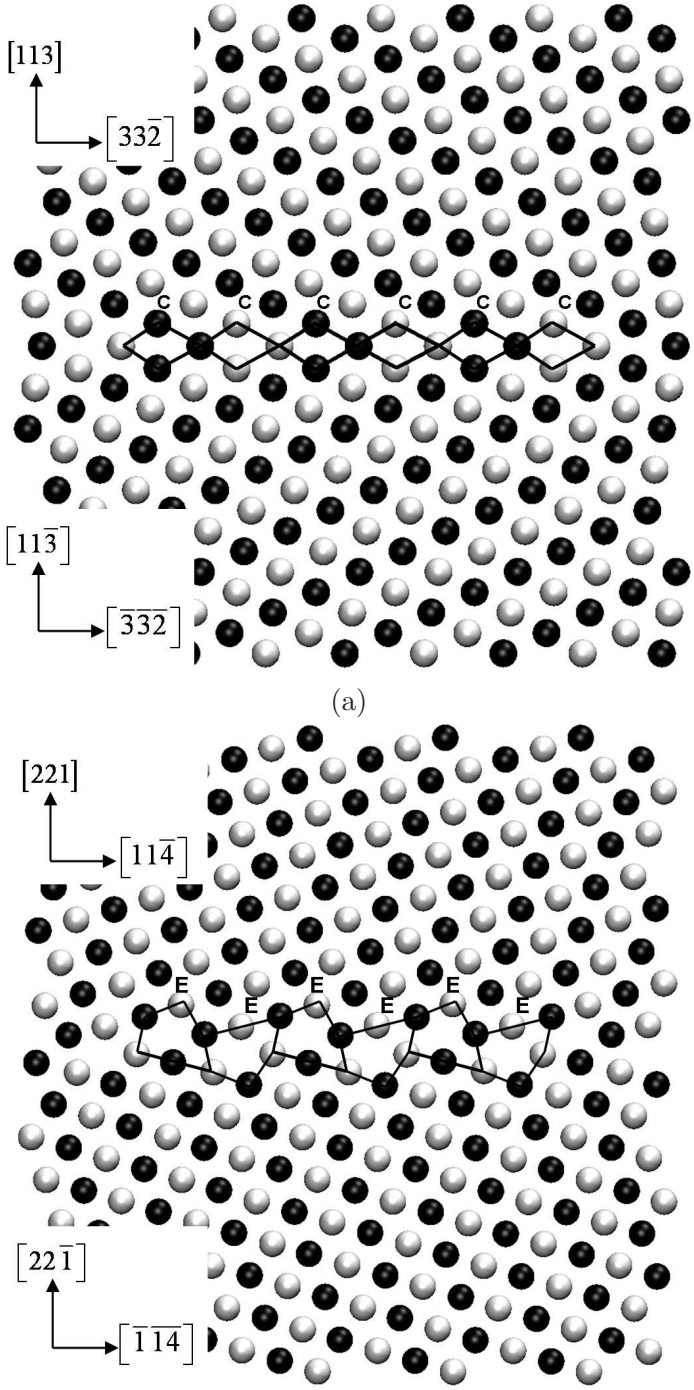

Figure 51: Initial equilibrium atomic structures for (a) Σ11 and (b) Σ9 symmetric tilt grain boundaries, including the lattice orientation vectors and structural units (C and E, respectively).

connectivity, two-point correlation functions (TPCFs) and lineal path functions (LPFs) are calculated within the GB region. Traditionally, TPCFs are utilized to understand the mean

probability that two points separated by a distance r are contained within a particular phase of interest. For example, from inclusion to inclusion within a matrix. In the present case, we wish to only calculate these properties for free volume in the X, Y, and Z directions. Accordingly, TPCF data are provided by the formula

$$P_{11}^{*}(r_k) = \frac{P_{11}(r_k)}{f_1} \tag{15}$$

where k represents the direction (i.e., 1: X-direction, 2:Y-direction, and 3:Z-direction), f_1 is the free volume fraction (to normalize data), and $P_{11}(r_k)$ is the probability that free volume will be found at a distance r in the k direction from a free volume site (subscript 1 represents free volume). The LPF data can also be calculated by a similar formula.

$$L_{11}^{*}(r_k) = \frac{L_{11}(r_k)}{f_1} \tag{16}$$

The LPF determines the probability that an entire line of length r is contained within a particular phase. This contrasts with TPCFs, where only endpoints are considered. Our implementation of LPFs provide information regarding connectivity and clustering of free volume along the X, Y, and Z directions. More information regarding the use of TPCF and LPF in GB free volume measurements can be found in [229], and Chapter 2.

In addition to free volume, it is also necessary to calculate stress throughout the deformation process to extract useful mechanical behavior from the simulations. The calculated stress values provided in this work are based on the virial definition without the kinetic portion ([326]), i.e.,

$$\sigma_{ij} = \frac{1}{N\Omega} \sum_{\alpha}^{N} \sum_{\beta \neq \alpha}^{N^{\alpha}} f_i^{\alpha\beta} r_j^{\alpha\beta} \tag{17}$$

Here, atomic volume is defined by Ω, N is the total atom count in the system, N^{α} represents the number of neighboring atoms for atom α, $f_i^{\alpha\beta}$ is the interatomic force vector between atom α and neighbor β along the i direction, and $r_j^{\alpha\beta}$ is the interatomic distance of atoms α and β in the j direction. This approach to stress would also enable us to define a volume averaged stress over particular regions similar to Horstemeyer and coworkers [97, 96, 98].

Table 3 lists important initial GB information such as the CSL-notation, GB normal, GB energy, normalized initial free volume, and atom count within the GB region. The GB

energy is higher in copper than aluminum for each GB structure; however, the calculated initial free volume is greater in Al. This result agrees with the findings discussed in Chapter 3 and in [229]. When comparing the two GB types within either copper or aluminum, it can be seen that the Σ11 boundary is more compact with less free volume, giving a lower GB energy value than the Σ9. Also, the initial free volume level in the Σ11 boundary is lower than in the Σ9. Now we will address the initial statistics and information concerning NEGBs for each boundary structure.

Table 3: Summary of GB information listing GB CSL, initial GB energy, normalized initial free volume, and the GB atom count.

Material	CSL	GB Normal	GB Energy (mJ/m^2)	Normalized Initial Free Volume	GB Atom #
Copper	Σ11	(113)	309.7	1.75e-05	2304
	Σ9	(221)	833.5	9.87e-05	3072
Aluminum	Σ11	(113)	150.7	3.16e-05	1848
	Σ9	(221)	446.9	2.30e-04	2464

4.3.2 Non-Equilibrium Grain Boundaries

This work considers the influence of excess free volume on GB structure, energy, atomic rearrangement under applied stress, and the associated mechanical behavior. Both 'low' and 'high' (relative to each other) NE GB states are instantiated and investigated for each corresponding EGB. A biased Monte Carlo method is employed for constructing NEGBs from corresponding near equilibrium GBs. After at least one hundred iterations and a highly NE state is achieved (using excess free volume as a measure), two NEGBs are selected (from this group of NEGBs) to compare to the near EGB. A high NE state GB with the greatest free volume (NEGB**) and a lower NE state GB containing less free volume than the NEGB** (NEGB*) are selected. Figure 52 compares the (a) EGB structure to both the (b) NEGB* and (c) NEGB** structures for the copper Σ9 (221) boundary.

All images in Figure 52 are viewed along the $[1\bar{1}0]$ tilt axis, where centrosymmetric atoms (< 0.25 $\mathring{A}^2$) are not shown to assist in GB atom visualization. Figure 52 shows evidence that excess interfacial free volume and higher atomic disorder exist in the non-equilibrium

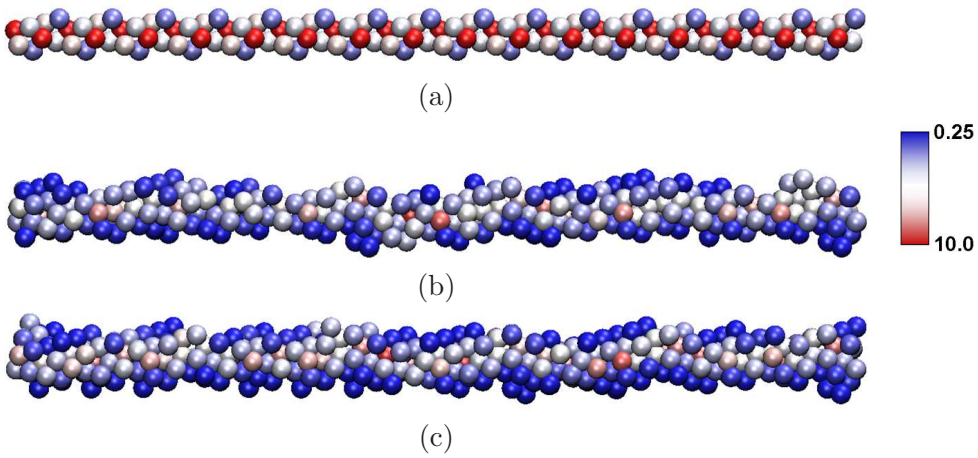

Figure 52: Comparing the (a) equilibrium and (b)-(c) non-equilibrium GB structures for the Σ9 copper boundary. Increasing NE state is seen in (b) and (c), where (b) NEGB* is of lower NE state than (c) NEGB**. These images are viewed along the tilt axis where centrosymmetric atoms have been removed for clarity and atoms are colored according to centrosymmetry.

structures as compared to the EGB shown in (a). The addition of excess free volume leads to changes in GB atomic structure and the degree of atomic order in the GB, as well as the observed GB region thickness. As Chuvil'deev *et al.* [42] suggest, the relative degree of excess free volume within a GB as compared to its equilibrium counterpart is a useful measure of the degree of NE state. However, the NEGB (shown in 52(b)) possesses greater interfacial energy than the EGB in (a), but also contains slightly less initial free volume. This behavior lends support to the notion that GB structure influences the ability of a GB to act as a sink for free volume and that atomic rearrangement/shuffling is a function of GB structure as well. GB free volume does not always increase with each iteration and higher NE states. Some NEGBs will contain lower free volume levels than the corresponding EGB, but will still be of higher energy. Therefore, using excess free volume as a measure of NE state is generally acceptable, but not always true.

The NEGBs shown in 52(b) and (c) differ with regard to apparent GB structural order and to a lesser extent, observed GB thickness. As we will discuss in greater detail, these structural distinctions have a direct influence on both the local and global mechanical behavior of each boundary by promoting coordinated atomic shuffling and reordering that trigger GB deformation mechanisms. Although the presence of NEGBs in metals that have

undergone SPD has been confirmed by HRTEM, it is important to point out that there are numerous types of NEGBs present in these materials. At this time, a clear understanding of the distribution of NEGB types in SPD metals is not well characterized/established. Thus, it must be stated that our work focuses on NEGBs with small deviations from the EGB structure.

To investigate the energetically metastable state of the NEGBs, a longer thermal equilibration run is performed at higher temperatures. For example, both copper and aluminum $\Sigma 9$ (221) NEGBs are equilibrated at 10K and 300K under NPT for 1 ns. The GB energy (γ_{GB}) is calculated every 0.1 ns during the simulation, and plotted as a function of time (as shown in Figure 53). The GB energy evolution in Figure 53 shows that the initial NEGBs are in fact in an energetically metastable state (more significant GB energy decrease with higher temperature), and that thermal equilibration at higher temperatures induces atomic reordering. The resulting GB structures after equilibration at both 10K and 300K have lower energies and free volume. However, the change in GB energy is greater for equilibration at 300K. At 300K, the change in GB energy is approximately 10% for aluminum and 5.5% for Cu. At 10K, for both copper and aluminum the change is less than 1%, but decreasing GB energy is observed. Compared to the EGBs, the structures after equilibration at 300K are approximately 18% and 9% greater energy, for aluminum and Cu, respectively. While this technique shows that these boundaries are reasonably metastable within the time limit imposed (up to 100ps), there is no guarantee that their structural equilibrium persists beyond the limit of MD time scales. To address this concern, extended time scale methods, such as parallel-replica dynamics [282] can be invoked. Then the metastable state of NEGBs can be explored without the time constraint of MD.

As Table 4 shows, the degree of NE state for each boundary type is related to excess free volume within the GB as compared to each near equilibrium boundary. For both boundaries considered, as additional free volume is added to the boundary, the overall energy increases as well as the GB atom count. This result agrees with notions in the literature that suggest GB energy correlates with both excess free volume and NE state ([41, 42, 154, 253, 273]). However, a definitive relationship is not known at this time for free volume and GB energy,

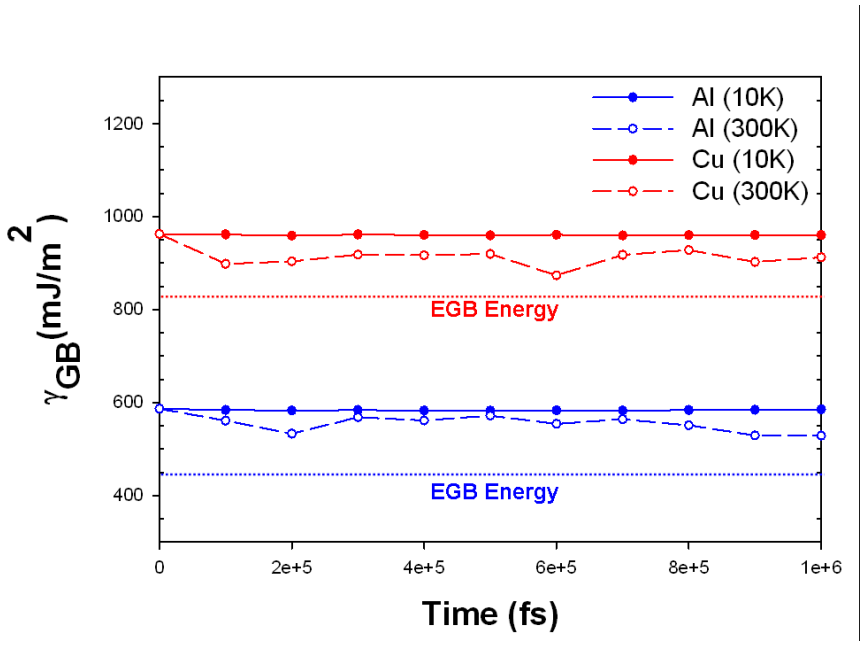

Figure 53: The evolution of GB energy during thermal equilibration at both 10K and 300K for copper (red) and aluminum (blue) Σ9 (221) NEGBs. The dotted lines represent the EGB energy after energy minimization.

as suggested by Olmsted *et al.* [159].

Table 4: Summary listing CSL , GB normal, GB type, GB energy, normalized initial free volume, and GB atom count.

	CSL	GB Normal	Type	GB Energy (mJ/m^2)	Normalized Free volume	# of GB atoms
Cu	Σ11	(113)	NEGB*	510.6	2.29e-04	2608
	Σ11	(113)	NEGB**	776.5	5.46e-04	2960
	Σ9	(221)	NEGB*	921.8	8.03e-05	3360
	Σ9	(221)	NEGB**	962.4	1.13e-04	3371
Al	Σ11	(113)	NEGB*	265.3	2.68e-04	2209
	Σ11	(113)	NEGB**	540.2	6.62e-04	3057
	Σ9	(221)	NEGB*	565.3	2.52e-04	2757
	Σ9	(221)	NEGB**	586.4	2.71e-04	2799

NEGB** is of higher NE state than NEGB*

The efficiency of a GB as a sink for vacancies or excess free volume (during energy minimization, equilibration, and deformation) depends on its initial structure (and free volume distribution). In other words, GBs with higher initial free volume (e.g., Σ9) do not proportionately retain the degree of excess free volume as do low initial free volume

boundaries. This behavior is identical to that described by Hahn and Gleiter [86] comparing 'good atomic fit' boundaries to 'poor atomic fit' boundaries. They noted that vacancies in short-periodic GBs with 'good atomic fit' tend to remain localized without causing atomic rearrangement in surrounding atoms, and vacancies in 'poor atomic fit' boundaries promote atomic rearrangement that delocalizes the vacancy and redistributes the associated free volume within the GB.

This trend can be seen in Table 4. In the Σ9 boundary, the added excess free volume is easily redistributed within the GB to be incorporated and associated with nearby free volume packets, and leads to higher free volume connectivity (which will be detailed later). The measured free volume within each NEGB for the Σ9 boundary is comparatively lower than that measured within the Σ11 NEGB**, and the extent of excess free volume (in the form of monovacancies) is much greater for the Σ11 boundary than the Σ9. These simulations also agree well with statements by Ungar *et al.* [242] referring to the importance of GB structure when analyzing vacancy and/or free volume agglomeration in GBs. In our simulations, it is clear that GB structure does strongly influence the resulting defect concentration within the boundary and its efficiency as a sink for vacancies and additional free volume.

Connecting atomic GB structure with excess free volume is important. As the structure changes, so does the free volume arrangement ([229]). To illustrate this point further, Figure 54 shows the free volume distributions within the GB for the copper Σ9 viewing from the GB plane normal direction. These free volume distributions correspond to the initial EGB and NEGB** structures shown in Figure 52 prior to deformation. It is clear that as GB atomic order decreases by the addition of excess free volume (and greater NE state), as shown in the radial distribution function (RDF) plot of Figure 55; free volume in the boundary plane loses its ordered arrangement as well. Although each plot in Figure 55 shows distinct neighbor peaks in the distribution, it is clear that for EGB (blue) and NEGB**(red) the peaks broaden as compared to the fcc (black) distribution. The fcc distribution is for a single crystal, and the peaks correspond to the first two nearest neighbor distances. For each of the additional boundaries, the g(r) peak values decrease and the peaks broaden

indicating that there is less atomic order in each structure. It is recalled that the GB region includes lattice regions on either side of the GB which will influence the RDF plots to be more ordered than if just the GB was considered.

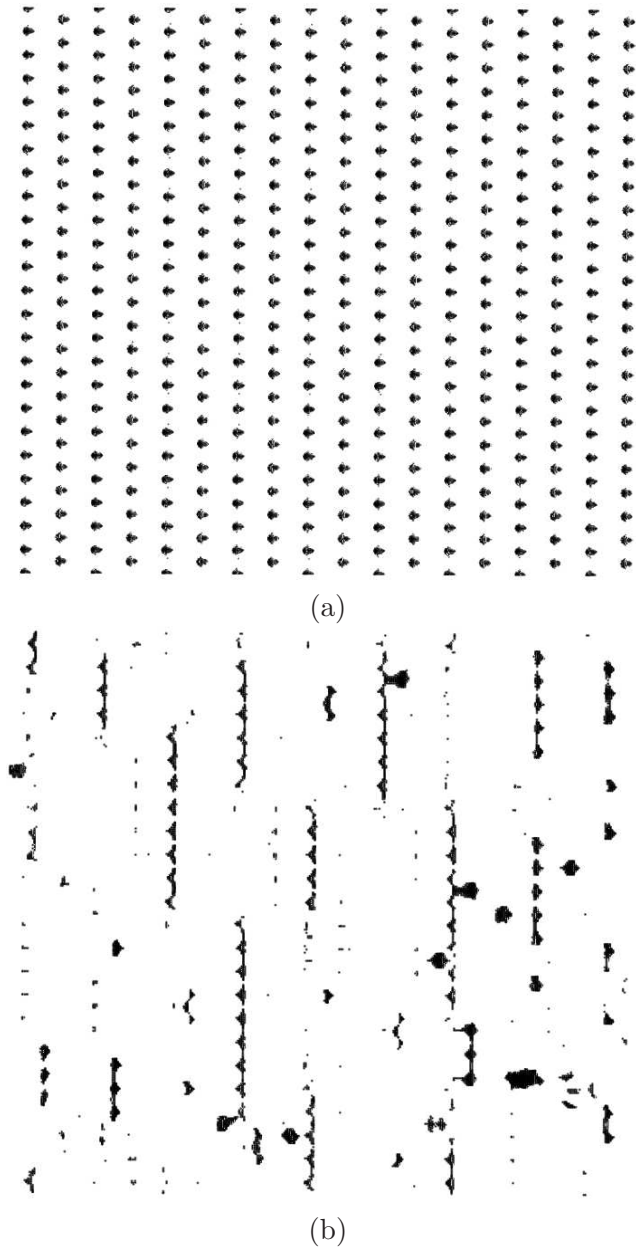

(a)

(b)

Figure 54: The initial (a) equilibrium and (b) non-equilibrium GB free volume distributions for the Σ9 copper boundary corresponding to the structures in Figure 52(a) and (c), respectively. These images are viewed along the GB plane normal, where the tilt axis is vertical and the GB period direction is horizontal.

As mentioned previously, due to higher levels of initial free volume within the Σ9 GB

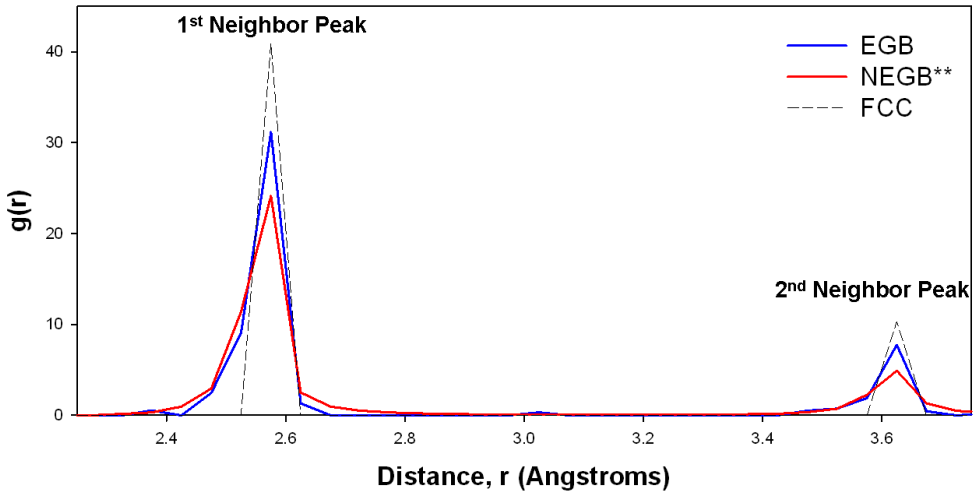

Figure 55: Radial distribution function (RDF), g(r), data for the copper Σ9 boundary comparing the EGB (blue), NEGB**(red), and fcc copper lattice (black). This plot shows that due to the GB and excess interfacial free volume (as compared to the fcc lattice data), atoms become more disordered from the equilibrium lattice positions. In the RDF data, the first two nearest neighbor positions are clearly seen as the large spikes in the data.

structure and lower atomic density, excess free volume is more easily accommodated and becomes delocalized more readily. This behavior also points to greater atomic rearrangements due to higher levels of free volume and a greater propensity for free volume redistribution as a consequence of excess free volume. This is also true in the aluminum structure where excess free volume tends to be higher for a given NE state. Free volume packets within higher free volume GBs delocalize more easily than in lower free volume GBs and are highly connected (especially along the GB tilt axis, $\langle 110 \rangle$), as shown in Figure 56.

Figure 56 shows TPCF along the tilt axis within the GB region only considering free volume. The EGB plot shows that at discrete distances, there is a high probability of finding another free volume packet. For NEGBs, the ordered structure is not as evident. Instead, Figure 56 shows that the ordered peaks for the EGB get broadened and display non-zero values for intermediate distances. Therefore, the initial free volume distribution in NEGBs is not as ordered and a repeating distribution pattern along the tilt axis is not observed. The trend is also observed in the GB period direction. This tendency toward free volume connectivity with increasing NE state is quite important with regard to atomic reordering

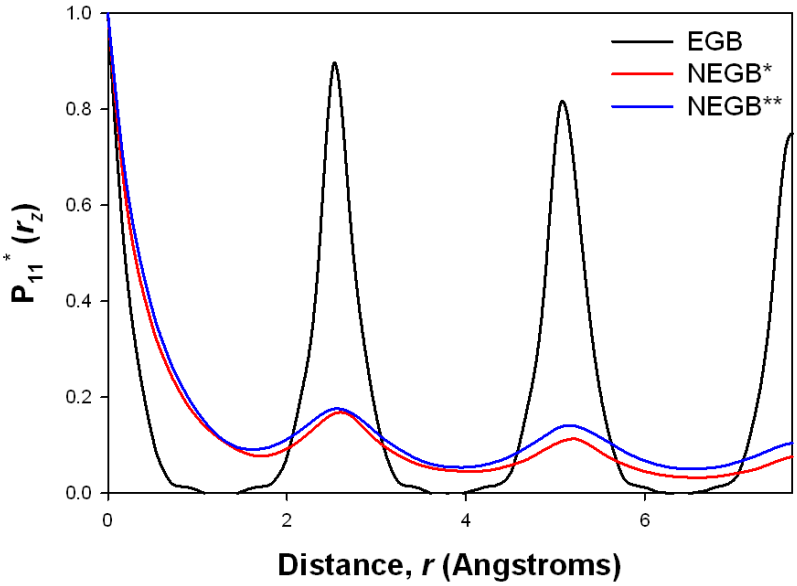

Figure 56: TPCF data for free volume in the Z-direction (tilt-axis) for the copper Σ9 (221) boundary. Clearly, as additional NE state increases, the free volume becomes less ordered and more connected along the tilt axis. This same trend is observed in aluminum as well.

and shuffling under applied load, as examined in the following section.

4.3.3 Mechanical Deformation

4.3.3.1 Tension

To investigate the influence of NE state (excess free volume) on GB mechanical behavior, uniaxial tension is applied perpendicular to the GB plane at a constant $10^9 s^{-1}$ strain-rate. In accordance with the 3D periodic boundary conditions of the simulation cell in these uniaxial tension simulations, a second GB is also present in the simulation cell but remains in its initial equilibrium state. It is located at both the upper and lower surfaces of the periodic simulation cell. For simulations investigating EGB mechanical behavior, both GBs remain in their initial near-equilibrium state, and no excess free volume is present in either GB. These simulations are identical to those performed in previous work ([207, 229, 230]). However, for additional simulations exploring NEGB tensile behavior (simulations leading to NEGB* and NEGB** data), the periodic GB remains in its initial near-equilibrium state

while the other GB is in a NE state.

Tensile deformation continues to strains beyond the point of maximum stress (which has been used to define the boundary strength by Spearot *et al.* [207] or peak stress by Tschopp *et al.* [230]). Stress is calculated from the virial definition (averaged over the entire domain) without the kinetic portion and strain under uniaxial tension is defined as $\epsilon = \delta_h/h$, where h is the initial height of the simulation cell and δ_h is the extension difference during straining from h. Just prior to maximum tensile stress or peak stress, partial dislocation nucleation from the GB is observed in each boundary studied. However, it must be stated that the actual nucleation/emission event does differ between each GB (e.g., EGB, NEGB*, and NEGB**).

Simultaneous emission events from GB nucleation sites occur along the tilt axis in the EGB. Due to the lower degree of atomic structural order present in each NEGB (NEGB* and NEGB**), the dislocation nucleation event(s) differ(s) substantially from that (those) of the EGB. In the NEGBs studied, there are preferred nucleation sites in the GB. Partial dislocations nucleated from these boundaries originate at these preferred sites, which tend to be localized in the GB. Under tension, heterogeneous dislocation nucleation is observed in these boundaries, agreeing with previous findings for equilibrium structures for low-order CSL boundaries in Cu, including both the $\Sigma 9$ and $\Sigma 11$ boundaries by Spearot *et al.* [207] and Tschopp [230]. Figure 57 shows the resulting tensile stress-strain responses for the copper (a) $\Sigma 11$ and (b) $\Sigma 9$ boundaries; both equilibrium (solid) and non-equilibrium (dotted) boundaries are included.

From Figure 57, it can be seen that although the addition of excess free volume influences the maximum tensile stress or strength of the boundary, it does not alter the elastic response of the computational cell prior to dislocation nucleation. This means that substantial changes to interfacial atomic structure do not influence the elastic behavior of these computational cells as was true for each EGB. In both Figures 57 (a) and (b), the stress-strain curves for each NEGB coincide with the stress-strain curve of the EGB prior to maximum stress. In addition, as NE state increases, the peak tensile stress and corresponding strain decrease for both the $\Sigma 11$ and $\Sigma 9$ boundaries. It must be emphasized that

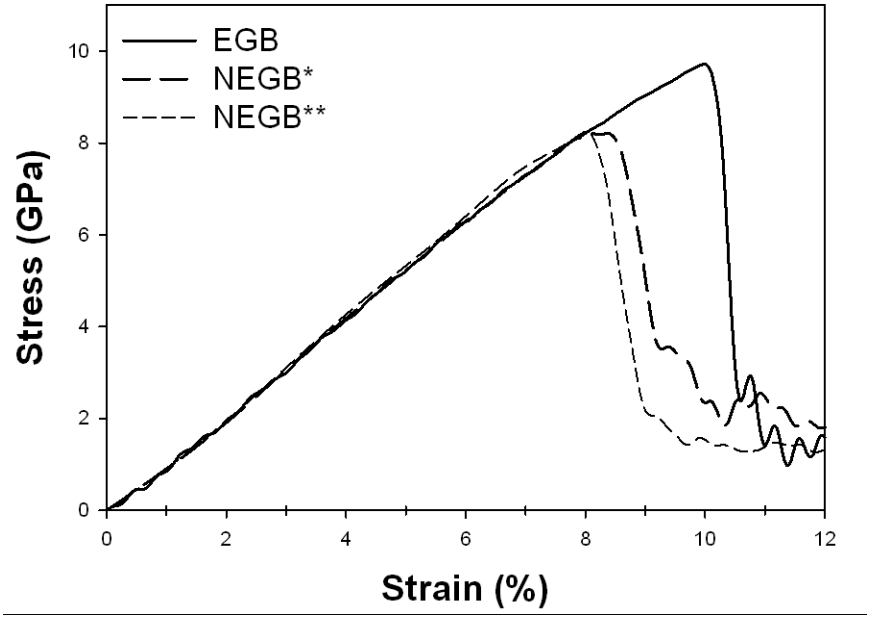

(a)

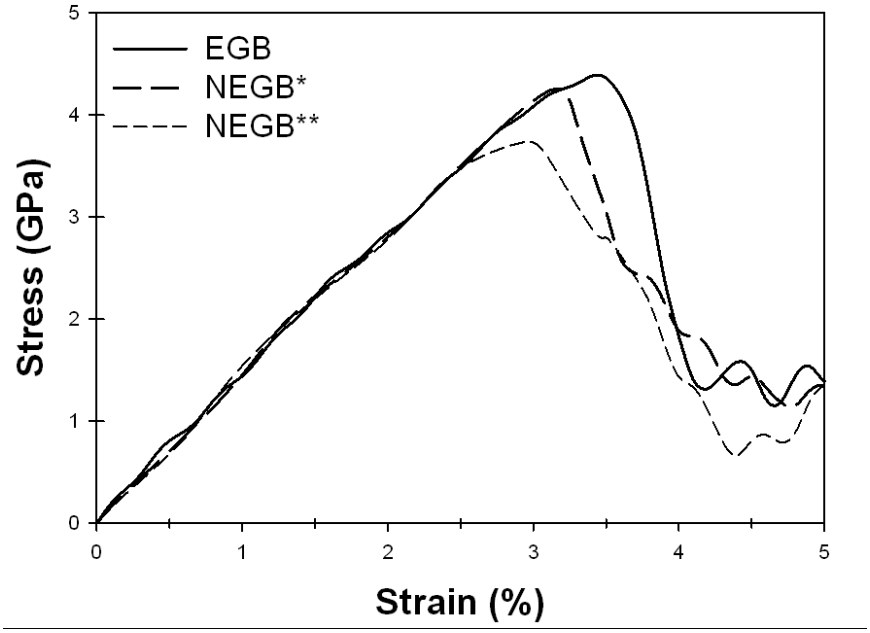

(b)

Figure 57: Tensile stress-strain curves including both the equilibrium (solid) and non-equilibrium (dotted) copper (a) Σ11 and (b) Σ9 boundaries.

a direct correlation between the change in boundary strength and the amount of excess GB free volume is not well understood at this time. However, it is clear that for these ordered,

low-Σ value copper bicrystalline GBs, excess interfacial free volume influences the inelastic deformation response under uniaxial tension.

Another important feature is the noticeable difference in peak tensile stress for the $\Sigma 11$ boundary as compared to the $\Sigma 9$ boundary. This result coincides with findings by Spearot *et al.* [207] who noted a significant drop in the tensile strength of E structural unit boundaries, due to higher interfacial 'nanoporosity' or free volume, compared to other $\langle 110 \rangle$ symmetric tilt boundaries. This point was further substantiated by Tschopp *et al.* [229], who discussed both the importance of free volume and its influence on tensile dislocation nucleation stress. Additional efforts also investigated the deformation of E structural unit boundaries under tension and compression ([230]) as well as under shear ([183, 184]) with atomistic simulations.

Figure 58 shows the tensile response for both (a) $\Sigma 11$ and (b) $\Sigma 9$ aluminum boundaries. Again, a significant drop in boundary strength is observed for each GB as the NE state increases. Very similar GB responses are observed in aluminum as in copper for NEGBs in terms of the effect of excess interfacial free volume on inelastic deformation under uniaxial tension.

For dislocation nucleation (which was observed in each GB under tension), excess free volume in the GB region enhances local atomic rearrangements and shuffling type events, which is considered to be the activation for dislocation nucleation and other vital mechanisms. Atoms are able to rearrange more easily under local stress states in the neighborhood of free volume clusters, which influences the required stress needed to nucleate dislocations.

Figure 59 shows that dislocation nucleation from GBs depends on the NE state. Simultaneous emission events are observed in the ordered near-equilibrium structure seen in Figure 59(a). As excess free volume increases, Figures 59(b)-(c), dislocation nucleation becomes more localized in the GB region and isolated nucleation events are observed. Despite increasing the NE state, dislocation nucleation still occurs on identical slip planes for all boundaries shown in 59(a)-(c). Therefore, while GB structure affects nucleation, the lattice orientation is still important when considering dislocation nucleation in NEGBs. Similar behavior is also noticed in the $\Sigma 11$ GB, which is a lower free volume, near-equilibrium

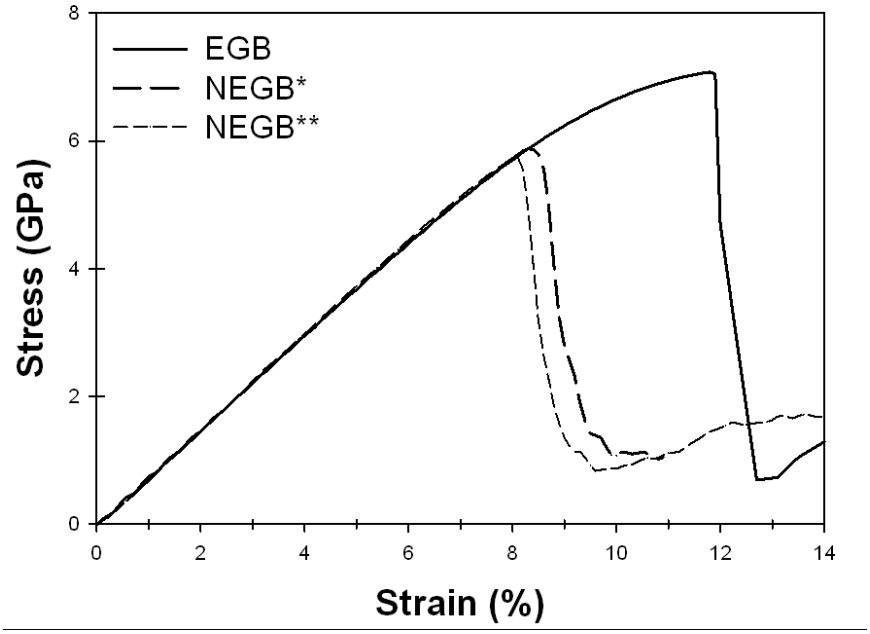

(a)

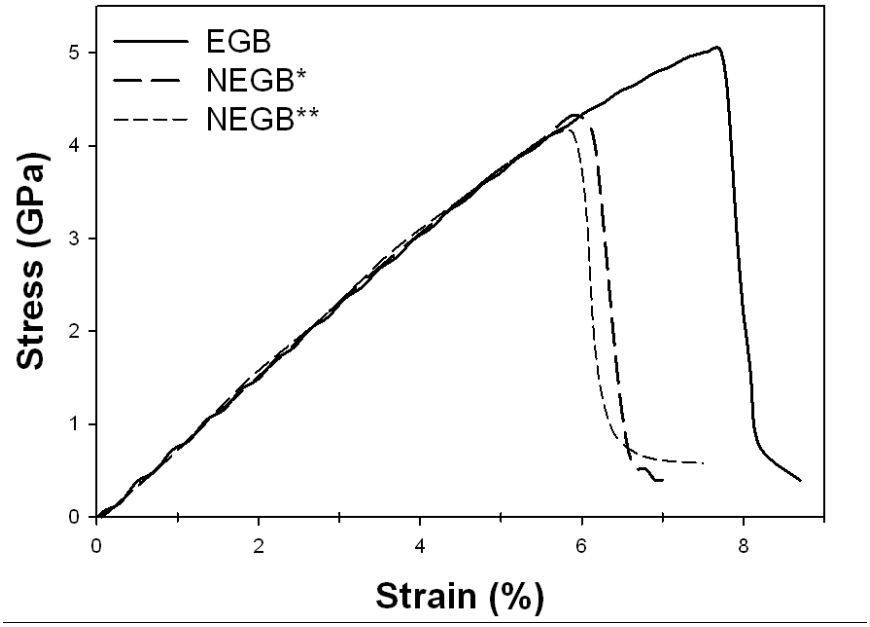

(b)

Figure 58: Tensile stress-strain curves including both the equilibrium (solid) and non-equilibrium (dotted) aluminum (a) Σ11 and (b) Σ9 boundaries.

boundary. In Al, the same trend is also observed with regard to dislocation nucleation under uniaxial tension at 10K.

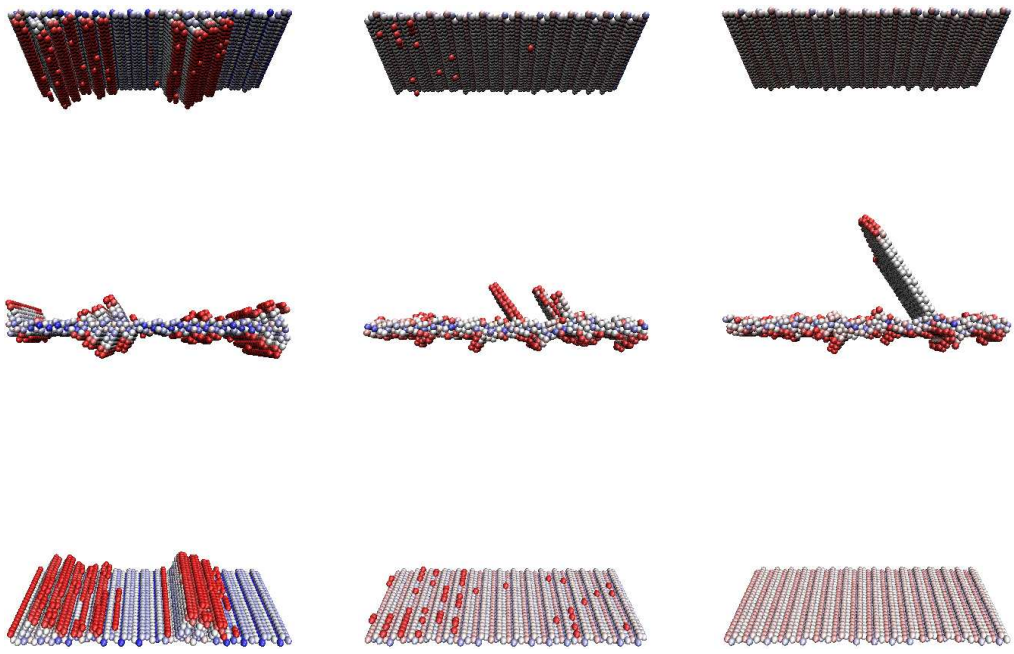

Figure 59: A comparison of dislocation nucleation in the high free volume Σ9 boundary in copper, including the (a) EGB, (b) NEGB*, and (c) NEGB**. Images represent a strain level just following peak tensile stress, and atoms are colored according to centrosymmetry.

4.3.3.2 Shear

Figure 60 presents the shear stress-strain response for the (a) Σ11 and (b) Σ9 boundaries for both copper and aluminum for comparison. Shear stress (σ_{12}) is computed using the virial definition, and shear strain (γ_{12}) as $\gamma = arctan(l/d_o)$, where l is the shear displacement (or the relative displacement of the upper and lower rigid atomic groups) in the X-direction and d_o is the distance between the two rigid atomic groups in the Y-direction. In Figure 60, only one NEGB is shown to compare to the EGB because the additional NEGB's behavior does not alter the key results or interpretation. In this Figure, it is clear that a similar change in behavior is seen under shear as was observed in uniaxial tension. For both copper and aluminum NEGBs, the peak shear stress is lower than that of the corresponding EGB (which parallels the tensile behavior), so GBs at a higher NE state exhibit less resistance to shear deformation than those near equilibrium. As straining continues, the mechanical behavior of each EGB and NEGB pair exhibit a nearly perfect plastic response. This behavior once again highlights the influential nature of interfacial free volume (and atomic structure) on

GB atomic rearrangement during deformation. Clearly, resistance to shear deformation is influenced by the degree of GB atomic order. However, questions still remain concerning changes in the deformation mechanism under shear and its dependence on NE state. Sansoz and Molinari first investigated the shear deformation response of numerous tilt GBs in both copper and aluminum ([184]), and they observed a variety of mechanisms accommodating strain under shear (e.g., GB migration, GB shuffling, and partial nucleation).

In both the Σ11 and Σ9 boundaries, copper yields under shear at lower strains than aluminum. A higher peak stress is noted for the copper Σ11 boundary than the same boundary in aluminum, while the Σ9 boundary in copper has a slightly lower peak stress. In both copper and aluminum, the Σ9 GBs deform via GB sliding, activated once the peak stress is reached. Therefore, we can conclude from Figure 60(b) that excess free volume enhances interfacial atomic activity required for GB sliding and lessens the obstacle for atomic shear shuffling and sliding required prior to GB sliding. The tendency for lower activation barriers for GB sliding observed in these simulations for NE structures as compared to EGBs is consistent with previous results [108, 245, 244, 246]. However, for the Σ11 EGBs, GB migration is observed in Cu, and dislocation nucleation is seen in aluminum. So a change in deformation mechanism is observed in the Σ11 GB between copper and aluminum EGBs, but in both copper and aluminum Σ11 NEGBs migration is observed. Figures 61 (aluminum) and 62 (Cu) show atomically detailed comparisons of the shear mechanisms observed comparing the EGBs to the NEGBs.

Figure 61 shows that for Al, a change in mechanism also accompanies a higher NE state. In this Figure, (a) represents the aluminum Σ11 (113) EGB just after heterogeneous dislocation nucleation near peak shear stress, and (b) displays the NEGB deformation response under shear. For the EGB, partial dislocations are emitted from the GB near maximum shear strength, and for the NEGB, the boundary migrates perpendicular to the GB plane. Figure 62 provides a comparison of the shear response of the (a) equilibrium and (b) non-equilibrium GBs for copper Σ11. No change in deformation accommodation mechanism was observed in the case of Cu. For both the EGB and NEGB, migration was observed during shear straining. However, for NEGBs in both copper and aluminum

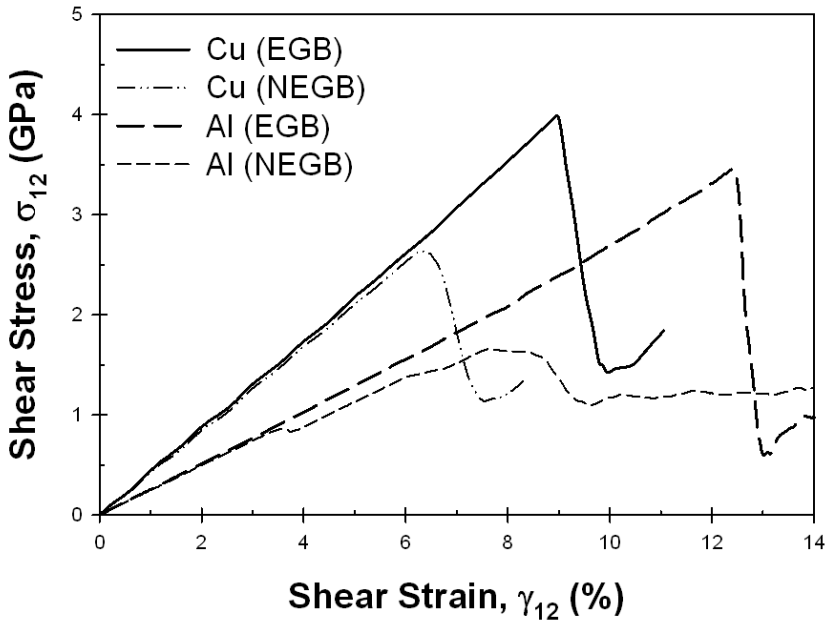

(a)

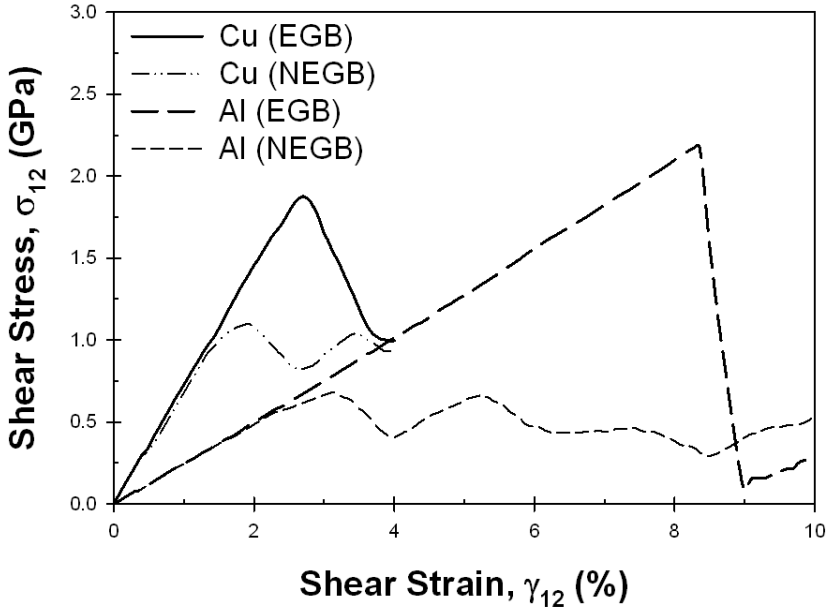

(b)

Figure 60: A comparison of the shear stress-strain curves for the (a) $\Sigma 11$ and (b) $\Sigma 9$ boundaries of both copper and aluminum. In addition to the EGB behavior, the NEGB behavior is also shown.

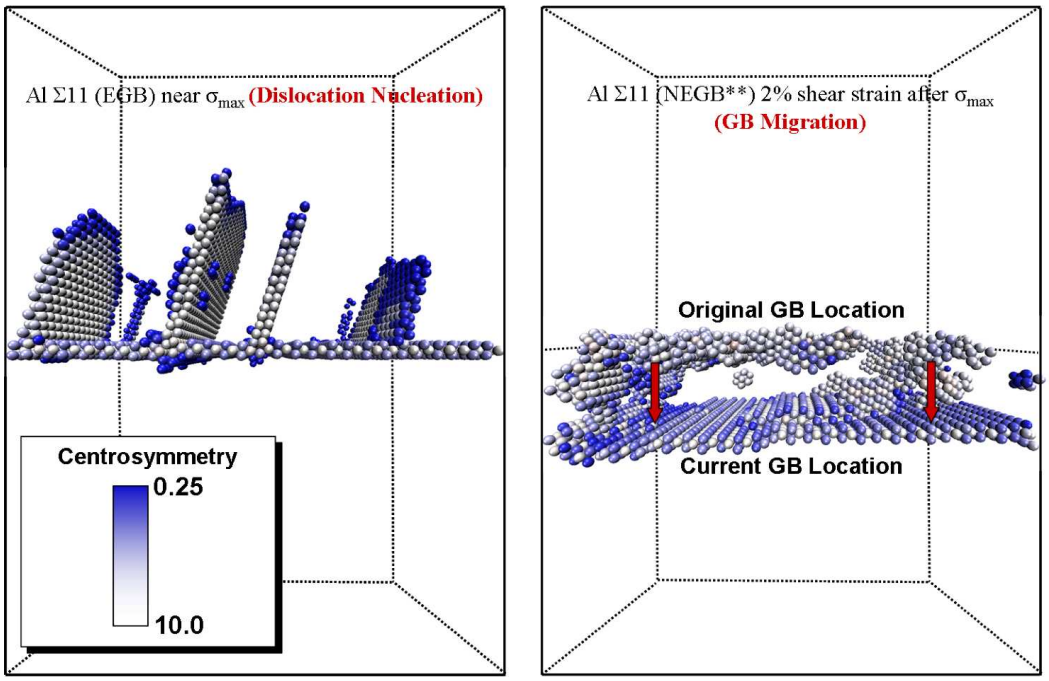

(a) (b)

Figure 61: Comparing the shear deformation of both the (a) EGB and (b) NEGB aluminum Σ11 (113) GBs. In the EGB (a), heterogeneous dislocation nucleation is observed, while in the NEGB (b), GB migration is observed. This comparison demonstrates a change in the observed deformation mechanism during shear for different NE states.

(which display lower peak stresses), there are boundary regions which begin to undergo migration at strains corresponding to the peak stress, while other boundary regions are pinned momentarily by the excess defect population in the GB. Therefore, excess free volume in this boundary (which tends to be in the form of monovacancies) lowers the migration resistance in some regions by enhancing local atomic shuffling leading to a behavior that resembles boundary pinning in other regions. Once the pinned regions begin migrating, ordinary migration behavior is observed, and the GB structures resemble those observed in EGB deformation, leaving behind defects in the lattice. In both Figures 61 and 62, the extrinsic defect population which was initially located within the NEGB is deposited in lattice regions trailing the migrating boundary. The GB continually transforms to a lower energy (closer to equilibrium) structure with decreasing defect concentrations as migration continues.

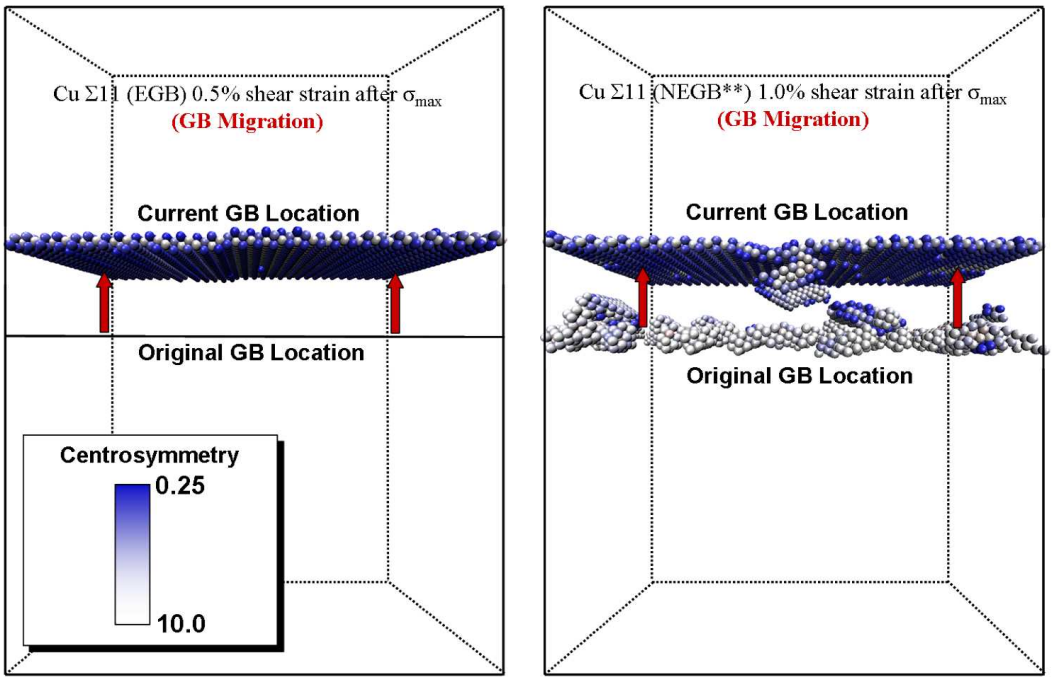

(a) (b)

Figure 62: Comparing the shear deformation of both the (a) EGB and (b) NEGB copper Σ11 (113) GBs. In both (a) the EGB, and (b) the NEGB GB migration is observed. No change in the observed deformation mechanism was observed during shear for different NE states.

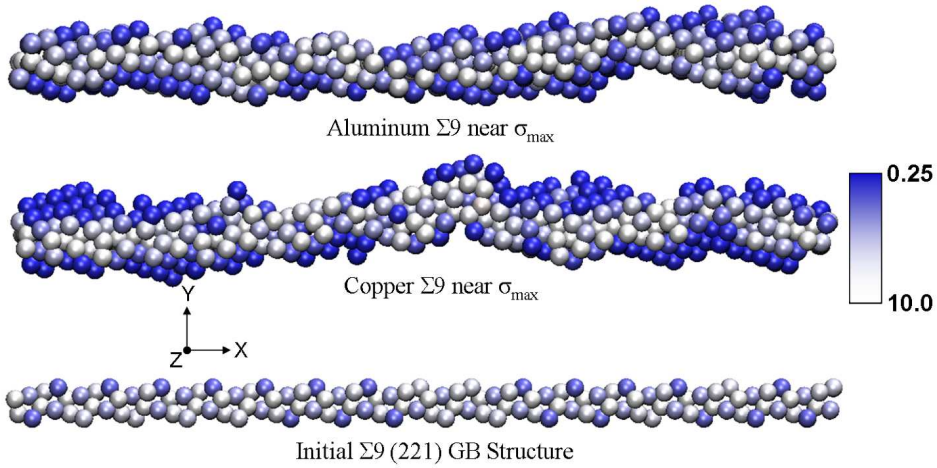

Figure 63: A displaced comparison of shear deformation mechanisms observed in the Σ9 (221) EGB. Both the top (Al) and middle (Cu) images shows GB sliding is the observed strain accommodating mechanism under shear at 10K for the EGB (where the lower image is the initial EGB structure for both copper and aluminum.

On the other hand, Figure 63 provides a comparison of the shear deformation mechanisms observed in copper and aluminum for the Σ9 boundary. For this boundary, GB

sliding is observed during shear for both copper and aluminum. The Σ9 NEGBs deform by sliding as well (as displayed in the two upper images of 63), and the only difference is the resistance to GB sliding as noted in the stress-strain curve in Figure 60(b). As each boundary is strained, the initially ordered EGB structure transforms to a more disordered structure (similar to the initial NEGB structures shown in Figure 52). For each NEGB, the initial configuration begins slightly disordered (as shown in Figure 52) and remains in a NE state during straining. Observations of these structures, and those of the NEGBs during straining, suggest that during GB sliding of Σ9 boundaries (and possibly other high free volume boundaries), a steady-state configuration is approached at higher strain levels. In other words, as the deformation of each Σ9 boundary continues (via sliding and atomic shuffling), the atomic configuration of the boundary is more disordered than the EGB. This can be understood by comparing stereology-based two-point statistical data for interfacial free volume during straining (like that used in [229]).

Figure 64 shows both the TPCF (a) and LPF (b) plots for free volume along the tilt axis (Z-direction) for both copper and aluminum. Plots for both an EGB and a NEGB are shown in this Figure prior to straining (solid) and at a strain just after peak stress (dotted). First, notice in Figure 64(a) that in both copper and aluminum, free volume in the tilt axis direction is more spatially ordered in each EGB than in the NEGB. Then, as each EGB is strained under shear, free volume becomes more disordered (indicated by higher values in between each peak and peak broadening). This is true in all boundaries investigated except for the aluminum NEGB, which becomes slightly more ordered during shear deformation. Second, each boundary approaches a similar steady-state configuration at higher shear strains (agreeing with observations made earlier) in both copper and aluminum. Figure 64(b) shows that each NEGB begins with more connected free volume packets along the tilt axis direction compared to the corresponding EGB, and that the initial free volume in each EGB evolves to become more connected during inelastic shear deformation. The LPF data also shows that at higher shear strains, free volume (in both the EGB and NEGB) become more connected along the tilt axis. This again shows that some kind of steady-state configuration is reached during GB sliding for high free volume boundaries as shear

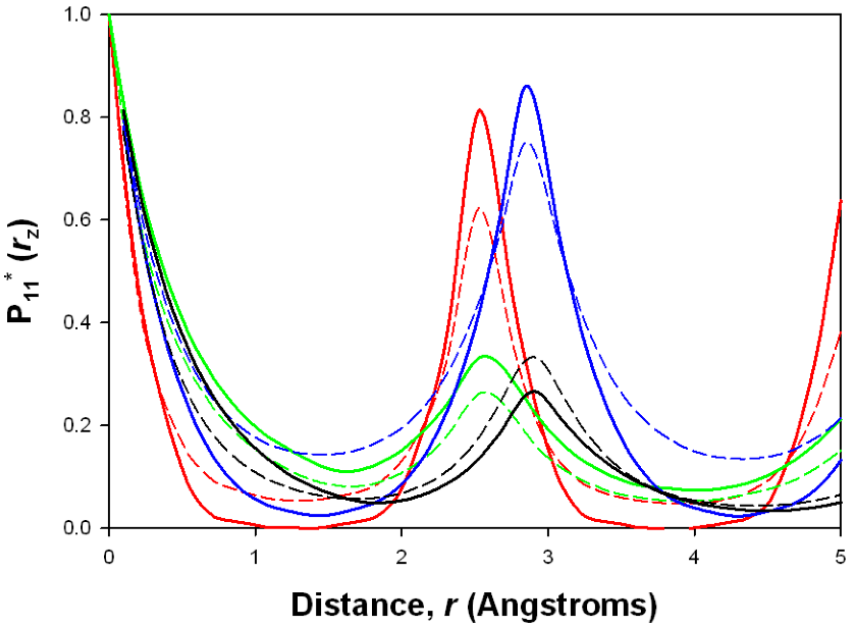

(a)

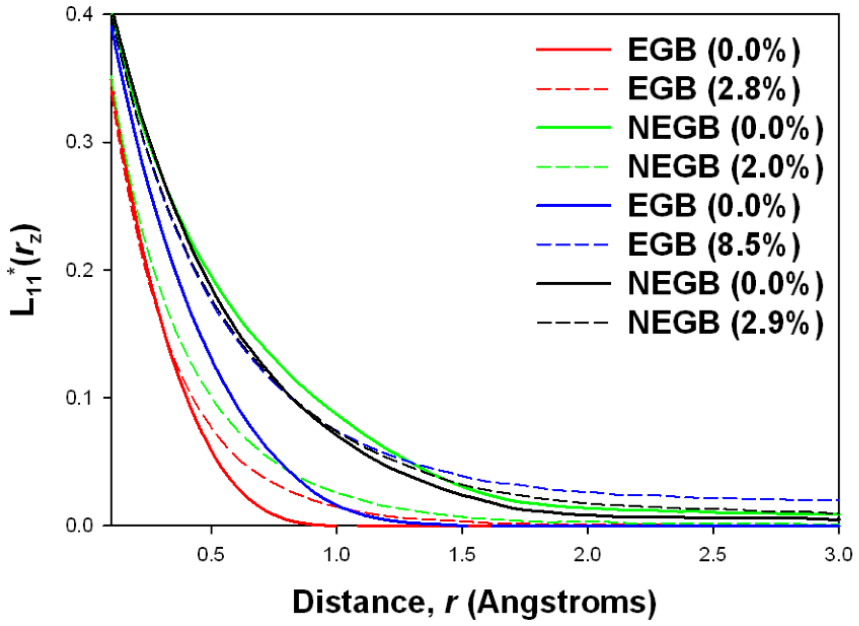

(b)

Figure 64: TPCF (a) and LPF (b) data for free volume along the tilt axis direction in the Σ9 GB in both copper (red and green) and aluminum (blue and black) during shear. Plots for both the EGB and a NEGB are shown prior to straining (solid) and at a strain just after peak stress is reached (dotted).

continues.

4.3.4 Free Volume Evolution

The evolution of interfacial free volume as a function of strain is shown in Figure 65. Each plot displays free volume evolution behavior for both EGBs and NEGBs. The results from uniaxial tensile deformation are shown in (a) and (b), while the resulting behaviors during shear are displayed in (c) and (d). All strain values in Figure 65 (Strain*) are normalized by the strain where peak stress is first observed. This state corresponds approximately to the strain at which dislocation nucleation, GB sliding, or GB migration is activated. Accordingly, all reported free volume values (FV*) in Figure 65 are also normalized, but by the appropriate initial GB free volume concentration for each GB provided in Tables 3 and 4. Therefore, for all GBs, initial FV* is equal to one and the resulting relative change in free volume during straining is displayed.

For uniaxial tension simulations, dislocation nucleation coincides with a drop in GB free volume concentration. As seen in Figure 65(a) and (b), computed free volume concentrations decrease at an approximate Strain* of 1.0. NEGB free volume evolution tends to remain closer to a relative value of unity with little change prior to dislocation nucleation, as compared to each EGB counterpart. This phenomena means that GBs accommodate dislocation nucleation by atomic rearrangement and free volume evolution. However, for the aluminum (113) EGB, a large increase in computed free volume is observed due to multiple nucleation events occurring simultaneously within the interface region. The interface region thus becomes highly distorted leading to much greater computed free volume concentration after the first dislocation is nucleated. In both copper and aluminum, the $\Sigma 9$ (221) EGB experiences a large increase in free volume prior to nucleation. This is due to the E structural unit composition of this boundary and its ability to accommodate tensile strain through dilatation.

For $\Sigma 9$ (221) boundaries under shear, grain boundary sliding is observed in both EGBs and NEGBs. GB free volume decreases during sliding. For copper (shown in Figure 65(c)), free volume decreases prior to GB sliding in both the $\Sigma 9$ EGB and NEGB**. This behavior

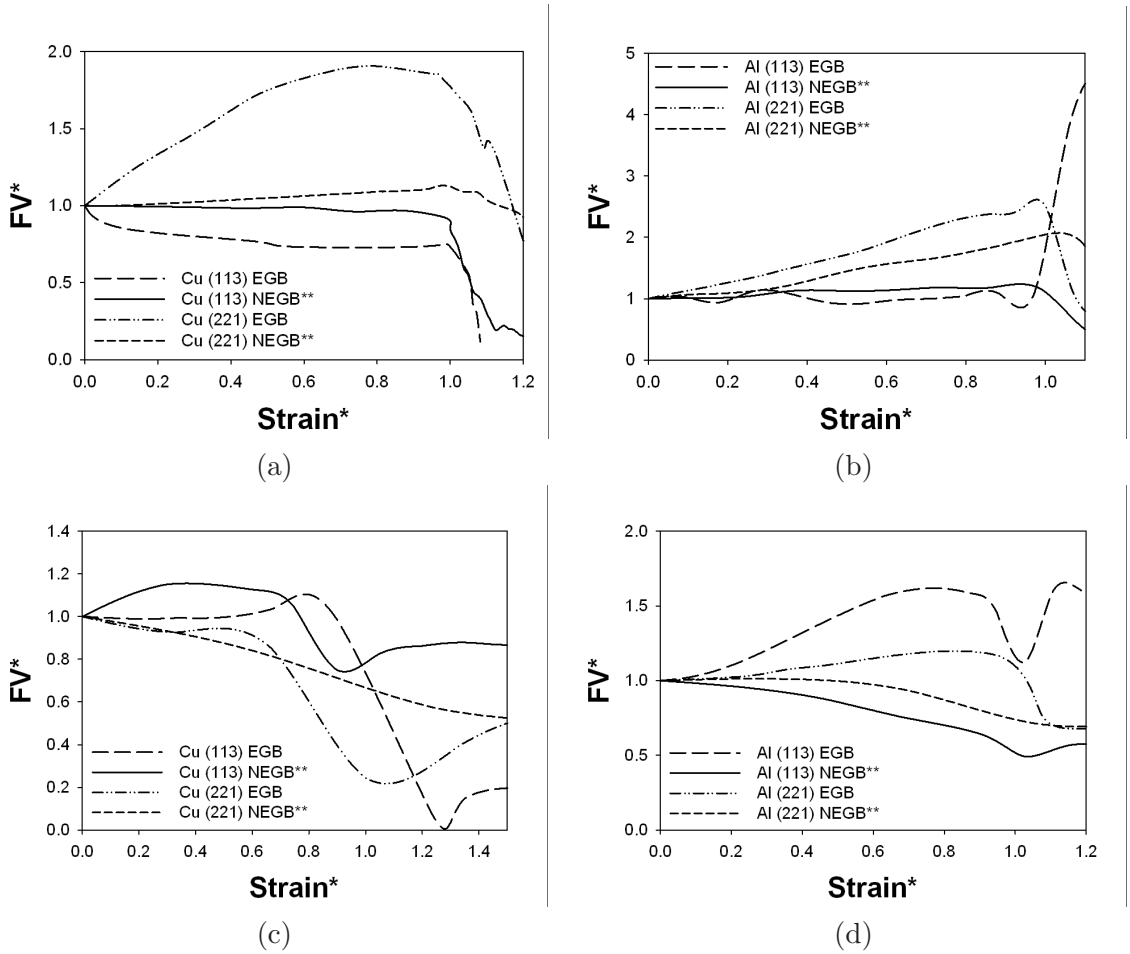

Figure 65: Free evolution as a function of strain for copper and aluminum boundaries under (a-b) uniaxial tension and (c-d) shear.

is because of local shear transformations occurring in the form of atomic rearrangements and shuffling in the boundary prior to the onset of complete boundary sliding under the application of shear. For aluminum (shown in Figure 65(d)), a slight increase in free volume is seen prior to sliding in the EGB, while free volume in the NEGB** continually decreases as is observed in the copper Σ9 NEGB**.

Free volume evolution in the Σ11 (113) GBs is more complex. Both the EGB and NEGB** in copper accommodate the imposed shear strain via GB migration. The evolution of free volume in both these boundaries differs from one another due to the atomic rearrangements activated under shear. In the EGB, a slight increase in GB free volume is observed prior to migration, while a decrease in free volume is observed in the NEGB**.

However, free volume evolution in both boundaries appears to reach a plateau after the initial instance of migration. The decrease in computed EGB free volume is due to the shear distortion of the structural units during migration, while the small change in computed NEGB** free volume is due to remaining vacancies and other defects being left behind the migrating boundary (as shown in 62(b)). In Al, the difference in the evolution of free volume for the Σ11 (113) EGB and NEGB** is mainly due to a change in deformation mechanism (as shown in Figure 61). Dislocation nucleation from the interface is observed in the EGB (61(a)) leading to a sudden decrease in free volume at a Strain* value of one, but then increases again with further imposed shear strain due to structural unit distortion within the GB. In the NEGB** (61(b)), GB migration is observed where defects are left behind the migrating boundary and significant atomic rearrangement leads to lower computed free volume. By computing interfacial free volume as a function of strain, significant insight into GB deformation and atomic processes can be obtained, and differences in accommodation behavior can be better understood.

4.4 Summary

This research has shown that representative NEGBs can be instantiated using excess free volume as an approximate measure of the degree of NE state. Excess interfacial free volume alters the structure and mechanical behavior of GBs. Bicrystalline boundaries in both copper and aluminum were investigated under uniaxial tension and simple shear to elucidate GB structural effects on deformation response for varying degrees of NE state. The GB NE state was approximated by excess free volume as compared to the near equilibrium counterpart for each boundary as previously suggested by Chuvil'deev [42]. The GB NE state increases with the addition of excess free volume, which directly influences interfacial atomic properties. This GB state corresponds to changes in initial energy, atomic structure, and free volume as well as vital changes to the deformation behavior of the boundary as compared to EGBs. It also appears from this research that the activation energy barriers for key plastic deformation mechanisms are lowered (such as dislocation nucleation, GB sliding via atomic shuffling, and migration). Collectively, this research has shown the following:

- Initial GB structure influences the efficiency of GBs as a sink for vacancies and excess free volume. Different GBs will accommodate excess free volume differently (during equilibration and energy minimization) and atomic rearrangements critical for vacancy delocalization do not occur as readily in all GBs.

- Under uniaxial tension, the peak stress (tensile strength) is lowered as a function of increasing NE state. Also, GB dislocation nucleation becomes localized in the GB as higher degrees of excess interfacial free volume are present. This is due to lower activation energy barriers required for dislocation nucleation as a consequence of higher free volume, and connected free volume packets along preferred directions promote atomic reordering necessary for nucleation.

- Under shear, resistance to GB sliding and migration decrease with excess interfacial free volume. At higher shear strains, NEGB behavior is similar to EGB behavior, and each EGB/NEGB pair exhibit nearly perfect plastic behavior. The presence of excess free volume in GBs (as compared to near equilibrium boundaries) promotes atomic shear shuffling and stress-induced atomic rearrangements at lower stresses.

To my knowledge, this work is the first to explore the effects of NE states of bicrystalline boundary structures on deformation behavior using excess free volume as an approximate measure of the NE state. Also, this research investigated the relationship between NE state and deformation behavior under both uniaxial tension and shear at 10K, and found a direct correlation between the GB state and mechanical response. Future work will include a larger parametric study of additional GBs of more general character (including various tilt/twist geometries), consider additional loading states (e.g., compression, tension/shear, and compression/shear), and investigate the temperature dependence on atomic process (e.g., shuffling and diffusion) present during both equilibration and deformation.

CHAPTER V

METRICS FOR KINEMATICS OF DEFORMATION

5.1 Introduction

Considerable progress has been made in understanding key structure/property relationships governing the mechanical behavior in many engineered materials. However, questions remain regarding behavior at the nanoscale and its relationship to larger-scaled behavior commonly observed for these materials. For example, deviation from the Hall-Petch relation [166, 87] in NC metals has recently been measured experimentally and examined computationally [39, 182, 140, 186]. Researchers have found that as grain size is reduced to the nanometer scale, inelastic deformation mechanisms accommodating plastic strain differ from those found in larger-grained PC materials. It has been suggested that intercrystalline regions such as GBs and TJs possibly serve as nucleation sites and carriers of the majority of inelastic deformation modes [274, 260, 311, 265]. However, the influence of processes such as dislocation/GB interactions, interfacial dislocation nucleation, and the onset of GB sliding and migration occurring within these structures on macroscopic material behavior is not well understood.

Since it is known that GBs and their deformation accommodation mechanisms significantly influence the mechanical behavior of NC materials [80, 112, 117, 116, 211], in recent years, tremendous efforts have been undertaken to understand and define their fundamental structure/property relationships [117, 45, 84, 288]. In NC metals, a variety of GB processes during annealing and deformation have been observed both experimentally [35, 36, 121, 124, 125] and with atomistic simulations [151, 188, 269, 262, 274, 308]. Some commonly observed GB-mediated processes include heterogeneous dislocation nucleation [125, 264, 226], GB sliding [186, 187, 260, 67], and GB migration [2, 66, 109]. Furthermore, combinations of these have been observed in NC fcc metals [269, 311, 324], and their interplay in constituting deformation accommodation in NC metals is still largely unknown.

To improve our knowledge of these types of processes, computational simulations have emerged to provide valuable insight into these events that tend to evade traditional experimental techniques. However, difficulty remains in that although dislocation mediation at a GB can be understand from an atomic perspective, the interactions of dislocation populations is well beyond the reach of most nanometer scale modeling techniques. MD simulations have the capability of probing atomic-scale behavior, such as dislocation nucleation and slip transfer reactions at interfaces in NC materials [260, 226, 188, 269], but inherently lack the ability to connect to larger-scale computational methods founded on continuum mechanics principles. There has been significant progress in the scientific community to understand these material processes and the relationships therein through the use of improved multiscale computational models [217, 26, 198, 110], but severe limitations exist in methods such as domain decomposition in exchanging dislocations between atomistic and continuum domains.

Developing a theoretical understanding of GB deformation mechanisms in NC metals is no trivial task. While atomistic simulation methods have provided insight into competing inelastic deformation mechanisms, few efforts have been made to connect these observed mechanisms to continuum theory, which would be useful for engineering analysis of material phenomena at length and time-scales beyond the limit inherent to atomistic simulations. One strategy for addressing this issue is to extract time and volume-averaged continuum measurables from atomistic simulations, which have direct implications for continuum-level theories. Accordingly, Zimmerman *et al.* [330] defined an atomic deformation gradient that is easily calculated within atomistic simulations. The research here [236, 237] builds upon the work of Zimmerman *et al.* to develop formulations for microrotation, vorticity, dilatation, and Green's strain that can also be calculated from atomistic simulation data. These efforts are useful in interpreting the kinematics of materials at the nanoscale in the context of continuum mechanics, and build upon key concepts developed by Eringen and coworkers (cf. [60]) to illuminate microscale behavior of materials. Much of Eringen's contributions are especially relevant to atomistics, as they involve nonlocal continuum theories [61] and the inter-atomic potentials used are typically non-local in nature, extending beyond

nearest-neighbor interactions.

The connection between Eringen's concepts for micromorphic materials and the atomic deformation gradient developed in [330] was noted in the recent article by Zimmerman *et al.* [331], and warrants further exploration. The objective of the current work is to investigate the inelastic deformation of GBs utilizing the nano/microscale continuum metrics developed in [236, 237, 330]. Simulations of STGBs of copper using a bicrystal interface model are performed wherein the bicrystal configuration is subject to uniaxial tension and simple shear loading conditions. Various GBs are employed under either tension or shear to activate different deformation mechanisms (e.g., dislocation emission, GB sliding, GB migration) and are subsequently analyzed with respect to these metrics for deformation and microrotation. This analysis also includes a comparison of how the microrotation varies with distance from the GB and with increasing applied strain for the various GBs.

5.2 Mathematical Methodology

5.2.1 Deformation Gradient

We now outline the methodology to estimate the deformation gradient tensor ($\mathbf{F}$), rotation tensor ($\mathbf{R}$), velocity gradient tensor ($\mathbf{L}$), and vorticity tensor ($\mathbf{W}$), so that additional kinematic metrics such as microrotation (ϕ), the vorticity vector (ω), dilatation (e), and Green's strain tensor ($\mathbf{E}$) can be formulated. Atomic strain measurements are defined from the interatomic separation distance between an atom α and its neighbor β. The deformation mapping $\mathbf{F} = \partial\mathbf{x}/\partial\mathbf{X}$ will be outlined here, with more details provided by Zimmerman *et al.* in [330]. Reference configuration quantities will be noted by upper case symbols while current configuration quantities will be lowercase, this includes all subscripts which refer to coordinate components of each quantity. Using the interatomic separation distance, $(x^{\alpha\beta})_i$, the deformation mapping of atom α and one of its neighbors β can be written as

$$(x^{\alpha\beta})_i = F_{iI}(X^{\alpha\beta})_I \tag{18}$$

However, equation (18) will not be true for all neighbors of α, so a more accurate estimation of $\mathbf{F}$ requires averaging over some finite domain incorporating multiple neighboring atoms,

a neighbor list. Therefore, summing over all neighbors ($\beta = 1...n$) and minimizing the squared errors with respect to $\mathbf{F}$, the atomic deformation gradient for each atom α is defined as a function of both reference and current interatomic spacings based on the reference configuration neighbor list, i.e.,

$$(\omega^{\alpha})_{iM} = (F^{\alpha})_{iI}(\eta^{\alpha})_{IM} \tag{19}$$

where ω^{α} and η^{α} are defined as

$$(\omega^{\alpha})_{iM} = \sum_{\beta=1}^{n}(x^{\alpha\beta})_{i}(X^{\alpha\beta})_{M} \tag{20}$$

and

$$(\eta^{\alpha})_{IM} = \sum_{\beta=1}^{n}(X^{\alpha\beta})_{I}(X^{\alpha\beta})_{M} \tag{21}$$

It should be noted that this method for estimating $\mathbf{F}$ based on nearest neighbors can be expanded to incorporate additional neighbor lists (e.g. 2^{nd}, 3^{rd}, etc.) to provide various averaging domains. This will be discussed later with accompanying details of weight functions.

5.2.2 Microrotation and Velocity Gradient

After estimating $\mathbf{F}$, the method outlined by Franca *et al.* [73] is followed to determine the right Cauchy-Green strain tensor ($\mathbf{C}$), the right stretch tensor ($\mathbf{U}$), and its inverse ($\mathbf{U}^{-1}$) in order to calculate $\mathbf{R}$. Once $\mathbf{U}^{-1}$ is calculated from this approach, $\mathbf{R}$ is determined from right polar decomposition as

$$\mathbf{R} = \mathbf{F}\mathbf{U}^{-1} \tag{22}$$

Then the skew-symmetric part of $\mathbf{R}$ ($\mathbf{R}_{skew}$), permits calculation of an associated axial vector that defines the microrotation vector, ϕ, i.e.,

$$\mathbf{R}_{skew} = \frac{1}{2}(\mathbf{R} - \mathbf{R}^{T}) \tag{23}$$

$$\phi_{k} = -\frac{1}{2}\epsilon_{ijk}(R_{skew})_{ij} \tag{24}$$

Here, ϵ_{ijk} is the permutation tensor.

We next extend this consideration to current configuration kinematic quantities, which do not rely on reference configuration neighbor lists, but rather on updated neighbor lists at each timestep. In addition to estimating lattice curvature from ϕ and its gradient, it is also instructive to calculate the vorticity or spin tensor during inelastic deformation processes. To do such, the velocity gradient tensor ($\mathbf{L}$) is calculated as a function of the instantaneous atomic velocities ($\mathbf{v}$) at each timestep, i.e.,

$$\mathbf{L} = \frac{\partial \mathbf{v}}{\partial \mathbf{x}} \tag{25}$$

Then, $\mathbf{W}$ is found by utilizing the additive decomposition of $\mathbf{L}$ into the summation of the symmetric part of $\mathbf{L}$, the rate of deformation tensor ($\mathbf{D}$), and the skew-symmetric part of $\mathbf{L}$, the vorticity or spin tensor ($\mathbf{W}$), as follows.

$$\mathbf{L} = \mathbf{D} + \mathbf{W} \tag{26}$$

Where $\mathbf{W}$ is calculated as

$$\mathbf{W} = \frac{1}{2}(\mathbf{L} - \mathbf{L}^T) \tag{27}$$

As before, a dual vector representation of $\mathbf{W}$ exists in terms of the vorticity vector (ω), given by

$$\omega_k = -\frac{1}{2}\epsilon_{ijk} W_{ij} \tag{28}$$

For our analysis, we can calculate $\mathbf{L}$ using three different approaches. First, a method analogous to that used for $\mathbf{F}$ can be employed, where equation (25) is used to define $\mathbf{L}$ in terms of the spatial atomic velocity and neighbor distances.

$$(v^{\alpha\beta})_i = L_{ik}(x^{\alpha\beta})_k \tag{29}$$

Then the sum of the squared errors is minimized, i.e.,

$$\sum_{\beta=1}^{n} \left[(v^{\alpha\beta})_i (x^{\alpha\beta})_m - (L^{\alpha})_{ik} (x^{\alpha\beta})_k (x^{\alpha\beta})_m \right] = 0 \tag{30}$$

This equation can be simplified to

$$(\rho^{\alpha})_{im} = (L^{\alpha})_{ik}(\tau^{\alpha})_{km} \tag{31}$$

where

$$(\rho^{\alpha})_{im} = \sum_{\beta=1}^{n}(v^{\alpha\beta})_i(x^{\alpha\beta})_m \tag{32}$$

and

$$(\tau^{\alpha})_{km} = \sum_{\beta=1}^{n}(x^{\alpha\beta})_k(x^{\alpha\beta})_m \tag{33}$$

Then ω can be calculated according to equations (27) and (28).

The second approach is to utilize another formulation of $\mathbf{L}$, using the material time rate of change of $\mathbf{F}$, $\dot{\mathbf{F}}$, and the inverse $\mathbf{F}^{-1}$, i.e.,

$$\mathbf{L} = \dot{\mathbf{F}}\mathbf{F}^{-1} = \frac{\partial \mathbf{v}}{\partial \mathbf{x}} \tag{34}$$

where

$$\dot{\mathbf{F}} = \frac{\partial \mathbf{v}}{\partial \mathbf{X}} \tag{35}$$

and once again minimizing the sum of the squared errors to estimate $\dot{\mathbf{F}}$.

$$(\lambda^{\alpha})_{iM} = (\dot{F}^{\alpha})_{IK}(\eta^{\alpha})_{KM} \tag{36}$$

where

$$(\lambda^{\alpha})_{iM} = \sum_{\beta=1}^{n}(v^{\alpha\beta})_i(X^{\alpha\beta})_M \tag{37}$$

and η has been previously defined in (21). Then ω can once again be calculated from equations (27) and (28).

The final approach is to calculate $\dot{\mathbf{F}}$ explicitly from the calculation of $\mathbf{F}$ in successive timesteps, i.e.,

$$\dot{\mathbf{F}} = \frac{\mathbf{F}_{current} - \mathbf{F}_{past}}{\delta t} \tag{38}$$

where δt is the time interval between the configurations used for calculating $\mathbf{F}$. Then $\mathbf{L}$ is calculated from equation (34), and ω follows from (27) and (28).

5.2.3 Strain Metrics

In addition to the common kinematic metrics used from continuum mechanics, such as **F**, **R**, **W**, **L**, and **D**, it is often necessary to calculated strain in atomistic simulations. Therefore, stemming from the derivation of the deformation gradient, Green's strain (**E**) is estimated as

$$\mathbf{E} = \frac{1}{2}\left(\mathbf{F}^T\mathbf{F} - \mathbf{I}\right) \tag{39}$$

where **I** is the identity tensor, and $\mathbf{F}^T$ is the transpose of **F**. Since **F** is computed using the defined neighbor list from the reference configuration, **E** is also a volume-averaged kinematic quantity for atom α that includes deformation history. From **E**, a scalar quantity that defines the expansion/contraction without regard to shape change can be calculated. In continuum mechanics (for small strain), this value is called dilatation (e), and is defined as

$$e = tr(\mathbf{E}) \tag{40}$$

In this thesis, both measures of strain (**E** and e) are used to understand nanoscale kinematic properties in GBs and NC materials. For the case of **E**, it will be useful in understanding the contributions to overall strain of various atomic groups or NC deformation mechanisms. The total **E** tensor is calculated for all atoms in the system, and can be resolved according to the atomic group. Furthermore, this description allows us to evolution of stored elastic strain energy in the lattice as compared to traditional strain accommodation mechanisms in NC metals, such as dislocation glide and GB plasticity.

5.2.4 Increasing the Volume-Averaging

To obtain more nonlocal information to estimate each continuum quantity, additional neighbors can be included in the calculation of each continuum quantity. However, as more neighbors are considered, the influence of each must be duly weighted. A weight function is an appropriate measure to implement in the calculations as neighbors further from the atom of interest are included. As previously outlined by Gullett *et al.* [85], the approximate form of the weight function and cutoff radius can influence the calculated results. It is therefore

vital to understand the effect of including additional neighbors on each calculation. For example, Gullett *et al.* have found that in the case of slip, neighbors not directly involved in the slip process but included in the calculation can have a distinct contribution to the calculated strain. In our calculations, as a larger cutoff distance is used and a weight function is required, our method ensures that nearest neighbors have the greatest influence in each calculation. Those neighboring atoms designated as first nearest neighbors, are given the weighting value of unity, and all other neighbors' values according to equation,

$$W(r) = \left[1 - \left(\frac{r - R_1}{R_c - R_1}\right)^2\right]^2 \tag{41}$$

In this equation, W(r) is the weight value dependent on the interatomic distance (r). R_1 is the first nearest neighbor distance and R_c is the cutoff distance.

Once W(r) is calculated for each atom, each neighbor atom's contribution to the kinematic quantity being calculated is weighted accordingly. For example, when F_{11} is being calculated with two neighbor shells, a second neighbor shell atom's influence on F_{11} will be multiplied by its W(r) value, and a first neighbor shell atom's weight will be one. A representative comparison for different neighbor sets (i.e., more nonlocal averaging) will be shown in the next chapter when the kinematic description of vorticity is calculated for dislocation emission from GBs in NC copper. As Gullett *et al.* pointed out, including more neighbors has a direct effect on the calculated values of interesting phenomena. In addition, it must be remembered that including more neighbors in the calculations must be premised on the effective range of the process under consideration.

5.3 Results and Discussion

5.3.1 Two-Dimensional Interface Deformation

Equilibrium bicrystalline GB structures were produced of 2D character. The interface structure is composed of a STGB located in the center of the simulation domain with the interface normal vector in the vertical (Y) direction and the GB period vector in the shear (X) direction. Periodic boundary conditions are employed for the X-direction, parallel with the GB, but not in the vertical (Y) direction. Free surfaces thus formed in the Y-direction

are constrained such that all atoms located within a specified distance from each free surface are forced to move as a rigid group (free from interatomic interactions) in the X-direction during shear loading as displayed in Figure 66.

The interatomic potential used in the 2D simulations is a modified Lennard-Jones potential that has been shifted and truncated so that the potential energy and its first derivative are zero at the specified cutoff distance of 7.6364Å . The important parameters are the atomic mass (196.97 amu), the finite distance at which the potential is zero (σ=3.63638Å), and the depth of potential (ϵ=1.5726 eV). These parameters lead to a lattice parameter of 4.08Å and cohesive energy of -3.93eV. Minimum energy configurations were calculated using a conjugate gradient method in LAMMPS [167] using a relative energy convergence criteria of 10^{-25}. After energy minimization, each simulation cell was then allowed to equilibrate at 10 K for 10 ps. In the simulations, the time step used was 1 fs and all atomic dynamics simulations were performed in the microcanonical ensemble (NVE).

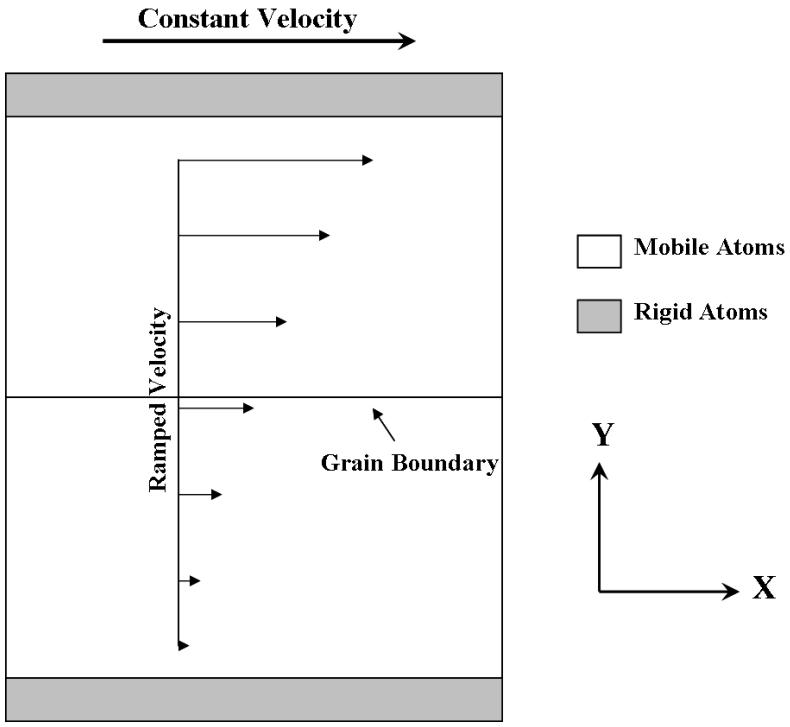

Figure 66: A 2D schematic of the simulation cell and conditions for prescribing simple shear.

To apply shear, the lower rigid atomic region containing all atoms within three times

the potential cutoff distance of the bottom free surface is held fixed, and the upper rigid atomic region is prescribed a constant velocity in the shear X-direction. This velocity superimposes on temperature induced fluctuations. Because of the inherent high strain rate condition of atomistic simulations, a linearly ramped velocity field is also prescribed to each atom located between the upper and lower rigid regions to alleviate possible shock wave generation [98, 49]. As shown in Figure 66, atoms located near the lower rigid region are given an additional velocity value close to zero and those near the upper region are given values near to the shear velocity. The applied shear velocity corresponds to an approximate shear strain rate of $10^8 s^{-1}$, where shear strain is defined as $\gamma = arctan(l/d_o)$. In this equation, l is the shear displacement, or relative displacement of the upper boundary to the lower boundary in the X-direction, and d_o is the vertical distance between the lower and upper rigid atomic regions.

Three different symmetric tilt bicrystalline structures were used in the 2D shear analysis. Each structure is approximately 300Å x 300Å containing around 7,000 atoms with a varying disorientation (minimum misorientation) angle (Ψ). The resulting equilibrium structures are shown in Figures 67(a-c), colored according to potential energy (eV), and it is clear that the atomic structure composing each bicrystal varies with Ψ. The three different Ψ values are 9.4°, 15.2° and 27.8°. Each structure displays a different mechanical response under shear. The deformation mechanisms are grain boundary migration, sliding, and dissociation respectively, and it is clear from Figures 67(d-f) that a unique deformation field accompanies each mechanism, and that only the migration mechanism preserves the initial grain boundary structure. These results show the relationship between structure and mechanical behavior, and suggest the influence of atomic interface composition on deformation. These three 2D symmetric tilt bicrystal grain boundaries were chosen because each displayed a unique deformation mechanism.

To gain additional insight into the shear deformation behavior of these boundaries and obtain more useful information, the previously outlined continuum quantities were calculated for each structure. Since **F** is a deformation mapping formulated using the reference neighbor list calculated in the initial reference configuration (0% strain), a sense of path

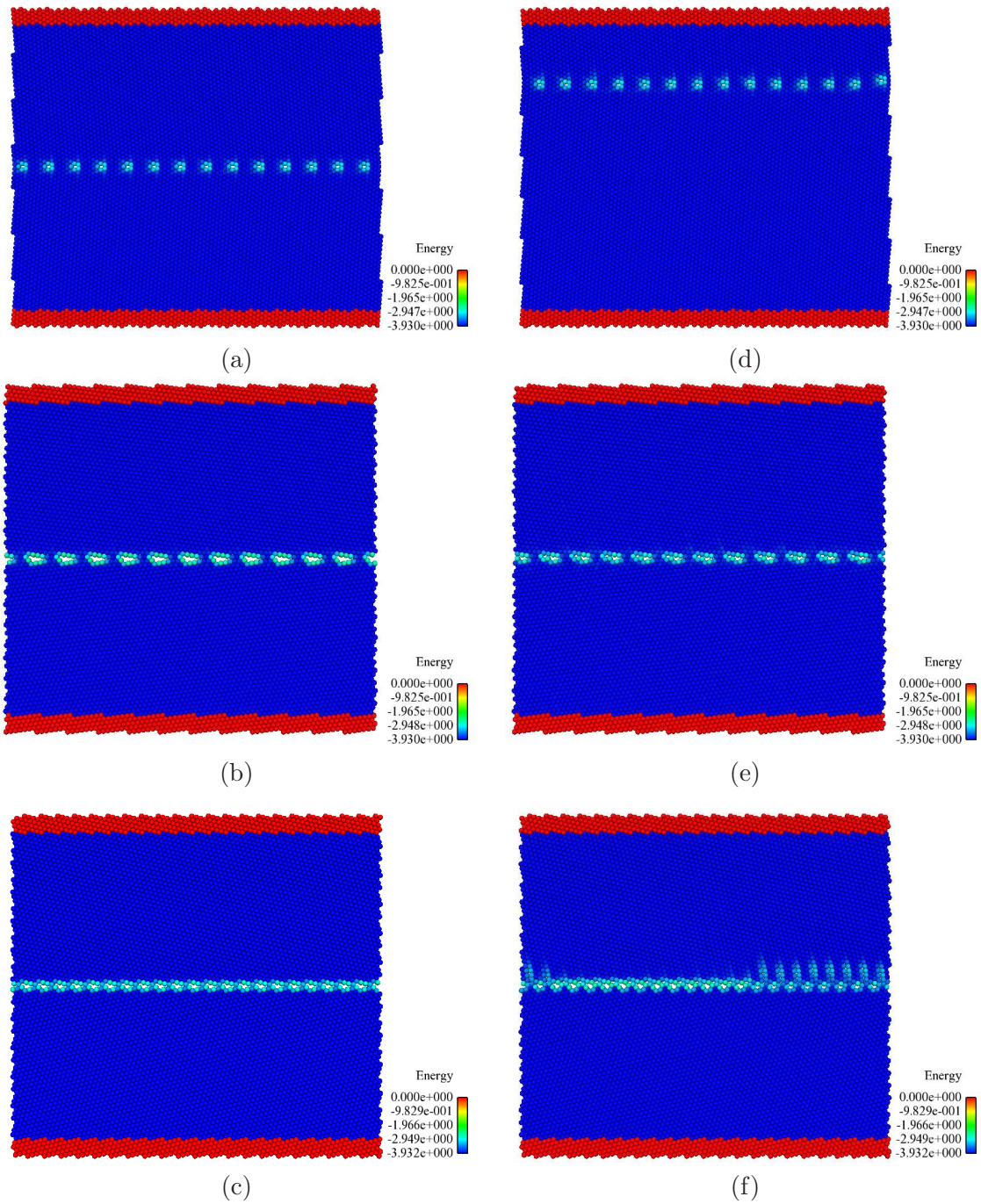

Figure 67: Initial grain boundary structures for (a) $\Psi = 9.4°$, (b) $\Psi = 15.2°$, (c) $\Psi = 27.8°$, and after approximately 5% shear strain in (d), (e) and (f), respectively. Atoms are colored according to their potential energy (eV).

dependence or path history is found by calculating components of $\mathbf{F}$ for all atoms with the simulation domain. For example, in the grain boundary migration mechanism, Figure

67(a) and 67(d) have shown that the initial defect atomic structure composing the grain boundary is preserved after boundary migration at 5% shear strain. Accordingly, Figure 68 shows F_{12} and F_{11} calculated from first nearest neighbors only, and it is shown that these components of $\mathbf{F}$ provide detailed information concerning the deformation path of atoms traversed by the migrating grain boundary. Although atoms located within the red-colored region in Figure 68(a) currently reside in their equilibrium lattice positions, the deformation gradient captures some degree of their deformation history. This region has undergone lattice rotation as a consequence of the migrating grain boundary, so that the orientation vectors of this lattice region now correspond with those describing the lower lattice region before migration. The relatively constant F_{12} value for these atoms results from similar horizontal shifts with regard to vertical position after boundary migration.

Figure 68(b) shows F_{11} for the grain boundary migration mechanism, this image varies from 68(a) because it displays a different component of $\mathbf{F}$. However, atoms traversed by the interfacial defect structures show a different F_{11} value than those atoms located between the defect structure migration path. Therefore, atoms directly involved in the defect structure migration undergo a larger shift with regard to the horizontal direction. This difference is seen in the highlighted migration paths of Figure 68(b). The stress-driven mechanism of grain boundary migration outlined here also suggests that coupled shear behavior detailed by Cahn *et al.* [29] exists in this boundary. The migration paths in Figure 68(b) show that a small tangential translation of the upper lattice with respect to the lower lattice occurs during shear deformation.

Figure 69 shows F_{12} and F_{11} for grain boundary dissociation, this deformation mechanism differs from the grain boundary migration results shown in Figure 68 leading to the conclusion that as the mechanism changes, so does the resulting deformation field. In Figure 69(a), lattice regions where dissociation has occurred show higher F_{12} values. Atoms located within first nearest neighbor distances of these dissociation regions experience a notable change in position relative to their reference neighbors regarding vertical position, leading to a higher calculated F_{12}. Figure 69(b) shows F_{11} for the dissociation mechanism,

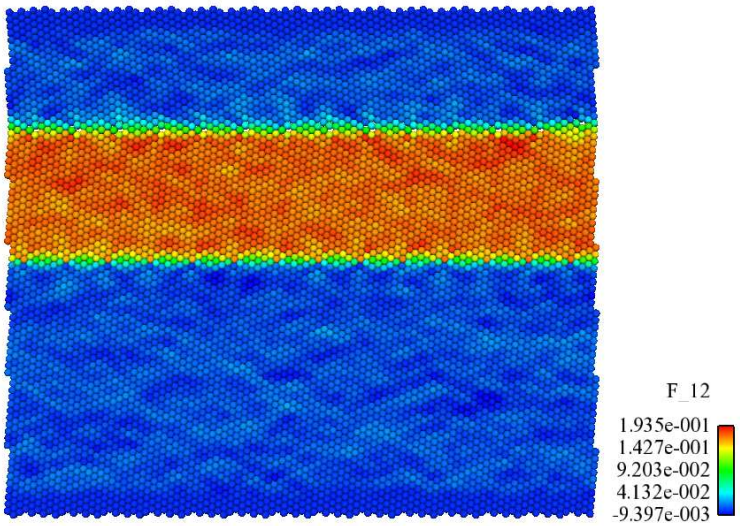

(a)

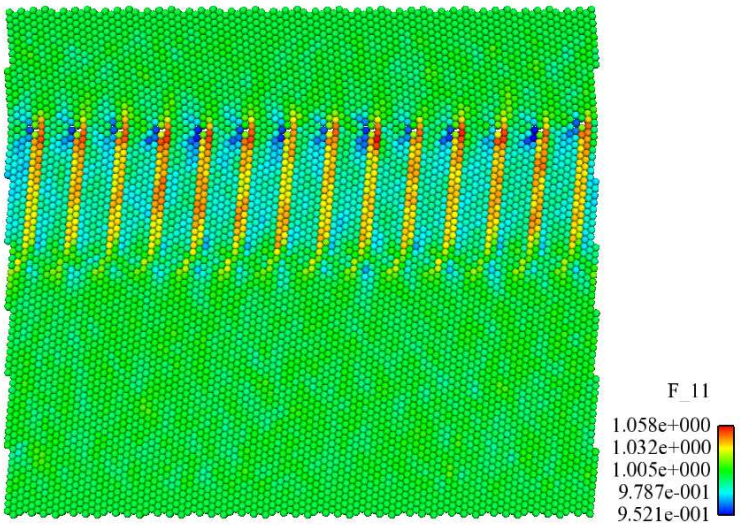

(b)

Figure 68: (a) F_{12} and (b) F_{11} calculated for grain boundary migration ($\Psi = 9.4°$) at approximately 5% shear strain.

and it is clear that atomic movement within the dissociation regions does not produce significant changes in horizontal position relative to the initial configuration. These examples show that calculating **F** for atoms during deformation provides some insight into the path history of the atomic configurations.

Figure 70(a-b) display F_{12} and F_{11} calculated for grain boundary sliding, and it is clear

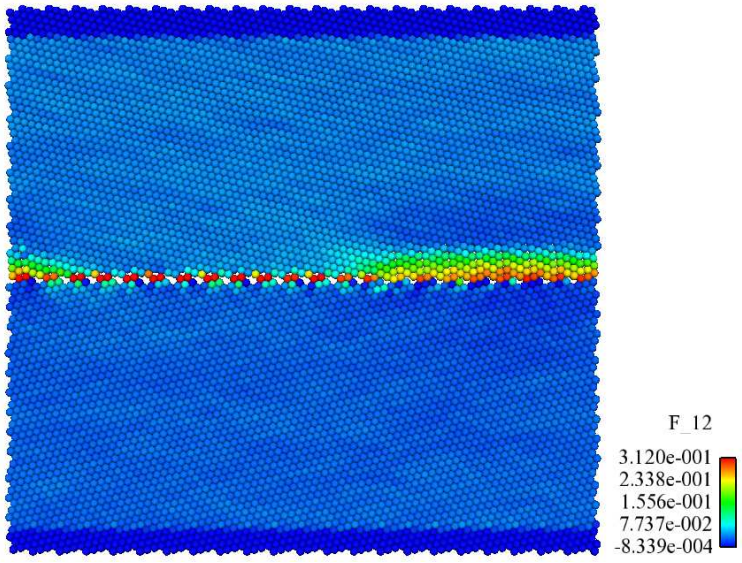

(a)

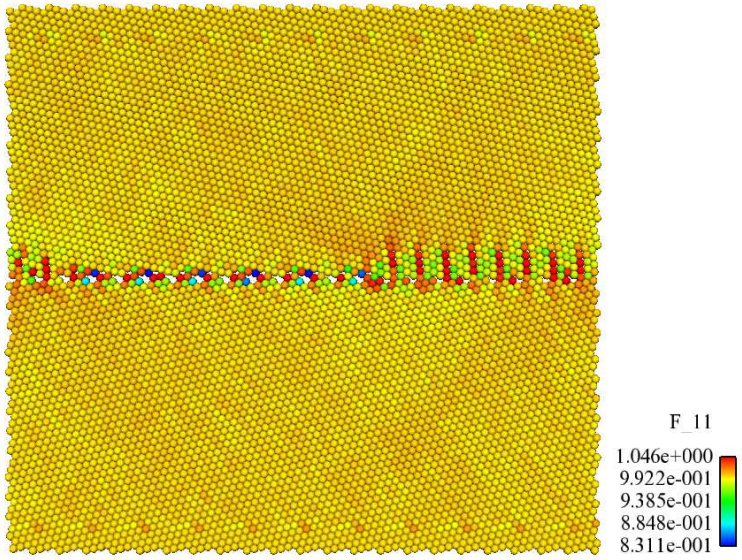

(b)

Figure 69: (a) F_{12} and (b) F_{11} calculated for grain boundary dissociation ($\Psi = 27.8°$) at approximately 5% shear strain.

that this deformation mechanism differs from the others with regard to the extent of lattice deformation. This mechanism produces limited deformation into the lattice apart from that contained at the boundary; therefore, further analysis of this boundary and deformation mechanism will be ignored in this work.

Calculating additional continuum quantities such as lattice curvature can also provide

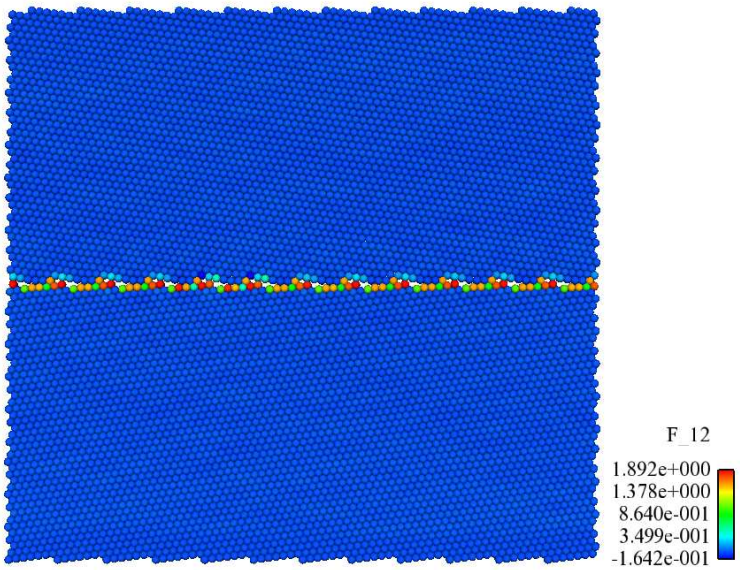

(a)

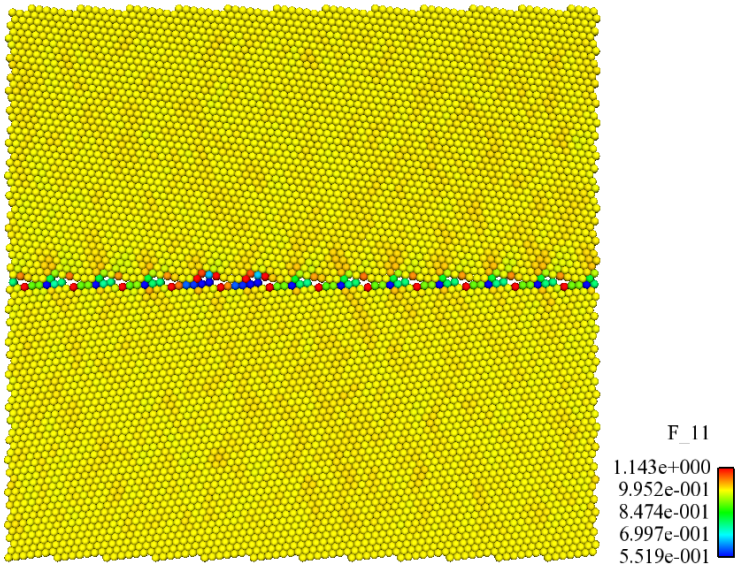

(b)

Figure 70: (a) F_{12} and (b) F_{11} calculated for grain boundary sliding ($\Psi = 15.2°$) at approximately 5% shear strain.

useful insight into atomic behavior during grain boundary plasticity. According to equation (24), components of the microrotation vector are calculated for each mechanism. Figures 71(a-b) show ϕ_3 for the migration and dissociation mechanisms, respectively.

In both cases, the calculation of ϕ_3 shows atomic microrotation fields accompanying each mechanism. In (a), there are two clear regions of microrotation, the migration path of

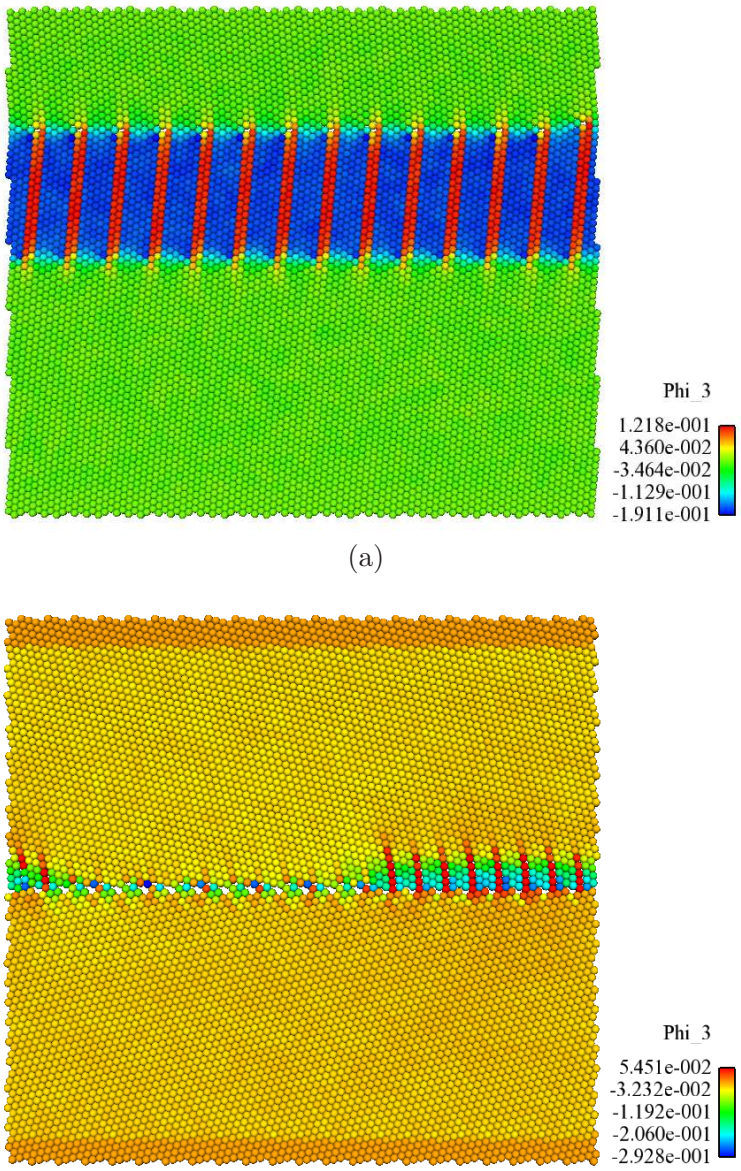

Figure 71: ϕ_3 for (a) grain boundary migration ($\Psi = 9.4°$) and (b) grain boundary dissociation ($\Psi = 27.8°$) at approximately 5% shear strain.

the boundary defect structures (colored red) and the regions between these paths (colored blue), where atoms within each region have opposite microrotation values. In (b), regions where dissociation has occurred coincide with high microrotation magnitude; however, the value is of opposite sign on either side of the dissociation. In addition, it is noted that smaller microrotation is experienced by atoms located within the boundary even where

dissociation has not occurred, and their microrotation value is approximately that of some atoms within the dissociation regions.

Vorticity is an additional metric used to gain insight into the deformation behavior of material substructures. Since vorticity is a measure of instantaneous atomic behavior, the current atomic velocities along with an updated neighbor list is used for all vorticity calculations. After calculating ω_3 with each approach, we have come to the following conclusions as the results of each approach give varying information.

The first approach contains much more calculated noise than the other two methods and no apparent vorticity fields around the grain boundary dissociations. We speculate the source of the noise is due to utilizing two correlated atomic properties that vary with time in the method, $\mathbf{v}$ and $\mathbf{x}$. The effect of this correlation could enhance thermal contributions to the velocity gradient calculations using instantaneous atomic velocities. The second and third approaches offer much smoother vorticity fields, but also differ from each other substantially. Calculated atomic vorticity values in the second approach (Figure 72b) are much greater than both methods 1 and 3, and both methods 2 and 3 capture vorticity fields near the leading and trailing edges of the dissociations. Additionally, method 2 only uses one atomic property that varies in time, $\mathbf{v}$. Method 3 provides very clear vorticity fields in regions surrounding the dissociated planes and their intersection with the grain boundary plane. We postulate that the reason for many of the disparities in the images shown in Figure 72 is the two-dimensional nature of these boundaries. In these two-dimensional structures, the number of neighbors is small; therefore, as compared to three-dimensional systems, the number of atoms contributing to the averaging is limited. As we see later, when full three-dimensional boundaries are considered, Method 1 (as used throughout this thesis) provides very good kinematic information about atomic vorticity fields that emerge during deformation.

5.3.2 Three-Dimensional Interface Deformation

Three-dimensional STGBs were created as bicrystal interfaces for this study. To obtain the proper GB structures, two distinct crystal lattices, symmetrically rotated around a

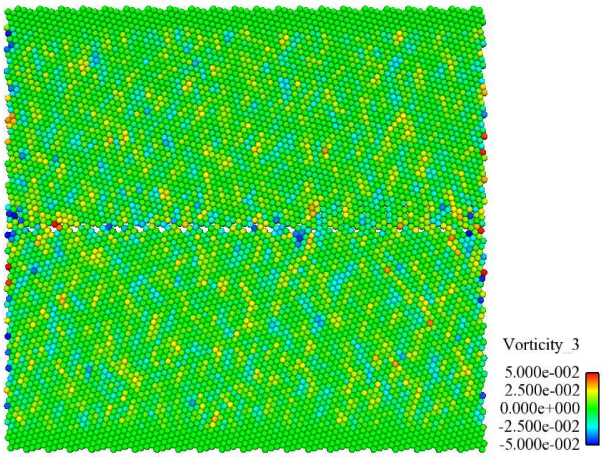

(a)

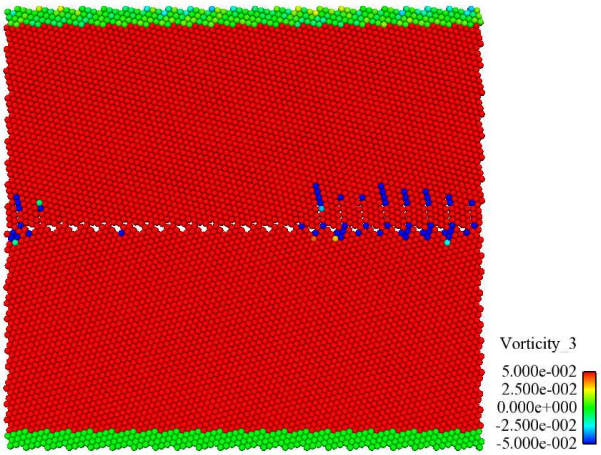

(b)

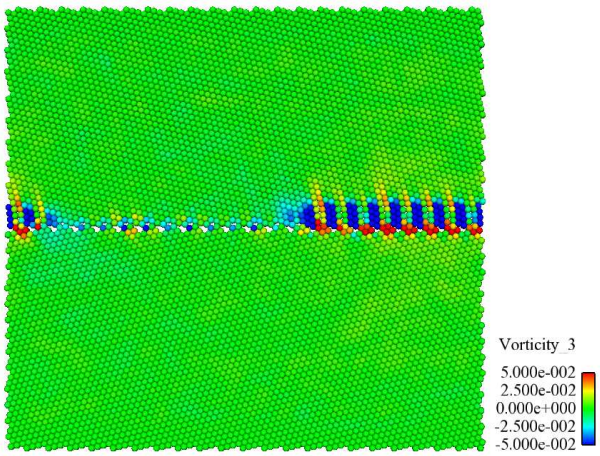

(c)

Figure 72: ω_3 calculated with the (a) first, (b) second, and (c) third approaches for the grain boundary dissociation mechanism ($\Psi = 27.8°$)

common tilt axis ($\langle 001 \rangle$ or $\langle 110 \rangle$), were separated by a planar STGB with its normal in the Y-direction, tilt axis in the Z-direction, and GB period in the X-direction. Using MS employing an EAM potential for copper [150] and 3D periodic boundary conditions, initial minimum energy GB structures were determined. The initial GB structures were consistent with previous computational studies [180, 184, 207, 230]. Then MD simulations were performed to achieve thermal equilibration at 10 K under NPT for at least 10 ps. The resulting bicrystalline simulation cell dimensions were approximately 16nm x 32nm x 16nm, containing at least 700,000 atoms.

To investigate deformation mechanisms, two different methodologies were implemented to impose uniaxial tension and simple shear. For uniaxial tension (Figure 6, a constant strain rate ($10^9 s^{-1}$) deformation was applied in the Y-direction (perpendicular to the GB plane) under NPT at 10K. Three-dimensional periodic boundary conditions were maintained, while simulation cell stresses along the lateral bounds were allowed to relax to zero stress. Simulations continued until 1-2% tensile strain beyond maximum tensile stress and after significant GB deformation (i.e., leading partial dislocation nucleation) occurred.

In shear (Figure 7, periodic boundary conditions were maintained in the X and Z-directions (parallel to GB plane), but constrained surfaces were imposed normal to the GB plane (Y-direction). As performed for 2D simulations, atoms located within three times the potential cutoff distance from either the top or bottom surface (normal to the Y-direction) were held fixed in their fcc lattice positions and confined to move as rigid groups. All atoms located between these two rigid atomic groups were mobile in the MD simulations, while atoms belonging to either rigid group were not. This constraint imposed interatomic forces on neighboring mobile atoms, and suppressed the influence of free surfaces on mobile atom behavior. Next, a constant velocity in the X-direction was applied to the top rigid group, while the bottom rigid group was held fixed in all directions. However, due to the small time-step of MD (1 fs) used and large value of velocity applied to the top group (corresponding to a $10^9 s^{-1}$ constant strain rate) , a linearly ramped velocity field was also applied to all mobile atoms to reduce the possibility of shock wave generation [98, 49].

Commonly observed deformation mechanisms in NC metals (e.g., dislocation nucleation,

GB sliding and migration) are examined in this work using microscale continuum metrics. Different copper STGBs are deformed at a constant $10^9 s^{-1}$ strain rate, either perpendicular (tension) or parallel (shear) to the GB plane. Both uniaxial tension and simple shear deformation are employed in this work to activate different deformation mechanisms: dislocation nucleation, GB sliding, and GB migration.

5.3.2.1 Dislocation Nucleation

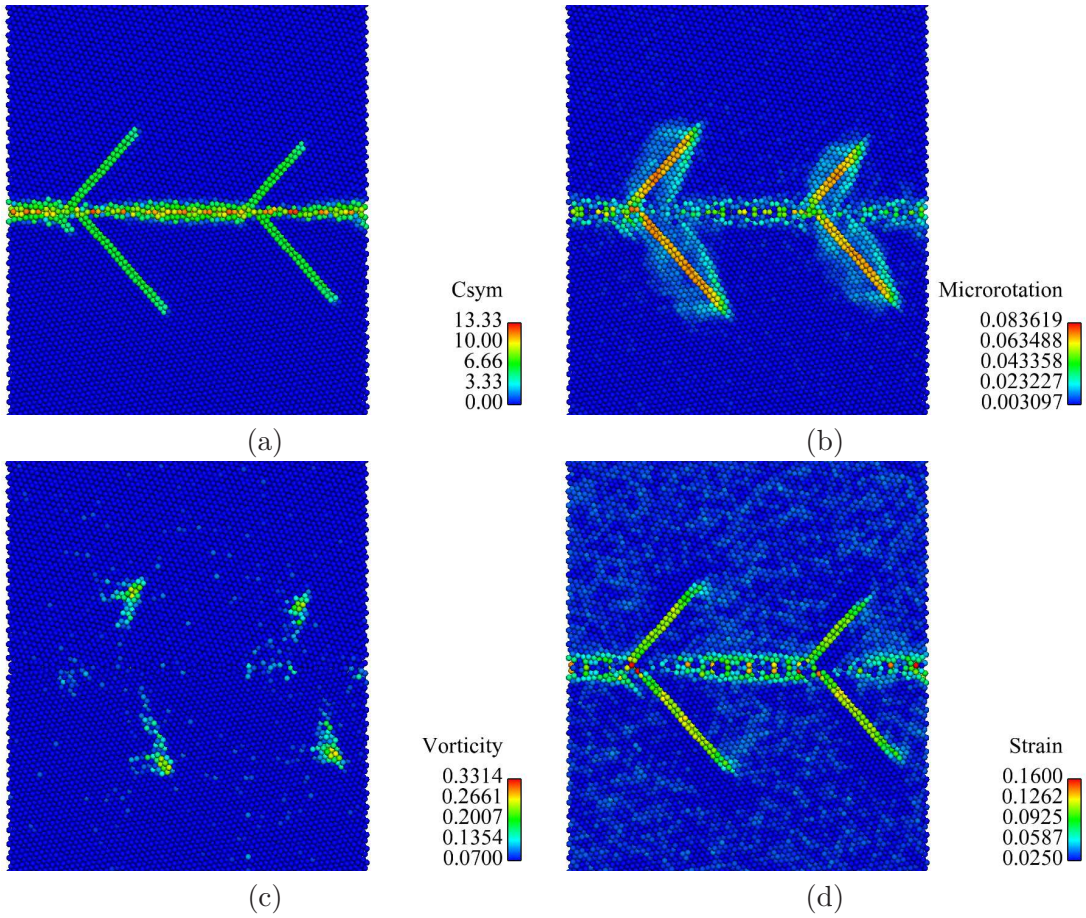

Figure 73: Contour plots showing (a) centrosymmetry, (b) microrotation, (c) axial vector, and (d) e viewing along $\langle 110 \rangle$ for the $\Sigma 5$ (310) boundary under uniaxial tension at approximately 8.8% strain. At this strain, partial dislocations have been nucleated from the GB into both the upper and lower lattices, connected to the interface by a stacking fault. Notice that each metric provides different information regarding dislocation nucleation and deformation accommodation in both the lattice and GB.

To investigate dislocation nucleation under uniaxial tension, the $\Sigma 5$ (310)$\langle 001 \rangle$ $\theta = 36.9°$ STGB is used, where (310) designates the GB plane normal, $\langle 001 \rangle$ is the tilt axis, and the

symmetric misorientation angle is 36.9°. At approximately 8.7% tensile strain, partial dislocations nucleate from the GBs into both lattices. Shown in Figure 73 is a series of snapshots of contours based on (a) centrosymmetry, (b) microrotation, ϕ, (c) axial vector, $\mathbf{w}$, and (d) the first invariant of the strain tensor ($\mathbf{E}$), e, viewing along $\langle 110 \rangle$ just after maximum tensile stress (8.8%). For uniaxial tension, the simulation setup shown in Figure 6 is followed.

Figure 73(a) shows partial dislocations nucleating from the GB into the lattice during uniaxial tension. Boundary regions adjacent to the nucleation sites also undergo deformation, but do not nucleate/emit dislocations. Each microscale continuum metric offers additional information concerning this deformation. In Figure 73(b), rendering of microrotation shows that the effect of dislocation slip extends outside the partial dislocation and trailing stacking fault. Distinct microrotation fields are apparent for the stacking fault and nearby lattice regions, while the GB shows no clear microrotation fields. The average atomic microrotation (considering first nearest neighbors only) for the stacking fault is approximately 0.07, while in lattice regions adjacent to the emitted partial dislocation and stacking fault, atomic microrotation ranges between 0.003 and 0.03. However, no atomic slip occurs in these regions. Additionally, GB regions near the nucleation site display no comparable levels of microrotation as that calculated along the stacking fault.

Figures 73(c)-(d) show the axial vector, $\mathbf{w}$, and the first invariant of strain (e) calculated at 8.8% uniaxial strain. In 73(c), it is apparent that $\mathbf{w}$ captures the current deformation at the leading partial dislocations, while no fields emerge in other lattice or GB regions. This is primarily due to the dependence of $\mathbf{w}$ on instantaneous atomic velocities and neighbor lists in the current (spatial) configuration. Figure 73(d) displays an estimate for atomic dilatation, e, for dislocation nucleation in the $\Sigma 5$ boundary. This metric shows that atoms involved with dislocation nucleation and slip constitute the majority of calculated strain. However, scattered interfacial regions also exhibit high values of e, meaning that GB reordering and shuffling during dislocation nucleation is captured by e and is relevant to understanding strain accommodation in GBs. GB atomic structures (i.e., structural units)

with greater free volume promote reordering and shuffling events. Therefore, during dislocation nucleation, higher free volume GB regions not directly involved in nucleation also demonstrate noticeable strain.

5.3.2.2 Grain Boundary Sliding

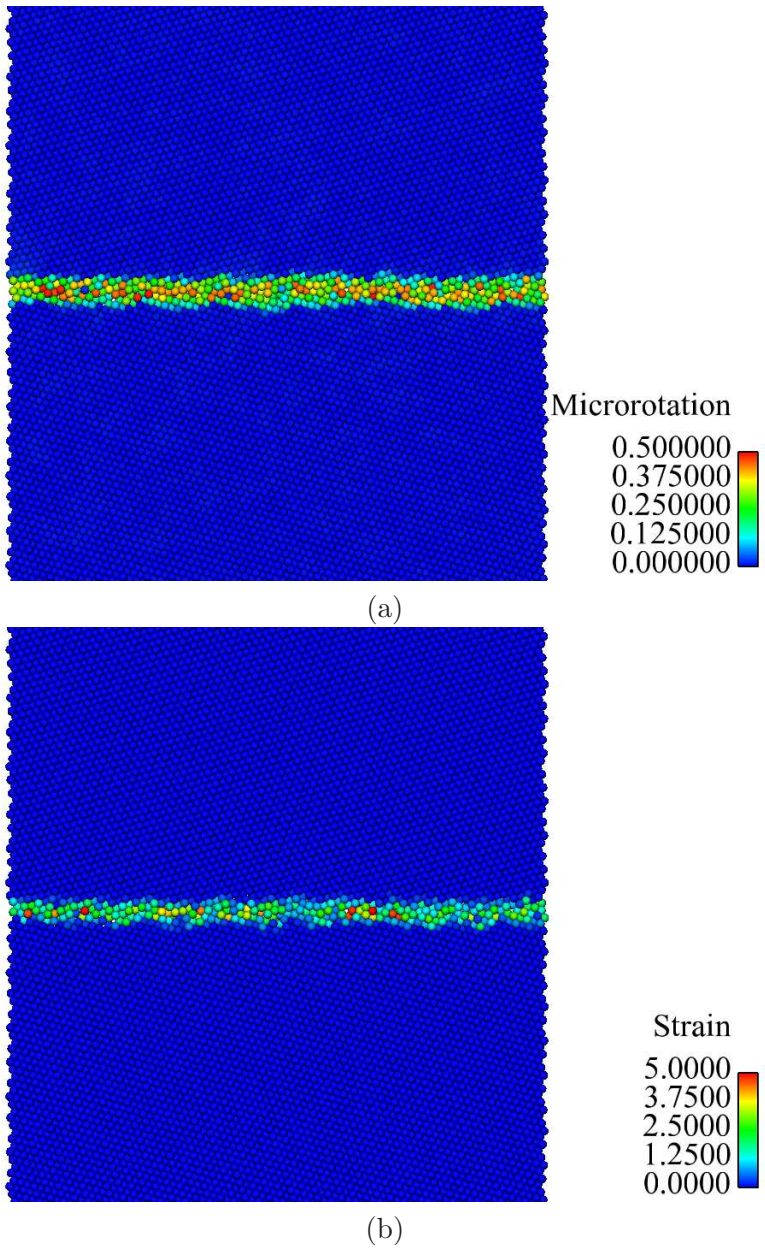

Figure 74: Contour plots showing (a) microrotation and (b) e viewing along the $\langle 110 \rangle$ tilt axis for the $\Sigma 9$ (221) boundary at approximately 6.0% shear strain. Each plot shows that GB sliding has been activated at this imposed strain and deformation is confined to the GB region.

To investigate GB sliding, the Σ9 (221)⟨110⟩ $\theta = 141.1°$ copper boundary is deformed under simple shear. At approximately 4.5% shear strain, the peak shear stress (2.1 GPa) is reached activating GB sliding. Once this critical shear stress is reached, the GB continues to deform via sliding with further imposed shear. Figure 74 shows (a) microrotation and (b) strain (e) for the Σ9 (221) copper boundary under shear at approximately 6.0% strain. At this strain, the Σ9 boundary deforms in a near perfectly plastic manner via GB sliding. The shear deformation of this boundary was investigated in previous work [236]. In that work, the periodic simulation cell length along the tilt axis (Z-direction) was about 0.5nm, but in the current investigation it has been lengthened to about 16nm. Both dislocation nucleation and GB sliding were observed during shear in [236]; however, only GB sliding is observed in the current investigation. Therefore, the observed deformation mechanism(s) in this boundary depends on the simulation cell dimensions.

A possible reason for this disparity in the observed deformation mechanism is that certain atomic structural units have a 3D character. This is important when configurations with small periodic lengths in the tilt axis are considered, because the full character of the structural units might not be sufficiently sampled. Also, for dislocation nucleation to occur, a critical resolved shear stress value must be reached on the activated {111} slip plane in the slip direction. Previous results [207, 230] show that the E structural unit does indeed influence the dislocation nucleation stress under uniaxial tension from the Σ9 boundary due to atomic structure and interfacial free volume. However, under shear, the higher free volume E structural units might induce GB sliding at lower resolved shear stress in larger periodic structures prior to the activation of dislocation nucleation from the interface. For this boundary, images showing contours of additional metrics (e.g., $\mathbf{w}$) do not present any substantial or interesting behavior; therefore, they are not included in Figure 74. Shear deformation is imposed using the setup shown in Figure 7.

All significant deformation in the Σ9 (221) boundary, shown in Figure 74, exists entirely within the GB region during GB sliding. However, certain boundary regions show higher microrotation, while other regions show greater e. Sansoz and Molinari [183, 184] have previously shown that atomic shuffling is prevalent during shear for this Σ9 boundary,

and point to the importance of particular interface structural units when interpreting shear deformation behavior. For the Σ9 (221) boundary, atoms showing the greatest microrotation in Figure 74(a) are those located within these high free volume structural units. Such units may be locations where atomic shuffling processes initiate, eventually resulting in GB sliding. Calculated e values for these same GB regions do not show a similar trend (Figure 74(b)). The calculated e for each atom estimates the local volume expansion of the lattice without regard to shape change of the local neighborhood. Although atoms with the greatest dilatation are located within high free volume interfacial regions, they do not necessarily possess high microrotation as well. This indicates that consideration of multiple metrics is necessary to gain a complete picture of the kinematics that occur at and near the GB.

5.3.2.3 Grain Boundary Migration

The Σ3 (111)⟨110⟩ $\theta = 109.5°$ coherent twin boundary (TB) and the Σ129 (881)⟨110⟩ $\theta = 169.9°$ boundary are investigated to explore the deformation response during GB migration under shear. These two boundaries are studied because their migration mechanisms differ. The Σ3 (111) TB migrates via the glide of twinning disconnections [8, 93] along the twin boundary plane, while the Σ129 (881) behavior is dictated by the migration of the GB dislocation cores (with translation as well as migration components parallel and normal to the boundary plane, respectively, as discussed by Cahn *et al.* [29]). Twinning disconnections contain both dislocation and step character [93]. They glide along the twin boundary, resulting in twin migration normal to the plane. These differences in the boundary migration behavior are captured using microscale continuum metrics in post-processing, averaged over a nonlocal atomic neighborhood. By employing reference neighbor lists, microrotation and e contours shown in Section 3.3.2 provide a detailed rendering of the GB dislocation core paths (both translation and migration) during shear deformation, while F_{12} shows the atomic deformation within the lattice region traversed by the migrating boundary. To impose shear on both the Σ3 and Σ129 boundaries, the methodology shown in Figure 7 is used.

5.3.2.4 Σ3 (111) Coherent Twin Boundary

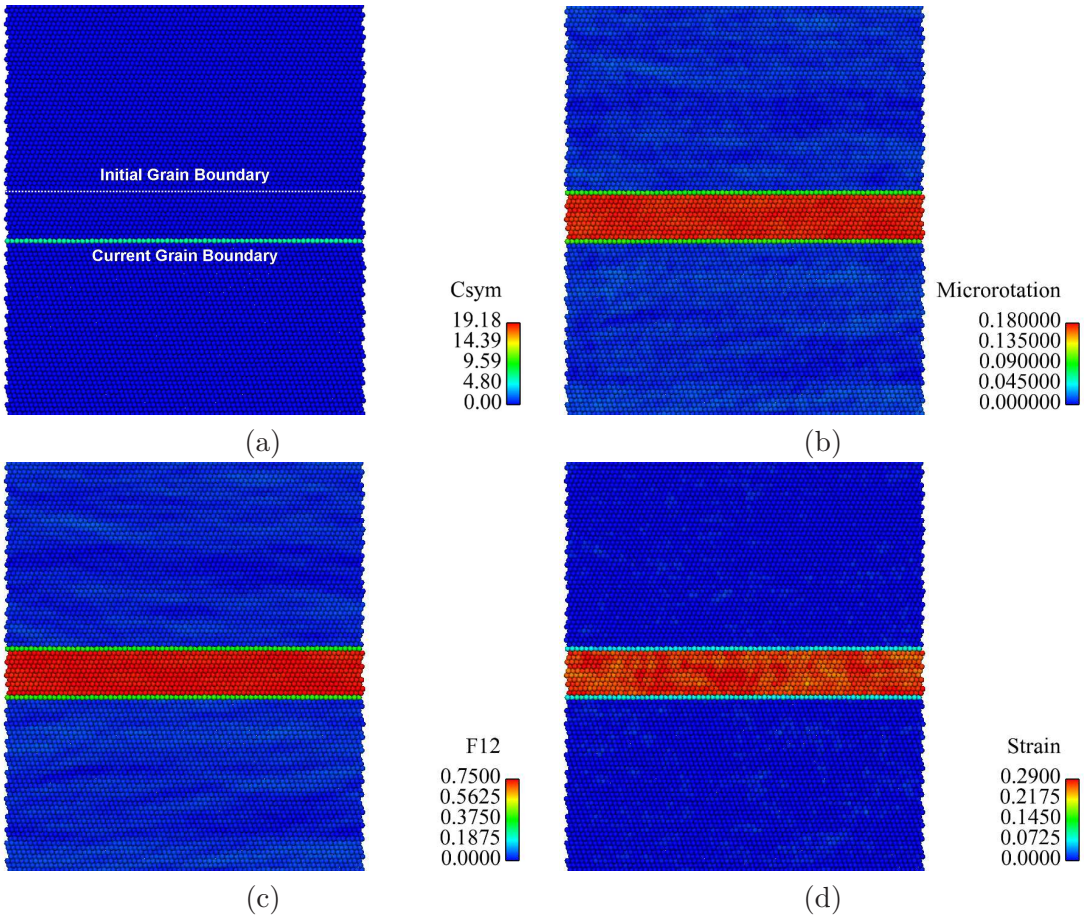

Figure 75: Contour plots showing (a) centrosymmetry, (b) microrotation, (c) F_{12}, and (d) e viewing along the $\langle 110 \rangle$ tilt axis for the Σ3 (111) coherent TB at approximately 11.0% shear strain. In (a), the original GB location is shown by the dashed white line. During shear deformation the GB migrates perpendicular to its plane to the current location shown in (a).

Under shear, the Σ3 (111) boundary migrates in a direction perpendicular to the GB plane as shown in Figure 75(a). The peak shear stress occurs at approximately 9.5% shear strain coinciding with the onset of GB migration normal to the GB plane. During GB migration, regions traversed by the migrating GB undergo rotation, so that the new lattice orientation vectors of this region correspond to those in the upper lattice. The resulting microrotation estimate is provided in Figure 75(b), F_{12} in 75(c), and e in 75(d). Each contour plot in Figure 75 corresponds to 11% shear strain, but migration continues at higher strains as well.

For each metric calculated in Figures 75(b)-(d), the lattice region traversed by the migrating boundary is visible. The calculated values for each metric are relatively constant within this lattice region. The deformation of each atom within this region relative to its neighbors is similar and is not a function of position, as shown in 75(b)-(d). In other words, the deformation of each atom relative to its nearest neighbors is similar for all atoms traversed by the migrating boundary, indicating a relatively uniform atomic deformation mechanism underlying GB migration in this boundary. For the Σ3 (111) boundary, the dislocation loop mechanism is observed to lead to migration. However, this same mechanism is not always active for migrating GBs. For example, the Σ129 (881) boundary is a low-angle boundary (disorientation angle is 10.1°), and the dislocation core structures have definite paths through the traversed lattice region.

5.3.2.5 Σ129 (881) Grain Boundary

GB migration is activated in the Σ129 (881) boundary at approximately 1.8% shear strain. Figure 76(a) displays both the original (dotted white line) and current GB location. The metrics used to produce the images shown in 76(b)-(d) correspond to those in Figure 75(b)-(d). However, in Figure 76(b) and (d), the migration path of each dislocation core is evident, while no such pattern is seen in the migration of the Σ3 coherent TB in Figure 75.

Figure 76(b) shows the microrotation for the Σ129 (881) GB, and the paths of the dislocation core structures display lower microrotation than the majority of atoms not directly traversed by the migrating dislocation core structure. This indicates that the deformation of the neighboring fields of these atoms varies with respect to other nearby atoms. Figure 76(c) shows F_{12}, and once again, a relatively uniform deformation field is observed as was seen for the Σ3 (111) boundary. However, e also shows the migration path of the dislocation cores, and atoms lying between these migration paths show no calculated strain (e). This is again in contrast to the results of the Σ3 (111) boundary (Figure 75(d)), where no spatial variation of e emerged.

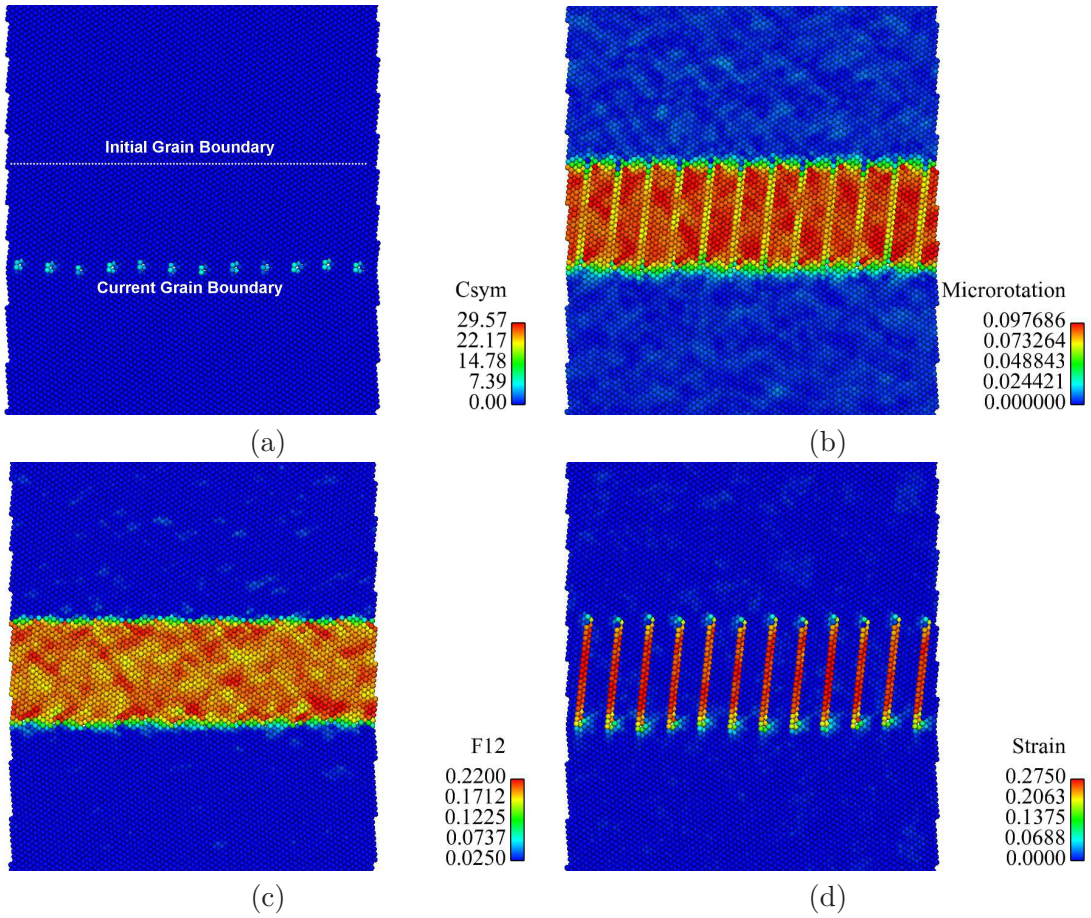

Figure 76: Contour plots showing (a) centrosymmetry, (b) microrotation, (c) F_{12}, and (d) e viewing along the $\langle 110 \rangle$ tilt axis for the $\Sigma 129$ (881) boundary at approximately 3.5% shear strain. In (a), the original GB location is shown by the dashed white line. During shear deformation the GB migrates perpendicular to its plane to the current location shown in (a).

5.3.2.6 Microrotation Comparison

Although atomic-scale deformation is complex, the microscale continuum metrics (e.g., deformation gradient, microrotation, vorticity, and strain) utilized in this work offer additional and sometimes complementary insight into atomic deformation behavior. Figures 73, 74, 75, and 76 show that microrotation provides distinct information regarding the deformation history of each atom. Moreover, as clearly highlighted in Section 3.3 on GB migration, microrotation renders clear deformation paths based on current atomic quantities relative to reference configuration neighbor lists [236]. To further evaluate microrotation, Figure 77 shows the distribution of average atomic microrotation as a function of distance from

the original GB location (GB_o) for increasing strain, where blue strain labels in 77(a), (b), (c), and (d) mark the corresponding strain for contours shown in Figures 73, 74, 75, and 76, respectively. To determine average microrotation in the vicinity of the GB, atoms within 20Å on either side of GB_o are considered during straining. Average microrotation is then calculated per atomic layer (perpendicular to the GB plane), where each layer is approximately 2Å thick. This thickness value provided accurate estimations of average microrotation while preserving computational efficiency. It is important to remember that lattice regions on both sides of GB_o are included in the average microrotation calculation.

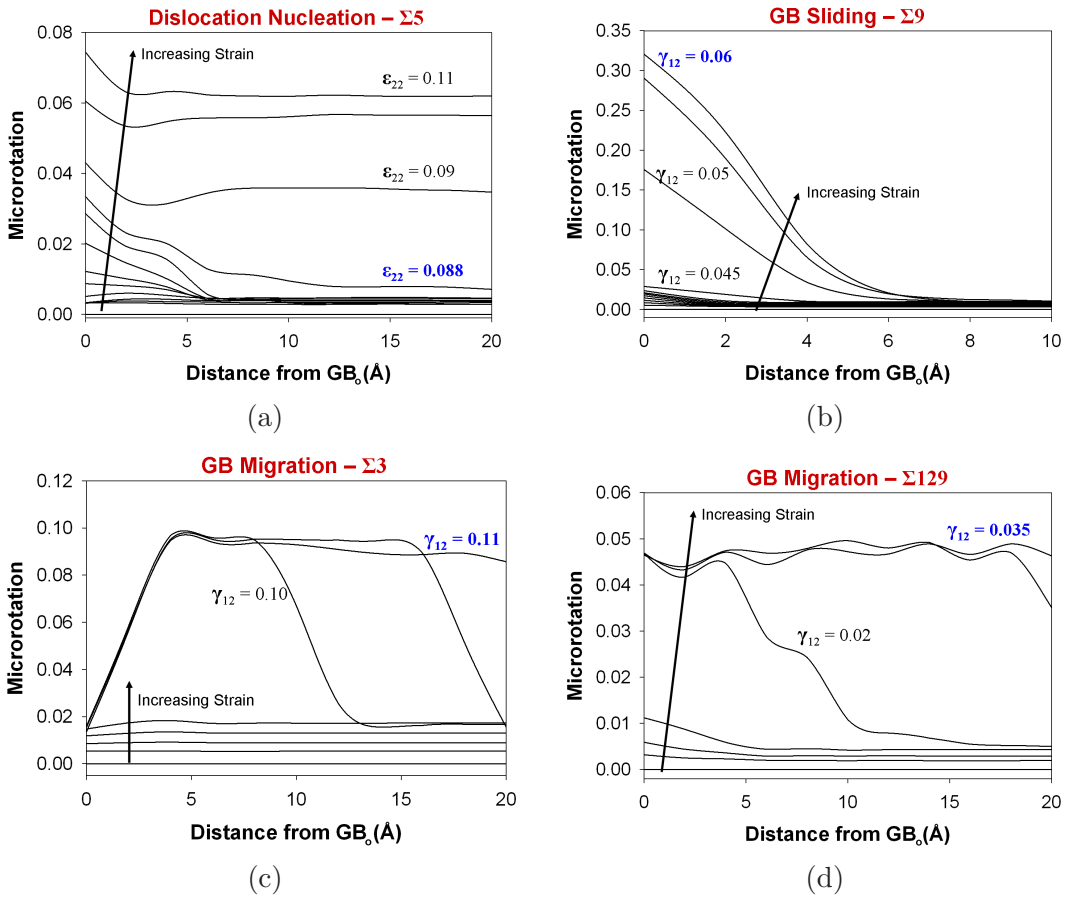

Figure 77: Average atomic microrotation as a function of distance from the original GB for (a) dislocation nucleation in the Σ5 (310) boundary, (b) GB sliding in the Σ9 (221) boundary, (c) GB migration in the Σ3 (111) boundary, and (d) GB migration in the Σ129 (881) boundary. In each plot, the strain evolution of microrotation is provided, and strains which correspond to nucleation and activation events for each mechanism are noted. The included arrows indicate plots of increasing strain.

Figure 77(a) shows microrotation evolution through dislocation nucleation in the Σ5

(310) boundary, 77(b) represents GB sliding in the Σ9 (221) boundary, and 77(c) and (d) represent GB migration of the Σ3 (111) and Σ129 (881) boundaries, respectively. Each image shows that average atomic microrotation increases as strain increases, independent of distance from the GB. As each bicrystalline computational cell is strained, the lattices undergo elastic distortions to accommodate the imposed strain until activating the corresponding deformation mechanism. Once the stress required for activating inelastic deformation is achieved within the computation cell, an increase in the average microrotation is observed in a manner which reflects the strain accommodating mechanism. This behavior continues with further imposed strain during both dislocation nucleation (77(a)) and GB sliding (77(b)).

Partial dislocation nucleation occurs at approximately 8.7% uniaxial tensile strain in the Σ5 GB, and GB sliding is activated near 4.5% shear strain in the Σ9 boundary. For the Σ5 GB, as additional dislocations are emitted from the boundary, average microrotation in the vicinity of the GB increases. In Figure 77(a), the initial set of partial dislocations have traveled more than 20Å from GB_o by a strain of 0.088, which leads to the relatively large increase in microrotation at 20Å from GB_o. GB sliding in the Σ9 boundary exhibits a marked concentration of microrotation near the boundary compared to tensile dislocation nucleation. As shear strain increases, the average microrotation within about 5Å of GB_o increases substantially compared to lattice regions greater than 5Å from GB_o, indicating the role of this GB structure during shear deformation and the localization of atomic microrotation.

However, the evolution of microrotation during GB migration differs from both partial dislocation nucleation and GB sliding. Once migration is activated, significant microrotation occurs as the migrating boundary traverses lattice regions. As evident in Figures 77(c) and (d), the maximum level of microrotation within the bicrystal does not increase proportionately with strain. Rather, microrotation indicates the propagation of the GB as a moving front through the lattice and the migration distance from the original GB location. For example, in Figure 77(c), at approximately 10% shear strain (just after peak shear stress), the Σ3 boundary has migrated a distance of about 13Å resulting in an average

microrotation of about 0.095-0.097 for atoms traversed by the migrating GB. For the Σ129 GB, at 2% shear strain (just after peak shear stress), the maximum average microrotation of about 0.045 is achieved and the GB has traversed approximately 10Å from GB_o. Also displayed in 77(c) and (d), both the Σ3 and Σ129 boundaries have propagated more than the 20Å from GB_o at the strain corresponding to the contours shown in Figures 75 and 76.

5.4 Conclusions

Volume-averaged kinematic metrics were formulated from continuum mechanics theory to analyze the results of atomistic simulations. Both two-dimensional and three-dimensional bicrystalline boundaries were constructed, deformed, and analyzed with the proposed metrics. For the two-dimensional bicrystals under shear, three different deformation mechanisms were observed as a function of disorientation angle: GB migration normal to the GB plane, GB sliding parallel to the GB plane, and GB dissociation. Each metric displayed unique nonlocal deformation fields, and the deformation path of atomic regions under GB migration were highlighted.

For the three-dimensional simulations, both uniaxial tension and shear deformation were imposed to induce different strain accommodation mechanisms. Under tension, heterogeneous dislocation nucleation was observed, while GB sliding and GB migration were seen under shear. For the emission of a partial dislocation from a GB, the metrics provided new insight into the deformation of both interfacial and adjacent lattice regions. Microrotation, for example, uncovered lattice distortion due to the stacking fault in atomic regions surrounding the fault. This insight has not been previously uncovered using traditional measures of energy, centrosymmetry, slip vector, or CNA. In addition, many of the kinematic metrics are functions of both the reference configuration neighbor lists and interatomic vectors. Therefore, their calculation provides a sense of the nonlocal deformation history of atoms and their surrounding neighbors. This utility is highlighted in the deformation mechanism of GB migration. Two different boundaries were observed to undergo migration, but using the deformation gradient, microrotation, and dilatation metrics, detailed differences in the actual atomic deformation paths were uncovered.

CHAPTER VI

NANOCRYSTALLINE MATERIALS

6.1 The Deformation of Nanocrystalline Copper

6.1.1 Introduction

NC materials are defined as PC materials with an average grain size less than 100 nm. The engineering importance of NC metals is mainly due to their potential to enhance material functionality through advanced properties compared to larger-grained metals. Some of the structural benefits that arise due to nanostructuring include ultrahigh yield strength [103, 317], improved fracture and fatigue properties [171, 325, 162], and the potential for superplasticity [138, 169]. Improved processing routes and modified grain structures have also led to an increase in ductility of NC materials [62, 136, 194, 244, 320]. Interest in NC metals is therefore due to the potential enhancements of many bulk material properties, and the scientific interest is rooted in the alternative nanoscale mechanisms that arise because of the limited grain size and dominance of nanoscale effects.

It is thought that traditional strengthening mechanisms, such as dislocation pile-ups along interfaces, are lacking in NC materials, and GB-mediated processes begin to govern material deformation at these small grain sizes. As grain size continues to decrease below 100 nm, the energetic barrier for traditional strengthening and strain accommodation processes increases substantially, leading to the activation of alternative mechanisms (e.g., heterogeneous dislocation nucleation and GB sliding) that signify the regime where intergranular mechanisms begin to govern material deformation. The transition in deformation accommodation from being primarily intragranular to intergranular has also been noted to coincide with the maximum strength in the 'Hall-Petch' relationship [87, 166] as a function of average grain size [187]. In the NC regime, GBs are thought to become the primary carriers of plastic deformation, as a larger percentage of atoms are located within GBs. Recent computer simulations of NC metals have validated this perspective and have provided

tremendous insight into NC material deformation [186, 187, 226, 260, 263, 274, 314]. Furthermore, it has also been found that the structure of GBs in both NC and ultrafine-grained materials affects bulk response [62, 108, 244, 246, 249, 273, 297].

MD simulations are capable of providing unique insight into the microstructural evolution of materials during plastic deformation. Heterogeneous dislocation nucleation (which is an important mechanism in fcc NC metals) has been extensively studied using MD under uniaxial tension applied normal to bicrystalline boundaries [207, 204, 203, 225, 230], and vital information concerning the role of GB structure on nucleation has been provided. The role of GB structure [29, 49, 184, 183] and excess defect concentrations [215, 216, 234] on shear deformation has also been investigated using MD simulations. In NC materials, recent work has also explored the competition of different mechanisms using MD [17, 123, 269], and have provided extensive insight into the plastic deformation of NC metals [187, 189, 75, 79, 258, 260, 264, 261, 265, 263, 274, 301, 313, 308, 314, 311].

Although tremendous advances in understanding deformation in NC metals have been achieved using atomistic simulations, a full understanding of how material behavior at the nanoscale affects macroscopic properties is beyond the current capabilities of MD simulations. For example, Buehler *et al.* [28] conducted an MD simulation with 1 billion atoms, investigating dislocation plasticity near a crack tip. Although the results provided new insight concerning dislocation nucleation, migration, and interaction in metals, the translation of this information and incorporation of interface-mediated behavior into larger-scaled models is still to be undertaken. Accordingly, many researchers have sought solutions from multiscale modeling techniques [26, 110, 198, 217] and continuum models considering deformation rules for GB processes [298, 299]. Many existing models lack the underlying physical rationale to accurately reflect GB and nanoscale defect behavior, even though good agreement with experimental data has been achieved. In addition to these, other novel computational approaches aimed at capturing nanoscale information in higher scaled models are still being developed [7, 33, 122, 165, 199, 306].

One useful approach for computing nanoscale kinematic behavior from atomistic simulations has recently been provided by Zimmerman *et al.* [330]. Zimmerman *et al.* developed

a method to estimate a non-local atomic deformation gradient metric as a function of the deformation an atom's local neighborhood from the reference state to the current state. An advantage of this approach is that the non-locality is varied easily by changing atomic neighbor lists. Once the deformation gradient is estimated, additional kinematic metrics from continuum mechanics theory can be formulated based on similar methods. Each kinematic metric provides new insight into the deformation of an atom's neighborhood and strain accommodation mechanisms activated in NC materials. This approach for analyzing nanoscale simulation data has also shown potential when applied to MD simulations of bicrystalline boundaries being deformed under shear [236]. A sense of deformation history is uncovered through the use of the metrics by leveraging the reference configuration and neighbor lists. The objective of the current work is to extend this computational framework even further by exploiting the complex deformation landscape inherent to NC metals. The continuum kinematic metrics are utilized to resolve the various deformation accommodation mechanisms observed in low temperatures simulations of NC ensembles as a function of grain size with an eye towards gauging their potential to inform coarse-grained models of nanoscale deformation behavior.

6.1.2 Computational Methodology

We constructed 3D periodic simulation cells, each containing 25 grains, utilizing the Voronoi method [280]. To extract grain size dependent behavior from the simulations, three different simulation cells were constructed for this research with varying average grain size (e.g., 5 nm, 10 nm, and 15 nm). S_1 will signify the structure with an average grain size of 5 nm, S_2 for the sample with an average grain size of 10 nm, and S_3 for the 15 nm sample. For each structure, the grain morphology and chosen lattice orientations were identical, the only difference being the average grain size of each configuration. By varying the average grain size from 5 nm to 15 nm, the total number of atoms in the simulation cell increased from about 2.5×10^5 to 7.0×10^6.

After each NC cell was constructed, MS (energy minimization) employing an embedded atom method potential for copper developed by Mishin *et al.* [150] was then performed to

a final relative energy convergence of 10^{-12}. Prior to any imposed deformation, boundary normal stresses within each simulation cell were then allowed to relax to zero, according to the isobaric-isothermal (NPT) ensemble at 10K for an additional 50 ps. The resulting initial NC structures with an average grain size of (a) 5 nm (S_1) and (b) 15 nm (S_3) are shown in Figure 78, where atoms are colored according to the CNA method [63, 232]. This coloring scheme defines the local crystalline structure of each atom according to its atomic neighborhood. The calculated atomic CNA values define an atom as fcc (1), hcp (2), bcc (3), icosahedral (4), or other (5). In all work in this manuscript, we refer to GB atoms as those with CNA equal to 5, or 'other' atoms. All simulations in this work were performed using the MD simulation code LAMMPS (developed at Sandia National Laboratories, lammps.sandia.gov, [167]).

For all deformation simulations, uniaxial tension was imposed in the X_2 direction at a constant strain rate ($10^9 s^{-1}$). Periodicity was maintained in all three dimensions during straining and all deformation simulations were consistent with the NPT ensemble equations of motion at 10K. During uniaxial tension, zero normal stress conditions were imposed on the lateral bounds of the simulation cell (X_1 and X_3 directions). Therefore, stress in only the X_1 and X_3 directions was controlled by the NPT equations of motion, while stress in the X_2 direction was calculated from the virial definition and was a consequence of the imposed strain. The virial stress tensor (without the kinetic term, as discussed in [326]) was calculated according to

$$\sigma_{ij} = \frac{1}{N\Omega} \sum_{\alpha}^{N} \sum_{\beta \neq \alpha}^{N^{\alpha}} f_i^{\alpha\beta} r_j^{\alpha\beta} \tag{42}$$

In this equation, atomic volume is defined by Ω, N is the total atom count in the system, N^{α} represents the number of neighboring atoms for atom α, $f_i^{\alpha\beta}$ is the interatomic force vector between atom α and neighbor β along the i direction, and $r_j^{\alpha\beta}$ is the interatomic distance of atoms α and β in the j direction. For further reference on calculating stress within atomistic simulations, the reader is referred to the manuscript by Zimmerman *et al.* [332]. Tensile strain is defined in terms of engineering strain, i.e.,

$$\epsilon = \frac{\Delta h}{h_o} \tag{43}$$

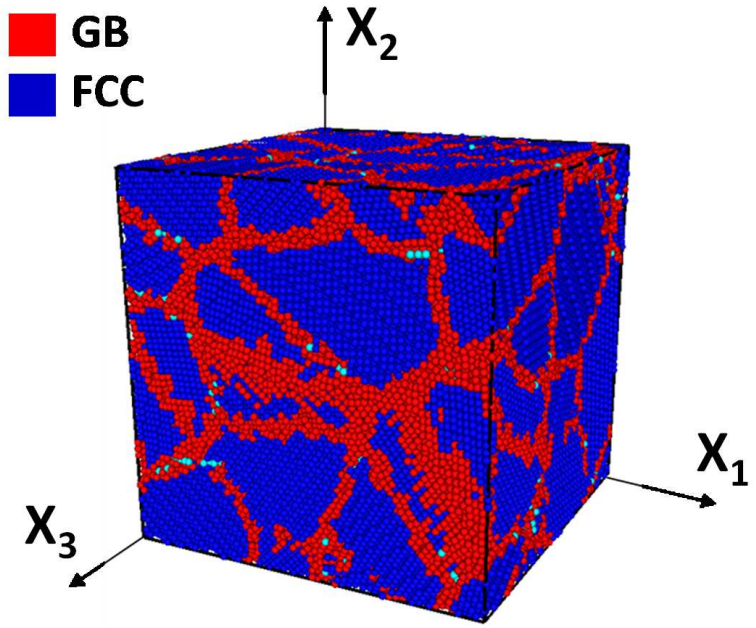

(a)

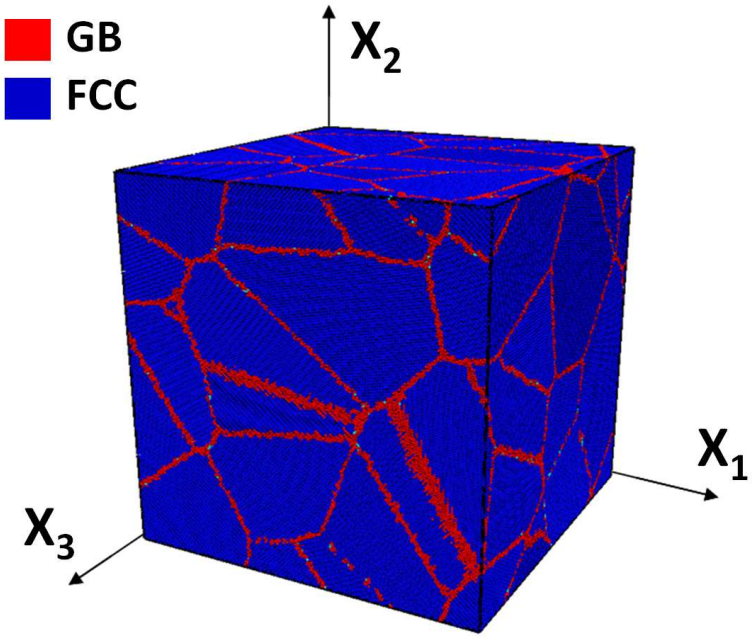

(b)

Figure 78: Initial NC structures of an average grain size of approximately (a) 5 nm and (b) 15 nm. Atoms are colored according to the CNA method. In this method, blue = fcc, aqua = hcp, and red = other (GB) atoms.

where Δh is the length change and h_o is the original simulation length along X_2.

6.1.2.1 Kinematical Framework

To investigate the kinematics of deformation within the NC structures, we leverage various non-local continuum metrics that have been recently applied to atomistic simulations by both Zimmerman *et al.* [330] and Tucker *et al.* [236]. For instance, an atomic deformation gradient ($\mathbf{F}$) was formulated in [330] and applied to a number of examples where it was shown to be consistent with the continuum mechanical deformation gradient. Tucker *et al.* [236] then expanded this formulation to include additional continuum kinematic measures of velocity gradient ($\mathbf{L}$), microrotation (ϕ), and vorticity ($\mathbf{w}$) applied to bicrystalline grain boundaries deformed under shear. The results provided by both Zimmerman *et al.* [330] and Tucker *et al.* [236] highlight the ability of each metric to provide valuable nanoscale information regarding interfacial and bulk lattice deformation. In addition, the use of certain metrics outlined in this work provide insight into the deformation history of atomic fields during straining, and illustrate a significant advantage over traditionally utilized metrics in atomistic simulation analysis. For example, in [237] it was demonstrated how differences in GB migration observed in bicrystalline boundaries under shear are captured using metrics that rely on the reference configuration.

The atomic deformation gradient ($\mathbf{F}$) for an atom α, according to each neighbor β in the neighbor list, is estimated from a least squares error minimization approach as

$$(\omega^{\alpha})_{iM} = (F^{\alpha})_{iI}(\eta^{\alpha})_{IM} \tag{44}$$

where $\boldsymbol{\omega^{\alpha}}$ and $\boldsymbol{\eta^{\alpha}}$ are defined as

$$(\omega^{\alpha})_{iM} = \sum_{\beta=1}^{n}(x^{\alpha\beta})_i(X^{\alpha\beta})_M \tag{45}$$

and

$$(\eta^{\alpha})_{IM} = \sum_{\beta=1}^{n}(X^{\alpha\beta})_I(X^{\alpha\beta})_M \tag{46}$$

In these equations, upper case letters refer to quantities in the reference configuration, while lower case letters refer to those in the current configuration. For example, $\mathbf{x^{\alpha\beta}}$ and

$\mathbf{X^{\alpha\beta}}$ refer to the interatomic vector of atom α and its neighbor β in both the spatial and reference configurations, respectively. This approach for estimating kinematic metrics provides the opportunity to include a greater degree of non-local averaging through additional neighbor sets or updated neighbor sets during the simulation (e.g., $2^{nd}, 3^{rd}, etc$). However, in simulations results in this work, we have restricted our calculations to the first nearest neighbor set. Including additional neighbor sets should be accompanied, however, by weight functions to limit the influence of additional neighbors on each computed quantity [236].

Once $\mathbf{F}$ is calculated, multiplicative decomposition provides both the stretch ($\mathbf{U}$) and rotation ($\mathbf{R}$) components of $\mathbf{F}$ as in [236]. The skew-symmetric part of $\mathbf{R}$, $\mathbf{R_{skew}}$, is then used to calculate the microrotation vector, ϕ, i.e.,

$$\phi_k = -\frac{1}{2}\epsilon_{ijk}\left(R_{skew}\right)_{ij}, \tag{47}$$

where ϵ_{ijk} is the permutation tensor. In addition, we also estimate atomic strain, e (referred to as dilatation for small strain), from the first invariant of the Green strain tensor, $\mathbf{E}$, i.e.,

$$e = tr(\mathbf{E}) \tag{48}$$

where $\mathbf{E}$ is defined as

$$\mathbf{E} = \frac{1}{2}\left[\mathbf{F}^T\mathbf{F} - \mathbf{I}\right] \tag{49}$$

and $\mathbf{I}$ is the identity tensor.

The current configuration velocity gradient, $\mathbf{L}$, is calculated using a similar approach to that used for calculating $\mathbf{F}$, i.e.,

$$\left(\sum_{\beta=1}^{n}(v^{\alpha\beta})_i(x^{\alpha\beta})_m\right)_{im} = L^{\alpha}_{ik}\left(\sum_{\beta=1}^{n}(x^{\alpha\beta})_k(x^{\alpha\beta})_m\right)_{km} \tag{50}$$

This description depends on the instantaneous atomic velocities ($\mathbf{v}$) and neighbor lists in the current (or spatial) configuration. The vorticity or spin tensor, $\mathbf{W}$, is then calculated from both $\mathbf{L}$ and its transpose according to

$$\mathbf{W} = \frac{1}{2}\left(\mathbf{L} - \mathbf{L}^T\right) \tag{51}$$

The vorticity vector, $\mathbf{w}$, is then calculated as the dual vector of $\mathbf{W}$, i.e.,

$$w_k = -\frac{1}{2}\epsilon_{ijk}\left(W\right)_{ij} \tag{52}$$

6.1.3 Results and Discussion

6.1.3.1 Mechanical Behavior

The uniaxial tensile stress-strain behavior of the three NC structures at 10K are shown in Figure 79(a). This Figure shows a clear dependence of NC mechanical response on average grain size. As the average grain size is reduced from 15 nm to 5 nm, the elastic modulus, peak stress, and flow stress decrease. Clearly, smaller grain sizes and consequently a larger volume fraction of GBs influence the macroscopic response of these NC simulation cells under tension at low temperature, and this behavior indicates an 'Inverse Hall-Petch' behavior at these small grain sizes. The elastic modulus (measured up to 1.5% tensile strain) of the three NC structures varies between about 100 and 120 GPa, corresponding very well with reported values in the literature [182, 193] (and references therein) of both PC and NC copper. More specifically, in the smaller structure (S_1), the elastic modulus is less than in the larger structure (S_3), indicating the influence of GB processes on elastic deformation behavior prior to the activation of inelastic deformation mechanisms near peak tensile stress (e.g., GB sliding and dislocation nucleation/emission). It is also worthy to highlight the differences in GB structure as a function of average grain size. In S_1, GBs appear more disordered containing excess free volume than in corresponding boundaries in S_3, and the interfacial volume of thickness changes as well with grain size. These distinctions add to the complexity in understanding the deformation behavior of smaller grained NC structures, but the overall elastic response of our NC structures is similar to those in the literature.

Figure 79(b) shows the evolution of fcc, hcp, and other atomic groups as a function of tensile strain for S_1 (5 nm) and S_3 (15 nm), calculated using CNA. Atoms that belong to the 'other' group with a CNA value of 5 include both GB and TJ atoms. Although atoms that do not reside in GBs might have a CNA value of 5, the percentage is extremely low, and therefore their inclusion in the 'other' group do not skew the results presented here. As this Figure demonstrates, the atomic fraction of fcc and GB atoms evolve for S_1 and S_3 as a function of strain. Initially, S_1 is composed of approximately 68% fcc atoms and 26% GB atoms, while S_3 is composed of approximately 89% fcc atoms and 10% GB atoms. However, at a strain of 0.06, these atomic fractions have changed due to deformation processes (e.g.,

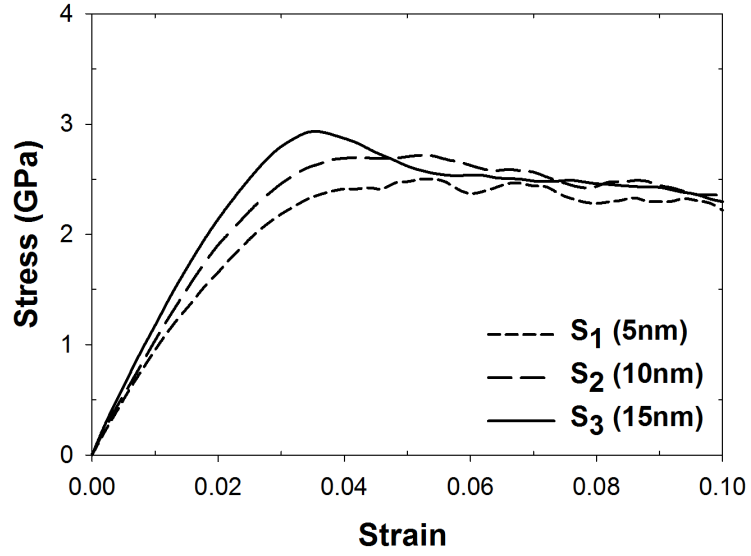

(a)

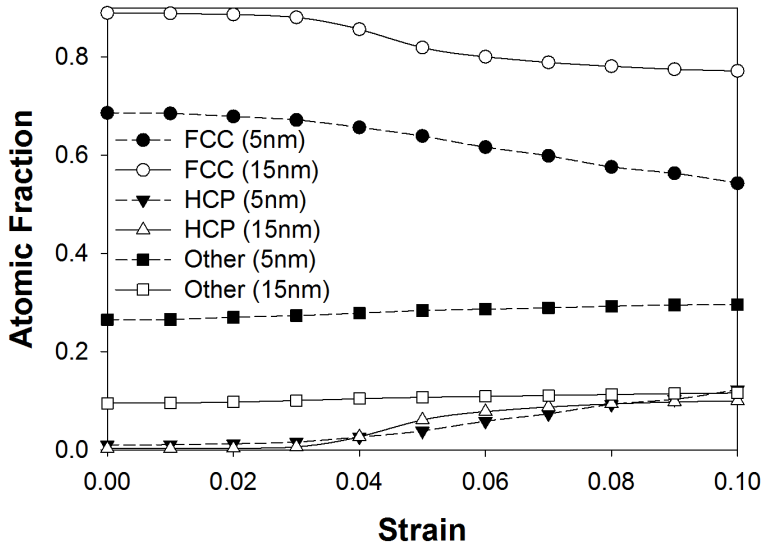

(b)

Figure 79: (a) Uniaxial tension stress-strain behavior of the 5 nm (S_1), 10 nm (S_2), and 15 nm (S_3) grain size structures at 10K with a constant strain rate of $10^9 s^{-1}$. (b) The evolution of the fcc, hcp, and other (GB) atomic groups identified by common neighbor analysis for both S_1 (dashed) and S_3 (solid).

dislocation nucleation/migration, GB sliding/shuffling, etc.). Atomic fractions calculated as hcp in both S_1 and S_3 have risen to approximately 6% and 7%, respectively, at 0.06 strain. This behavior generally indicates the presence of stacking faults and twins in the

substructures, due to emitted partial dislocations from GBs and TJ regions, as well as a small degree of twin boundary segments within GB regions.

To explore dislocation activity in our structures, the slip vector [329] of each atom was calculated as

$$\mathbf{s}^{\alpha} = -\frac{1}{n_s}\sum_{\beta\neq\alpha}^{n}(\mathbf{x}^{\alpha\beta} - \mathbf{X}^{\alpha\beta}) \tag{53}$$

where $\mathbf{s}^{\alpha}$ is the slip vector of atom α, n is the number of nearest neighbors (β), n_s is the number of slipped neighbors, and $\mathbf{x}^{\alpha\beta}$ and $\mathbf{X}^{\alpha\beta}$ represent the interatomic distance vectors between atom α and neighbor β in the current and reference configurations, respectively. Therefore, slip vector defines the deformation of an atom's neighborhood by calculating the slip of its nearest neighbors with respect to the reference configuration. An advantage of calculating the slip vector is that an estimate of the Burgers vector can be computed for dislocation structures. For example, atoms located within a stacking fault will have a slip vector magnitude near the magnitude of the theoretical Burgers vector for a partial dislocation ($\|\mathbf{b_p}\| = \frac{a}{\sqrt{6}}$) and a CNA value of 2, while atoms in regions that have undergone full slip of a perfect dislocation will have a slip vector magnitude of approximately $\|\mathbf{b_f}\| = \frac{a}{\sqrt{2}}$ and a CNA value of 1. In these estimations of the slip vector magnitude, a defines the lattice parameter, while $\|\mathbf{b_p}\|$ and $\|\mathbf{b_f}\|$ represent the magnitudes of partial and full dislocation Burgers vectors, respectively. Using both the calculated slip vector and CNA values for each atom, we estimate the atomic fraction of atoms that have undergone both partial and full slip as a function of tensile strain. As the results in Figure 80(a) demonstrate, dislocation activity is suppressed in smaller grain sized NC structures (e.g., S_1) as compared to larger grained structures (e.g., S_3).

Figure 80(a) plots the fraction of atoms that have undergone both partial (filled) and full (open) slip as a function of strain for S_1 (short-dash), S_2 (long-dash), and S_3 (solid). As stated, this calculation is based on both the slip vector magnitude and each atom's crystallographic group (i.e., fcc, hcp, or GB). At approximately 3% tensile strain, partial dislocations are emitted and consequently stacking faults begin to appear in each NC structure, but S_3 exhibits a greater percentage of partially slipped atoms than either S_1 and S_2. Partial dislocations are generally nucleated from GBs and then glide through the crystalline

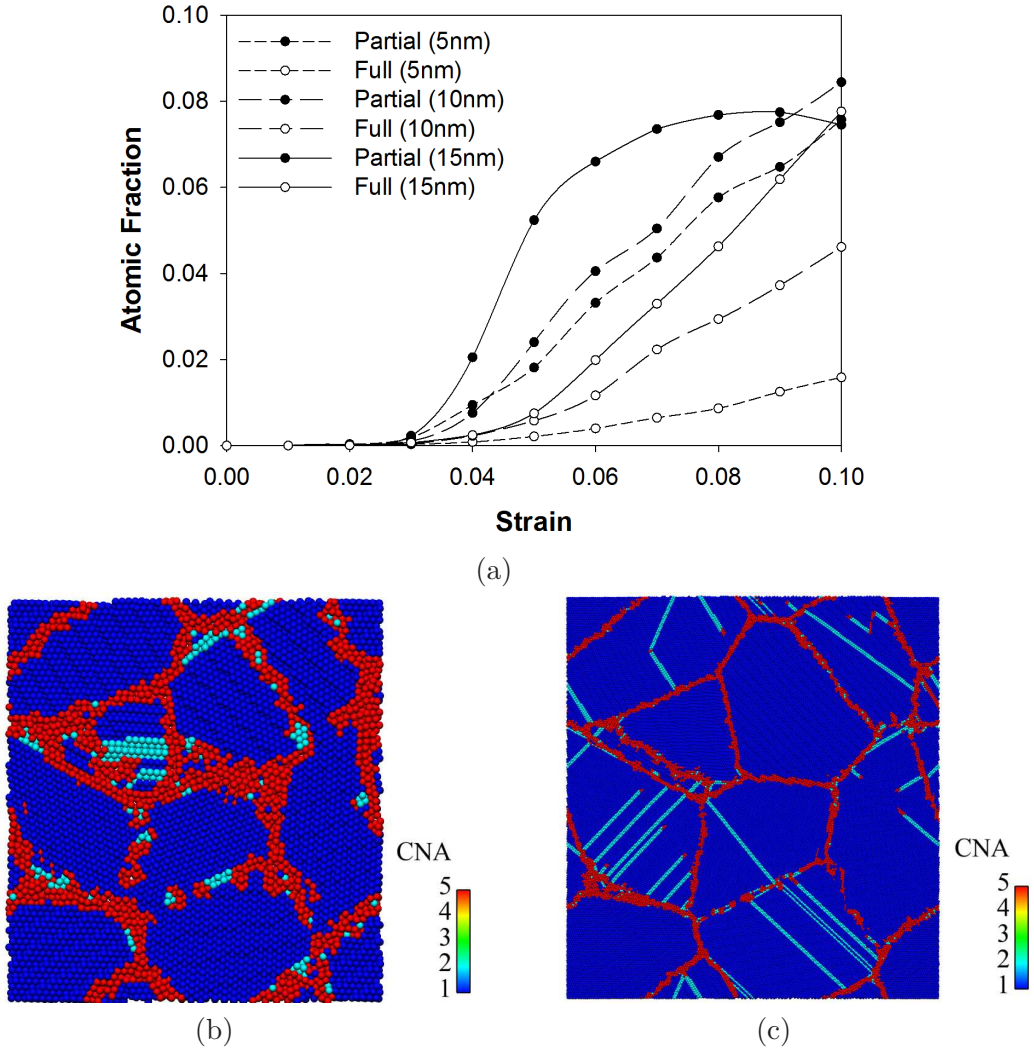

Figure 80: (a) The atomic fraction of both partial (filled) and full (open) dislocations as a function of strain for S_1 (short-dash), S_2 (long-dash), and S_3 (solid). Slices through the simulation cell at 5% tensile strain for (b) S_1 and (c) S_3, where atoms are colored according to CNA and the tensile axis is vertical.

lattice on {111} planes of high resolved shear stress. The leading partial dislocations tend to travel across the grain and become absorbed into the opposite GB prior to any emission of the trailing partial dislocation. However, in S_1, dislocation slip is not a major accommodation mechanism, in contrast to S_3. The lack of significant partial slip in S_1 indicates that alternative deformation mechanisms, such as GB sliding and migration, must be activated to accommodate strain, while crystallographic slip processes are suppressed. This comparison illustrates the competition between dislocation activity and GB deformation in

NC metals to accommodate the imposed tensile strain.

In all three structures, as tensile strain continues, the fraction of atoms that have been traversed by a full dislocation increases. This behavior is true for partial slip as well, except for S_3, where the atomic fraction of atoms involved in partial slip begins to level off near 8% strain, and decreases slightly at 10%. The rate at which partial slip occurs in S_3 increases rapidly between 3 and 5% strain. This trend is quite different for both S_1 and S_2, where the rate of partial slip increase is relatively constant between 5 and 9% tensile strain. For the smaller grain sizes in both S_1 and S_2, the activation criteria and the availability of alternative deformation mechanisms (e.g., GB sliding and atomic shuffling) most likely lead to the lower fraction of dislocations in these structures. For full dislocation activity to be recorded, the trailing partial dislocation must be emitted on the same slip plane as the leading partial dislocation and remove the stacking fault from the grain interior. Clearly, if GBs begin to deform in the smaller grains prior to the emission of the trailing partial dislocation, a full dislocation will not be observed and the stacking fault will remain.

Figures 80(b) and (c) show slices through S_1 and S_3 respectively, at approximately 5% strain in relatively identical locations within the simulation cell with the tensile axis in the vertical direction. The grain morphologies are still similar, but the deformation activity differs for the two NC structures. In S_1 (80(b)), very little dislocation activity is evident within the lattices, agreeing with the plotted atomic fractions shown in 80(a) of dislocation activity, and the GBs appear to be slightly deformed. In 80(c), greater dislocation activity is present within the lattices and the GBs appear to be relatively undeformed as compared to boundaries in S_1. In addition (as shown in Figure 80(c)), the majority of emitted partial dislocations in S_3 travel completely across the grain and become absorbed into other GBs prior to the emission of the trailing partial dislocation, leaving behind stacking faults that traverse the entire grain. Moreover, we see greater evidence of dislocation locks and full dislocation slip in S_3 (80(c)) than in S_1 (80(b)), and more GB accommodation processes (e.g., sliding, shuffling, and migration) in S_1 than in S_3.

GB deformation processes, such as atomic shuffling, sliding, and migration are important in NC metals and often accompany dislocation mechanisms in NC metal structures [269,

260, 301, 314]. In the NC structures examined here, the cooperation of GB mechanisms and dislocation activity to accommodate the imposed strain differs for each NC configuration (as observed in 80(b) and (c)), and also depends on the imposed strain level. However, it is rather difficult to decompose or partition the influence of GB processes on overall deformation within NC metals. One avenue to gain insight into GB deformation is to leverage atomic calculations of potential energy and slip vector. These data can then be plotted according to either a distribution profile at selected strain levels (Figure 81(a)) or tracked as a function of strain (Figure 81(b)) for various atomic groups (e.g., fcc, hcp, and GB) and for each NC structure.

The potential energy distributions shown in Figure 81(a) only consider GB atoms, and are normalized by the total number of atoms within each structure at various strain intervals. Only S_1 (filled) and S_3 (open) are plotted and the three tensile strain levels are 0%, 6%, and 10%. The energy profiles for S_1 show that the percentage of GB atoms increases dramatically as inelastic deformation occurs between 0% and 6% tensile strain, and the distribution for GB atoms experiences a slight increase in energy as tensile strain approaches 10%. In S_3, however, there is a smaller increase in the fraction of GB atoms accompanied by a slight increase to higher energies in the profile as well. However, a couple disparities are noteworthy between S_1 and S_3. First, the fractional increase of GB atoms is greater in S_1 than in S_3 between 0% and 10% tensile strain, and the difference in the profiles between 6% and 10% is greater in S_3 than in S_1. This means that a larger degree of GB atoms cooperate in deformation processes leading to higher potential energy states in S_1 than in S_3, but the majority of the accommodation mechanisms leading to this trend occur by approximately 6% strain in S_1. In S_3 however, GB mechanisms responsible for increasing the energy profile do not appear to be enhanced within any particular strain regime. Rather there appears to be a continuous shift to higher energies in the potential energy profile as tensile strain increases.

Figure 81(b) shows the fraction of the total computed slip vector as a function of atomic group and strain. Once again, only S_1 (short-dash) and S_3 (solid) are shown, and the plots displayed represent the fcc (circle), hcp (triangle), and GB (square) atomic groups.

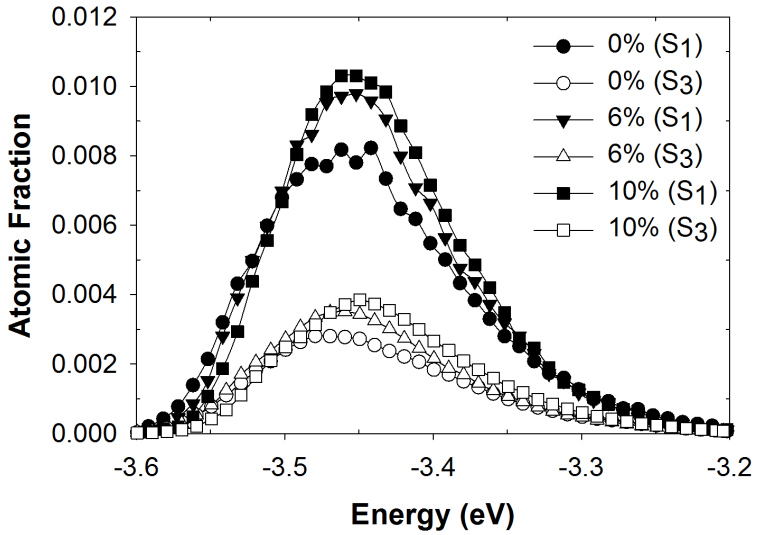

(a)

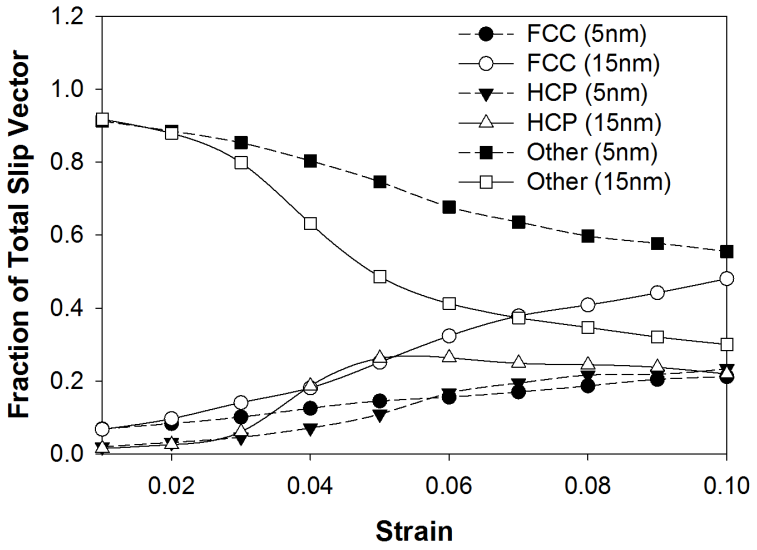

(b)

Figure 81: (a) The distribution of potential energy for atoms in the GBs for both S_1 (filled) and S_3 (open) at 0%, 6%, and 10% tensile strain. The distributions are normalized by the total number of atoms in each NC simulation cell. (b) The fraction of the total computed slip vector as a function of strain for the fcc, hcp, and other atomic groups in S_1 (short-dash) and S_3 (solid). The total slip vector for each group is calculated and normalized by the total slip vector for all atoms in the structure.

The total slip vector is computed by summing all atomic slip vectors within the entire system, while the total slip vector of each atomic group is computed by only considering the computed slip vector of atoms belonging to that group. Once these totals are calculated,

the total slip vector is subdivided into fractional components based on the atomic groups and their total computed slip vector. The results shown in Figure 81(b) provide some insight into the deformation within fcc, hcp, and GB atomic groups. For example, in both S_1 and S_3, a high percentage of the total slip vector is due to processes within the GB atomic group at low strains. However, as tensile straining continues, the GB fraction of total slip vector in S_3 drops drastically more than that observed in S_1, as both partial and full dislocations are emitted into the lattices. Furthermore, the fcc group in S_3 experiences a larger increase than S_1 (highlighting full slip), and the slip vector of the hcp group in S_3 plateaus at approximately 5% tensile strain whereas hcp slip in S_1 continues to increase at larger strains. The data shown in Figure 81(b) indicates that GB reordering is a dominant mechanism in both S_1 and S_3, but is more influential in accommodating strain in S_1 than in S_3.

6.1.3.2 Deformation Kinematics

The deformation kinematics of the NC structures were explored using the microscale kinematic metrics of deformation gradient ($\mathbf{F}$), rotation ($\mathbf{R}$), Green strain ($\mathbf{E}$), microrotation vector (ϕ), vorticity vector ($\mathbf{w}$), and dilatation (e) outlined in Section 6.1.2.1. Each metric provides different and vital information concerning the atomic deformation fields produced within the NC structures. Some metrics (e.g., $\mathbf{F}$, $\mathbf{R}$, $\mathbf{E}$, ϕ, and e) uncover history dependent kinematics (using reference neighbor lists), while others (e.g., $\mathbf{L}$ and $\mathbf{w}$) rely only on instantaneous atomic quantities and current neighbor lists. Figure 82 shows results for S_1 at 10% tensile strain, where atoms are visualized using (a) CNA, (b) $\mathbf{F}$ (F_{22}), (c) e, and (d) $\boldsymbol{\phi}$. The lack of significant stacking faults and other dislocation structures at 10% tensile strain is evident in 82(a), but there is evidence of GB deformation (e.g., sliding, migration, and atomic shuffling) agreeing with data shown in Figure 81. Moreover, a sense of the deformation history of each atom's neighborhood is captured using the volume-averaged kinematic metrics to visualize atoms as shown in (b), (c), and (d).

One component of the deformation gradient is displayed in 82(b), where atoms are colored according to F_{22} (the X_2 direction parallel to the tensile axis). The most intense

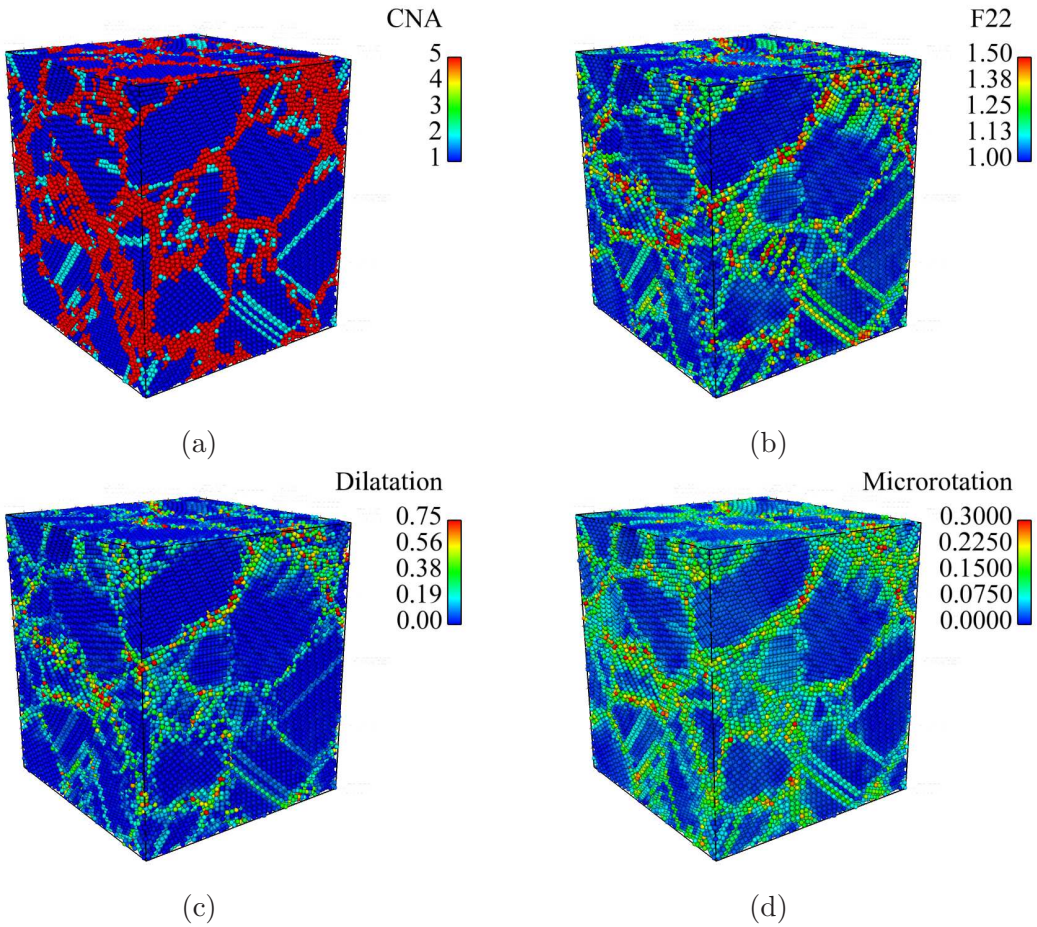

Figure 82: Snapshots showing S_1 at 10% tensile strain, where atoms are colored according to (a) CNA, (b) F_{22}, (c) dilatation, e, and (d) microrotation, ϕ.

deformation fields tend to be located within GBs in S_1 with limited lattice deformation. In numerous interfacial regions, $F_{22} \geq 1.5$, while in most lattice regions, $F_{22} \leq 1.25$; this means that GBs account for the largest deformation while there is minimal deformation within the lattices. Dilatation, e, is computed from the Green strain tensor, $\mathbf{E}$, and estimates the change in volume normalized by the reference volume. Applied to atomistic simulations, this metric computes a volumetric change according to an atom's neighbors without shape change. In 82(c), atoms are colored according to e, and it is observed that the largest dilatation occurs within GB regions for S_1 under uniaxial tension. Stacking faults appear to have small computed dilatation, on the order of $0.1 - 0.2$. Microrotation, $\boldsymbol{\phi}$, is another useful measure for determining deformation, see [236] and [237] for additional discussion on $\boldsymbol{\phi}$ and its physical meaning. Figure 82(d) shows S_1 where atoms are colored according to the

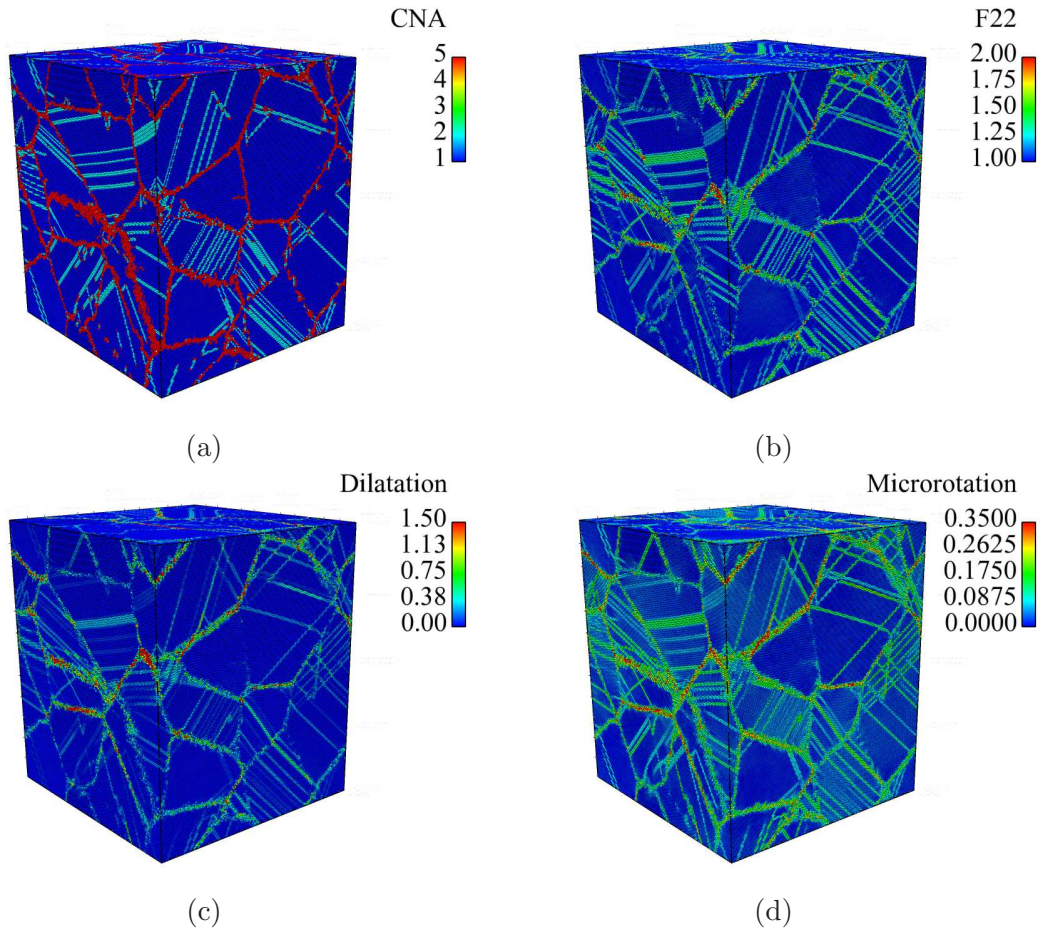

Figure 83: Snapshots showing S_3 at 10% tensile strain, where atoms are colored according to (a) CNA, (b) F_{22}, (c) dilatation, e, and (d) microrotation, ϕ.

magnitude of $\boldsymbol{\phi}$. Interestingly, many lattice regions show non-zero microrotation even where stacking faults are absent. Microrotation is able to capture previously discussed mechanisms responsible for atomic deformation (e.g., dislocation slip, GB sliding, and migration), in addition to suggesting lattice rotation. Additional calculations of the gradient of ϕ could also lend insight into lattice curvature, but is not including in this work.

Figure 83 displays the same kinematic metrics for S_3 at 10% tensile strain as shown in Figure 82 for S_1. A number of differences are evident between Figures 82 and 83. First, 83(a) shows a much larger concentration of stacking faults in S_3 than in S_1 and a lower degree of GB deformation, the values of both (b) F_{22} and (c) e are more uniform throughout the deformed structures than in S_1, and (d) shows that significant microrotation is observed in lattice regions not directly involved in dislocation slip. Some GB regions experience high

microrotation (often coincident with higher e levels), indicating that higher free volume interfacial regions undergoing greater atomic shuffling and dilatation also experience greater microrotation than lower free volume (more compact) GB regions. The distribution of microrotation throughout S_3 is also quite interesting. As mentioned, in some grains microrotation is only observed for slipped regions (i.e., stacking faults and fcc regions where full dislocation slip has occurred) and GBs; however, in other grains non-zero microrotation is evident in lattice regions not involved with slip, and the level of microrotation is less than that corresponding to partial slip. In addition, twinning is also captured by microrotation (discussed in the next section) exhibiting the potential of this metric to be used to resolve the distribution of different mechanisms in NC structures.

In Figure 84, by averaging over all atoms in the simulation cell, the evolution of the average (a) dilatation and (b) microrotation is shown as a function of strain for different atomic groups (e.g., fcc, hcp, and other). The plots in this Figure represent different atomic groups classified using calculated CNA values and two different NC structures, S_1 and S_3. For dilatation, the average value is low for fcc atoms in both S_1 and S_3, but for GB atoms, dilatation continues to rise with increasing tensile strain. A stark difference, however, between S_1 and S_3 is that average dilatation for GBs is much greater in S_3 than in S_1. But, it must be recalled that the atomic fraction of this group in S_3 is much lower than in S_1, corresponding to the lower percentage of interfacial atoms in larger grained systems. Another interesting feature in Figure 84(a) is the coincidence of average dilatation for hcp atoms in both structures at higher strains. This means that as strain increases, the variation in calculated dilatation for hcp atoms decreases in both S_1 and S_3. For microrotation, we observe similar trends in Figure 84(b) as in 84(a). The average microrotation for fcc atoms is low, but steadily rises with strain. The steady rise in average microrotation in the fcc group is generally due to elastic strain or fully slipped atoms. GB atoms in both S_1 and S_3 have microrotation values that also continue to increase with strain, but the average microrotation for hcp atoms tends to plateau at higher strains. The strain at which average microrotation for hcp tends to plateau is lower in S_3 than in S_1 meaning that stacking faults and twins tend to be more abundant at lower strains in S_3 than in S_1, which also agrees

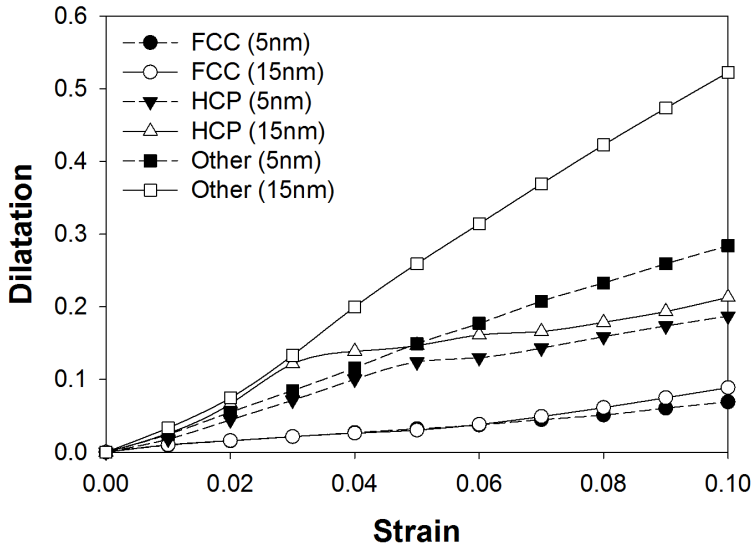

(a)

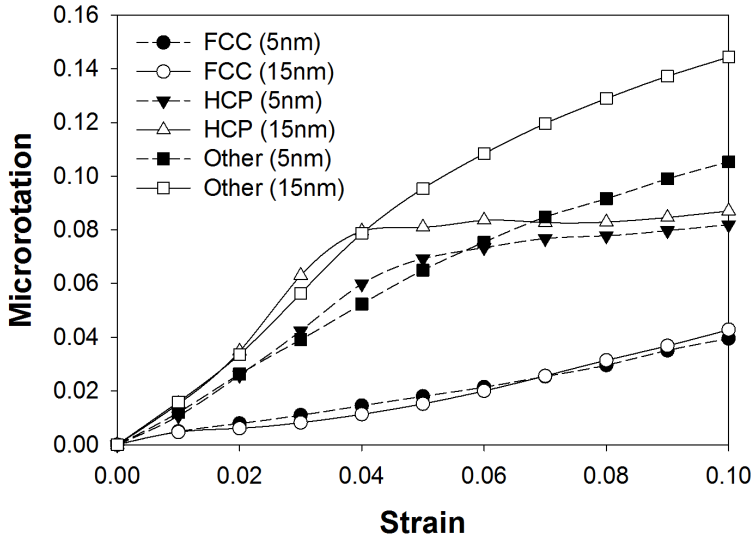

(b)

Figure 84: The evolution of the average (a) dilatation and (b) microrotation as a function of strain for S_1 (filled) and S_3 (open) for fcc (circle), hcp (triangle), and other (square) atomic groups.

with previous observations and discussions.

To better understand the utility and role of microrotation and vorticity in resolving lattice deformation (i.e., dislocation slip), Figure 85 shows a dislocation being emitted from a GB in grain 11 on a maximum resolved shear stress {111} plane and colored according to

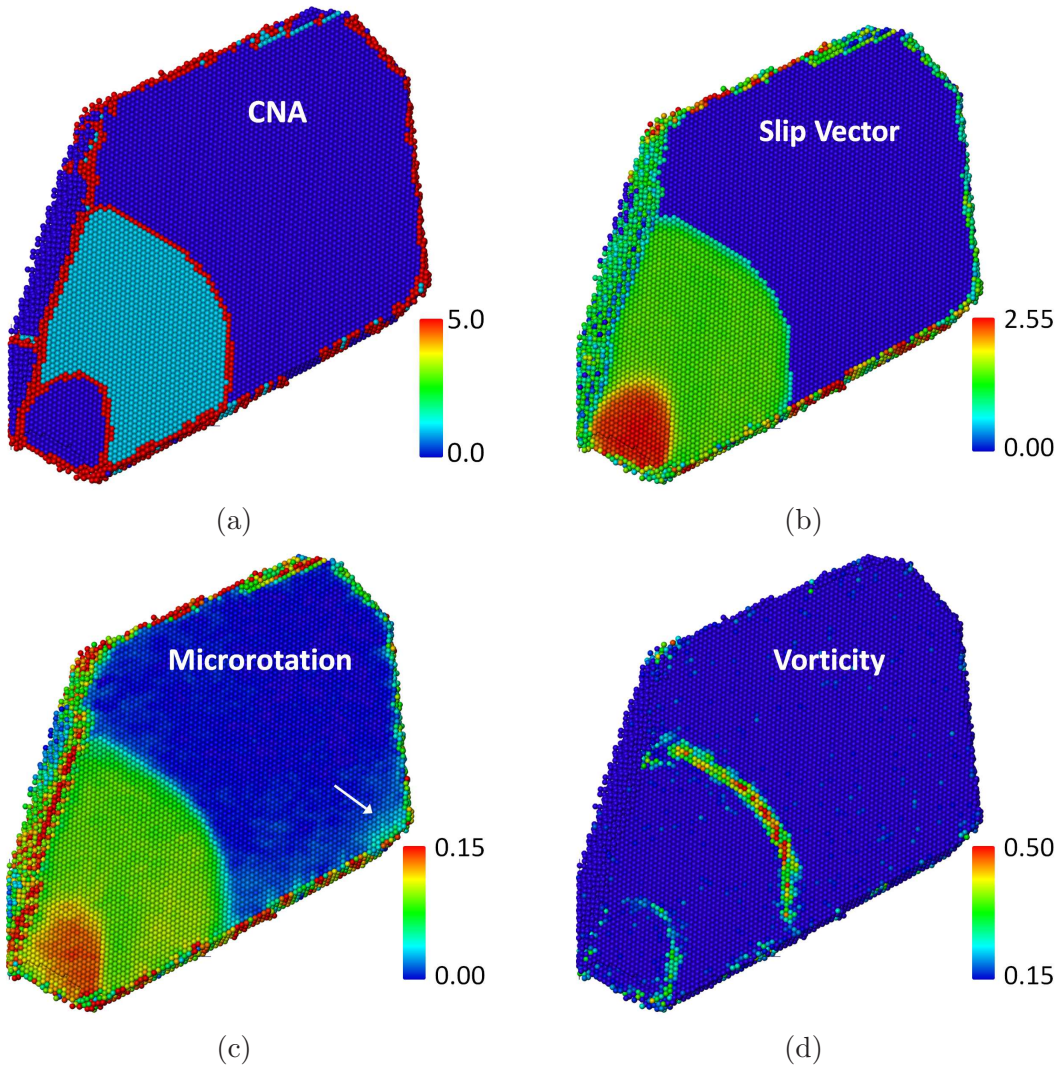

Figure 85: Dislocation emission in S_3 at 4% tensile strain, visualized according to (a) CNA, (b) slip vector, (c) microrotation, and (d) vorticity. The leading and trailing partial dislocations are separated by a stacking fault, and atoms behind the trailing partial have undergone full slip.

(a) CNA, (b) slip vector, (c) microrotation, and (d) vorticity. The dislocation is split into two partial dislocations separated by a stacking fault where the trailing partial dislocation has been pinned momentarily by a TJ. The resolved stress on the {111} plane eventually causes the leading partial to glide across the grain and become absorbed into GBs on the opposite side of the grain, leaving a stacking fault that connects to the trailing partial dislocation. In (a), CNA clearly identifies the GBs, dislocations, and stacking fault. Atoms in 85(b) are colored according to the calculated slip vector, where green atoms correspond

to a Burgers vector magnitude approximately equal to the theoretical value for a partial dislocation ($\sim$ 1.48Å) and red atoms represent full slip ($\sim$ 2.56Å). The leading partial dislocation is colored aqua and the trailing partial dislocation, yellow.

In Figure 85(c), each atom's microrotation value is shown and captures regions that have undergone both partial and full slip. As with slip vector, microrotation is dependent on the reference neighbor list; therefore, microrotation varies for partially slipped regions (i.e., stacking faults) as compared to fully slipped regions. Another interesting feature of microrotation, is its ability to highlight lattice distortion located near a TJ on the right side of grain 11 (indicated by an arrow). Significant atomic rearrangement accompanied the migration of this TJ, producing elastic strain in nearby lattice regions. In (d), atoms are viewed according to their calculated vorticity. To calculate vorticity, instantaneous atomic velocities and current neighbor lists are utilized that are able to uncover deformation at the current timestep. This metric is uniquely capable of capturing localized GB/TJ deformation and, to a larger extent, dislocation glide as evidenced in Figure 85(d). Both the leading and trailing partial dislocations are clearly highlighted using vorticity, but the leading partial dislocation in grain 11 shows greater vorticity. Dislocation glide velocity can be estimated using vorticity in these NC structures, but is not addressed in this work. Therefore, vorticity appears to hold great promise for purposes of revealing the propagation of dislocation fronts.

6.1.3.3 Microrotation Analysis

As mentioned, microrotation is able to capture both partial and full slip within these NC structures, and it was also shown in Figure 85(c) that computing microrotation also highlights lattice distortion near TJs following significant strain accommodation. However, the microrotation metric is also able to shed light on additional deformation mechanisms as well. Figure 86 shows a slice through grain 23 in S_3 at 10% tensile strain where atoms are colored according to (a) CNA, (b) slip vector, and (c) microrotation. As clearly seen in (a), grain 23 contains both stacking faults and twin boundaries. The single hcp atomic planes separate twinned atomic regions where dotted lines have been added to follow the lattice directors on either side of the twin boundaries. The viewing direction in Figure 86

is along the ⟨110⟩ axis of grain 23 and the misorientation angle of each twin boundary is approximately 109.5°.

When each atom's slip vector is calculated (86(b)), the stacking faults and twin boundaries in grain 23 are evident, and atoms that have undergone full slip in neighboring grains are also clearly seen. However, for atoms between the twin boundaries, their computed slip vector is still zero. Therefore, in this instance, the mechanism of twinning by successive partial dislocation glide on neighboring slip planes produces no net slip vector for atoms that have been twinned. Furthermore, the twin boundaries retain a slip vector magnitude approximately equal to that of a stacking fault and atoms that have undergone partial slip.

In Figure 86(c), however, each of these mechanisms (including twinning) is captured by calculating microrotation. For the twinned region between the twin boundaries, the microrotation metric is non-zero (approximately 0.15-0.16). For stacking fault atoms, microrotation is between 0.05 and 0.09, and for atoms that have undergone full slip, microrotation is between 0.1 and 0.14. However, it must be noted that these values are for microrotation computed using only first nearest neighbors, and larger volume-averaging will require the inclusion of a weighting function (see discussion of weighting functions in [236]). This example clearly shows an advantage of using the microrotation metric to analyze atomistic deformation fields in NC structures and the associated deformation mechanisms.

Another technique to resolve deformation in these NC structures is to plot the distribution of atomic kinematic quantities as a function of strain for different atomic groups. Similar to Figure 84(b), which showed the evolution of average microrotation as a function of strain, Figure 87 displays the distribution of microrotation for the different atomic groups at various tensile strains. Figure 87(a) shows microrotation for all atoms in both the S_1 and S_3 NC structures at 2%, 4%, and 10% tensile strain. At 10% tensile strain, there are obvious regions of microrotation that are heavily populated. Partial slip is approximated by microrotation values between 0.05 and 0.09, where full dislocation slip and twinning are represented by microrotation between 0.10 and 0.17. In Figure 87(a), at 10% strain, S_3 exhibits higher atomic fraction levels for the region of 0.10 to 0.17 corresponding to full slip and twinning, while S_1 shows higher fraction for microrotation corresponding to partial slip.

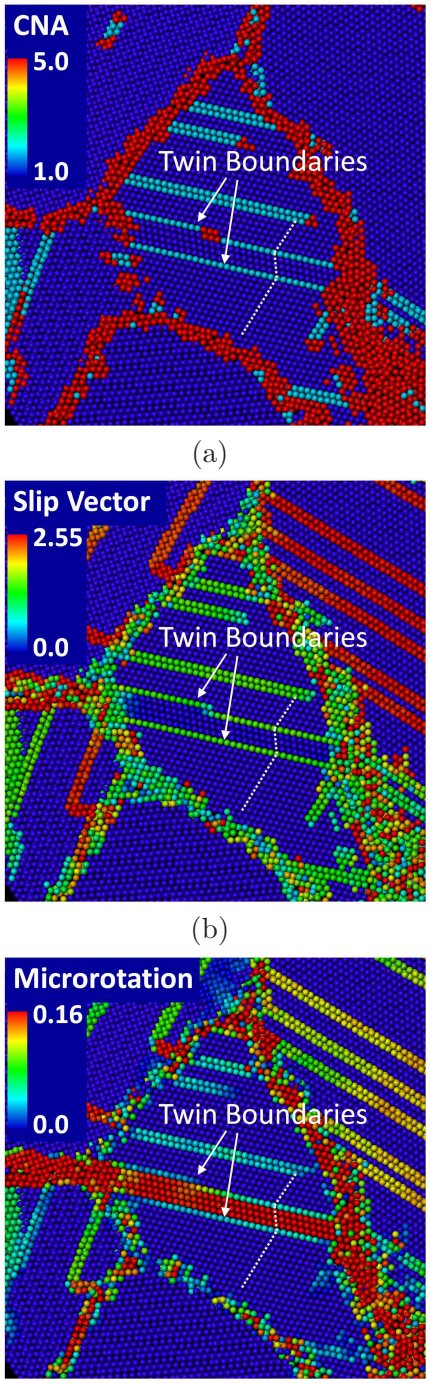

Figure 86: A comparison of the deformation in grain 23 of S_3 at 10% tensile strain according to (a) CNA, (b) slip vector, and (c) microrotation. Twin boundaries and stacking faults are clearly captured by the microrotation metric, in addition to the twinned region between the twin boundaries.

At 4% tensile strain, S_3 shows a small population corresponding to partial slip. This type of analysis shows the utility in the kinematic metrics for resolving different deformation mechanisms in NC structures. In (b), (c), and (d), the microrotation for fcc, hcp, and GB atoms are shown, and normalized by the total number of atoms in each respective atomic group.

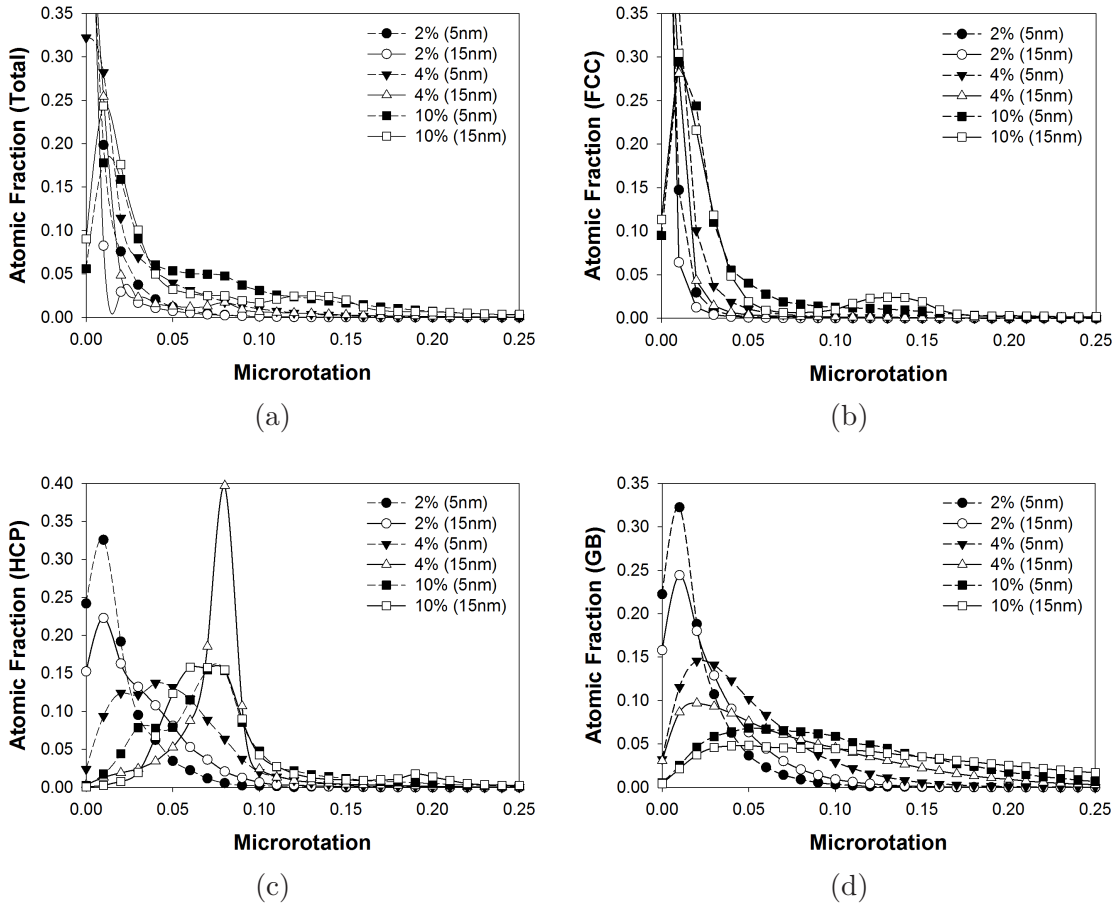

Figure 87: Microrotation distributions of (a) all atoms, (b) fcc atoms, (c) hcp atoms, and (d) GB atoms.

For fcc atoms (Figure 87(b)), in both S_1 and S_3, the distribution increases or broadens at higher microrotation values with increasing strain. At 10% tensile strain, there is a sudden increase in the atomic fraction of atoms possessing microrotation in the range of 0.10 to 0.17, shown as a small peak in the plot in Figure 87(b). Fully slipped atoms and atoms within twinned regions contribute to this range of microrotation. Therefore, at 10% tensile strain, the population of fcc atoms that have undergone full slip or those within twinned

regions comprise a noticeable fraction of the total number of fcc atoms in S_3. Furthermore, at 10% strain, the fraction of fcc atoms in both S_1 and S_3 with no microrotation is only 0.10.

Atoms within stacking faults and twin boundaries are in the hcp group. For hcp atoms (Figure 87(c)), as strain increases, a large peak appears for the microrotation range of 0.05 to 0.10. As shown in Figure 86, this corresponds to both stacking faults and twin boundaries. Therefore, a larger percentage of hcp atoms lie within either stacking faults or twin boundaries with increasing tensile strain. For GB atoms (Figure 87(d)), a continuous shift to higher microrotation and peak broadening occur with strain. This corresponds to GB deformation and sliding events in both S_1 and S_3, which lead to higher computed microrotation with a relative uniform distribution (i.e., no distinct peaks). The broadening of the distribution corresponds to continuous GB deformation and strain accommodation processes within GBs. But, the role of GBs and dislocation activity in the overall strain of the NC structure is still not clear.

6.1.3.4 Green Strain

One way to estimate the contribution of different mechanisms to the overall plastic strain of the NC ensemble is to utilize the calculated Green strain tensor, **E**, from the computed deformation gradient, **F**. To distinguish different atomic groups, both computed slip vector magnitudes and CNA values are used. Each group will have distinct strain components in the tensile axis direction, E_{22}, roughly estimating the contribution of different mechanisms. Atoms identified as hcp and a slip vector magnitude near the theoretical Burgers vector value for partial slip (1.48Å) belong to the 'Dislocation' group. Also, fcc atoms with slip vector values near the Burgers vector magnitude corresponding to full slip (2.56Å) are also included in the 'Dislocation' group. The 'Other' group (CNA=5) is composed almost entirely of GB atoms throughout the entire strain range, but a small fraction of those atoms are located within partial dislocations. Lattice contributions to tensile strain are computed from fcc atoms (CNA=1) not already identified with the 'Dislocation' group. Thus, the 'FCC' group consists of fcc atoms that have not undergone full slip and contribute to tensile strain only

through elastic deformation.

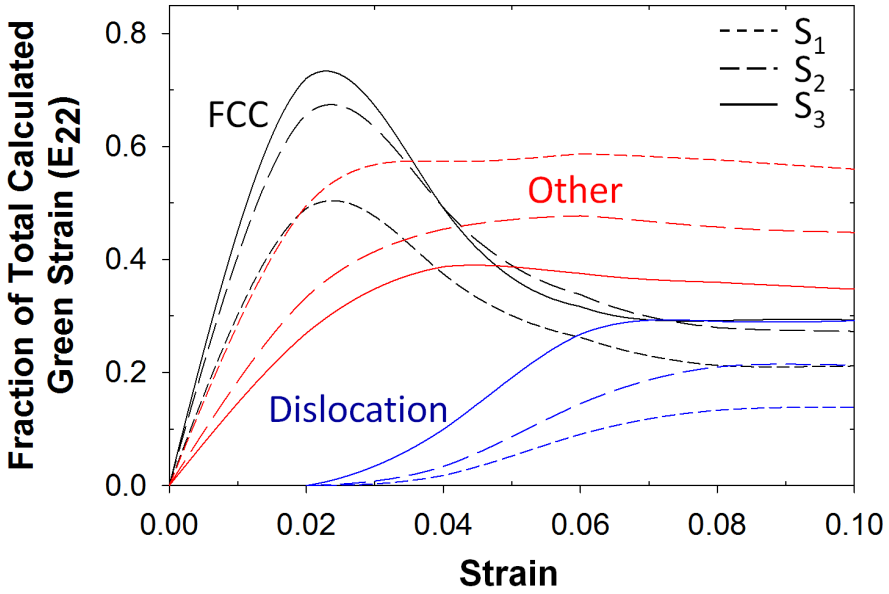

Figure 88: The computed fraction of Green strain of fcc (black), dislocation (blue), and GB (red) atomic groups in the tensile direction as a function of grain size for S_1 (short-dash), S_2 (long-dash), and S_3 (solid).

As shown in Figure 88, the fractions of total calculated Green strain component in the tensile direction (E_{22}) for different atomic groups vary as a function of imposed strain. Distributions for all three NC structures are included in this Figure to elucidate the influence of grain size on the contributions. For fcc atoms (black), a large increase in the fraction of total calculated Green strain occurs at low imposed strain levels. This is due to elastic deformation in the grain interiors, prior to any accommodation due to dislocation mechanisms (blue) or GB processes (red). However, the fraction of total tensile strain due to fcc atoms continues to decrease with further imposed strain, as contributions of both GBs and dislocations increase. The fraction of strain for fcc atoms in S_3 is much greater than that in S_1. This is due to a higher concentration of GBs and a lower concentration of fcc lattice atoms in the S_1 NC structure, as compared to S_3. In S_1, the fraction of total calculated tensile strain is almost identical for both GBs and lattices in the low strain regime, while in S_3, the contributions are quite different. For GB deformation, contributions are much greater in S_1, showing the influence of grain size on the role of GB processes such as sliding

in the plasticity of NC metals.

At approximately 3 to 4% tensile strain, the role of dislocation mechanisms becomes apparent in all three NC structures. It was stated earlier, that in S_3, dislocation activity is greater than in S_1 at comparable strain levels, and plays a more significant role in the deformation of NC structures. Figure 88 shows quantitative evidence that this is true. The fraction of total calculated strain in the tensile direction is greater for dislocation processes in S_3 than S_1 in all strain regimes studied in this work. As the imposed strain increases, the fraction of strain due to dislocation slip increases. An interesting feature of Figure 88 is the influence of grain size on the behavior of each group shown. For S_3, a larger fraction of the total calculated Green strain in both fcc and dislocation groups is shown as compared to S_1, while for strain accommodation in GBs, the opposite is true. Clearly, as grain size is reduced from 15 nm to 5 nm, and the volume fraction of GBs increases, the role of different mechanisms in both the elastic and plastic deformation of NC metals change accordingly.

6.1.4 Conclusions and Future Work

The objective of this work was to investigate the deformation of NC copper ensembles using atomistic simulations. Microscale kinematic metrics based on continuum mechanics were estimated with atomistic data and leveraged to resolve deformation mechanisms. Three different NC structures were used in this work that vary as a function of the average grain size. It was determined that insight into non-local atomic deformation was provided by analyzing the simulation results with different metrics averaged over nearest neighbors. Differences in the ability of the metrics to capture fundamental deformation processes as compared to traditional employed measures were highlighted with regard to dislocation migration and twinning.

It was demonstrated that microrotation and Green strain, in particular, were able to resolve different deformation mechanisms activated within the NC structures. Distributions of microrotation as a function of imposed strain provide key information concerning the extent of different accommodation mechanisms within various atomic groups, and illustrated their dependence on grain size. As previously discussed, in smaller grained structures GBs

are observed to play a more significant role in deformation and strain accommodation, while lattice strain and dislocation slip are more dominant in larger grained structures. However, utilizing the calculation of Green strain, we were able to estimate the contributions of different mechanisms to the overall strain of the NC structures. The results quantitatively show that the contribution of GBs to tensile strain in smaller grained NC copper is indeed greater than in larger grained NC structures. Furthermore, at low temperatures, dislocation slip continues to be an important strain accommodation mechanism, even in finer grained structures when the fraction of atoms participating in slip is low.

Although these results are promising, and show the potential of the metrics in characterizing vital nanoscale behavior, the extension of the metrics to larger averaging domains is needed. One possibility is through the use of additional neighbor lists, accompanied by weighting functions, while another is to utilize the partitioning of Green strain to formulate deformation and flow rules for dislocation and GB plasticity to the total inelastic strain rate. Future work will consider the potential of the information gathered from such kinematic metrics to inform coarse-grained continuum models of yield and flow in NC materials.

6.2 Tension-Compression Asymmetry

6.2.1 Introduction

Tension-compression asymmetry has been observed in the strength and flow stress of bulk PC materials [129, 315] and NC materials [191, 287, 286]. As grain size is reduced and strain is accommodated by GBs rather than by dislocation migration, research indicates that the degree of asymmetry is altered [38, 100]. Differences in the distribution of underlying deformation mechanisms during both tension and compression are also thought to be major factors in the strength asymmetry behavior [38, 133, 191]. In a recent paper by Lund *et al.* [132], NC nickel (with average grain sizes $< 5nm$) was investigated using MD simulations, where tension-compression asymmetry was observed to be due to disordered grain GB regions and their influence on interfacial strain accommodation. Additional studies utilizing MD simulations have provided complimentary insight into the deformation asymmetry behavior due to GBs and dislocation sources in both NC and NS materials [56, 58]. Since GB

sliding is an important mechanism in the deformation of NC metals [260], additional work has also shown the influence of normal pressure on GB plasticity [25]. Many of these results indicate that GB sliding is inhibited because of a resolved compressive stress state at interfacial regions during compressive loading, leading to higher yield strengths and increased dislocation activity in compression as compared to tension.

Current interest in NC materials is largely due to potential improvements in material functionality, such as enhanced mechanical properties [103, 112]. A maximum in the strength of NC metals has been noted to coincide with a transition from dislocation dominated plasticity to GB-mediated plasticity [187]. However, understanding the distribution of inelastic deformation mechanisms during both tensile and compressive loading and resolving their role in the observed asymmetry is still limited. In the last section [233], we showed that leveraging volume-averaged calculations of microscale continuum metrics from atomistic simulations provided a unique perspective into strain accommodation mechanisms in NC copper. The metrics captured the underlying processes responsible for deformation and provided a new way to quantitatively track their contribution to the overall plastic strain of the NC structure. The objective of the current work is to perform MD simulations of NC copper and investigate the deformation mechanisms behind the observed asymmetry in NC copper for average grain sizes between 5 nm and 15 nm. In addition, we utilize the volume-averaged metric of Green strain to further explore the contribution of the deformation mechanisms to the overall strain of the simulation cell, and relate this behavior to grain size.

6.2.2 Results and Discussion

In this work, we use the three NC structures used in the last section. In addition, simulation cell averages of both the peak and flow stress are used for analysis, computed according to the virial definition [139]. The peak stress is the maximum stress calculated in each simulation parallel to the loading direction, and the flow stress is the average loading stress between 0.07 and 0.10 strain [186, 187]. As Figure 89(a) shows, both the peak (σ_p) and flow stress (σ_f) are greater in compression (open) than in tension (filled) for all three NC

systems. As the average grain size is reduced from 15 nm (S_3) to 5 nm (S_1), a softening behavior is observed under both tension and compression. It is also noteworthy that the large σ_p exhibited in these simulations is likely due to the high imposed strain rate, as discussed by Brandl *et al.* [22]. Figure 89(b) shows a comparison of both σ_p and σ_f as a function of grain size and loading direction.

Under both tension and compression, lower σ_p and σ_f are observed for S_1 than S_3; however, the tension-compression asymmetry in σ_p is less pronounced in S_1 but more pronounced in the computed σ_f. For example, σ_f under tension (σ_f^T) in S_1 is 2.32 GPa and 2.71 GPa under compression (σ_f^C), corresponding to an asymmetry of 1.17 (σ_f^C/σ_f^T), while the σ_f asymmetry in S_3 is 1.15. On the other hand, the σ_p tension-compression asymmetry is greater in S_3 (1.21) than in S_1 (1.14). Since GBs are more abundant and influential on material behavior in S_1 than in S_3, the difference in σ_f asymmetry (as outlined above) indicates the effect of the resolved normal stress on GB and lattice deformation in NC materials. A compressive normal stress (under compression) inhibits the ability of GBs to accommodate strain by sliding and atomic shuffling processes, while a resolved tensile stress (under tension) normal to the boundary can enhance these mechanisms by lowering their activation stress. Similar findings for both homogeneous dislocation nucleation [224] and dislocation nucleation from STGBs [230] have been noted. Therefore, under compression, other deformation mechanisms play a more significant role in accommodating imposed strain.

To explore the role of both partial and full dislocations in strain accommodation, the slip vector [329] of each atom is calculated along with an approximation of its local crystalline structure through the CNA method [63, 232], as performed in the last section. Atoms located within stacking faults, due to partial dislocation glide, will have a slip vector magnitude near the theoretical value of the Burgers vector of a partial dislocation in copper (1.48$\mathring{A}$) and a CNA value of 2 (representing hcp structure). While the slip vector magnitude of atoms that have participated in full slip will be near the theoretical Burgers vector magnitude of a full dislocation (2.56$\mathring{A}$) and be fcc (CNA=1). Defining atomic groups within the simulation cell using this approach enables us to compute the atomic fraction

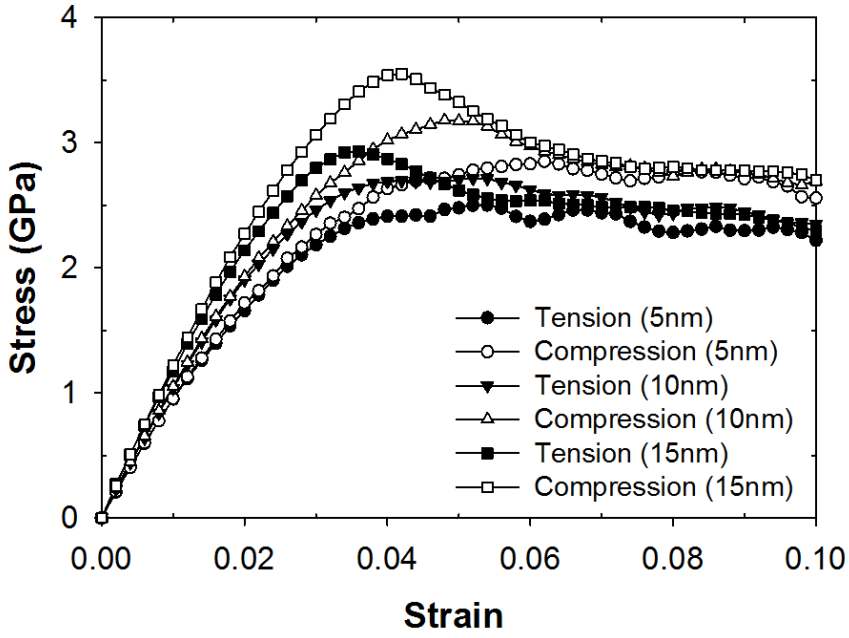

(a)

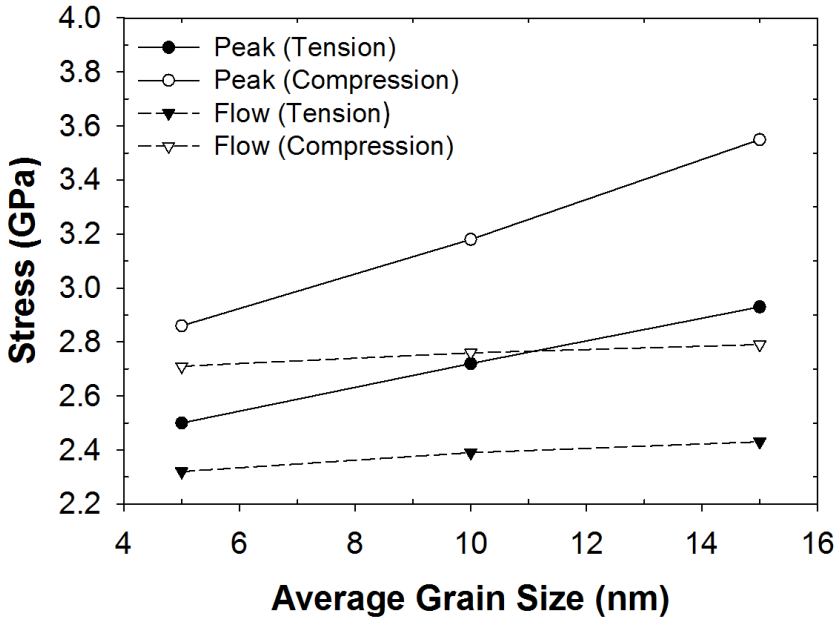

(b)

Figure 89: (a) The stress-strain plots for all three NC structures under both uniaxial tension and compression at 10K. (b) The dependence of both peak (σ_p) and flow (σ_f) stress on average grain size and loading direction.

of atoms participating in dislocation glide as a function of imposed strain. For example, Figure 90 shows the evolution of both (a) partial and (b) full slip under tension (filled) and compression (open) for S_1 (circle), S_2 (triangle), and S_3 (square).

As Figure 90(a) shows, partial slip is more significant in accommodating strain under uniaxial tension in all three NC structures than under compression. In general, partial dislocation slip is more abundant in S_3 than in either S_1 or S_2 under tension (at least until about 0.09 strain), while S_2 shows a larger fraction of atoms participating in partial slip during compression than either S_1 or S_3. In Figure 90(b), the evolution of full slip as a function of strain is shown. The plots in 90(b) display a clear dependence of full slip on grain size. As grain size is reduced, a lower fraction of atoms participate in full slip. This relationship is true under uniaxial tension and compression, but as Figure 90(b) shows, full slip is more favorable under compression than under tension. The work by Tschopp *et al.* [230, 224] demonstrates the importance of resolved normal stress for dislocation nucleation processes, similar to the findings shown here.

The role of GBs, partial and full dislocations, and the lattices in accommodating the imposed tensile or compressive strain can be approximated using the metric of Green strain [233]. Atomic groups identified as Other (primarily composed of GB atoms), dislocations (including both partial and full), and fcc lattices can be distinguished from each other using the calculation of both the slip vector and local crystal structure (i.e., CNA) of each atom. GB atoms are easily identified as atoms with a CNA value of 5. As previously outlined, the Other group contains GB atoms in addition to atoms not located within GBs, but the percentage of atoms not located in GBs is a small percentage and does not influence the results. Atoms that have participated in either partial or full slip are identified through the use of both slip vector and CNA, as previously described. Finally, the fcc lattice group will be all atoms with a CNA value of 1 that have not been included in the dislocation group as a consequence of full dislocation slip.

The Green strain metric [233] for each atom is computed from the calculation of the atomic deformation gradient [236, 330] based on the reference configuration neighbor list and interatomic distance vectors in both the reference and current configurations. The total

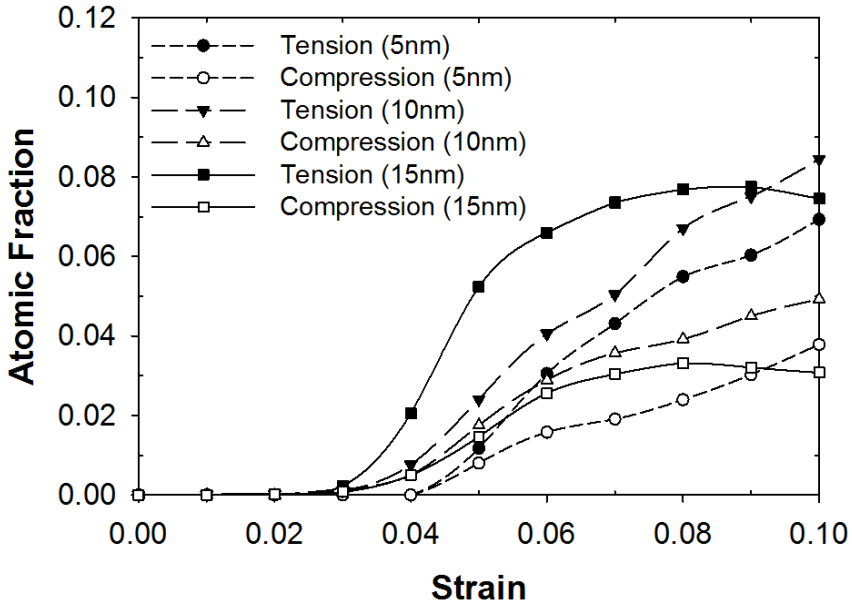

(a)

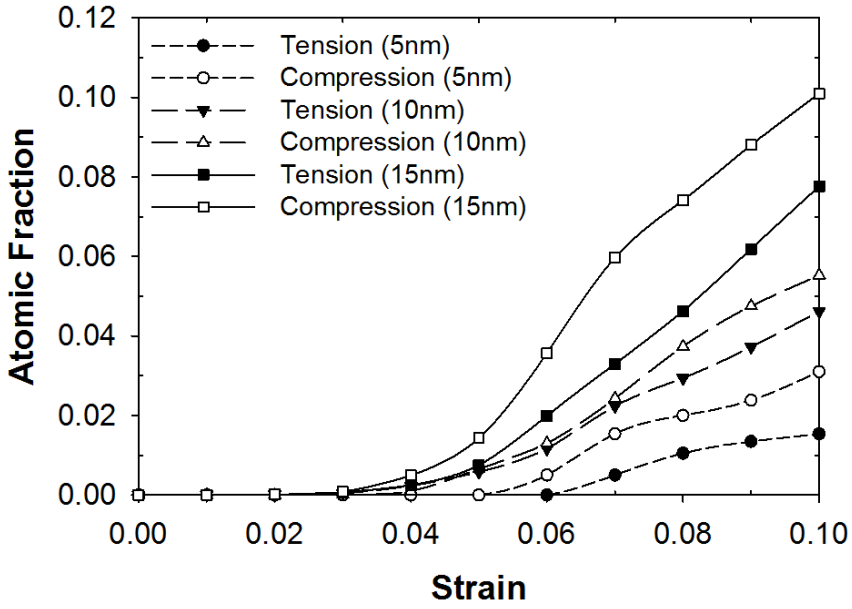

(b)

Figure 90: The evolution of both (a) partial and (b) full slip in the NC structures by tracking the atomic fraction of atoms in each group as a function of imposed strain. Both uniaxial tension (filled) and compression (open) behavior are considered for S_1, S_2, and S_3.

computed Green strain under both tension and compression is calculated by summing the component of each atomic Green strain in the tensile or compressive loading direction for

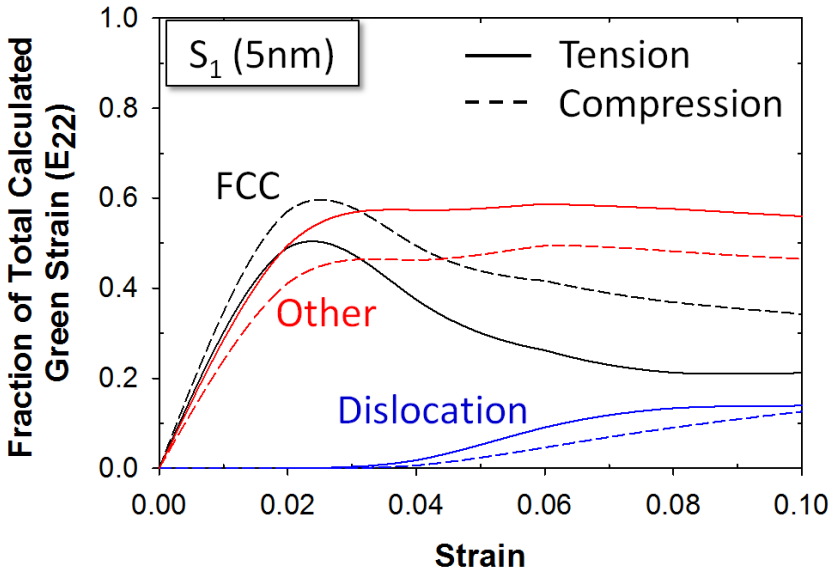

(a)

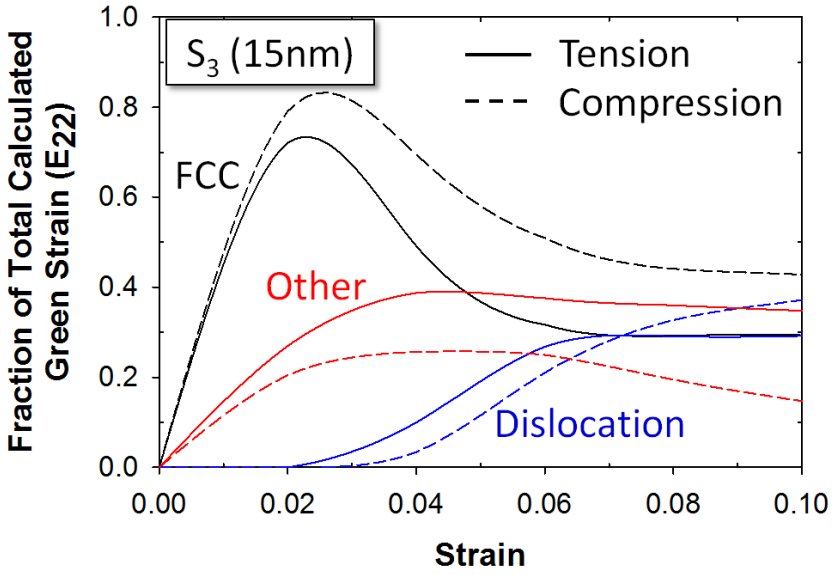

(b)

Figure 91: The computed fraction of Green strain of fcc (black), dislocation (blue), and GB (red) atomic groups in the loading direction as a function of grain size for (a) S_1 (b) S_3. Both tension (solid) and compression (dotted) results are shown as a function of imposed strain.

all atoms in the structure. Then, we resolve the contribution of each atomic group to the total calculated Green strain by summing the component of atomic Green strain in the loading axis direction for all atoms in each group, and normalize by the total computed

Green strain.

The evolution of each atomic group's contribution to the overall strain in the loading direction is shown in Figure 91 for S_1 (a) and S_3 (b). In S_1 (91(a)), the contribution of GBs (i.e., Other) is much greater than dislocation mechanisms (i.e., Dislocation) under both uniaxial tension (solid) and compression (dotted), while the role of the lattice (i.e., FCC) is significant at strains prior to inelastic deformation (i.e., 0.03-0.04 strain). At higher imposed strains (i.e., 0.06-0.10), GBs accommodate the majority of the imposed strains in S_1, but it is more significant in tension than in compression. Dislocation processes account for a small fraction of the overall computed Green strain in both tension and compression, while the role of the lattice is greater in compression than in tension.

For S_3 (91(b)), lattice strain is significant prior to 0.05 imposed strain, and is more significant in compression than in tension, similar to S_1. As straining continues, the role of the lattice in accommodating imposed strain decreases. However, the role of GBs under tension is greater than in compression, and dislocation mechanisms are more significant at higher imposed strains. Under compression, GB deformation is suppressed (similar to S_1) and dislocation mechanisms (such as full slip) continue to be more influential as imposed strain increases. As grain size increases, the role of both the lattice and dislocation glide in accommodating imposed strain becomes more significant.

In both small (i.e., 5 nm) and larger (i.e., 15 nm) average grain sizes, the influence of resolved normal stress on the GBs is evident. By hindering GB deformation via sliding and atomic rearrangement due to a compressive normal stress, both lattice and dislocation processes become more crucial in accommodating imposed strain. This transition in the activated deformation mechanisms due to loading direction is likely the source for the tension-compression asymmetry observed in the strength of NC copper for average grain sizes between 5 nm and 15 nm.

6.2.3 Conclusions

These results show that the resolved normal stress influences both lattice (i.e., partial and full dislocation slip) and GB deformation mechanisms. At smaller grain sizes, where GBs are

about 25% of the total volume [233], GBs play a more significant role in accommodating imposed strain than either lattice strain or dislocation slip. However, under a resolved compressive normal stress (during uniaxial compression), GB deformation is hindered and both lattice strain and dislocation slip become more influential as compared to tensile loading. In larger-grain systems (i.e., S_3), GBs account for a lower fraction of the total Green strain, while both lattice strain and dislocation slip are more significant, but the effect of loading direction and resolved normal stress is similar to S_1 in enhancing full slip and hindering GB deformation. In addition, the competition between partial and full slip in all three NC structures as a function of imposed strain is also influenced by the resolved normal stress. Under a compressive normal resolved stress, partial slip is suppressed while full slip is enhanced. The volume-averaged kinematic metrics utilized in this work provide a unique perspective into the deformation of NC copper and the associated mechanisms responsible for the observed tension-compression asymmetry seen in structures with an average grain size between 5 nm and 15 nm.

As the loading direction changes, the activation of different mechanisms is captured using Green strain and the combination of slip vector and CNA to define different atomic groups. Using this approach, we are also able to resolve the contribution of various strain accommodation processes to the overall strain of the structure. This ability could potentially help larger-scaled models capture fundamental phenomena critical in the deformation of NC materials, including the role of dislocation glide and GBs. Furthermore, this work might lend insight into the mechanistic landscape of NC fcc metals to improve deformation and flow rules. The tools outlined in this work could be leveraged to improve GB flow rules for NC metals that depend on the competition of multiple deformation mechanisms, the resolved stress state, and imposed strain. Future work will include multi-axial loading, higher temperature simulations, and the development of novel metrics to further resolve the deformation and influence of GBs in NC materials.

CHAPTER VII

CONCLUSIONS AND RECOMMENDATIONS

7.1 Overview

The research presented in this dissertation encompasses various aspects of GB structure and deformation, interfacial free volume, inelastic deformation mechanisms, and NC material plasticity. Considerable interest in understanding both GBs and NC materials for materials functionality motivates the work. Furthermore, the influence of nanoscale features and processes on bulk material behavior and the need to capture such phenomena in computational models has directed various aspects of this work. A number of individual studies were undertaken in this dissertation to explore nanoscale structure and deformation in both GBs and NC fcc metals. These studies:

- Employ atomistic simulations to investigate the minimum energy structure and interfacial free volume of $\langle 110 \rangle$ STGBs in fcc metals.
- Employ MD to investigate the evolution of both the structure and free volume during dislocation nucleation in planar bicrystals.
- Investigate the asymmetry in bicrystalline deformation under both tension and compression at low temperatures.
- Use atomistic methods to instantiate NEGBs using excess free volume, and study the influence of NE state on tensile and shear deformation.
- Develop microscale kinematic metrics from continuum mechanics to analyze deformation in atomistic systems.
- Apply the metrics to bicrystalline GBs, and investigate how the metrics provide unique insight nanoscale deformation mechanisms.

- Conduct atomistic simulations to explore the deformation of NC copper, and resolve nanoscale deformation mechanisms with microscale metrics.

Collectively, each of these topics are addressed within the chapters in this thesis, and provide new insight into the structure and deformation of both GBs and NC metals. Each chapter presents the appropriate introduction, computational methodology, results, and discussion of the work. Clearly, each topic is addressed by work presented in this dissertation. Moreover, significant contributions and innovative findings of this research are summarized in the following sections.

7.1.1 The Structure and Free Volume of E Structural Unit Grain Boundaries

Atomistic simulations were employed to study the minimum energy GB structure and associated free volume in ⟨110⟩ copper STGBs. MS with an EAM potential for both copper and aluminum was used to construct the initial 0K bicrystalline boundaries. In-plane rigid body translations and expansion was leveraged to converge on the appropriate interface structure, and the resulting energies were compared with previous measure values from the literature. A new and novel technique for computing interfacial free volume was presented based on a 3D grid and indicator matrix. This approach for computing free volume is beneficial for calculating both one and two-point statistical data within the GB. Also, visualization of the spatial distribution of free volume is easily accessible by this method. The purpose of this research was to relate GB structure and free volume using atomistic simulations. In addition, the correlation between certain structural units composing the GB structure and free volume was discussed. The results have implications on the potential for GBs to evolve differently during deformation based on the free volume.

The significant conclusions of this research include:

1. There is a clear relationship between GB atomic structure and free volume concentration/distribution. Certain structural units (e.g., E) are the source of high free volume in certain groups of ⟨110⟩ STGBs. As interface structure changes with symmetric tilt boundary misorientation angle, free volume changes as well.

2. The Σ9 (221) GB is the favored ⟨110⟩ STGB within the misorientation range of 109.5° to 180°. This boundary is composed entirely of E structural units, where the higher free volume associated with this boundary is due to the E structural unit.

3. All boundaries within this misorientation range contain some fraction of E structural units. The spatial distribution of free volume within the GB plane changes as structure evolves. Free volume becomes more highly connected along the tilt axis as misorientation is increased, and acts as a significant source for partial dislocations under uniaxial tension.

7.1.2 Evolution of Structure and Free Volume During Interfacial Dislocation Nucleation

Minimum energy STGBs (i.e., those boundaries constructed from the research summarized in the previous section) were deformed under uniaxial tension at 10K using MD simulations to probe how both structure and free volume evolve during dislocation nucleation/emission. In all boundaries studied, partial dislocations are emitted from the boundary into the lattices on maximum Schmid factor {111} planes. Different GB geometries and structures were employed in this work to show how certain atomic structural units are more prone for elastic distortion and collapse during dislocation nucleation. Specific attention to the relationship between structural unit geometry and free volume was noted in this work. The method previously outlined for computing free volume was utilized in all GBs studied.

The significant conclusions of this research include:

1. As the atomic interface structures are deformed, the associated free volume packets deform as well. Free volume migration away from nucleation regions within the GB plane is observed during dislocation nucleation. In ⟨110⟩ STGBs, simultaneous migration perpendicular to the tilt axis is observed, while in ⟨100⟩ STGBs, the migration is localized.

2. The E structural units elastically deform prior to dislocation emission and peak tensile stress. In some boundaries the free volume decreases and in other it increases. This

behavior depends on the propensity for the unit to shear deform under the application of tension. It is observed that some interfacial structural units elastically dilate instead of shearing, leading to an increase in free volume prior to dislocation nucleation, instead of a collapse of the free volume packet.

7.1.3 Tension/Compression Asymmetry in E Structural Unit Boundaries

Atomistic simulations were employed in this work to investigate the tension/compression asymmetry in E structural unit ⟨110⟩ STGBs at 10K. Nine different GBs with misorientation angles between 109.5° and 180° were constructed and deformed under both uniaxial tension and compression at a constant strain rate to investigate the inelastic deformation behavior. The mechanical behavior of each boundary was measured and compared under both loading conditions. Dislocation emission from the GBs was detailed, and it was shown that there are stark differences between tension and compression with regard to interfacial strength and dislocation activity. The activated slip planes are found in each bicrystal along with an accompanying discussion about the nature of GB dislocation emission. To understand the nucleation asymmetry under tension and compression, a detailed analysis of the resolved stress states on {111} and {001} slip planes was also provided.

The significant conclusions of this research include:

1. GBs containing the E structural unit are on average about three times stronger in compression than in tension. Under tension, the largest peak stress was observed for boundaries with smaller spacing of the E structural unit along the GB period, indicating a potential influence of GB dislocation sources on emission behavior. Also, quasistatic simulations showed similar elastic behavior and peak stress values as compared to constant strain rate simulations for both uniaxial tension and compression.

2. Partial dislocation nucleation is observed in all boundaries under tension on maximum Schmid factor {111} slip planes. Under uniaxial compression, full dislocations are seen in addition to partial dislocations being emitted into the lattices. However, both

{111} and {100} slip planes are active under compression, while slip under tension only occurs on {111} planes.

3. An investigation into the function of both Schmid and Normal factors on misorientation angle could explain the difference in dislocation emission from GBs. It was found that the normal stress is an influential factor in determining whether partial or full slip is preferred on {111} or {100} slip planes. The resolved normal stress is compressive under compression and tensile under tension; therefore, the evolution of the normal factor with misorientation angle is an integral factor in determining the dislocation nucleation/emission process.

7.1.4 Non-equilibrium Grain Boundary Structure and Deformation

Representative NEGBs were instantiated based on the principle that excess free volume is a useful measure for the degree of NE state of a boundary. Utilizing previously constructed equilibrium GB structures and a biased Monte Carlo approach, high energy GB structures containing excess free volume and defect populations were generated. Compared to their equilibrium counterparts, the newly formed NEGBs contain atomic interfacial regions which are more disordered, excess free volume, and lower atomic density. These attributes are common to NEGBs observed in metallic materials. Different GBs were employed in this work to elucidate the influence of interface structure on the propensity to absorb and disseminate excess free volume. Uniaxial tension and shear deformation were then applied to each boundary of varying NE states. Dislocation nucleation and GB deformation were observed and the influence of NE state on each observed strain accommodation mechanism was discussed.

The significant conclusions of this research include:

1. Using excess free volume, NEGBs can be instantiated within an atomistic framework without simulating heavily deformed structures with numerous GB/defect interactions. The structure, energy, atomic mobility, and free volume of NEGBs differ from

near-equilibrium counterparts in fcc metals. As the NE state increases, the energy and free volume increase as well.

2. Under both uniaxial tension and simple shear deformation at 10K, it is found that the peak stress is a function of the NE state. With excess free volume and higher interfacial energy, the stress required to activate dislocation nucleation and GB deformation processes decreases. However, the elastic stress-strain behavior does not differ for higher NE state boundaries. This trend confirms the fundamental influence of GBs on deformation response within bicrystalline cells, even with slightly perturbed interface structures in an energetically metastable state.

3. The process of dislocation nucleation/emission from GBs differs for NEGBs as compared to near-equilibrium GBs. As the NE state increases, dislocation nucleation becomes more localized, and activates at lower tensile stresses. During shear deformation, both GB sliding and migration are influenced by excess free volume as well. GB sliding is enhanced with excess free volume, and during GB migration, excess interfacial defects pin certain boundary segments momentarily. However, as the boundary migrates, lattice defects are left behind the migrating boundary, transforming the boundary into a lower energy structure.

7.1.5 Formulation of Kinematic Metrics for Atomistic Deformation

Based on the description of an atomic deformation gradient provided previously by Zimmerman *et al.* [330], this work extended the formulation of microscale kinematic metrics from continuum mechanics theory in atomistic simulations. Metrics approximating rotation, vorticity, strain, velocity gradient, and microrotation were defined. Utilizing a volume-averaging scheme for each metric, nonlocal nanoscale deformation behavior was extracted from atomistic simulation data, as shown. Two-dimensional bicrystalline boundaries were deformed under shear to identify the utility of these metrics in identifying unique deformation fields that corresponds to each mechanism. Three different boundaries were

constructed according to different disorientation angles and shown to deform via GB dissociation, GB sliding, and GB migration. The deformed states were analyzed with the metrics and significant insight was gained into the nonlocal deformation fields associated with each accommodation mechanism.

Three-dimensional copper bicrystals were constructed and deformed under both uniaxial tension and simple shear to activate different mechanisms common to NC metals. In particular, the mechanisms observed were heterogeneous dislocation nucleation, GB sliding, and GB migration. These mechanisms are important in the deformation behavior of NC metals; therefore, the application of the metrics in analyzing their deformation fields, is crucial for understanding the utility of the metrics. Under uniaxial tension, the $\Sigma 5$ (310) STGB nucleated partial dislocations into the lattices with a trailing stacking fault connected to the boundary. To investigate GB sliding, the $\Sigma 9$ (221) boundary was deformed under simple shear, and the coherent twin boundary ($\Sigma 3$ (111)) and $\Sigma 129$ (881) were deformed under shear to activate GB migration. The reason two different boundaries were investigated for GB migration is because the atomic processes behind the migration of each GB differs. As discussed, the application of the metrics in resolving the deformation and rotation fields highlights the differences in the migration process, and displays the potential of the metrics in distinguishing detailed behavior at the nanoscale.

The significant conclusions of this research include:

1. Volume-averaged kinematic metrics were estimated from atomistic simulation data using interatomic strain calculations in both the current and reference configurations. Utilizing the minimization of the squared errors approach (as described in [330]), metrics other than the deformation gradient from continuum mechanics theory were calculated.

2. Using the reference structure, some kinematic metrics provided detailed insight into the deformation fields associated with GB deformation. Furthermore, current neighbor lists and atomic quantities were used in other non-local calculations to estimate current deformation behavior.

3. The extent of non-locality can be extended in these calculations by including additional neighbors in the volume-averaging scheme, but as discussed, this inclusion must be accompanied by some sort of weighting function on the additional neighbors.

4. During GB dislocation nucleation, the metrics provided new insight into the deformation of both GB regions and lattice regions adjacent to the emitted dislocation. Microrotation showed lattice distortion near the partial dislocation, while vorticity highlighted the current deformation associated with the dislocation core.

5. During GB sliding, deformation did not reach lattice regions far away from the GB. By applying the volume-averaged metrics, additional insight was gained concerning the dilatation and microrotation near high free volume regions in the GB. Higher free volume regions, such as those associated with the E structural unit, might enhance local microrotation displaying their role in the nucleation process.

6. Differences in the migration of GBs normal to their plane were uncovered using the metrics of microrotation and dilatation. For the glide of twinning disconnections, relatively uniform deformation and rotation fields were observed; however, for the migration of the GB dislocation core structures, both the microrotation and dilatation metrics showed the path of the cores. The ability of the metrics to highlight these differences is due to both the volume-averaging and dependence on reference configuration quantities (i.e., neighbor lists and interatomic distances).

7.1.6 Atomistic Simulations of Nanocrystalline Deformation

Three-dimensional NC structure containing 25 grains were deformed under uniaxial tension at a constant strain rate to elucidate the influence of grain size on behavior. Average grain size ranged from 5 nm to 15 nm, and was the only difference between the NC structures. Grain morphologies and lattice orientations were identical for each structure. It was shown that as grain size is reduced, GBs constitute a larger volume fraction of the simulation cell. The uniaxial tension stress-strain plots showed that average grain size influences both

the peak and flow stress at 10K, where 'softening' is observed with decreasing grain size. Dislocation and GB activity during deformation was investigated using calculations of slip vector and CNA. As imposed strain increases, the role of GBs in accommodating strain differs as a function of grain size. GB deformation in the smaller grained structure is more prevalent than in the larger grained structure, while dislocation activity is more prevalent in the larger grained structure as compared to the smaller grained structure. The deformation in the NC structures was also investigated using the volume-averaged kinematic metrics previously outlined. Finally, the tension-compression asymmetry is explored in these three NC structure under uniaxial loading at 10K. The metrics are used to investigate the deformation mechanisms behind the asymmetry, and resolve their contribution to the overall strain as a function of grain size.

The significant conclusions of this research include:

1. The tensile response of the NC structures is influenced by average grain size. Smaller grains led to a higher volume fraction of GBs, and GB deformation dictates strain accommodation in the smaller grained NC structures.

2. Dislocations are more abundant in the larger grained structure, and are therefore more influential in accommodating imposed strain as compared to the smaller grained structure.

3. The evolution of both partial and full slip as a function of imposed strain and average grain size was also investigated. In all three NC structures, partial slip is more abundant than full slip under tension, and the fraction of each tends to rise with increasing imposed strain.

4. The distribution of microrotation for different atomic groups (i.e., lattice, GBs, and dislocations) showed potential in identifying the evolution of different mechanisms as a function of imposed strain. In other words, microrotation is able to capture the different accommodation mechanisms common in NC metals (e.g., partial slip, full slip, twinning, and GB deformation); therefore, its distribution uncovers the evolution of the different deformation mechanisms.

5. The role of different atomic groups and their associated mechanisms in the overall strain of the NC structure can be resolved using the Green strain metric. By partitioning the NC structure into different atomic groups (e.g., fcc lattice, GBs, and dislocations), the fraction of strain due to each group can be quantitatively tracked as a function of grain size and imposed strain.

6. Tension-compression asymmetry in the NC structures was shown to be dependent on the grain size and be a consequence of activating different mechanisms due to the resolved normal stress. Full dislocations were more abundant under compression than tension, and the role of GBs in accommodating strain was lower as well. The Green strain metric was again utilized to partition the contribution of different mechanisms in accommodating imposed strain. Under compression, the role of GBs was suppressed, while the contribution from both the lattices and dislocation processes were enhanced as compared to under tension.

7.1.7 Novel Contributions and Findings of this Research

Research conducted in this thesis utilized atomistic simulations and multiple post-processing algorithms to investigate the deformation behavior of both GBs and NC metals. The goal of the interface studies was to elucidate structure and free volume in symmetric tilt GBs in fcc metals and explore the resulting mechanical properties under tension, compression, and shear. In simulations of NC structures, newly developed volume-averaged metrics were leveraged to provide insight into the myriad of deformation mechanisms and explore their contribution to the overall strain accommodation as a function of grain size and loading conditions. Collectively, this thesis has answered many fundamental questions and addressed the issues outlined in Chapter 1; however, the major accomplishments of this work include:

- Specific correlations were explored with atomistic simulations between interface structure and free volume in homogeneous fcc symmetric tilt GBs. A new technique was developed for computing free volume in GB regions. The free volume associated with

certain atomic structural units was found to affect dislocation nucleation under tension, and GB sliding under shear. Also, the evolution of free volume varied for different GBs, and the migration of free volume within the GB was quantitatively measured during dislocation nucleation.

- The instantiation of representative NEGBs using a biased Monte Carlo method was outlined where excess free volume was added to the GB, as compared to the equilibrium GB free volume concentration. Simulations showed that excess interfacial free volume significantly influences both GB structure and deformation under uniaxial tension and shear at 10K. Specifically, the strength of bicrystalline boundaries decreases under tension and shear as the NE state of the GB increases with excess free volume. In addition, dislocation nucleation becomes localized in the boundary and migrating interfaces are initially pinned by extrinsic defects in GBs with excess free volume.

- Volume-averaged kinematic metrics defining aspects of atomic deformation, strain, and vorticity were developed and shown to provide unique insight into nonlocal nanoscale deformation in atomistic simulation data. Specific deformation fields in NC copper were analyzed with the metrics, and the distribution of the various strain accommodation mechanisms was estimated using microrotation. Furthermore, using the Green strain metric, the contributions from different mechanisms and atomic groups to the overall strain of the NC structures was calculated as a function of both grain size and imposed strain.

7.2 Recommendations for Future Work

The results of atomistic simulations shown in this dissertation provide a wealth of information concerning the deformation of both GBs and NC metals. Furthermore, we have shown that atomistic simulations are capable of providing information regarding the role of interface structure on GB plasticity, and nanoscale phenomena critical for understanding the mechanical behavior of NC metals. The volume-averaged metrics outlined in this work have also provided significant insight into deformation mechanisms common to NC metals, and

displayed the potential to link nanoscale behavior with coarse-grained models. Although this dissertation has addressed the questions listed in Chapter 1, additional questions and issues remain. Some possible extensions of work conducted in this dissertation and future directions are as follows:

- In this work, symmetric tilt GBs were investigated with regard to the relationship between structure, free volume, and inelastic deformation behavior. Extending these investigations to include asymmetric tilt boundaries would be useful. Preliminary studies on asymmetric tilt GBs by Tschopp *et al.* [225, 221, 223, 222, 220] have shown interesting behavior and structure of asymmetric tilt GBs as compared to symmetric tilt GBs. However, the distribution of free volume and its evolution during dislocation nucleation is warranted in these boundaries as well. Research areas such as GBE would benefit greatly from further atomistic studies of asymmetric tilt GBs, twist GBs, and general HAGBs with combined tilt/twist character regarding structure-property relationships, free volume, and tension-compression asymmetry. Additionally, GBs in real materials will have more complex resolved stress states than those utilized in this work. In this dissertation, we only address uniaxial tension/compression and simple shear of bicrystalline GBs. Further work exploring the influence of resolved normal stress on the shear behavior of GBs is needed. Also, it is not known how the applied shear direction can influence GB behavior. GBs would likely experience shear stresses not necessarily parallel to the GB period direction, but in other in-plane directions.

- As discussed in this dissertation, NEGBs are important when considering materials that have undergone SPD. However, the work here only address two specific symmetric tilt GBs in copper and aluminum. Additional boundaries should be considered (i.e., general HAGBs), and be related to the influence of NE state on strain accommodation mechanisms. Dislocation-GB interactions is an additional area of importance that should be addressed regarding NEGBs. The absorption and transmission of lattice dislocations with GBs is a common phenomenon in materials with initial lattice defect concentrations and mobile interfaces. It is not known how the NE state and excess

free volume inherent to NEGBs would influence the absorption and/or transmission of impinging dislocations. Related to NEGBs and their excess free volume, it would also be worthwhile to investigate the distribution and migration of interfacial free volume in NC structures. Excess interfacial free volume will alter the mechanical behavior of NC systems through modified GB plasticity. An interesting problem to explore with atomistic simulations concerns the influence of GB state and network on free volume evolution in NC structures under multiple loading conditions. Furthermore, the ability of TJs to act as a source or sink for free volume can be investigated leveraging our method for computing free volume in conjunction with the generated NC structures with varying average grain size.

- The combination of MD simulation results and the applied kinematic metrics provided in this thesis on NC metals have provided a foundation for further studies. It is not known the influence of temperature on the tension-compression asymmetry investigated in this work. The role of GBs and interfacial mechanisms on NC strain accommodation to be significantly altered with higher temperatures. In addition, the affect of impurities on deformation mechanisms and GB plasticity is still largely unknown. MD simulations investigated GB mobility and growth as a function of GB network character is still needed. Finally, we have shown that detailed kinematical information can be extracted from MD simulations using volume-averaged metrics from continuum mechanics theory. However, a framework is needed for translating the nanoscale information obtained from the kinematic metrics or modification of existing deformation and GB flow rules for continuum models aiming to explore NC materials.

REFERENCES

[1] Aaron, H. and Bolling, G., "Free volume as a guide to grain boundary phenomena.," *Scripta Metallurgica*, vol. 6, no. 7, pp. 553 – 561, 1972.

[2] Agnew, S., Elliott, B., Youngdahl, C., Hemker, K., and Weertman, J., "Microstructure and mechanical behavior of nanocrystalline metals," *Materials Science and Engineering A*, vol. 285, no. 1, pp. 391 – 396, 2000.

[3] Aifantis, K. and Willis, J., "The role of interfaces in enhancing the yield strength of composites and polycrystals," *Journal of the Mechanics and Physics of Solids*, vol. 53, pp. 1047–1070, 2005.

[4] Alder, B. and Wainwright, T., "Studies in molecular dynamics. 1. general method," *Journal of Chemical Physics*, vol. 31, pp. 459–466, 1959.

[5] Alder, B. and Wainwright, T., "Phase transformations for a hard sphere system," *Journal of Chemical Physics*, vol. 31, pp. 1208–1209, 1957.

[6] Allen, M. and Tildesley, D., *Computer Simulations of Liquids*. Oxford: Clarendon Press, 1987.

[7] Anciaux, G. and Molinari, J. F., "Sliding of rough surfaces and energy dissipation with a 3D multiscale approach," *International Journal for Numerical Methods in Engineering*, vol. 83, no. 8-9, pp. 1255–1271, 2010.

[8] Anderoglu, O., Misra, A., Wang, J., Hoagland, R., Hirth, J., and Zhang, X., "Plastic flow stability of nanotwinned Cu foils," *International Journal of Plasticity*, vol. 26, no. 6, pp. 875 – 86, 2010.

[9] Ashby, M., Spaepen, F., and Williams, S., "Structure of grain boundaries described as a packing of polyhedra," *Acta Metallurgica*, vol. 26, no. 11, pp. 1647 – 1663, 1978.

[10] Barai, P. and Weng, G. J., "Mechanics of very fine-grained nanocrystalline materials with contributions from grain interior, gb zone, and grain-boundary sliding," *International Journal of Plasticity*, vol. 25, no. 12, pp. 2410 – 2434, 2009.

[11] Baskes, M., "Application of the embedded-atom method to covalent materials: A semiempirical potential for silicon," *Physical Review Letters*, vol. 59, pp. 2666–2669, 1987.

[12] Baskes, M., "Modified embedded-atom method potentials for cubic materials and impurities," *Physical Review B*, vol. 46, pp. 2727–2742, 1992.

[13] Baskes, M. and Johnson, R., "Modified embedded atom potentials for hcp metals," *Modelling and Simulation in Materials Science and Engineering*, vol. 2, pp. 147–163, 1994.

[14] Baskes, M., Nelson, J., and Wright, A., "Semiempirical modified embedded-atom method potentials for silicon and germanium," *Physical Review B*, vol. 40, pp. 6085–6100, 1989.

[15] Bayer, F., Fischer-Buhner, J., and Gottstein, G., "Mechanisms of compatible deformation in NiAl-bicrystals," *Intermetallics*, vol. 7, no. 3, pp. 467 – 478, 1999.

[16] Benson, D. J., Fu, H.-H., and Meyers, M. A., "On the effect of grain size on yield stress: extension into nanocrystalline domain," *Materials Science and Engineering A*, vol. 319-321, pp. 854–861, 2001.

[17] Bitzek, E., Derlet, P., Anderson, P., and Van Swygenhoven, H., "The stress-strain response of nanocrystalline metals: A statistical analysis of atomistic simulations," *Acta Materialia*, vol. 56, no. 17, pp. 4846 – 4857, 2008.

[18] Bobylev, S. V., Gutkin, M. Y., and Ovid'ko, I. A., "Partial and split dislocation configurations in nanocrystalline metals," *Physical Review B*, vol. 73, pp. 064102:1–8, 2005.

[19] Bobylev, S., Mukherjee, A., and Ovidko, I., "Emission of partial dislocations from amorphous intergranular boundaries in deformed nanocrystalline ceramics," *Scripta Materialia*, vol. 60, no. 1, pp. 36 – 9, 2009.

[20] Bohn, R., Oehring, M., Pfullmann, T., Appel, F., and Bormann, R., "Mechanical properties of nanocrystalline TiAl-based intermetallics," *Processing and Properties of Nanocrystalline Materials*, pp. 355 – 366, 1996.

[21] Boyer, R., Li, J., Ogata, S., and Yip, S., "Analysis of shear deformations in Al and Cu: empirical potentials versus density functional theory," *Modelling and Simulation in Materials Science and Engineering*, vol. 12, no. 5, pp. 1017–1029, 2004.

[22] Brandl, C., Derlet, P. M., and Van Swygenhoven, H., "Strain rates in molecular dynamics simulations of nanocrystalline metals," *Philosophical Magazine*, vol. 89, no. 34-36, pp. 3465 – 3475, 2009.

[23] Brandon, D. G., "The structure of high-angle grain boundaries," *Acta Metallurgica*, vol. 14, no. 11, pp. 1479–1484, 1966.

[24] Bringa, E. M., Caro, A., Wang, Y. M., Victoria, M., McNaney, J. M., Remington, B. A., Smith, R. F., Torralva, B. R., and Van Swygenhoven, H., "Ultrahigh strength in nanocrystalline materials under shock loading," *Science*, vol. 309, no. 5742, pp. 1838–1841, 2005.

[25] Bringa, E., Caro, A., and Leveugle, E., "Pressure effects on grain boundary plasticity in nanophase metals," *Applied Physics Letters*, vol. 89, no. 2, pp. 23101 – 1, 2006.

[26] Broughton, J., Abraham, F., Bernstein, N., and Kaxiras, E., "Concurrent coupling of length scales: Methodology and application," *Physical Review B (Condensed Matter)*, vol. 60, no. 4, pp. 2391 – 403, 1999.

[27] Buehler, M., *Atomistic Modeling of Materials Failure*. Springer, 2008.

[28] Buehler, M., Hartmaier, A., Gao, H., Duchaineau, M., and Abraham, F., "Atomic plasticity: description and analysis of a one-billion atom simulation of ductile materials failure," *Computer Methods in Applied Mechanics and Engineering*, vol. 193, no. 48-51, pp. 5257–5282, 2004.

[29] Cahn, J. W., Mishin, Y., and Suzuki, A., "Coupling grain boundary motion to shear deformation," *Acta Materialia*, vol. 54, no. 19, pp. 4953–4975, 2006.

[30] Cao, A., Wei, Y., and Ma, E., "Grain boundary effects on plastic deformation and fracture mechanisms in Cu nanowires: molecular dynamics simulations," *Physical Review B (Condensed Matter and Materials Physics)*, vol. 77, no. 19, pp. 195429 – 1, 2008.

[31] Capolungo, L., Benkassem, S., Cherkaoui, M., and Qu, J., "Self-consistent scale transition with imperfect interfaces: Application to nanocrystalline materials," *Acta Materialia*, vol. 56, no. 7, pp. 1546 – 1554, 2008.

[32] Capolungo, L., Jochum, C., Cherkaoui, M., and Qu, J., "Homogenization method for strength and inelastic behavior of nanocrystalline materials," *International Journal of Plasticity*, vol. 21, pp. 67–81, 2005.

[33] Capolungo, L., Spearot, D., Cherkaoui, M., McDowell, D., Qu, J., and Jacob, K., "Dislocation nucleation from bicrystal interfaces and grain boundary ledges: Relationship to nanocrystalline deformation," *Journal of the Mechanics and Physics of Solids*, vol. 55, no. 11, pp. 2300 – 2327, 2007.

[34] Carter, C. and Ray, I., "On the stacking-fault energies of copper alloys," *Philosophical Magazine*, vol. 35, no. 1, pp. 189 – 200, 1977.

[35] Chen, J., Wang, W., Qian, L., and Lu, K., "Critical shear stress for onset of plasticity in nanocrystalline Cu determined by using nanoindentation," *Scripta Materialia*, vol. 49, pp. 645–650, 2003.

[36] Chen, M., Ma, E., Hemker, K. J., Sheng, H., Wang, Y., and Cheng, X., "Deformation twinning in nanocrystalline aluminum," *Science*, vol. 300, pp. 1275–1277, 2003.

[37] Cheng, S., Ma, E., Wang, Y. M., Kecskes, L. J., Youssef, K. M., Koch, C. C., Trociewitz, U. P., and Han, K., "Tensile properties of in situ consolidated nanocrystalline Cu," *Acta Materialia*, vol. 53, no. 5, pp. 1521–1533, 2005.

[38] Cheng, S., Spencer, J., and Milligan, W., "Strength and tension/compression asymmetry in nanostructured and ultrafine-grain metals," *Acta Materialia*, vol. 51, no. 15, pp. 4505 – 4518, 2003.

[39] Chokshi, A. H., Rosen, A., Karch, J., and Gleiter, H., "On the validity of the Hall-Petch relationship in nanocrystalline materials," *Scripta Metallurgica*, vol. 23, no. 10, pp. 1679–84, 1989.

[40] Chuvil'deev, V., "Micromechanisms of deformation-stimulated grain boundary self-diffusion. communication 1. Influence of excess free volume on free energy and diffusion parameters of grain boundaries," *Fizika Metallov i Metallovedenie*, vol. 81, no. 4, pp. 6 – 13, 1996.

[41] Chuvil'deev, V., "Effect of grain-boundary free volume on the deformation behavior of materials under conditions of superplasticity," *Physics of Metals and Metallography*, vol. 86, no. 5, pp. 521 – 7, 1998.

[42] Chuvil'deev, V., Kopylov, V., and Zeiger, W., "A theory of non-equilibrium grain boundaries and its applications to nanoand micro-crystalline materials processed by ECAP," *Annales de Chimie (Science des Materiaux)*, vol. 27, no. 3, pp. 55 – 64, 2002.

[43] Couzinià, J. P., Dècamps, B., and Priester, L., "Interaction of dissociated lattice dislocations with a Σ3 grain boundary in copper," *International Journal of Plasticity*, vol. 21, no. 4, pp. 759–75, 2005.

[44] Dalla Torre, F., Van Swygenhoven, H., Schaublin, R., Spatig, P., and Victoria, M., "Mechanical behaviour of nanocrystalline electrodeposited Ni above room temperature," *Scripta Materialia*, vol. 53, no. 1, pp. 23–27, 2005.

[45] Dao, M., Lu, L., Asaro, R., De Hosson, J., and Ma, E., "Toward a quantitative understanding of mechanical behavior of nanocrystalline metals," *Acta Materialia*, vol. 55, no. 12, pp. 4041 – 4065, 2007.

[46] Daw, M. S. and Baskes, M. I., "Semiempirical, quantum mechanical calculation of hydrogen embrittlement in metals," *Physical Review Letters*, vol. 50, no. 17, pp. 1285–8, 1983.

[47] Daw, M. S. and Baskes, M. I., "Embedded-atom method: derivation and application to impurities, surfaces, and other defects in metals," *Physical Review B*, vol. 29, no. 12, pp. 6443–53, 1984.

[48] Daw, M. S., Foiles, S. M., and Baskes, M. I., "The embedded-atom method - a review of theory and applications," *Materials Science Reports*, vol. 9, no. 7-8, pp. 251–310, 1993.

[49] Delogu, F., "Dynamics of atomic species involved in shear-induced displacements at sliding symmetrical grain boundaries: A numerical study," *Journal of Physics Condensed Matter*, vol. 19, no. 9, pp. 096008 –, 2007.

[50] den Buekal, A. V., *Vacancies and Interstitials of Metals*. North Holland Publishing Company, 1969.

[51] Derlet, P. M., Frøseth, A. G., and Van Swygenhoven, H., "Vicinal twin boundaries providing dislocation sources in nanocrystalline Al," *Scripta Materialia*, vol. 54, no. 3, pp. 477–81, 2006.

[52] Derlet, P. M. and Van Swygenhoven, H., "Length scale effects in the simulation of deformation properties of nanocrystalline metals," *Scripta Materialia*, vol. 47, no. 11, pp. 719–24, 2002.

[53] Derlet, P. M. and Van Swygenhoven, H., "The role played by two parallel free surfaces in the deformation mechanism of nanocrystalline metals: A molecular dynamics simulation," *Philosophical Magazine A*, vol. 82, no. 1, pp. 1–15, 2002.

[54] Derlet, P. M. and Van Swygenhoven, H., "Atomic positional disorder in fcc metal nanocrystalline grain boundaries," *Physical Review B*, vol. 67, no. 1, pp. 14202–1, 2003.

[55] Derlet, P. M., Van Swygenhoven, H., and Hasnaoui, A., "Atomistic simulation of dislocation emission in nanosized grain boundaries," *Philosophical Magazine*, vol. 83, pp. 3569–3575, 2003.

[56] Diao, J., Gall, K., and Dunn, M., "Yield strength asymmetry in metal nanowires," *Nano Letters*, vol. 4, no. 10, pp. 1863 – 7, 2004.

[57] Dimiduk, D., Woodward, C., LeSar, R., and Uchic, M., "Scale-free intermittent flow in crystal plasticity," *Science*, vol. 312, pp. 1188–1190, 2006.

[58] Dongare, A. M., Rajendran, A. M., Lamattina, B., Zikry, M. A., and Brenner, D. W., "Tension-compression asymmetry in nanocrystalline Cu: High strain rate vs. quasi-static deformation," *Computational Materials Science*, vol. 49, no. 2, pp. 260 – 265, 2010.

[59] Ercolessi, F. and Adams, J. B., "Interatomic potentials from first-principles calculations: the force-matching method," *Europhysics Letters*, vol. 26, no. 8, pp. 583–8, 1994.

[60] Eringen, A. C., *Microcontinuum Field Theories I: Foundations and Solids*. New York, NY: Springer-Verlag New York Inc., 1999.

[61] Eringen, A. C., *Nonlocal Continuum Field Theories*. New York, NY: Springer-Verlag New York Inc., 2002.

[62] Ertorer, O., Topping, T., Li, Y., Moss, W., and Lavernia, E., "Enhanced tensile strength and high ductility in cryomilled commercially pure titanium," *Scripta Materialia*, vol. 60, no. 7, pp. 586 – 9, 2009.

[63] Faken, D. and Jonsson, H., "Systematic analysis of local atomic structure combined with 3D computer graphics," *Computational Materials Science*, vol. 2, no. 2, pp. 279 – 286, 1994.

[64] Farkas, D. and Hyde, B., "Improving the ductility of nanocrystalline bcc metals," *Nano Letters*, vol. 5, no. 12, pp. 2403–2407, 2005.

[65] Farkas, D., "Fracture mechanisms of symmetrical tilt grain boundaries," *Philosophical Magazine Letters*, vol. 80, no. 4, pp. 229 – 237, 2000.

[66] Farkas, D., Froseth, A., and Van Swygenhoven, H., "Grain boundary migration during room temperature deformation of nanocrystalline Ni," *Scripta Materialia*, vol. 55, no. 8, pp. 695 – 698, 2006.

[67] Farkas, D., Mohanty, S., and Monk, J., "Strain-driven grain boundary motion in nanocrystalline materials," *Materials Science and Engineering A*, vol. 493, no. 1-2, pp. 33 – 40, 2008.

[68] Farkas, D., Nogueira, R., Ruda, M., and Hyde, B., "Atomistic simulations of the effects of segregated elements on grain-boundary fracture in body-centered-cubic Fe," *Metallurgical and Materials Transactions A: Physical Metallurgy and Materials Science*, vol. 36, no. 8, pp. 2067 – 2072, 2005.

[69] Farrokh, B. and Khan, A. S., "Grain size, strain rate, and temperature dependence of flow stress in ultra-fine grained and nanocrystalline Cu and Al: Synthesis, experiment, and constitutive modeling," *International Journal of Plasticity*, vol. 25, no. 5, pp. 715 – 732, 2009.

[70] Feynman, R., "There's plenty of room at the bottom: An invitation to enter a new world of physics.," February 1959.

[71] Foiles, S. M., Baskes, M. I., and Daw, M. S., "Embedded-atom-method functions for the FCC metals Cu, Ag, Au, Ni, Pd, Pt, and their alloys," *Physical Review B*, vol. 33, no. 12, pp. 7983–91, 1986.

[72] Fougere, G., Riester, L., Ferber, M., Weertman, J., and Siegel, R., "Young's modulus of nanocrystalline Fe measured by nanoindentation," *Materials Science and Engineering A*, vol. A204, no. 1-2, pp. 1 – 6, 1995.

[73] Franca, L., "Algorithm to compute the square root of a 3×3 positive definite matrix," *Computers & Mathematics with Applications*, vol. 18, no. 5, pp. 459 – 466, 1989.

[74] Froseth, A., Van Swygenhoven, H., and Derlet, P. M., "The influence of twins on the mechanical properties of nc-Al," *Acta Materialia*, vol. 52, no. 8, pp. 2259–2268, 2004.

[75] Frøseth, A. G., Derlet, P. M., and Van Swygenhoven, H., "Dislocations emitted from nanocrystalline grain boundaries: nucleation and splitting distance," *Acta Materialia*, vol. 52, no. 20, pp. 5863–70, 2004.

[76] Froseth, A. G., Derlet, P. M., and Van Swygenhoven, H., "Dislocations emitted from nanocrystalline grain boundaries: nucleation and splitting distance," *Acta Materialia*, vol. 52, no. 20, pp. 5863–5870, 2004.

[77] Frøseth, A. G., Derlet, P. M., and Van Swygenhoven, H., "Vicinal twin boundaries providing dislocation sources in nanocrystalline Al," *Scripta Materialia*, vol. 54, no. 3, pp. 477–481, 2006.

[78] Frøseth, A. G., Van Swygenhoven, H., and Derlet, P. M., "Developing realistic grain boundary networks for use in molecular dynamics simulations," *Acta Materialia*, vol. 53, no. 18, pp. 4847–4856, 2005.

[79] Frøseth, A. G., Derlet, P. M., and Van Swygenhoven, H., "Twinning in nanocrystalline fcc metals," *Advanced Engineering Materials*, vol. 7, no. 1-2, pp. 16–20, 2005.

[80] Gleiter, H., "Nanocrystalline materials," *Progress in Materials Science*, vol. 33, no. 4, pp. 223–315, 1989.

[81] Gleiter, H., "Nanostructured materials," *Advanced Materials*, vol. 4, no. 7-8, pp. 474–481, 1992.

[82] Gleiter, H., "Nanostructured materials: Basic concepts and microstructure," *Acta Materialia*, vol. 48, no. 1, pp. 1–29, 2000.

[83] Gokhale, A. M., Tewari, A., and Garmestani, H., "Constraints on microstructural two-point correlation functions," *Scripta Materialia*, vol. 53, no. 8, pp. 989–93, 2005.

[84] Guduru, R. K., Murty, K. L., Youssef, K. M., Scattergood, R. O., and Koch, C. C., "Mechanical behavior of nanocrystalline copper," *Materials Science and Engineering A*, vol. 463, no. 1-2, pp. 14 – 21, 2007.

[85] Gullett, P., Horstemeyer, M., Baskes, M., and Fang, H., "A deformation gradient tensor and strain tensors for atomistic simulations," *Modelling and Simulation in Materials Science and Engineering*, vol. 16, no. 1, p. 015001, 2008.

[86] Hahn, W. and Gleiter, H., "On the structure of vacancies in grain boundaries," *Acta Metallurgica*, vol. 29, no. 4, pp. 601 – 6, 1981.

[87] Hall, E., "The deformation and aging of mild steel," *Proceedings of the Royal Society of London B*, vol. 64, p. 747, 1951.

[88] Hartford, J., von Sydow, B., Wahnstrom, G., and Lundqvist, B. I., "Peierls barriers and stresses for edge dislocations in Pd and Al calculated from first principles," *Physical Review B*, vol. 58, no. 5, pp. 2487–2496, 1998.

[89] Hasnaoui, A., Derlet, P. M., and Van Swygenhoven, H., "Interaction between dislocations and grain boundaries under an indenter - a molecular dynamics simulation," *Acta Materialia*, vol. 52, no. 8, pp. 2251–2258, 2004.

[90] Heinisch, H., Hoagland, R., Kurtz, R., and Hirth, J., "Computer simulation of a [110] edge dislocation intersecting a $\Sigma 11$ $\langle 101 \rangle$ $\{131\}$ grain boundary in aluminum," *Scripta Materialia*, vol. 39, no. 4-5, pp. 451 – 456, 1998.

[91] Hirth, J., Hoagland, R., and Kurtz, R., "Motion of multiple height ledges and disconnections in phase transformations," *Metallurgical and Materials Transactions A: Physical Metallurgy and Materials Science*, vol. 29 A, no. 8, pp. 2033 – 2038, 1998.

[92] Hirth, J. and Lothe, J., *Theory of Dislocations*. New York: John Wiley and Sons, 1982.

[93] Hirth, J. and Pond, R., "Steps, dislocations and disconnections as interface defects relating to structure and phase transformations," *Acta Materialia*, vol. 44, no. 12, pp. 4749 – 4763, 1996.

[94] Horita, Z., Smith, D. J., Furukawa, M., Nemoto, M., Valiev, R. Z., and Langdon, T. G., "Investigation of grain boundaries in submicrometer-grained Al-Mg solid solution alloys using high-resolution electron microscopy," *Journal of Materials Research*, vol. 11, no. 8, pp. 1880 – 1890, 1996.

[95] Horita, Z., Smith, D. J., Nemoto, M., Zaliev, R. Z., and Langdon, T. G., "Observations of grain boundary structure in submicrometer-grained Cu and Ni using high-resolution electron," *Journal of Materials Research*, vol. 13, no. 2, pp. 446 – 450, 1998.

[96] Horstemeyer, M. F., Baskes, M. I., and Plimpton, S. J., "Computational nanoscale plasticity simulations using embedded atom potentials," *Theoretical and Applied Fracture Mechanics*, vol. 37, no. 1-3, pp. 49–98, 2001.

[97] Horstemeyer, M. F. and Baskes, M., "Atomistic finite deformation simulations: A discussion on length scale effects in relation to mechanical stresses," *Journal of Engineering Materials and Technology, Transactions of the ASME*, vol. 121, no. 2, pp. 114 – 119, 1999.

[98] Horstemeyer, M., Baskes, M., Prantil, V., Philliber, J., and Vonderheide, S., "A multiscale analysis of fixed-end simple shear using molecular dynamics, crystal plasticity, and a macroscopic internal state variable theory," *Modelling and Simulation in Materials Science and Engineering*, vol. 11, no. 3, pp. 265 – 286, 2003.

[99] Islamgaliev, R. and Valiev, R., "Non-equilibrium grain boundaries in ultrafine-grained materials processed by severe plastic deformation," *Materials Science Forum*, vol. 294-296, pp. 361 – 4, 1999.

[100] Jiang, B. and Weng, G., "A composite model for the grain-size dependence of yield stress of nanograined materials," *Metallurgical and Materials Transactions A: Physical Metallurgy and Materials Science*, vol. 34, no. 13, pp. 765 – 772, 2003.

[101] Kadau, K., Germann, T. C., and Lomdahl, P. S., "Molecular dynamics comes of age: 320 billion atom simulation on bluegene/l," *International Journal of Modern Physics C*, vol. 17, no. 12, pp. 1755–1761, 2006.

[102] Karimpoor, A., Erb, U., Aust, K., and Palumbo, G., "High strength nanocrystalline cobalt with high tensile ductility," *Scr. Mater. (USA)*, vol. 49, no. 7, pp. 651 – 6, 2003.

[103] Karimpoor, A., Erb, U., Aust, K., and Palumbo, G., "High strength nanocrystalline cobalt with high tensile ductility," *Scripta Materialia*, vol. 49, no. 7, pp. 651 – 656, 2003.

[104] Kato, M., "Thermally activated dislocation depinning at a grain boundary in nanocrystalline and ultrafine-grained materials," *Materials Science & Engineering: A (Structural Materials: Properties, Microstructure and Processing)*, vol. 516, no. 1-2, pp. 276 – 82, 2009.

[105] Kelchner, C. L., Plimpton, S. J., and Hamilton, J. C., "Dislocation nucleation and defect structure during surface indentation," *Physical Review B*, vol. 58, no. 17, pp. 11085–8, 1998.

[106] Khan, A. S., Suh, Y. S., Xu, C., Takacs, L., and Haoyue, Z., "Nanocrystalline aluminum and iron: Mechanical behavior at quasi-static and high strain rates, and constitutive modeling," *International Journal of Plasticity*, vol. 22, no. 2, pp. 195–209, 2006.

[107] Khan, A. S., Farrokh, B., and Takacs, L., "Compressive properties of Cu with different grain sizes: Sub-micron to nanometer realm," *Journal of Materials Science*, vol. 43, no. 9, pp. 3305 – 3313, 2008.

[108] Khon, Y., Kolobov, Y., Ivanov, M., and Butenko, A., "Nonequilibrium state of grain boundaries and spontaneous grain-boundary slippage in bicrystals," *Technical Physics*, vol. 53, no. 3, pp. 328 – 33, 2008.

[109] Kizuka, T., "Atomistic process of twin-boundary migration induced by shear deformation in gold," *Japanese Journal of Applied Physics, Part 1: Regular Papers and Short Notes and Review Papers*, vol. 46, no. 11, pp. 7396 – 7398, 2007.

[110] Klein, P. and Zimmerman, J., "Coupled atomistic-continuum simulations using arbitrary overlapping domains," *Journal of Computational Physics*, vol. 213, no. 1, pp. 86 – 116, 2006.

[111] Koch, C. C., Youssef, K. M., Scattergood, R. O., and Murty, K. L., "Breakthroughs in optimization of mechanical properties of nanostructured metals and alloys," *Advanced Engineering Materials*, vol. 7, no. 9, pp. 787 – 794, 2005.

[112] Koch, C., "Optimization of strength and ductility in nanocrystalline and ultrafine grained metals," *Scripta Materialia*, vol. 49, no. 7, pp. 657 – 662, 2003.

[113] Koch, C., Morris, D., Lu, K., and Inoue, A., "Ductility of nanostructured materials," *MRS Bulletin*, vol. 24, no. 2, pp. 54 – 58, 1999.

[114] Koch, C., Ovid'ko, I., Seal, S., and Veprek, S., *Structural Nanocrystalline Materials: Fundamentals and Applications*. Cambridge University Press, 2007.

[115] Kovacs, I., "The mechanism of the work-hardening in f.c.c. metals," *Acta Metallurgica*, vol. 15, no. 11, pp. 1731 – 1736, 1967.

[116] Krasilnikov, N. and Raab, G., "Grain boundary effects in nanocrystalline copper," *Materials Science Forum*, vol. 294-296, pp. 701 – 706, 1999.

[117] Kumar, K. S., Van Swygenhoven, H., and Suresh, S., "Mechanical behavior of nanocrystalline metals and alloys," *Acta Materialia*, vol. 51, no. 19, pp. 5743–5774, 2003.

[118] Kuriplach, J., Melikhova, O., Hou, M., Van Petegem, S., Zhurkin, E., and Sob, M., "Positron annihilation in vacancies at grain boundaries in metals," *Applied Surface Science*, vol. 255, no. 1, pp. 128 – 131, 2008.

[119] Lee, B. J. and Baskes, M. I., "Second nearest-neighbor modified embedded-atom-method potential," *Physical Review B*, vol. 62, no. 13, pp. 8564–8567, 2000.

[120] Lee, S. B., Sigle, W., and Ruhle, M., "Faceting behavior of an asymmetric $SrTiO_3$ $\Sigma 5$ [100] tilt grain boundary close to its defaceting transition," *Acta Materialia*, vol. 51, no. 15, pp. 4583–8, 2003.

[121] Li, H., Choo, H., Ren, Y., Saleh, T., Lienert, U., Liaw, P., and Ebrahimi, F., "Strain-dependent deformation behavior in nanocrystalline metals," *Physical Review Letters*, vol. 101, no. 1, p. 015502, 2008.

[122] Li, X., "A coarse-grained molecular dynamics model for crystalline solids," *International Journal for Numerical Methods in Engineering*, vol. 83, no. 8-9, pp. 986–997, 2010.

[123] Li, X., Wei, Y., Yang, W., and Gao, H., "Competing grain-boundary-and dislocation-mediated mechanisms in plastic strain recovery in nanocrystalline aluminum," *Proceedings of the National Academy of Sciences of the United States of America*, vol. 106, no. 38, pp. 16108 – 13, 2009.

[124] Liao, X. Z., Srinivasan, S. G., Zhao, Y. H., Baskes, M. I., Zhu, Y. T., Zhou, F., Lavernia, E. J., and Xu, H. F., "Formation mechanism of wide stacking faults in nanocrystalline Al," *Applied Physics Letters*, vol. 84, no. 18, pp. 3564–3566, 2004.

[125] Liao, X. Z., Zhou, F., Lavernia, E. J., Srinivasan, S. G., Baskes, M. I., He, D. W., and Zhu, Y. T., "Deformation mechanism in nanocrystalline Al: Partial dislocation slip," *Applied Physics Letters*, vol. 83, no. 4, pp. 632–634, 2003.

[126] Liao, X., Zhao, Y., Srinivasan, S., Zhu, Y., Valiev, R., and Gunderov, D., "Deformation twinning in nanocrystalline copper at room temperature and low strain rate," *Applied Physics Letters*, vol. 84, no. 4, pp. 592 – 4, 2004/01/26.

[127] Liao, X., Zhao, Y., Zhu, Y., Valiev, R., and Gunderov, D., "Grain-size effect on the deformation mechanisms of nanostructured copper processed by high-pressure torsion," *Journal of Applied Physics*, vol. 96, no. 1, pp. 636 – 40, 2004/07/01.

[128] Liu, X.-Y., Ercolessi, F., and Adams, J. B., "Aluminium interatomic potential from density functional theory calculations with improved stacking fault energy," *Modelling and Simulation in Materials Science and Engineering*, vol. 12, no. 4, pp. 665–670, 2004.

[129] Liu, Y., Xie, Z., Van Humbeeck, J., and Delaey, L., "Asymmetry of stress-strain curves under tension and compression for NiTi shape memory alloys," *Acta Materialia*, vol. 46, no. 12, pp. 4325 – 4338, 1998.

[130] Lu, B. and Torquato, S., "Lineal-path function for random heterogeneous materials," *Physical Review A (Statistical Physics, Plasmas, Fluids, and Related Interdisciplinary Topics)*, vol. 45, no. 2, pp. 922 – 9, 1992.

[131] Lu, L., Shen, Y. F., Chen, X. H., Qian, L. H., and Lu, K., "Ultrahigh strength and high electrical conductivity in copper," *Science*, vol. 304, no. 5669, pp. 422–426, 2004.

[132] Lund, A., Nieh, T., and Schuh, C., "Tension/compression strength asymmetry in a simulated nanocrystalline metal," *Physical Review B (Condensed Matter and Materials Physics)*, vol. 69, no. 1, pp. 12101 – 1, 2004.

[133] Luo, H., Shaw, L., Zhang, L., and Miracle, D., "On tension/compression asymmetry of an extruded nanocrystalline Al-Fe-Cr-Ti alloy," *Materials Science and Engineering A*, vol. 409, no. 1-2, pp. 249 – 256, 2005.

[134] Ma, E., "Instabilities and ductility of nanocrystalline and ultrafine-grained metals," *Scripta Materialia*, vol. 49, no. 7, pp. 663 – 668, 2003.

[135] Ma, E., "Nanocrystalline materials - controlling plastic instability," *Nature Materials*, vol. 2, no. 1, pp. 7–8, 2003.

[136] Ma, E., "Eight routes to improve the tensile ductility of bulk nanostructured metals and alloys," *JOM*, vol. 58, no. 4, pp. 49 – 53, 2006.

[137] Ma, E., Wang, Y. M., Lu, Q. H., Sui, M. L., Lu, L., and Lu, K., "Strain hardening and large tensile elongation in ultrahigh-strength nano-twinned copper," *Applied Physics Letters*, vol. 85, no. 21, pp. 4932–4934, 2004.

[138] Mara, N., Sergueeva, A., Mara, T., McFadden, S., and Mukherjee, A., "Superplasticity and cooperative grain boundary sliding in nanocrystalline Ni_3Al," *Materials Science and Engineering A*, vol. 463, no. 1-2, pp. 238 – 244, 2007.

[139] Marc, G. and McMillan, W., "The virial-theorem," *Advances in Chemical Physics*, vol. 58, pp. 209–361, 1985.

[140] Masumura, R., Hazzledine, P., and Pande, C., "Yield stress of fine grained materials," *Acta Materialia*, vol. 46, no. 13, pp. 4527 – 34, 1998.

[141] Mehl, M., Papaconstantopoulos, D., Kioussis, N., and Herbranson, M., "Tight-binding study of stacking fault energies and the rice criterion of ductility in the fcc metals," *Physical Review B (Condensed Matter)*, vol. 61, no. 7, pp. 4894 – 7, 2000.

[142] Melchionna, S., Ciccotti, G., and Holian, B. L., "Hoover *NPT* dynamics for systems varying in shape and size," *Molecular Physics*, vol. 78, no. 3, pp. 533–44, 1993.

[143] Metropolis, N., Rosenbluth, A. W., Rosenbluth, M. N., Teller, A. H., and Teller, E., "Equation of state calculations by fast computing machines," *Journal of Chemical Physics*, vol. 21, no. 6, pp. 1087–1092, 1953.

[144] Metropolis, N. and Ulam, S., "The monte carlo method," *Journal of the American Statistical Association*, vol. 44, no. 247, pp. 335–341, 1949.

[145] Meyers, M. A., Mishra, A., and Benson, D. J., "Mechanical properties of nanocrystalline materials," *Progress in Materials Science*, vol. 51, no. 4, pp. 427–556, 2006.

[146] Milligan, W. W., *Comprehensive Structural Integrity*. Elsevier, 2003.

[147] Mills, M. J., Daw, M. S., Thomas, G. J., and Cosandey, F., "High-resolution transmission electron microscopy of grain boundaries in aluminum and correlation with atomistic calculations," *Ultramicroscopy*, vol. 40, no. 3, pp. 247–257, 1992.

[148] Mishin, O., Gertsman, V., Valiev, R., and Gottstein, G., "Grain boundary distribution and texture in ultrafine-grained copper produced by severe plastic deformation," *Scripta Materialia*, vol. 35, no. 7, pp. 873 – 878, 1996.

[149] Mishin, Y., Farkas, D., Mehl, M. J., and Papaconstantopoulos, D. A., "Interatomic potentials for monoatomic metals from experimental data and *ab initio* calculations," *Physical Review B*, vol. 59, no. 5, pp. 3393–407, 1999.

[150] Mishin, Y., Mehl, M. J., Papaconstantopoulos, D. A., Voter, A. F., and Kress, J. D., "Structural stability and lattice defects in copper: *Ab initio*, tight-binding, and embedded-atom calculations," *Physical Review B*, vol. 63, no. 22, pp. 224106–1, 2001.

[151] Monk, J. and Farkas, D., "Tension-compression asymmetry and size effects in nanocrystalline Ni nanowires," *Philosophical Magazine*, vol. 87, no. 14-15, pp. 223 – 44, 2007.

[152] Murr, L., *Interfacial Phenomena in Metals and Alloys*. Addison-Wesley (Reading, MA), 1975.

[153] Musalimov, R. and Valiev, R., "Dilatometric analysis of aluminium alloy with submicrometre grained structure," *Scripta metallurgica et materialia*, vol. 27, no. 12, pp. 1685 – 1690, 1992.

[154] Nazarov, A., Romanov, A., and Valiev, R., "On the structure, stress fields and energy of nonequilibrium grain boundaries," *Acta metallurgica et materialia*, vol. 41, no. 4, pp. 1033 – 1040, 1993.

[155] Nazarov, A., Romanov, A., and Valiev, R., "Models of the defect structure and analysis of the mechanical behavior of nanocrystals," *Nanostructured Materials*, vol. 6, no. 5-8, pp. 775 – 778, 1995.

[156] Nazarov, A., Shenderova, O., and Brenner, D., "On the disclination-structural unit model of grain boundaries," *Materials Science & Engineering A (Structural Materials: Properties, Microstructure and Processing)*, vol. A281, no. 1-2, pp. 148–55, 2000.

[157] Nomura, K.-i., Chen, Y.-C., Weiqiang, W., Kalia, R. K., Nakano, A., Vashishta, P., and Yang, L. H., "Interaction and coalescence of nanovoids and dynamic fracture in silica glass: multimillion-to-billion atom molecular dynamics simulations," *Journal of Physics D - Applied Physics*, vol. 42, no. 21, 2009.

[158] Ogata, S., Ju, L., and Yip, S., "Ideal pure shear strength of aluminum and copper," *Science*, vol. 298, no. 5594, pp. 807–11, 2002.

[159] Olmsted, D. L., Foiles, S. M., and Holm, E. A., "Survey of computed grain boundary properties in face-centered cubic metals: I. grain boundary energy," *Acta Materialia*, vol. 57, no. 13, pp. 3694–3703, 2009.

[160] Ovid'ko, I., "Deformation and diffusion modes in nanocrystalline materials," *Int. Mater. Rev. (UK)*, vol. 50, no. 2, pp. 65 – 82, 2005.

[161] Ovid'ko, I., "Superplasticity and ductility of superstrong nanomaterials," *Reviews on Advanced Materials Science*, vol. 10, no. 2, pp. 89 – 104, 2005.

[162] Padilla II, H. and Boyce, B., "A review of fatigue behavior in nanocrystalline metals," *Experimental Mechanics*, vol. 50, no. 1, pp. 5 – 23, 2010.

[163] Padmanabhan, K. and Gleiter, H., "Optimal structural superplasticity in metals and ceramics of microcrystalline- and nanocrystalline-grain sizes," *Materials Science and Engineering A*, vol. 381, no. 1-2, pp. 28 – 38, 2004.

[164] Pande, C. and Cooper, K., "Nanomechanics of hall-petch relationship in nanocrystalline materials," *Progress in Materials Science*, vol. 54, no. 6, pp. 689 – 706, 2009.

[165] Park, H. S., "A multiscale finite element method for the dynamic analysis of surface-dominated nanomaterials," *International Journal for Numerical Methods in Engineering*, vol. 83, no. 8-9, pp. 1237 – 1254, 2010.

[166] Petch, N. J., "Cleavage strength of polycrystals," *Iron and Steel Institute - Journal*, vol. 174, no. Part 1, pp. 25–28, 1953.

[167] Plimpton, S., "Fast parallel algorithms for short-range molecular dynamics," *Journal of Computational Physics*, vol. 117, no. 1, pp. 1–19, 1995.

[168] Pond, R., Smith, D., and Vitek, V., "Model for grain-boundary structure based on random close packing," *Scripta Metallurgica*, vol. 12, no. 8, pp. 699–702, 1978.

[169] Prasad, M. and Chokshi, A., "Superplasticity in electrodeposited nanocrystalline nickel," *Acta Materialia*, vol. 58, no. 17, pp. 5724 – 5736, 2010.

[170] Qian, X., Chou, Y., and Kamenetzky, E., "The structure dependence of grain boundary corrosion in niobium bicrystals," *Journal of the Less-Common Metals*, vol. 134, no. 2, pp. 179 – 85, 1987.

[171] Qin, E., Lu, L., Tao, N., Tan, J., and Lu, K., "Enhanced fracture toughness and strength in bulk nanocrystalline Cu with nanoscale twin bundles," *Acta Materialia*, vol. 57, no. 20, pp. 6215 – 6225, 2009.

[172] Rahman, A., "Correlations in the motions of atoms in liquid argon," *Physical Review*, vol. 136, p. A405A411, 1964.

[173] Randle, V., *The Role of the Coincident Site Lattice in Grain Boundary Engineering*. Cambridge: The University Press, 1996.

[174] Randle, V., "Mechanism of twinning-induced grain boundary engineering in low stacking-fault energy materials," *Acta Materialia*, vol. 47, pp. 4187–96, 1999.

[175] Randle, V., Coleman, M., and Waterton, M., "The role of Σ9 boundaries in grain boundary engineering," *Metallurgical and Materials Transactions A: Physical Metallurgy and Materials Science*, vol. 42, no. 3, pp. 582 – 586, 2011.

[176] Randle, V. and Hu, Y., "The role of vicinal Σ3 boundaries and Σ9 boundaries in grain boundary engineering," *Journal of Materials Science*, vol. 40, no. 12, pp. 3243 – 3246, 2005.

[177] Randle, V., "Twinning-related grain boundary engineering," *Acta Materialia*, vol. 52, no. 14, pp. 4067–4081, 2004.

[178] Randle, V., "'Special' boundaries and grain boundary plane engineering," *Scripta Materialia*, vol. 54, no. 6, pp. 1011–1015, 2006.

[179] Rice, J. R., "Dislocation nucleation from a crack tip: an analysis based on the Peierls concept," *Journal of the Mechanics and Physics of Solids*, vol. 40, no. 2, pp. 239–71, 1992.

[180] Rittner, J. D. and Seidman, D. N., "⟨110⟩ symmetric tilt grain-boundary structures in fcc metals with low stacking-fault energies," *Physical Review B*, vol. 54, no. 10, p. 6999, 1996.

[181] Rittner, J. D., Seidman, D. N., and Merkle, K. L., "Grain-boundary dissociation by the emission of stacking faults," *Physical Review B*, vol. 53, no. 8, pp. 4241–4, 1996.

[182] Sanders, P. G., Eastman, J. A., and Weertman, J. R., "Elastic and tensile behavior of nanocrystalline copper and palladium," *Acta Materialia*, vol. 45, no. 10, pp. 4019–4025, 1997.

[183] Sansoz, F. and Molinari, J. F., "Incidence of atom shuffling on the shear and decohesion behavior of a symmetric tilt grain boundary in copper," *Scripta Materialia*, vol. 50, no. 10, pp. 1283–8, 2004.

[184] Sansoz, F. and Molinari, J. F., "Mechanical behavior of Σ tilt grain boundaries in nanoscale Cu and Al: A quasicontinuum study," *Acta Materialia*, vol. 53, no. 7, pp. 1931–1944, 2005.

[185] Schafler, E., Steiner, G., Korznikova, E., Kerber, M., and Zehetbauer, M., "Lattice defect investigation of ECAP-Cu by means of X-ray line profile analysis, calorimetry and electrical resistometry," *Mater. Sci. Eng. A, Struct. Mater., Prop. Microstruct. Process. (Switzerland)*, vol. 410-411, pp. 169 – 73, 2005.

[186] Schiøtz, J., Di Tolla, F. D., and Jacobsen, K. W., "Softening of nanocrystalline metals at very small grain sizes," *Nature*, vol. 391, no. 6667, pp. 561–3, 1998.

[187] Schiøtz, J. and Jacobsen, K. W., "A maximum in the strength of nanocrystalline copper," *Science*, vol. 301, no. 5638, pp. 1357–9, 2003.

[188] Schiøtz, J., Vegge, T., Di Tolla, F. D., and Jacobsen, K. W., "Atomic-scale simulations of the mechanical deformation of nanocrystalline metals," *Physical Review B*, vol. 60, no. 17, pp. 11971–83, 1999.

[189] Schiøtz, J., "Atomic-scale modeling of plastic deformation of nanocrystalline copper," *Scripta Materialia*, vol. 51, no. 8 SPEC ISS, pp. 837–841, 2004.

[190] Schuh, C., Nieh, T., and Yamasaki, T., "Hall-petch breakdown, manifested in abrasive wear resistance of nanocrystalline nickel," *Scr. Mater. (USA)*, vol. 46, no. 10, pp. 735 – 40, 2002.

[191] Schuster, B., Wei, Q., Zhang, H., and Ramesh, K., "Microcompression of nanocrystalline nickel," *Applied Physics Letters*, vol. 88, no. 10, pp. 103112 – 1, 2006.

[192] Shan, Z., Stach, E. A., Wiezorek, J. M. K., Knapp, J. A., Follstaedt, D. M., and Mao, S. X., "Grain boundary-mediated plasticity in nanocrystalline nickel," *Science*, vol. 305, no. 5684, pp. 654–657, 2004.

[193] Shen, T., Koch, C., Tsui, T., and Pharr, G., "On the elastic moduli of nanocrystalline Fe, Cu, Ni, and Cu-Ni alloys prepared by mechanical milling/alloying," *Journal of Materials Research*, vol. 10, no. 11, pp. 2892 – 2896, 1995.

[194] Shen, X., Lian, J., Jiang, Z., and Jiang, Q., "The optimal grain sized nanocrystalline Ni with high strength and good ductility fabricated by a direct current electrodeposition," *Advanced Engineering Materials*, vol. 10, no. 6, pp. 539 – 46, 2008.

[195] Shen, X., Lian, J., Jiang, Z., and Jiang, Q., "High strength and high ductility of electrodeposited nanocrystalline Ni with a broad grain size distribution," *Materials Science & Engineering: A (Structural Materials: Properties, Microstructure and Processing)*, vol. 487, no. 1-2, pp. 410 – 16, 2008.

[196] Shewchuk, J., "An introduction to the conjugate gradient method without the agonizing pain," 1994.

[197] Shi, J. and Zikry, M., "Grain size, grain boundary sliding, and grain boundary interaction effects on nanocrystalline behavior," *Materials Science and Engineering A*, vol. 520, no. 1-2, pp. 121 – 133, 2009.

[198] Shilkrot, L., Miller, R., and Curtin, W., "Coupled atomistic and discrete dislocation plasticity," *Physical Review Letters*, vol. 89, no. 2, pp. 025501 – 1, 2002.

[199] Shilkrot, L., Miller, R. E., and Curtin, W. A., "Multiscale plasticity modeling: Coupled atomistics and discrete dislocation mechanics," *Journal of the Mechanics and Physics of Solids*, vol. 52, no. 4, pp. 755 – 787, 2004.

[200] Shvindlerman, L. and Gottstein, G., "Unexplored topics and potentials of grain boundary engineering," *Scripta Materialia*, vol. 54, no. 6, pp. 1041 – 1045, 2006.

[201] Siegel, R., "Mechanical properties of nanophase materials," *Materials Science Forum*, vol. 235-238, no. pt 2, pp. 851 – 860, 1997.

[202] Smith, D., Vitek, V., and Pond, R., "Computer-simulation of symmetrical high angle boundaries in aluminum," *Acta Metallurgica*, vol. 25, no. 5, pp. 475–483, 1977.

[203] Spearot, D. E., Jacob, K. I., and McDowell, D. L., "Nucleation of dislocations from [001] bicrystal interfaces in aluminum," *Acta Materialia*, vol. 53, no. 13, pp. 3579–89, 2005.

[204] Spearot, D. E., Jacob, K. I., and McDowell, D. L., "Dislocation nucleation from bicrystal interfaces with dissociated structure," *International Journal of Plasticity*, vol. 23, no. 1, pp. 143–160, 2007.

[205] Spearot, D., *Atomistic Calculations of Nanoscale Interface Behavior in FCC Metals*. PhD thesis, Georgia Institute of Technology, 2005.

[206] Spearot, D., Capolungo, L., Qu, J., and Cherkaoui, M., "On the elastic tensile deformation of ⟨100⟩ bicrystal interfaces in copper," *Computational Materials Science*, vol. 42, no. 1, pp. 57 – 67, 2008.

[207] Spearot, D., Tschopp, M., Jacob, K., and McDowell, D., "Tensile strength of ⟨100⟩ and ⟨110⟩ tilt bicrystal copper interfaces," *Acta Materialia*, vol. 55, no. 2, pp. 705–714, 2007.

[208] Spearot, D. E., "Evolution of the E structural unit during uniaxial and constrained tensile deformation," *Mechanics Research Communications*, vol. 35, no. 1-2, pp. 81 – 88, 2008.

[209] Spearot, D. E., Jacob, K. I., and McDowell, D. L., "Non-local separation constitutive laws for interfaces and their relation to nanoscale simulations," *Mechanics of Materials*, vol. 36, no. 9, pp. 825–847, 2004.

[210] Suryanarayana, C., "Nanocrystalline materials," *International Materials Reviews*, vol. 40, no. 2, pp. 41 – 64, 1995.

[211] Sutton, A. P. and Balluffi, R. W., *Interfaces in Crystalline Materials*. Oxford: Clarendon Press, 1995.

[212] Sutton, A. P. and Vitek, V., "On the structure of tilt grain boundaries in cubic metals. I. Symmetrical tilt boundaries," *Philosophical Transactions of the Royal Society of London A*, vol. 309, no. 1506, pp. 1–36, 1983.

[213] Sutton, A. P. and Vitek, V., "On the structure of tilt grain boundaries in cubic metals. II. Asymmetrical tilt boundaries," *Philosophical Transactions of the Royal Society of London A*, vol. 309, no. 1506, pp. 37–54, 1983.

[214] Sutton, A. P. and Vitek, V., "On the structure of tilt grain boundaries in cubic metals. III. Generalizations of the structural study and implications for the properties of grain boundaries," *Philosophical Transactions of the Royal Society of London A*, vol. 309, no. 1506, pp. 55–68, 1983.

[215] Suzuki, A. and Mishin, Y., "Atomistic modeling of point defects and diffusion in copper grain boundaries," *Interface Science*, vol. 11, no. 1, pp. 131 – 48, 2003.

[216] Suzuki, A. and Mishin, Y., "Interaction of point defects with grain boundaries in fcc metals," *Interface Science*, vol. 11, no. 4, pp. 425 – 37, 2003.

[217] Tadmor, E. B., Ortiz, M., and Phillips, R., "Quasicontinuum analysis of defects in solids," *Philosophical Magazine A*, vol. 73, no. 6, pp. 1529–63, 1996.

[218] Tewari, A., Gokhale, A. M., Spowart, J. E., and Miracle, D. B., "Quantitative characterization of spatial clustering in three-dimensional microstructures using two-point correlation functions," *Acta Materialia*, vol. 52, no. 2, pp. 307–19, 2004.

[219] Trelewicz, J. R. and Schuh, C. A., "The hall-petch breakdown in nanocrystalline metals: A crossover to glass-like deformation," *Acta Materialia*, vol. 55, no. 17, pp. 5948 – 5958, 2007.

[220] Tschopp, M. and McDowell, D., "Asymmetric tilt grain boundary structure and energy in copper and aluminum," *Philosophical Magazine*, vol. 87, no. 25, pp. 3871–3892, 2007.

[221] Tschopp, M. and McDowell, D., "Structural unit and faceting description for $\Sigma 3$ asymmetric tilt grain boundaries," *Journal of Materials Science*, pp. doi: 10.1007 / s10853–007–1626–6, 2007.

[222] Tschopp, M. and McDowell, D., "Structures and energies of $\Sigma 3$ asymmetric tilt grain boundaries in Cu and Al," *Philosophical Magazine*, vol. 87, no. 22-24, pp. 3147–73, 2007.

[223] Tschopp, M. and McDowell, D., "Structures, energies and dislocation nucleation behaviours of Σ3 asymmetric tilt grain boundaries," in *TMS 2007 Symposium Proceedings: Plasticity from the Atomic Scale to Constitutive Laws*, 2007.

[224] Tschopp, M. and McDowell, D., "Tension-compression asymmetry in homogeneous dislocation nucleation in single crystal copper," *Applied Physics Letters*, vol. 90, pp. 121916:1–3, 2007.

[225] Tschopp, M. and McDowell, D., "Dislocation nucleation in Σ3 asymmetric tilt grain boundaries," *International Journal of Plasticity*, vol. 24, no. 2, pp. 191–217, 2008.

[226] Tschopp, M. and McDowell, D., "Grain boundary dislocation sources in nanocrystalline copper," *Scripta Materialia*, vol. 58, no. 4, pp. 299 – 302, 2008.

[227] Tschopp, M. and McDowell, D., "Influence of single crystal orientation on homogeneous dislocation nucleation under uniaxial loading," *J. Mech. Phys. Solids*, vol. 56, no. 5, pp. 1806 – 30, 2008.

[228] Tschopp, M., Spearot, D., and McDowell, D., "Atomistic simulations of homogeneous dislocation nucleation in single crystal copper," *Modelling and Simulation in Materials Science and Engineering*, vol. 15, no. 7, pp. 693 – 709, 2007.

[229] Tschopp, M., Tucker, G., and McDowell, D., "Structure and free volume of ⟨110⟩ symmetric tilt grain boundaries with the E structural unit," *Acta Materialia*, vol. 55, pp. 3959–3969, 2007.

[230] Tschopp, M., Tucker, G., and McDowell, D., "Atomistic simulations of tension-compression asymmetry in dislocation nucleation for copper grain boundaries," *Computational Materials Science*, vol. 44, no. 2, pp. 351 – 362, 2008.

[231] Tsuzuki, H., Branicio, P., and Rino, J., "Structural characterization of deformed crystals by analysis of common atomic neighborhood," *Computer Physics Communications*, vol. 177, no. 6, pp. 518 – 23, 2007.

[232] Tsuzuki, H., Branicio, P. S., and Rino, J. P., "Structural characterization of deformed crystals by analysis of common atomic neighborhood," *Computer Physics Communications*, vol. 177, no. 6, pp. 518 – 523, 2007.

[233] Tucker, G., Tiwari, S., Zimmerman, J., and McDowell, D., "Investigating the deformation of nanocrystalline copper with microscale kinematic metrics and molecular dynamics," *Journal of the Mechanics and Physics of Solids*, p. Submitted, 2011.

[234] Tucker, G. J. and McDowell, D. L., "Non-equilibrium grain boundary structure and inelastic deformation using atomistic simulations," *International Journal of Plasticity*, 2010. , In press.

[235] Tucker, G. J., Tschopp, M. A., and McDowell, D. L., "Evolution of structure and free volume in symmetric tilt grain boundaries during dislocation nucleation," *Acta Materialia*, vol. 58, no. 19, pp. 6464 – 6473, 2010.

[236] Tucker, G., Zimmerman, J., and McDowell, D., "Shear deformation kinematics of bicrystalline grain boundaries in atomistic simulations," *Modelling and Simulation in Materials Science and Engineering*, vol. 18, no. 1, p. 015002, 2010.

[237] Tucker, G., Zimmerman, J., and McDowell, D., "Continuum metrics for deformation and microrotation from atomistic simulations: Application to grain boundaries," *International Journal of Engineering Science*, 2011. In Review.

[238] Uchic, M. and Dimiduk, D., "A methodology to investigate size scale effects in crystalline plasticity using uniaxial compression testing," *Materials Science and Engineering A*, vol. 400-401, pp. 268–278, 2005.

[239] Uchic, M., Dimiduk, D., Florando, J., and Nix, W., "Sample dimensions influence strength and crystal plasticity," *Science*, vol. 305, pp. 986–989, 2004.

[240] Ungar, T., "Subgrain size-distributions, dislocation structures, stacking- and twin faults and vacancy concentrations in SPD materials determined by x-ray line profile analysis," *Materials Science Forum*, vol. 503-504, pp. 133 – 40, 2006.

[241] Ungar, T., Schafler, E., Hanak, P., Bernstorff, S., and Zehetbauer, M., "Vacancy concentrations determined from the diffuse background scattering of x-rays in plastically deformed copper," *Z. Met.kd. (Germany)*, vol. 96, no. 6, pp. 578 – 83, 2005.

[242] Ungar, T., Schafler, E., Hanak, P., Bernstorff, S., and Zehetbauer, M., "Vacancy production during plastic deformation in copper determined by in situ x-ray diffraction," *Materials Science and Engineering A*, vol. 462, no. 1-2, pp. 398 – 401, 2007.

[243] Valiev, R.Z. Alexandrov, I., "A paradox of severe plastic deformation in metals," *Doklady Physics*, vol. 6, pp. 633–635, 2001.

[244] Valiev, R., "Nanostructuring of metals by severe plastic deformation for advanced properties," *Nature Materials*, vol. 3, no. 8, pp. 511–516, 2004.

[245] Valiev, R., "The new trends in fabrication of bulk nanostructured materials by SPD processing," *Journal of Materials Science*, vol. 42, no. 5, pp. 1483 – 90, 2007.

[246] Valiev, R., Alexandrov, I., Zhu, Y., and Lowe, T., "Paradox of strength and ductility in metals processed by severe plastic deformation," *Journal of Materials Research*, vol. 17, no. 1, pp. 5 – 8, 2002.

[247] Valiev, R., Estrin, Y., Horita, Z., Langdon, T., Zehetbauer, M., and Zhu, Y., "Producing bulk ultrafine-grained materials by severe plastic deformation," *JOM*, vol. 58, no. 4, pp. 33 – 9, 2006.

[248] Valiev, R., Islamgaliev, R., and Alexandrov, I., "Bulk nanostructured materials from severe plastic deformation," *Progress in Materials Science*, vol. 45, no. 2, pp. 103 – 189, 2000.

[249] Valiev, R., Korznikov, A., and Mulyukov, R., "Structure and properties of ultrafine-grained materials produced by severe plastic deformation," *Materials Science and Engineering A*, vol. A168, no. 2, pp. 141 – 148, 1993.

[250] Valiev, R., Kozlov, E., Ivanov, Y., Lian, J., Nazarov, A., and Baudelet, B., "Deformation behaviour of ultra-fine-grained copper," *Acta metallurgica et materialia*, vol. 42, no. 7, pp. 2467 – 2475, 1994.

[251] Valiev, R., Krasilnikov, N., and Tsenev, N., "Plastic deformation of alloys with submicron-grained structure," *Materials Science and Engineering A*, vol. A137, pp. 35 – 40, 1991.

[252] Valiev, R., Zehetbauer, M., Estrin, Y., Hoppel, H., Ivanisenko, Y., Hahn, H., Wilde, G., Roven, H., Sauvage, X., and Langdon, T., "The innovation potential of bulk nanostructured materials," *Advanced Engineering Materials*, vol. 9, no. 7, pp. 527 – 33, 2007.

[253] Van Petegem, S., Dalla Torre, F., Segers, D., and Van Swygenhoven, H., "Free volume in nanostructured Ni," *Scripta Materialia*, vol. 48, no. 1, pp. 17–22, 2003.

[254] Van Petegem, S. and Kuriplach, J., "Calculation of free volume in computer generated grain boundaries," *Acta Physica Polonica A*, vol. 107, no. 5, pp. 769 – 775, 2005.

[255] Van Swygenhoven, H. and Caro, A., "Molecular dynamics computer simulation of nanophase ni: Structure and mechanical properties," *Nanostructured Materials*, vol. 9, no. 1-8, pp. 669–672, 1997.

[256] Van Swygenhoven, H. and Caro, A., "Plastic behavior of nanophase Ni: a molecular dynamics computer simulation," *Applied Physics Letters*, vol. 71, no. 12, p. 1652, 1997.

[257] Van Swygenhoven, H. and Caro, A., "Plastic behavior of nanophase metals studied by molecular dynamics," *Physical Review B*, vol. 58, no. 17, pp. 11246–51, 1998.

[258] Van Swygenhoven, H., Caro, A., and Farkas, D., "Grain boundary structure and its influence on plastic deformation of polycrystalline FCC metals at the nanoscale: A molecular dynamics study," *Scripta Materialia*, vol. 44, no. 8-9, pp. 1513–1516, 2001.

[259] Van Swygenhoven, H., Caro, A., and Farkas, D., "A molecular dynamics study of polycrystalline fcc metals at the nanoscale: Grain boundary structure and its influence on plastic deformation," *Materials Science and Engineering A*, vol. 309-310, pp. 440–444, 2001.

[260] Van Swygenhoven, H. and Derlet, P. M., "Grain boundary sliding in nanocrystalline fcc metals," *Physical Review B*, vol. 64, pp. 224105:1–8, 2001.

[261] Van Swygenhoven, H., Derlet, P. M., Budrovic, Z., and Hasnaoui, A., "Unconventional deformation mechanism in nanocrystalline metals?," *Zeitschrift Für Metallkunde*, vol. 94, no. 10, pp. 1106–10, 2003.

[262] Van Swygenhoven, H., Derlet, P. M., and Frøseth, A. G., "Stacking fault energies and slip in nanocrystalline metals," *Nature Materials*, vol. 3, no. 6, pp. 399–403, 2004.

[263] Van Swygenhoven, H., Derlet, P. M., and Frøseth, A. G., "Nucleation and propagation of dislocations in nanocrystalline fcc metals," *Acta Materialia*, vol. 54, no. 7, pp. 1975–83, 2006.

[264] Van Swygenhoven, H., Derlet, P. M., and Hasnaoui, A., "Atomic mechanism for dislocation emission from nanosized grain boundaries," *Physical Review B*, vol. 66, no. 2, pp. 024101–1, 2002.

[265] Van Swygenhoven, H., Derlet, P. M., and Hasnaoui, A., "Atomistic modeling of strength of nanocrystalline metals," *Advanced Engineering Materials*, vol. 5, no. 5, pp. 345–50, 2003.

[266] Van Swygenhoven, H., Spaczer, M., and Caro, A., "Role of low and high angle grain boundaries in the deformation mechanism of nanophase Ni: A molecular dynamics simulation study," *Nanostructured Materials*, vol. 10, no. 5, pp. 819–828, 1998.

[267] Van Swygenhoven, H., Spaczer, M., and Caro, A., "Characterisation of the microstructure of nanophase Ni: a molecular dynamics simulation study," *Nanostructured Materials*, vol. 12, no. 5, pp. 629–632, 1999.

[268] Van Swygenhoven, H., Spaczer, M., and Caro, A., "Microscopic description of plasticity in computer generated metallic nanophase samples: A comparison between Cu and Ni," *Acta Materialia*, vol. 47, no. 10, pp. 3117–3126, 1999.

[269] Van Swygenhoven, H., Spaczer, M., Caro, A., and Farkas, D., "Competing plastic deformation mechanisms in nanophase metals," *Physical Review B (Condensed Matter)*, vol. 60, no. 1, pp. 22 – 5, 1999.

[270] Van Swygenhoven, H., Spaczer, M., Farkas, D., and Caro, A., "Role of grain size and the presence of low and high angle grain boundaries in the deformation mechanism of nanophase Ni: a molecular dynamics computer simulation," *Nanostructured Materials*, vol. 12, no. 1, pp. 323–326, 1999.

[271] Van Swygenhoven, H., "Grain boundaries and dislocations," *Science*, vol. 296, no. 5565, pp. 66–67, 2002.

[272] Van Swygenhoven, H., Dalla Torre, F., and Victoria, M., "Nanocrystalline electrodeposited Ni: Microstructure and tensile properties," *Acta Materialia*, vol. 50, no. 15, pp. 3957–3970, 2002.

[273] Van Swygenhoven, H., Hasnaoui, A., and Derlet, P. M., "On non-equilibrium grain boundaries and their effect on thermal and mechanical behaviour: A molecular dynamics computer simulation," *Acta Materialia*, vol. 50, no. 15, pp. 3927–3939, 2002.

[274] Van Swygenhoven, H. and Weertman, J. R., "Deformation in nanocrystalline metals," *Materials Today*, vol. 9, no. 5, pp. 24–31, 2006.

[275] Vanderplaats, G., *Numerical Optimization Techniques for Engineering Design*. New York: McGraw-Hill, Inc., 1984.

[276] Vinogradov, A., Kaneko, Y., Kitagawa, K., Hashimoto, S., Stolyarov, V., and Valiev, R., "Cyclic response of ultrafine-grained copper at constant plastic strain amplitude," *Scripta Materialia*, vol. 36, no. 11, pp. 1345 – 1351, 1997.

[277] Vo, N., Averback, R., Bellon, P., Odunuga, S., and Caro, A., "Quantitative description of plastic deformation in nanocrystalline cu: dislocation glide versus grain boundary sliding," *Physical Review B (Condensed Matter and Materials Physics)*, vol. 77, no. 13, pp. 134108 – 1, 2008.

[278] Volkert, C. A. and Lilleodden, E. T., "Size effects in the deformation of sub-micron au columns," *Philosophical Magazine*, vol. 86, no. 33-35, pp. 5567–5579, 2006.

[279] Volkert, C. A., Lilleodden, E. T., Kramer, D., and Weissmuller, J., "Approaching the theoretical strength in nanoporous au," *Applied Physics Letters*, vol. 89, no. 6, 2006.

[280] Voronoi, G., "New applications of continuous parameters to the theory of quadratic forms. - first memoir - some properties of perfect positive quadratic forms," vol. 133, no. 1/4, pp. 97–178, 1908.

[281] Voter, A. F. and Chen, S. P., "Accurate interatomic potentials for Ni, Al and Ni_3Al," *Characterization of Defects in Materials Symposium*, pp. 175–80, 1987.

[282] Voter, A., "Parallel replica method for dynamics of infrequent events," *Physical Review B*, vol. 57, no. 22, pp. 13985–13988, 1998.

[283] Wang, Y. M., Chen, M. W., Zhou, F. H., and Ma, E., "High tensile ductility in a nanostructured metal," *Nature*, vol. 419, no. 6910, pp. 912–915, 2002.

[284] Wang, Y. M. and Ma, E., "Strain hardening, strain rate sensitivity, and ductility of nanostructured materials," *Materials Science and Engineering A*, vol. 375-377, pp. 46–52, 2004.

[285] Wang, Y. M., Wang, K., Pan, D., Lu, K., Hemker, K. J., and Ma, E., "Microsample tensile testing of nanocrystalline copper," *Scripta Materialia*, vol. 48, no. 12, pp. 1581–1586, 2003.

[286] Wang, Y. and Ma, E., "On the origin of ultrahigh cryogenic strength of nanocrystalline metals," *Applied Physics Letters*, vol. 85, no. 14, pp. 2750 – 2752, 2004.

[287] Wang, Y. and Ma, E., "Three strategies to achieve uniform tensile deformation in a nanostructured metal," *Acta Materialia*, vol. 52, no. 6, pp. 1699 – 709, 2004/04/05.

[288] Warner, D. H., Sansoz, F., and Molinari, J. F., "Atomistic based continuum investigation of plastic deformation in nanocrystalline copper," *International Journal of Plasticity*, vol. 22, no. 4, pp. 754–774, 2006.

[289] Watanabe, T., "An approach to grain boundary design for strong and ductile polycrystals," *Res Mechanica*, vol. 11, no. 1, pp. 47–84, 1984.

[290] Watanabe, T., "The impact of grain boundary character distribution on fracture in polycrystals," *Materials Science and Engineering A*, vol. 176, no. 1-2, pp. 39–49, 1994.

[291] Watanabe, T. and Tsurekawa, S., "The control of brittleness and development of desirable mechanical properties in polycrystalline systems by grain boundary engineering," *Acta Materialia*, vol. 47, no. 15-16, pp. 4171–4185, 1999.

[292] Watanabe, T., Tsurekawa, S., Kobayashi, S., and Yamaura, S., "Structure-dependent grain boundary deformation and fracture at high temperatures," *Materials Science and Engineering A*, vol. 410-411, pp. 140–7, 2005.

[293] Watanabe, T., Yamada, M., and Karashima, S., "Grain-boundary strengthening associated with sigma=9 near-coincidence boundary in (1010) twist zinc bicrystals at high-temperatures," *Philosophical Magazine A*, vol. 63, no. 5, pp. 1013–1022, 1991.

[294] Watanabe, T., "Grain boundary engineering: historical perspective and future prospects," *Journal of Materials Science*, pp. 1 – 21, 2011.

[295] Watts, B., *Dislocations in Solids*, vol. 8. Elsevier North Holland, 1989.

[296] Weertman, J., *Nanostructured Materials: Processing, Properties, and Applications*. William Andrew Publishing, 2002.

[297] Wei, Q., Zhang, H., Schuster, B., Ramesh, K., Valiev, R., Kecskes, L., Dowding, R., Magness, L., and Cho, K., "Microstructure and mechanical properties of super-strong nanocrystalline tungsten processed by high-pressure torsion," *Acta Materialia*, vol. 54, no. 15, pp. 4079 – 4089, 2006.

[298] Wei, Y. and Anand, L., "Grain-boundary sliding and separation in polycrystalline metals: Application to nanocrystalline fcc metals," *Journal of the Mechanics and Physics of Solids*, vol. 52, no. 11, pp. 2587 – 2616, 2004.

[299] Wei, Y. and Gao, H., "An elastic-viscoplastic model of deformation in nanocrystalline metals based on coupled mechanisms in grain boundaries and grain interiors," *Materials Science and Engineering A*, vol. 478, no. 1-2, pp. 16 – 25, 2008.

[300] Wei, Y., Su, C., and Anand, L., "A computational study of the mechanical behavior of nanocrystalline fcc metals," *Acta Materialia*, vol. 54, no. 12, pp. 3177 – 3190, 2006.

[301] Wolf, D., Yamakov, V., Phillpot, S. R., Mukherjee, A., and Gleiter, H., "Deformation of nanocrystalline materials by molecular-dynamics simulation: Relationship to experiments?," *Acta Materialia*, vol. 53, no. 1, pp. 1–40, 2005.

[302] Wong, L., Ostrander, D., Erb, U., Palumbo, G., and Aust, K., *Nanophases and Nanocrystalline Structures*. TMS, 1993.

[303] Wu, X., Ma, E., and Zhu, Y., "Deformation defects in nanocrystalline nickel," *Journal of Materials Science*, vol. 42, no. 5, pp. 1427 – 32, 2007.

[304] Wu, X. and Zhu, Y., "Partial-dislocation-mediated processes in nanocrystalline ni with nonequilibrium grain boundaries," *Applied Physics Letters*, vol. 89, no. 3, pp. 31922 – 1, 2006.

[305] Wurschum, R., Greiner, W., Valiev, R., Rapp, M., Sigle, W., Schneeweiss, O., and Schaefer, H.-E., "Interfacial free volumes in ultra-fine grained metals prepared by severe plastic deformation by spark erosion, or by crystallization of amorphous alloys," *Scripta Metallurgica et Materialia*, vol. 25, no. 11, pp. 2451 – 6, 1991.

[306] Xiong, L., Tucker, G., McDowell, D. L., and Chen, Y., "Coarse-grained atomistic simulation of dislocations," *Journal of the Mechanics and Physics of Solids*, vol. 59, no. 2, pp. 160 – 177, 2011.

[307] Xu, W., Dai, P., and Wu, X., "Deformation behaviour of electrodeposited nanocrystalline ni with broad grain size distribution," *Materials Science and Technology*, vol. 26, p. 591, 2010.

[308] Yamakov, V., Wolf, D., Phillpot, S. R., and Gleiter, H., "Deformation twinning in nanocrystalline Al by molecular-dynamics simulation," *Acta Materialia*, vol. 50, no. 20, pp. 5005–20, 2002.

[309] Yamakov, V., Wolf, D., Phillpot, S. R., and Gleiter, H., "Dislocation-dislocation and dislocation-twin reactions in nanocrystalline Al by molecular dynamics simulation," *Acta Materialia*, vol. 51, no. 14, pp. 4135–47, 2003.

[310] Yamakov, V., Wolf, D., Phillpot, S. R., Mukherjee, A. K., and Gleiter, H., "Deformation mechanism crossover and mechanical behaviour in nanocrystalline materials," *Philosophical Magazine Letters*, vol. 83, no. 6, pp. 385–393, 2003.

[311] Yamakov, V., Wolf, D., Phillpot, S. R., Mukherjee, A. K., and Gleiter, H., "Deformation-mechanism map for nanocrystalline metals by molecular-dynamics simulation," *Nature Materials*, vol. 3, no. 1, pp. 43–7, 2004.

[312] Yamakov, V., Wolf, D., Phillpot, S., and Gleiter, H., "Grain-boundary diffusion creep in nanocrystalline palladium by molecular-dynamics simulation," *Acta Materialia*, vol. 50, no. 1, pp. 61–73, 2002.

[313] Yamakov, V., Wolf, D., Salazar, M., Phillpot, S. R., and Gleiter, H., "Length-scale effects in the nucleation of extended dislocations in nanocrystalline Al by molecular-dynamics simulation," *Acta Materialia*, vol. 49, no. 14, pp. 2713–2722, 2001.

[314] Yamakov, V., Wolf, D., Phillpot, S. R., Mukherjee, A. K., and Gleiter, H., "Dislocation processes in the deformation of nanocrystalline aluminium by molecular-dynamics simulation," *Nature Materials*, vol. 1, no. 1, pp. 45–48, 2002.

[315] Yapici, G., Beyerlein, I., Karaman, I., and Tome, C., "Tension-compression asymmetry in severely deformed pure copper," *Acta Materialia*, vol. 55, no. 14, pp. 4603 – 4613, 2007.

[316] Youssef, K. M., Scattergood, R. O., Murty, K. L., and Koch, C. C., "Ultratough nanocrystalline copper with a narrow grain size distribution," *Applied Physics Letters*, vol. 85, no. 6, pp. 929–931, 2004.

[317] Youssef, K. M., Scattergood, R. O., Murty, K. L., Horton, J. A., and Koch, C. C., "Ultrahigh strength and high ductility of bulk nanocrystalline copper," *Applied Physics Letters*, vol. 87, no. 9, pp. 1 – 3, 2005.

[318] Zehetbauer, M., Schafler, E., and Ungar, T., "Vacancies in plastically deformed copper," *Z. Met.kd. (Germany)*, vol. 96, no. 9, pp. 1044 – 8, 2005.

[319] Zhang, X., Fujita, T., Pan, D., Yu, J., Sakurai, T., and Chen, M., "Influences of grain size and grain boundary segregation on mechanical behavior of nanocrystalline ni," *Materials Science and Engineering A*, vol. 527, no. 9, pp. 2297 – 2304, 2010.

[320] Zhao, Y., Bingert, J., Zhu, Y., Liao, X., Valiev, R., Horita, Z., Langdon, T., Zhou, Y., and Lavernia, E., "Tougher ultrafine grain cu via high-angle grain boundaries and low dislocation density," *Applied Physics Letters*, vol. 92, no. 8, pp. 081903 – 1, 2008.

[321] Zhao, Y.-H., Bingert, J. F., Liao, X.-Z., Cui, B.-Z., Han, K., Sergueeva, A. V., Mukherjee, A. K., Valiev, R. Z., Langdon, T. G., and Zhu, Y. T., "Simultaneously increasing the ductility and strength of ultra-fine-grained pure copper," *Advanced Materials*, vol. 18, no. 22, pp. 2949 – 2953, 2006.

[322] Zhao, Y.-H., Liao, X.-Z., Cheng, S., Ma, E., and Zhu, Y. T., "Simultaneously increasing the ductility and strength of nanostructured alloys," *Advanced Materials*, vol. 18, no. 17, pp. 2280 – 2283, 2006.

[323] Zhao, Y., Topping, T., Bingert, J. F., Thornton, J. J., Dangelewicz, A. M., Li, Y., Liu, W., Zhu, Y., Zhou, Y., and Lavernia, E. J., "High tensile ductility and strength in bulk nanostructured nickel," *Advanced Materials*, vol. 20, no. 16, pp. 3028 – 3033, 2008.

[324] Zheng, Y. G., Zhang, H. W., Chen, Z., Lu, C., and Mai, Y. W., "Roles of grain boundary and dislocations at different deformation stages of nanocrystalline copper under tension," *Physics Letters A*, vol. 373, no. 5, pp. 570–574, 2009.

[325] Zhou, H. and Qu, S., "The effect of nanoscale twin boundaries on fracture toughness in nanocrystalline ni," *Nanotechnology*, vol. 21, no. 3, 2010.

[326] Zhou, M., "A new look at the atomic level virial stress–On continuum-molecular system equivalence," *Proceedings of the Royal Society of London A*, vol. 459, pp. 2347–2392, 2003.

[327] Zikry, M. and Kameda, T., "Inelastic three dimensional high strain-rate dislocation density based analysis of grain-boundary effects and failure modes in ordered intermetallics," *Mechanics of Materials*, vol. 28, no. 1 /4, pp. 93 – 102, 1998.

[328] Zimmerman, J. A., Gao, H., and Abraham, F. F., "Generalized stacking fault energies for embedded atom FCC metals," *Modelling and Simulation in Materials Science and Engineering*, vol. 8, no. 2, pp. 103–15, 2000.

[329] Zimmerman, J. A., Kelchner, C. L., Klein, P. A., Hamilton, J. C., and Foiles, S. M., "Surface step effects on nanoindentation," *Physical Review Letters*, vol. 87, no. 16, pp. 165507–1, 2001.

[330] Zimmerman, J., Bammann, D., and Gao, H., "Deformation gradients for continuum mechanical analysis of atomistic simulations," *International Journal of Solids and Structures*, vol. 46, no. 2, pp. 238 – 53, 2009.

[331] Zimmerman, J., Jones, R., and Templeton, J., "A material frame approach for evaluating continuum variables in atomistic simulations," *Journal of Computational Physics*, vol. 229, pp. 2364 – 2389, 2010.

[332] Zimmerman, J., Webb III, E., Hoyt, J., Jones, R., Klein, P., and Bammann, D., "Calculation of stress in atomistic simulation," *Modelling and Simulation in Materials Science and Engineering*, vol. 12, pp. S319–S332, 2004.

[333] Zimmerman, J. A., Gao, H., and Abraham, F. F., "Generalized stacking fault energies for embedded atom fcc metals," *Modelling and Simulation in Materials Science and Engineering*, vol. 8, no. 2, pp. 103–116, 2000.